

ResearchOnline@JCU

This file is part of the following reference:

Afshar, Sepideh (2015) *Modelling and infrared thermal imagery of hot particle curtains*. PhD thesis, James Cook University.

Access to this file is available from:

<http://researchonline.jcu.edu.au/45964/>

The author has certified to JCU that they have made a reasonable effort to gain permission and acknowledge the owner of any third party copyright material included in this document. If you believe that this is not the case, please contact ResearchOnline@jcu.edu.au and quote
<http://researchonline.jcu.edu.au/45964/>

Modelling and Infrared Thermal Imagery of Hot Particle Curtains

by

Sepideh Afshar (B.Sc., M.Sc.)

Submitted in September 2015

For the degree of Doctor of Philosophy

**College of Science, Technology and Engineering
James Cook University**

Townsville, QLD, Australia

Statement of Access

I, the undersigned, author of this work, understand that the James Cook University will make this thesis available for use within the University Library and via the Australian Digital Theses network, for use elsewhere.

I understand that, as an unpublished work, a thesis has significant protection under the Copyright Act. and;

I do not wish to place any further restriction on access to this work.

Declaration

I declare that this thesis is my own work and has not been submitted in any form for another degree or diploma at any university or other institution of tertiary education.

Information derived from the published or unpublished work of others has been acknowledged in the text and a list of references is given.

2015

Sepideh Afshar

Acknowledgements

One of the joys of completion is to look over the journey past and remember all the friends and family who have helped and supported me along this long but fulfilling road.

First and foremost, this thesis grew out of a series of interactions with my supervisor Dr. Madoc Sheehan through his Socratic questioning, he brought me closer to the reality I had initially perceived, eventually enabling me to grasp its rich complexity. His comments on chapter drafts are themselves a course in critical thought upon which I will always draw. I am grateful for his steady encouragement and infinite attention to details that ensured quality of my work.

I would like to thank the other members of my committee, Dr. Wenxian Lin, and for the assistance they provided at all levels of the research project.

I would also like to thank my entire family: not only have they always given me love and support, but they have been a constant source of encouragement throughout my entire life.

I owe sincere and earnest thankfulness to my colleague Dr. Olukayode Oludamilola Ajayi for his friendship and the simulating exchanges of ideas.

I extend my sincere thanks to Dr. Amir Fazlollahi from CSIRO in Australian E-Health Research Centre for helping me to develop Reduced Order Model. His suggestions and critical comments on image processing helped to improve the results enormously.

I gratefully acknowledge the assistance of the James Cook University in providing me scholarship during my study, and GRS fund for laboratory facilities.

Last but not least, thanks to God for my life through all tests in the past four years. You have made my life more bountiful. May your name be exalted, honoured and glorified.

Table of Contents

Title Page	I
Statement of Access.....	II
Declaration.....	III
Acknowledgements	IV
Table of Contents	V
List of Publications	XI
List of Figures.....	XII
List of Tables	XX
Nomenclature	XXI
Abstract.....	1
Chapter 1 Introduction.....	5
1.1. Objective and Aim	7
Chapter 2 Literature Review	8
2.1. Introduction.....	8
2.2. Drying Equipments / Applications.....	9
2.3. Flighted Rotary Dryers (FRD)	10
2.4. Particle Properties	11
2.4.1. Particle size	11
2.5. Flighted Rotary Dryers (FRD's) Models	12
2.5.1. Empirical models	12
2.5.2. Compartment models	15
2.6. Computational Modelling of Multiphase Systems	16

2.6.1.	Eulerian-Eulerian approach	17
2.6.1.1.	Defining equations	18
2.7.	Critical Properties and Relations in Multiphase Systems	22
2.7.1.	Drag models	23
2.7.2.	Effect of temperature on drag coefficient	27
2.7.3.	Turbulence correlations	28
2.7.4.	Heat transfer.....	32
2.7.4.1.	Convective heat transfer	32
2.7.4.2.	Conductive heat transfer	34
2.7.4.2.1.	Biot number.....	35
2.7.4.3.	Radiation heat transfer	37
2.7.5.	Other modelling approaches	37
2.7.6.	Particle curtains modelling	39
2.8.	Summary of Literature Review.....	46
Chapter 3	Model Development	49
3.1.	Model Equations	50
3.1.1.	Heat transfer equations	50
3.1.2.	Drag model.....	51
3.1.3.	Turbulence model	52
3.1.4.	Single particle model (SPM).....	52
3.1.4.1.	Numerical details (SPM).....	54
3.2.	CFD Computational Set-up.....	54
3.2.1.	Geometry.....	55
3.2.2.	Initial conditions	57
3.2.3.	Mesh considerations.....	58
3.2.3.1.	Average heat loss in particle curtain	58
3.2.3.2.	Approach.....	60
3.2.3.3.	Mesh analysis.....	61
3.3.	Significance of Process Parameters on Average Heat Loss.....	62
3.4.	CFD and SPM Centreline Temperature Profiles Comparison	65
3.5.	Model Application: Reduced Order Modelling	68

3.5.1.	Temperature profiles	69
3.5.2.	Mean residence time	74
3.5.2.1.	Curtain hold-up	74
3.5.2.2.	Residence time distributions	75
3.5.2.3.	Results and discussion	77
3.5.3.	Curtain edges	80
3.5.3.1.	Methodology	81
3.5.3.2.	Results and discussion	84
3.6.	Conclusions.....	88
Chapter 4	Experimental Methodology.....	90
4.1.	Introduction.....	90
4.2.	Physical and Thermal Properties of Materials	92
4.2.1.	Particle size measurement techniques.....	93
4.3.	Experimental Apparatus.....	96
4.3.1.	Spreader box	98
4.3.2.	Mass flow rate.....	99
4.3.3.	Infrared thermography	100
4.3.3.1.	Theory	100
4.3.3.2.	Camera details.....	101
4.3.3.3.	Image capture procedure.....	102
4.3.4.	Visible imagery	104
4.3.4.1.	Visible camera details	104
4.3.4.2.	Light intensity considerations	104
4.3.4.3.	Visible high speed camera details.....	106
4.3.4.4.	Image processing	107
4.3.5.	Direct thermocouple measurement	110
4.3.5.1.	Temperature stability	112
4.4.	Experimental Procedure.....	115
Chapter 5	Image and Data Processing.....	118
5.1.	Raw Image Data Processing	119
5.1.1.	Infrared thermal image scaling	119

5.1.2.	Visible image scaling	121
5.1.3.	Image Alignment	122
5.1.4.	Initial conditions	125
5.1.5.	Profile filtering and smoothing	128
5.1.6.	Temperature uniformity	129
5.1.7.	Data repeatability	131
5.2.	Data Reliability	136
5.2.1.	Curtain depth.....	136
5.2.1.1.	Methods.....	138
5.2.1.2.	Results.....	141
5.2.2.	Infrared thermography temperature reliability.....	147
5.3.	Thermographic Filtering	154
5.4.	Visible Image Pixel Intensity.....	156
5.5.	Thermographic Models	159
5.5.1.	Model 1 verification.....	160
5.5.2.	Model 2	164
5.5.3.	Model 2 verification.....	164
5.6.	Data Processing for Curtain Edge Detection	173
5.6.1.	Methodology	174
5.6.2.	Examples and symmetry adjustment	179
5.7.	Conclusion	182
Chapter 6	Results	183
6.1.	Raw Thermography Results.....	183
6.1.1.	Centreline temperature profiles.....	184
6.1.1.1.	Effect of particle size	184
6.1.1.2.	Effect of mass flow rate	186
6.1.1.3.	Effect of slot width.....	191
6.1.2.	2D Infrared thermal profiles	193
6.1.3.	Shape of the curtain	197
6.2.	Comparison of CFD and Thermographic Data	203
6.2.1.	2D temperature profiles	209

6.2.2.	Centreline temperature profiles.....	210
6.2.3.	CFD model investigations.....	218
6.3.	Conclusion	221
Chapter 7	Conclusions and Recommendations.....	222
7.1.	Conclusion	222
7.2.	Recommendations.....	225
References		227
Appendix A, Engineering Equation Solver[®] Code		236
Single Particle Model (SPM).....		236
Appendix B, Matlab[®] Codes		239
B.1 Reduced Order Model (ROM)		239
B.2 Calculation of Particle Curtain Edges in the Thermal Images		244
B.3 Optimisation Code for Calculation of γ and δ		249
B.4 Optimisation Code for Calculation of x' Parameter		252
B.5 CFD-Hybrid Model		256
Appendix C, Apparatus Design		262
C.1 Perforated Plate for Slot width of 20mm.....		262
C.2 Perforated Plates for Slot Width of 60mm		263
C.3 Wire Mesh Screen for Slot Width of 20mm		265
C.4 Wire Mesh Screen for Slot Width of 60mm		266
C.5 Hopper Dimensions		267
C.6 Hopper Valve		268
C.7 Top View of Spreader Boxes: (a) 20mm (b) 60mm		269
C.8 Frontal View of Spreader Boxes: (a) 20mm (b) 60mm		270
C.9 Top View of Rails in 60mm Spreader Box		271
Appendix D, Temperature Profiles from Thermocouple		272

List of Publications

- 1. Sepideh Afshar**, Madoc Sheehan and Amir Fazlollahi, (2015), Using CFD to derive reduced order models for heat transfer in particle curtains. 15(2):71-80, Progress in Computational Fluid Dynamics.
- 2. Sepideh Afshar** and Madoc Sheehan, (2013), CFD and experimental study of convectional heat transfer in free falling particle curtains. Paper presented at 11th International Conference of Numerical Analysis and Applied Mathematics (ICNAAM), Rhodes Island Greece, 21-27 September, pp.2005-2008
- 3. Sepideh Afshar** and Madoc Sheehan, (2012), Using CFD to simulate heat transfer in particle curtains. Paper presented at CSIRO 9th International Conference on Computational Fluid Dynamics in the Minerals and Process Industries, Melbourne Australia, 10-12 December.

List of Figures

Figure 1.1: Particle curtains within a flighted rotary dryer.....	6
Figure 2.1: Flighted Rotary Dryer	10
Figure 2.2: Residence time distribution data for the flighted rotary sugar dryer (Reported from Britton et al. 2006 [7])	14
Figure 2.3: Compartment model developed by Sheehan et al. (2005) (Reported from Lee 2008 [16]).....	16
Figure 2.4: Temperature distribution for different Biot numbers	36
Figure 2.5: Effect of initial curtain width on the shape of the particle curtain; at $m^o = 0.04\text{kg/s}$ and initial curtain width (a) 20mm, (b) 100mm, (c) 20mm, (d) 100mm. Air velocity in cross-flow conditions (c,d) was 0.9m/s (○Run 1, □Run 2, ΔRun 3, —CFDmodel). (Reported from Wardjiman et al. [47, 48]).....	41
Figure 2.6: Model prediction and experimental data of gas and solid temperature for particle curtain with gas velocity of 0.9 m/s, initial curtain width of 10 cm, and solid mass flow rate of 0.040 kg/s. Inlet solid temperature=15.5°C and inlet gas temperature=41.3°C. (○ Solid (exp), Δ Gas (exp), Gas model and — Solid Model). (Reported from Wardjiman et al. 2009 [70])......	44
Figure 3.1: Schematic diagram of simulation domain (a) scenario A: L=450mm, H=900mm and W=225mm (b) scenario B: L=505mm, H=900mm and W=300mm	56
Figure 3.2: Sand mass flow rate vectors at ZX plane, 0.8m down from the entrance	60
Figure 3.3: Heat loss predictions using the indicated element numbers.....	61
Figure 3.4: Heat loss comparison at slot widths of 10mm, 30mm, 60mm, 80mm, particle sizes of 200μm, 400μm and 600μm and mass flow rates of 0.041kg/s,0.1kg/s and 0.2kg/s. Similar trends in the effect of particle size (0.041kg/s) were observed at higher mass flow rates of 0.1kg/s and 0.2kg/s	62
Figure 3.5: Average heat loss for interaction effect of particle size and mass flow rates	64
Figure 3.6: Heat loss per unit mass for different slot widths at mass flow rates of 0.041kg/s, 0.1kg/s and 0.2kg/s for partilce size of 200μm.....	65
Figure 3.7: Temperature comparison between single particle and particles in curtain in 10mm slot at three 0.041, 0.1 and 0.2kg/s mass flow rates and particle size of 200μm.....	67
Figure 3.8: Temperature comparison between single particle and particles in curtain in 60mm slot at three 0.041, 0.1 and 0.2kg/s mass flow rates and particle size of 200μm.....	67

Figure 3.9: Temperature comparison between single particle and particles in curtain in 80mm slot at three 0.041, 0.1 and 0.2kg/s mass flow rates and particle size of 200 μ m.....	68
Figure 3.10: Temperature profiles comparing single particle model to CFD simulation, $d_s=600\mu\text{m}$, $m^o=0.041\text{kg/s}$ and slot width=10mm.....	71
Figure 3.11: Temperature profiles comparing single particle model to CFD simulation, $d_s=400\mu\text{m}$, $m^o=0.1\text{kg/s}$ and slot width=10mm.....	71
Figure 3.12: Parameter estimation for B values using Equation 3.26, slot width=10mm	73
Figure 3.13: Residence time frequency distribution based on streamline ($d_s=200\mu\text{m}$, $m^o=0.041\text{kg/s}$ and $v_0=1.44\text{m/s}$) (a) slot width =10mm (b) slot width =30mm (c) slot width =60mm (d) slot width =80mm	76
Figure 3.14: Mean residence time comparison of streamlines and volume integral techniques at different slot widths ($d_s=200\mu\text{m}$, $m^o=0.041\text{kg/s}$)	78
Figure 3.15: Effect of particle size on mean residence time at different slot widths (mm), 3D volume integral method	79
Figure 3.16: Solid volume fraction contour at XY plane ($Z=0.15\text{m}$, $d_s=200\mu\text{m}$, $m^o=0.041\text{kg/s}$ and slot width=80mm)	81
Figure 3.17: Solid volume fraction at different heights of the middle plane ($d_s=200\mu\text{m}$, $m^o=$ 0.041kg/s and slot width=80mm). The sand inlet corresponds to $Y=0\text{m}$, and the base of the domain corresponds to $Y=0.9\text{m}$	82
Figure 3.18: Solid volume fraction gradeint at different heights of the middle plane ($d_s=200\mu\text{m}$, $m^o=0.041\text{kg/s}$ and slot width=80mm). The sand inlet corresponds to $Y=0\text{m}$, and the base of the domain corresponds to $Y=0.9\text{m}$	83
Figure 3.19: Critical solid volume fraction at different slot widths, $d_s=200\mu\text{m}$, $m^o=0.041\text{kg/s}$ (Dashed line and solid line represent critical solid volume fraction for the left and right edges of the curtain, respectively). The sand inlet corresponds to $Y=0\text{m}$, and the base of the domain corresponds to $Y=0.9\text{m}$	84
Figure 3.20: Edge identifying comparison techniques: a) slot width= 10mm, b) slot width= 30mm, c) slot width= 60mm, d) slot width=80mm ($d_s=200\mu\text{m}$, $m^o=0.041\text{kg/s}$, $T_s=400\text{K}$, $T_g=300\text{K}$ and initial velocity=1.44m/s). The sand inlet corresponds to $Y=0\text{m}$, and the base of the domain corresponds to $Y=0.9\text{m}$. Gray area, dashed lines and solid lines represent the streamlines, rate of change and constant solid volume fraction techniques respectively	85
Figure 3.21: (a) Frontal area of the curtain at different slot widths (b) Average volume fraction of particle curtain at two mass flow rates of 0.041kg/s and 0.1kg/s ($d_s=200\mu\text{m}$) - The dashed line and solid line present the mass flow rate of 0.1kg/s and 0.041kg/s respectively	87

Figure 4.1: Malvern Mastersizer analysis for $d_s = 290\mu\text{m}$, $D_v(50) = 241\mu\text{m}$	94
Figure 4.2: Malvern Mastersizer for $d_s = 400\mu\text{m}$, $D_v(50) = 416\mu\text{m}$	94
Figure 4.3: Malvern Mastersizer for $d_s = 610\mu\text{m}$, $D_v(50) = 656\mu\text{m}$	95
Figure 4.4: Experimental apparatus	97
Figure 4.5: Perforated plates (hole diameter=5mm) for slot widths of 20mm and 60mm	98
Figure 4.6: Examples of mass flow rate calculation using RinstrumView400 software, (a) $d_s = 290\mu\text{m}$, $m^o = 0.066\text{kg/s}$ and slot width=20mm (b) $d_s = 400\mu\text{m}$, $m^o = 0.141\text{kg/s}$ and slot width=60mm	99
Figure 4.7: The electromagnetic spectrum [99]	100
Figure 4.8: Infrared camera	102
Figure 4.9: (a) Visible image of the experimental set-up in the absence of particle curtain (b) The graph of pixel intensities versus height for the bright white area in Figure 4.12 (a)	105
Figure 4.10: Pixel intensities in cold and hot particle curtains ($d_s = 610\mu\text{m}$, $m^o = 0.085\text{kg/s}$ and slot width=20mm)	106
Figure 4.11: Particle pathway from inlet ($d_s = 610\mu\text{m}$, $m^o = 0.057\text{kg/s}$, slot width=20mm). The spreader box width (2cm) was used as known distance to scale and convert pixels to centimetres with the ImageJ software	108
Figure 4.12: Comparison of travelled distance by an individual particle between the model and experiment (a) $d_s = 400\mu\text{m}$, $m^o = 0.101\text{kg/s}$, slot width=20mm, (b) $d_s = 290\mu\text{m}$, $m^o = 0.114\text{kg/s}$, slot width = 60mm	109
Figure 4.13: The sampling cup fitted with a T type bead thermocouple	111
Figure 4.14: Location of cup in the experimental set-up (a) spreader box frontal view (b) spreader box side view. Note the edge of the cup aligned with the slot opening.	112
Figure 4.15: Direct thermocouple temperature measurements (a) $Y = 0.05\text{m}$, $d_s = 290\mu\text{m}$, $m^o = 0.15\text{kg/s}$ and slot width= 20, (b) $Y = 0.05\text{m}$, $d_s = 610\mu\text{m}$, $m^o = 0.045\text{kg/s}$ and slot width=60mm	114
Figure 5.1: Hot metal bar and spreader box showing metal bar height and particle curtain height (a) infrared image (b) visible image (c) ImageJ pixel conversion function.....	119
Figure 5.2: Experimental apparatus (a) infrared image (rectangular box (A) has an approximate area of $0.11 \times 0.62\text{m}^2$) (b) standard visible image (c) matrix of raw temperature data	121
Figure 5.3: Visible image of particle curtain showing the curtain fall height	122
Figure 5.4: Thermal image of particle curtain in (a) an unclosed lab (b) closed lab	123
Figure 5.5: (a) Raw temperature matrix and (b) corresponding thermal image illustrating the identification of the spreader box exit	126

Figure 5.6: Centreline temperatures ($d_s=290\mu\text{m}$, $m^o=0.066\text{kg/s}$ and slot width=20mm) (a) before identifying the initial temperature of particle curtain (b) after indentifying the initial temperature of the particle curtain (c) Temperature dispersion about the centreline	127
Figure 5.7: Developing particle curtain profile, with fully developed profile in the far right image (from left to right)	128
Figure 5.8: Thermal image of the particle curtain showing line A at the spreader box exit.....	129
Figure 5.9: Temperature profiles at the spreader box exit (a) $d_s=290\mu\text{m}$, $m^o=0.14\text{kg/s}$ and slot width=20mm (b) $d_s=400\mu\text{m}$, $m^o=0.129\text{kg/s}$ and slot width=20mm (c) $d_s=610\mu\text{m}$, $m^o=0.088\text{kg/s}$ and slot width=20mm (d) $d_s=290\mu\text{m}$, $m^o=0.55\text{kg/s}$ and slot width=60mm	130
Figure 5.10: (a) Side view thermal image (i.e. 150mm) of the particle curtain (b) The graph of the temperature profile across the spreader box exit from the side view (150mm) (Reported from Dare 2014 [102]).....	131
Figure 5.11: Infrared centreline temperature profiles (a) $d_s=610\mu\text{m}$, slot width=20mm (b) $d_s=400\mu\text{m}$, slot width=20mm (c) $d_s=290\mu\text{m}$, slot width=60mm	133
Figure 5.12: Discrete thermocouple temperature profiles (a) $Y=0.05\text{m}$, $d_s=290\mu\text{m}$ and slot width= 20mm (b) $Y=0.3\text{m}$, $d_s=400\mu\text{m}$ and slot width= 20mm (c) $Y=0.05\text{m}$, $d_s=610\mu\text{m}$ and slot width= 60mm	135
Figure 5.13: Visible images of the particle curtain showing the sparsity of particle at on the top and bottom of the curtain (a) $d_s=290\mu\text{m}$, $m^o=0.14\text{kg/s}$ and slot width=20mm (b) $d_s=610\mu\text{m}$, $m^o=0.088\text{kg/s}$ and slot width=20mm.....	137
Figure 5.14: Experimental set-up for changing the depth of the curtain (a) frontal view (b) side view	138
Figure 5.15: Centreline temperature profiles at varying curtain depth (a) $d_s =290\mu\text{m}$, $m^o=0.14-0.153\text{kg/s}$ and slot width=20mm (b) $d_s =610\mu\text{m}$, $m^o=0.082-0.1\text{kg/s}$ and slot width=20mm	141
Figure 5.16: Effect of particle curtain depth on inlet temperatures (a) $d_s =290\mu\text{m}$, $m^o=0.14-0.153\text{kg/s}$ and slot width=20mm (b) $d_s =610\mu\text{m}$, $m^o=0.082-0.1\text{kg/s}$ and slot width=20mm	143
Figure 5.17: 2D thermal image of particle curtain with varying depths ($d_s =290\mu\text{m}$, $m^o=0.14-0.153\text{kg/s}$ and slot width=20mm)	145
Figure 5.18: 2D thermal image of particle curtain with varying depths ($d_s =610\mu\text{m}$, $m^o=0.082-0.1\text{kg/s}$ and slot width=20mm)	146
Figure 5.19: Infrared and thermocouple measurement comparison, $d_s=290\mu\text{m}$, $m^o_{infrared}=0.15\text{kg/s}$ and slot width=20mm	149

Figure 5.20: Infrared and thermocouple measurement comparison, $d_s=290\mu\text{m}$, $m^o_{infrared}=0.066\text{kg/s}$ and slot width=20mm	150
Figure 5.21: Infrared and thermocouple measurement comparison, $d_s=400\mu\text{m}$, $m^o_{infrared}$ =0.132kg/s and slot width=20mm	150
Figure 5.22: Infrared and thermocouple measurement comparison, $d_s=610\mu\text{m}$, $m^o_{infrared}$ =0.047kg/s and slot width=60mm	151
Figure 5.23: Illustration of the blurred temperature (T_{bl}) in orange, particle true temperature (T_t) in red and background temperature (T_b) in black in a single thermographic pixel.....	156
Figure 5.24: Thermocouple and infrared temperatures along with particle pixel intensities calculated from visible photography (a) $d_s=290\mu\text{m}$, $m^o_{infrared}=0.15\text{kg/s}$ and slot width=20mm (b) $d_s=610\mu\text{m}$, $m^o_{infrared}=0.047\text{kg/s}$ and slot width=20mm	158
Figure 5.25: Interpolated thermocouple temperature in comparison to centreline infrared temperatures ($d_s=290\mu\text{m}$, $m^o_{infrared}=0.15\text{kg/s}$ and slot width=20mm)	161
Figure 5.26: Distribution of γ and δ values compared to their mean values (a) γ values (b) δ values	163
Figure 5.27: Comparison of modelled infrared, raw infrared and thermocouple temperature using Equation 5.8, $d_s=290\mu\text{m}$, $m^o_{infrared}=0.15\text{kg/s}$, slot width=20mm and and $I_{critical}=59.6$	165
Figure 5.28: Visible pixel intensity calculated at different x parameter values, $d_s=290\mu\text{m}$, $m^o_{infrared}=0.15\text{kg/s}$, slot width=20mm, $I_{critical}=59.6$ and $Y=0.15\text{m}$	166
Figure 5.29: Infrared temperature at different x' parameter values compared to thermocouple temperature, $d_s=290\mu\text{m}$, $m^o_{infrared}=0.15\text{kg/s}$, slot width=20mm, $I_{critical}=59.6$ and $Y=0.15\text{m}$	167
Figure 5.30: Comparison of thermocouple temperature and infrared temperature, $d_s=290\mu\text{m}$, $m^o_{infrared}=0.15\text{kg/s}$ and slot width=20mm	168
Figure 5.31: Comparison of thermocouple temperature and infrared temperature, $d_s=290\mu\text{m}$, $m^o_{infrared}=0.066\text{kg/s}$ and slot width=20mm	169
Figure 5.32: Comparison of thermocouple temperature and infrared temperature, $d_s=400\mu\text{m}$, $m^o_{infrared}=0.132\text{kg/s}$ and slot width=20mm	169
Figure 5.33: Comparison of thermocouple temperature and infrared temperature, $d_s=610\mu\text{m}$, $m^o_{infrared}=0.047\text{kg/s}$ and slot width=20mm	170
Figure 5.34: Infrared temperature at different x' parameter values compared to thermocouple, $d_s=290\mu\text{m}$, $m^o=0.15\text{kg/s}$ and slot width=20mm, $I_{critical}=57.6$ and $Y=0.19\text{m}$	170
Figure 5.35: Infrared temperature at different x' parameter values compared to thermocouple, $d_s=290\mu\text{m}$, $m^o=0.066\text{kg/s}$ and slot width=20mm, $I_{critical}=57.6$ and $Y=0\text{m}$	171

Figure 5.36: Infrared temperature at different x' parameter values compared to thermocouple, $d_s=400\mu\text{m}$, $m^o_{infrared}=0.132\text{kg/s}$ and slot width=20mm, $I_{critical}=45.9$ and Y=0.26m.....	171
Figure 5.37 Infrared temperature at different x' parameter values compared to thermocouple,	172
Figure 5.38: Visible pixel intensity at different x' parameter values, $d_s=610\mu\text{m}$, $m^o_{infrared}=0.047\text{kg/s}$, slot width=20mm, $I_{critical}=31.8$ and Y=0m	173
Figure 5.39: Thermal image of a hot particle curtain, $d_s=290\mu\text{m}$, $m^o=0.066\text{kg/s}$ and slot width=20mm	175
Figure 5.40: Raw data temperature profiles, $d_s=290\mu\text{m}$, $m^o=0.066\text{kg/s}$ and slot width=20mm	176
Figure 5.41: Temperature gradient profiles, $d_s=290\mu\text{m}$, $m^o=0.066\text{kg/s}$ and slot width=20mm	177
Figure 5.42: Maximum temperature gradient and two neighbour points	178
Figure 5.43: Overlaid edges on the thermal image, $d_s=290\mu\text{m}$, $m^o=0.066\text{kg/s}$ and slot width=20mm (a) Unsymmetrical image (b) asymmetrical image	180
Figure 5.44: Overlaid edges on the thermal image, $d_s=290\mu\text{m}$, $m^o=0.062\text{kg/s}$ and slot width=20mm (a) Unsymmetrical image (b) asymmetrical image	181
Figure 6.1: Effect of particle size on raw infrared centreline temperatures at constant mass flow rate (a) and (b) slot width=20mm (c) slot width=60mm	185
Figure 6.2: Effect of mass flow rate on raw infrared centreline temperatures at constant particle size and at slot width=20mm (a) $d_s=290\mu\text{m}$ (b) $d_s=400\mu\text{m}$	188
Figure 6.3: Effect of mass flow rate on raw infrared centreline temperatures at constant particle size and at slot width=60mm (a) $d_s=290\mu\text{m}$ (b) $d_s=400\mu\text{m}$ (c) $d_s=610\mu\text{m}$	189
Figure 6.4: Effect of mass flow rate on CFD centreline temperatures at constant particle size and at slot width=20mm (a) $d_s=290\mu\text{m}$ (b) $d_s=400\mu\text{m}$	190
Figure 6.5: Effect of slot width on raw infrared centreline temperatures at constant particle size (a) $d_s=400\mu\text{m}$ (b) $d_s=290\mu\text{m}$ (c) $d_s=610\mu\text{m}$	192
Figure 6.6: Temperature profiles in the x direction (scaled with regard to curtain width)	193
Figure 6.7: 2D thermal images of particle curtain at slot width=20mm (a) $d_s=290\mu\text{m}$, $m^o=0.066\text{kg/s}$ (b) $d_s=400\mu\text{m}$, $m^o=0.062\text{kg/s}$ (c) $d_s=610\mu\text{m}$, $m^o=0.088\text{kg/s}$	194
Figure 6.8: 2D thermal images of particle curtain at slot width=60mm (a) $d_s=290\mu\text{m}$, $m^o=0.063\text{kg/s}$ (b) $d_s=400\mu\text{m}$, $m^o=0.071\text{kg/s}$ (c) $d_s=610\mu\text{m}$, $m^o=0.075\text{kg/s}$	195
Figure 6.9: 2D thermal images of particle curtain at slot width=60mm (a) $d_s=290\mu\text{m}$, $m^o=0.14\text{kg/s}$ (b) $d_s=400\mu\text{m}$, $m^o=0.138\text{kg/s}$ (c) $d_s=290\mu\text{m}$, $m^o=0.138\text{kg/s}$ (d) $d_s=400\mu\text{m}$, $m^o=0.141\text{kg/s}$	196
Figure 6.10: Particle curtain shape, $d_s=290\mu\text{m}$, $m^o=0.066\text{kg/s}$ and slot width=20mm	198
Figure 6.11: Particle curtain shape, $d_s=290\mu\text{m}$, $m^o=0.14\text{kg/s}$ and slot width=20mm	198

Figure 6.12: Particle curtain shape, $d_s=400\mu\text{m}$, $m^o=0.062\text{kg/s}$ and slot width=20mm	199
Figure 6.13: Particle curtain shape, $d_s=400\mu\text{m}$, $m^o=0.138\text{kg/s}$ and slot width=20mm	199
Figure 6.14: Particle curtain shape, $d_s=610\mu\text{m}$, $m^o=0.088\text{kg/s}$ and slot width=20mm	200
Figure 6.15: Particle curtain shape, $d_s=290\mu\text{m}$, $m^o=0.063\text{kg/s}$ and slot width=60mm	200
Figure 6.16: Particle curtain shape, $d_s=290\mu\text{m}$, $m^o=0.138\text{kg/s}$ and slot width=60mm	201
Figure 6.17: Particle curtain shape, $d_s=400\mu\text{m}$, $m^o=0.071\text{kg/s}$ and slot width=60mm	201
Figure 6.18: Particle curtain shape, $d_s=400\mu\text{m}$, $m^o=0.141\text{kg/s}$ and slot width=60mm	202
Figure 6.19: Particle curtain shape, $d_s=610\mu\text{m}$, $m^o=0.096\text{kg/s}$ and slot width=60mm	202
Figure 6.20: Edges of the particle curtain in CFD and experiment overlaid on the thermal image (a) $d_s=290\mu\text{m}$, $m^o=0.066\text{kg/s}$ and slot width=20mm (b) $d_s=400\mu\text{m}$, $m^o=0.062\text{kg/s}$ and slot width=20mm (c) $d_s=290\mu\text{m}$, $m^o=0.14\text{kg/s}$ and slot width=20mm (d) $d_s=290\mu\text{m}$, $m^o=0.063\text{kg/s}$ and slot width=60mm (e) $d_s=400\mu\text{m}$, $m^o=0.138\text{kg/s}$ and slot width=20mm	205
Figure 6.21: Particle curtain edges in CFD and experiments	206
Figure 6.22: Particle curtain edges in CFD and experiments	207
Figure 6.23: Edges of the curtain in CFD and experiment using both constant solid volume fraction and gradient technique, $d_s=290\mu\text{m}$, $m^o=0.063\text{kg/s}$ and slot width=60mm	208
Figure 6.24: 2D temperature profiles, $d_s=290\mu\text{m}$, $m^o=0.15\text{kg/s}$ and slot width=20mm (a) CFD (b) thermal image	209
Figure 6.25: Comparison of CFD centreline temperature and discrete thermocouple temperature measurement, $d_s=290\mu\text{m}$, $m^o=0.15\text{kg/s}$ and slot width=20mm	211
Figure 6.26: Comparison of CFD centreline temperature and discrete thermocouple temperature measurement, $d_s=290\mu\text{m}$, $m^o=0.066\text{kg/s}$ and slot width=20mm	211
Figure 6.27: Comparison of CFD centreline temperature and discrete thermocouple temperature measurement, $d_s=400\mu\text{m}$, $m^o=0.132\text{kg/s}$ and slot width=20mm	212
Figure 6.28: Comparison of CFD centreline temperature and discrete thermocouple temperature measurement, $d_s=610\mu\text{m}$, $m^o=0.047\text{kg/s}$ and slot width=60mm	212
Figure 6.29: Comparison of CFD to raw and modelled infrared centreline temperatures, $d_s=290\mu\text{m}$, $m^o=0.15\text{kg/s}$ and slot width=20mm	214
Figure 6.30: Comparison of CFD to raw and modelled infrared centreline temperatures, $d_s=400\mu\text{m}$, $m^o=0.132\text{kg/s}$ and slot width=20mm	214
Figure 6.31: Comparison of CFD to raw and modelled infrared centreline temperatures, $d_s=400\mu\text{m}$, $m^o=0.141\text{kg/s}$ and slot width=60mm	215
Figure 6.32: Comparison of CFD to raw and modelled infrared centreline temperatures, $d_s=290\mu\text{m}$, $m^o=0.066\text{kg/s}$ and slot width=20mm	215

Figure 6.33: Comparison of CFD to raw and modelled infrared centreline temperatures, $d_s=400\mu\text{m}$, $m^o=0.141\text{kg/s}$ and slot width=60mm	216
Figure 6.34: Comparison of CFD to raw and modelled infrared centreline temperatures, $d_s=610\mu\text{m}$, $m^o=0.088\text{kg/s}$ and slot width=20mm	216
Figure 6.35: Comparison of CFD to raw and modelled infrared centreline temperatures, $d_s=610\mu\text{m}$, $m^o=0.047\text{kg/s}$ and slot width=60mm	217
Figure 6.36: Comparison of CFD to raw and modelled infrared centreline temperatures, $d_s=400\mu\text{m}$, $m^o=0.071\text{kg/s}$ and slot width=60mm	217
Figure 6.37: Radial distribution of temperature, $d_s=610\mu\text{m}$, $m^o=0.088\text{kg/s}$ and slot width=20mm	220

List of Tables

Table 2.1: Solid-fluid momentum exchange coefficient correlations.....	24
Table 3.1: Initial conditions of simulation domain in scenario A.....	57
Table 3.2: Physical and thermal properties of air and particle	58
Table 3.3: Summary of results obtained by ANOVA.....	63
Table 3.4: Inter-particle distances (slot width=10mm, $m^o=0.041\text{kg/s}$)	79
Table 4.1: Standard deviation and skewness of particle size distributions.....	96
Table 4.2: Regression constant at different conditions.....	110
Table 4.3: Experimental conditions	116
Table 4.4: Comparison of initial temperatures measurement at the hopper inlet using infrared camera and thermocouple	117
Table 5.1: Matrix of raw temperature data showing maximum temperatures across each row with corresponding x and y direction	125
Table 5.2: Experimental conditions for changing the depth of the particle curtain.....	140
Table 5.3: Experimental conditions chosen for direct comparison between infrared thermography and thermocouple measurements	148
Table 5.4: t-test results on infrared and thermocouple measurements.....	153
Table 5.5: Derived equations corresponding to Table 5.4 conditions	162
Table 5.6: Critical visible pixel intensities and x' parameters at different particle sizes.....	172

Nomenclature

A	area, [m^2]
A_b	background area, [m^2]
A_{bl}	blurred area, [m^2]
A_{xs}	cross – sectional area, [m^2]
B	a parameter in Equation 3.24 , [–]
Bi	Biot number, [–]
C_D	drag coefficient, [–]
C_p	specific heat capacity, [$\text{J} \cdot \text{kg}^{-1} \cdot \text{K}^{-1}$]
d	diameter, [m]
D	diameter of dryer, [m]
D	thermal diffusivity in Equation 2.44, [$\text{m}^2 \cdot \text{s}^{-1}$]
D_v	volume diameter, [m]
e	emmisivity, [–]
e_s	restitution coefficient of particles, [–]
F_D	drag force, [$\text{kg} \cdot \text{m} \cdot \text{s}^{-2}$]
F_G	gravitational force, [$\text{kg} \cdot \text{m} \cdot \text{s}^{-2}$]
g	acceleration due to gravity, $9.81[\text{m} \cdot \text{s}^{-2}]$
g_0	radial distribution function, [–]
$G_{kb,g}$	turbulent production due to buoyant forces in the gas phase, [$\text{kg} \cdot \text{m}^{-1} \cdot \text{s}^{-3}$]

$G_{k,g}$	turbulent production due to viscous and buoyant forces in the gas phase, [$\text{kg} \cdot \text{m}^{-1} \cdot \text{s}^{-3}$]
\mathcal{H}	hold – up, [kg]
h	convective heat transfer coefficient, [$\text{W} \cdot \text{m}^{-2} \cdot \text{K}^{-1}$]
I	pixel intensity of particles, [-]
$I_{critical}$	critical pixel intensity of particles, [-]
$\bar{\bar{I}}$	unit stress tensor, [-]
k	thermal conductivity, [$\text{W} \cdot \text{m}^{-1} \cdot \text{K}^{-1}$]
K	turbulent kinetic energy, [$\text{m}^2 \cdot \text{s}^{-2}$]
\dot{K}	emprirical constant in Equation 2.2, [-]
$k_{\Theta s}$	granular energy diffusion, [$\text{kg} \cdot \text{m}^{-1} \cdot \text{s}^{-1}$]
L	length of dryer, [m]
L_c	characteristic length, [m]
m	mass, [kg]
m^o	mass flow rate, [$\text{kg} \cdot \text{s}^{-1}$]
Nu	Nusselt number, [-]
P	pressure, [Pa]
Pr	Prandtl number, [-]
Q	Power, [W]
r	radial distance, [m]
R	radius, [m]

Re	Reynolds number, [-]
Re_m	modified Reynolds number in Equation 2.23 , [-]
T	temperature, [$^{\circ}\text{C}$]
T_o	initial temperature, [$^{\circ}\text{C}$]
T^*	non – dimensional temperature, [-]
T_b	background temperature,[$^{\circ}\text{C}$]
T_{bl}	blurred temperature,[$^{\circ}\text{C}$]
T_t	true temperature, [$^{\circ}\text{C}$]
t	time, [s]
v	velocity, [m. s^{-1}]
v'	fluctuating velocity, [m. s^{-1}]
v_r	relative fluctuating velocity, [m. s^{-1}]
V	volume, [m^3]
W	depth of the particle curtain, [m]
x'	scaling parameter to adjust the pixel intensity gradient, [-]
X	Inter – particle distance in Equation 3.29, [m]
Y	falling distance, [m]

**Greek
Letters**

α	volume fraction, [-]
$\acute{\alpha}$	dryer slope, [degrees]

β	interphase drag coefficient, [$\text{kg} \cdot \text{m}^{-3} \cdot \text{s}^{-1}$]
γ	model parameter value in Equation 5.7, [–]
δ	model parameter value in Equation 5.7, [–]
ε	turbulence dissipation rate, [$\text{m}^2 \cdot \text{s}^{-3}$]
s	granular temperature, [$\text{m}^2 \cdot \text{s}^{-2}$]
ρ	density, [$\text{kg} \cdot \text{m}^{-3}$]
σ	Stefan Boltzman – constant, [$\text{W} \cdot \text{m}^{-2} \cdot \text{K}^{-4}$]
λ	bulk viscosity, [$\text{Pa} \cdot \text{s}$]
μ	dynamic viscosity, [$\text{Pa} \cdot \text{s}$]
$\bar{\tau}$	mean residence time, [s]
$\bar{\tau}$	stress tensor, [Pa]
$\gamma_{\Theta s}$	collisional dissipation of energy, [$\text{kg} \cdot \text{s}^3 \cdot \text{m}$]
φ	sphericity, [–]
\emptyset_{gs}	transfer rate of kinetic energy, [$\text{kg} \cdot \text{s}^{-3} \cdot \text{m}^{-1}$]

Subscripts

c	critical
g	gas phase
s	particle phase
tr	turbulent
T	stress tensor

Abstract

In this research, the behaviours of hot particle curtains are investigated experimentally and numerically. An introduction to particle curtains and their importance in industry is given in Chapter 1, where the broad research aims are stated. These include developing a CFD model of hot particle curtains, to experimentally characterising the curtain bulk properties, and assessing the reliability of experimental methods and predictability of CFD modelling techniques.

Chapter 2 provides a literature review which first outlines typical industrial drying equipment and emphasises flighted rotary dryers, because they are examples of a device in which particle curtains are critical to their performance. Various approaches to modelling flighted rotary dryers were discussed and in particular, the methods used to model particle curtains were outlined. CFD was identified as a powerful tool for modelling particle curtains within flighted rotary dryers. The various Computational Fluid Dynamics (CFD) approaches were described and Eulerian-Eulerian was selected for further consideration because of its simplicity and potential for extracting bulk property predictions. Examples of modelling particle curtains in the literature were discussed in order to choose the most effective methods and equations. Drag and heat transfer were emphasised.

In this thesis, hot particle curtains were simulated using Eulerian-Eulerian CFD. Chapter 3 presents CFD models to generate single particle curtains which are bounded by a rectangular box with slot widths varying between 20mm and 80mm. Particles with mean diameters of 290 μm , 400 μm and 610 μm were modelled. The single particle model in the absence of internal heat conduction, widely used in modelling particle curtains in flighted rotary dryers, was also presented for

comparison. Centreline particle temperature profiles from CFD simulations were compared to those derived using the single particle model. The base CFD model was used to derive Reduced Order Models (ROM) suitable for implementation in larger scale process models. Furthermore, CFD simulations of the effects of particle mass flow, particle size, and particle slot width on temperature profiles and heat loss, were investigated using analysis of variance techniques. Good agreement was found between CFD and single particle at low mass flow rates and small particle sizes, but the single particle model was not able to predict the behaviour of particles in curtains at larger particle sizes and higher mass flow rates. A ROM correlation was developed to enable the single particle model to be used as a basis for predicting curtain behaviour. Key properties of particle curtains that were modelled included residence time, curtain area and average solid volume fraction. Methodologies based on image analysis techniques to identify the edges of the curtain from CFD data were also described.

Chapter 4 describes experimental apparatus and methods used to generate hot particle curtains. The primary apparatus consisted of a hopper, perforated plates, wire mesh screens, scale indicator, data logger and oven. Chapter 4 describes the methods used to heat the glass beads, and to ensure particles discharge from the hopper is uniform and consistent. The rate at which particles were discharged was recorded using scale indicator. Infrared and visible cameras were described, and the methods used to capture hot particle curtain images were outlined. The infrared camera was used to capture the temperature of particles. High speed photography, used to measure the initial velocities of the particles was described. Direct thermocouple measurements were outlined.

A variety of image processing techniques to manipulate and filter raw image data were described in Chapter 5. Centreline temperatures and 2D infrared temperature profiles were two key curtain attributes examined in this research. Repeatability of temperature profiles using infrared

thermography and thermocouple measurements in various examples was investigated. Thermography repeatability error varied between 0.9% and 2%, and a good repeatability was obtained in thermocouple measurements. Furthermore, the reliability of infrared thermography was investigated qualitatively and quantitatively. The qualitative analysis examined the effect of curtain depth on infrared recorded temperatures at two particle sizes ($290\mu\text{m}$ and $610\mu\text{m}$) and varying curtain depths (1.5cm to 15cm). It was found that thermal images were significantly affected by background ambient temperature. Quantitative analysis of the background effect using direct comparison between thermocouple data and thermography was described. There was a good agreement between infrared and thermocouple measurements for the smallest particles ($290\mu\text{m}$) at both high and low mass flow rates. However, a substantial mismatch was found for the largest particle sizes ($610\mu\text{m}$). Thermographic models which include data from visible images of curtains were developed to predict true particle temperatures. A final model for each particle size was selected, which was capable of more reliable temperature predictions.

Results and discussion of raw and modelled infrared thermography and CFD model predictions were provided in Chapter 6. The effects of particle size, mass flow rate and slot width on both centreline temperature profiles and 2D infrared thermographic images were examined. The reliability of infrared thermography was investigated, and trends in thermal characteristics of the hot curtains were presented. Results comparing curtain shape derived from both CFD and thermographic data were presented. The strengths and weaknesses of methodologies developed in this thesis, such as the gradient technique in edge detection were discussed in Chapter 6. Methodologies used to extract curtain edge locations from both CFD and thermographic data were successful. A good agreement was found between CFD and thermography curtain edge locations. However, the CFD model failed to predict the edges of the curtain at large slot widths (60mm).

Thermographic data was used to describe conditions where heat transfer in particle curtains can be maximised. A hybrid CFD model was introduced to examine the impact of internal heat conduction of particles because this was recognised to be a model deficiency.

Chapter 7 presents the conclusions and recommendations of the research.

Chapter 1 Introduction

Particle curtains are defined as a stream of particles falling a fixed distance through a gas or fluid phase. They are very common in industrial drying, particularly in the minerals and food industry. Drying is an essential operation in food, pharmaceutical, mineral, polymer and chemical industries and is governed by two-phase heat and mass transfer processes. Typical unit operations in drying industry are fluidized beds, spray dryers, flighted rotary dryers (FRD) and solid particle receivers (SPR). Flighted rotary dryers are used widely in industry because of their simplicity and their ability to handle very large throughputs. Typically a flighted rotary dryer consists of a relatively long cylindrical shell and internally fitted flights. In a flighted rotary dryer, the particles are picked up by the flights and moved to the upper half of the drum via rotation. As the flights rotate the particles fall as curtains of solids where heat transfer, mass transfer, drag and sometimes reaction may occur. Particle curtains are important in flighted rotary dryers. However, our understanding of the rates of exchange between gas and solids in particle curtains has been limited. Figure 1.1 shows particle curtains within a flighted rotary dryer.

Characterizing the interaction between gas and particles has spurred the interest of researchers for decades. Researchers have found that the properties of the individual particles, such as particle temperature and particle size, and the operational characteristics such as flow rates and curtain depth, solid volume fraction and rates of heat transfer are important in characterising the behaviour of particle curtains. Despite the importance of particle curtains in flighted rotary dryers, a comprehensive model that describes the influence of these properties has yet to be developed.

Computational Fluid Dynamic (CFD) is found to be a powerful numerical tool to enable a better understanding of the behaviours of curtains of particles. CFD has applied successfully to model

particle curtains in isothermal conditions; however, there are relatively few CFD studies of hot particle curtains. Furthermore, the use of CFD to approximate bulk curtain behaviour has not been described. There are a few examples of the use of image analysis to characterise particle curtains. These have shown promise and suggest that infrared thermal imagery might provide good data for characterising the thermal properties of particle curtains. However, there are no examples of this application to two-phase systems. This illustrates a gap in our understanding.

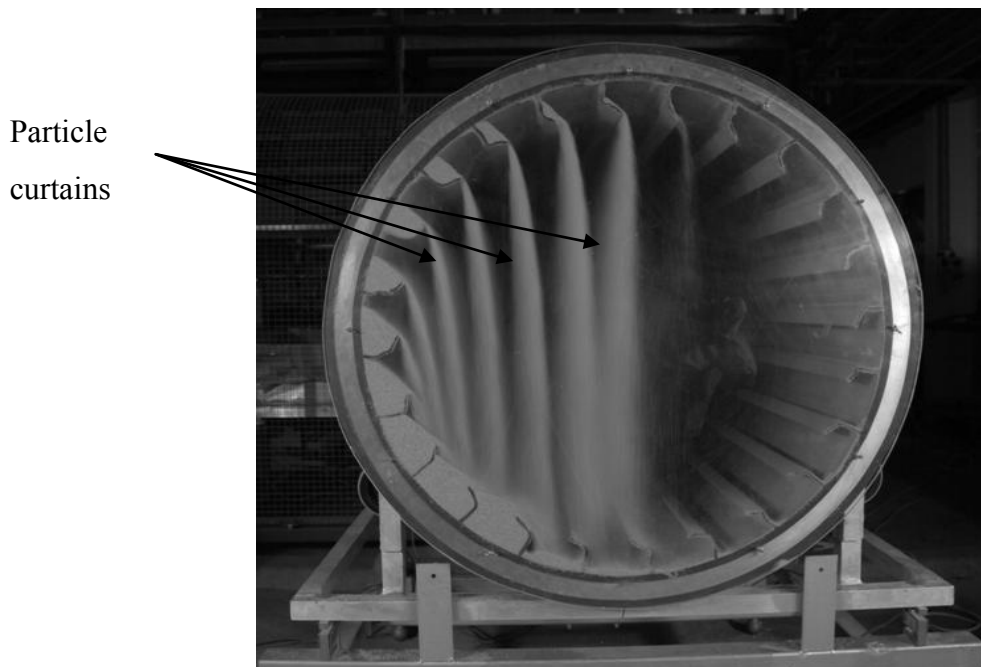


Figure 1.1: Particle curtains within a flighted rotary dryer

1.1. Objective and Aim

The aim of this study is to investigate the behaviours of hot particle curtains numerically and experimentally. In this research, CFD modelling of particle curtains is combined with thermography and visible imagery to evaluate various techniques to characterise the behaviour of hot particle curtains. The objectives of the study are as follows:

1. To develop a CFD model to simulate hot particles curtains and apply the model to generate approximations for use in flighted rotary dryers process model
2. To experimentally characterise hot particle curtains in terms of their temperature, shape and volume fraction
3. To assess both the reliability of experimental methods and the predictability of computational modelling techniques

Chapter 2 Literature Review

2.1. Introduction

This literature review outlines drying equipments and the application of flighted rotary dryers. A discussion of various approaches to modelling flighted rotary dryers is presented. The particle curtains characteristics and the importance of particle curtain modelling in flighted rotary dryers is emphasized. Furthermore, the application of Computational Fluid dynamics (CFD) in modelling particle curtains is highlighted.

There is a vast number of process examples where mass and heat is exchanged between solids and gases and characterising the interaction between these phases has spurred the interest of researchers for decades. Optimization of the exchange of heat and /or mass transfer between gases and solids is essential to various industrial processes particularly drying, heat exchange and reaction.

Drying in particular involves the transport of mass, usually water, from a solid to gas and the rates of exchange depend to a great extent on the thermal properties of the two phases. Many industrial applications ranging through the food, agricultural, mining and manufacturing sectors use drying [1]. Typical unit operations include, flighted rotary dryers, solid particle receivers (FRD), fluidised bed dryers, spray dryers and pneumatics conveyors [2-4].

Flighted rotary dryers are simple to operate, are versatile units and consume vast amounts of energy, but the solid transportation as well as the heat and mass transfer are very complex

phenomena that are influenced by a large number of parameters [3]. Nevertheless, the comprehension of the basic phenomena taking place in this type of dryer is still of great interest.

The considerable depth of literature in flighted rotary dryer modelling is testament to the complications involved in their design and control. In order to control and design dryers it is necessary to understand the effects of material, geometric and operational characteristics on the efficiency of gas-solid interactions. Particle curtains are most commonly used in flighted rotary dryers. Therefore, in order to model the flighted rotary dryers there is a need to better understand and characterise the behaviours of particles in curtains.

2.2. Drying Equipments / Applications

Drying is one of the oldest unit operations in chemical engineering. It is used in many industries including agriculture, biotechnology, mineral, food, pulp and paper, polymer, wood, pharmaceutical [5]. Drying is one of the largest energy consumers in industry. Recent data show that 10-15% of the global industrial energy use is consumed in drying operations [1].

Direct drying and indirect drying are two main types of classification. In direct drying there is direct contact between hot gases and feed materials. In indirect drying heat for drying is transferred to the wet solid through a retaining wall. Among direct drying systems, spray dryers, flighted rotary dryers and fluidised bed dryers are the most commonly used.

2.3. Flighted Rotary Dryers (FRD)

Flighted rotary dryers, utilise an inclined long cylindrical shell (typically 2-4 degrees) rotated at low rpm (typically 2-6 rpm) with lifting flights for drying of materials on a large scale. Moist solids are fed into the dryer at one end where they are collected in the flights. The flights carry the solids into the upper half of the drum, where they are released in a series of continuous curtains across the width of the dryer [6]. Flow of the gas can be co-current or counter-current to particle curtains [7]. Typical solids flow rates are 1 tonne/hr or greater for example in mineral and sugar industry solids flow rate is 100 tonne/hr. Industrial drums vary in size from 0.3m diameter by 2m long to 7m diameter by 90m long. Feed material of rotary dryer include powder, cakes, granules, flakes, pastes, gels and slurries [4]. They are particularly suited to coarse and cohesive material [8].

Figure 2.1 shows a schematic diagram of a rotary dryer [8, 9].

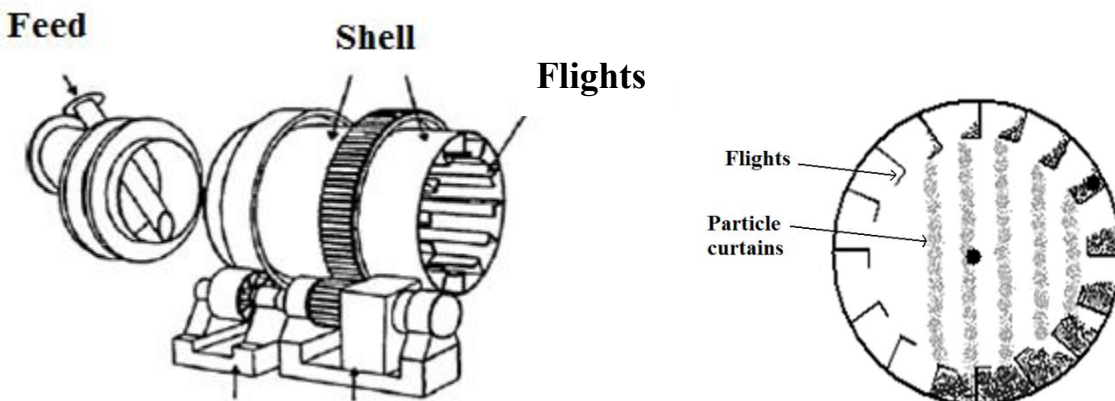


Figure 2.1: Flighted Rotary Dryer

Particles movement along the axis of a flighted rotary dryer is controlled by four mechanisms [10]:

- (1) Gravitational, due to the slope of the drum
- (2) Drag of the gas on the airborne particles
- (3) Bouncing of the particles on impact with the bottom of the dryer

(4) Rolling of the particles in the bed at the bottom of the dryer

Typically all the drying takes place during the airborne phase (i.e. particle curtains). Flighted rotary dryers represent a significant capital cost to industry. Therefore design and control of these unit operations is very essential to obtain desired product quality. Control/ optimisation and design of flighted rotary dryers is challenging due to the movements of particles, interaction with gas and complex physical properties of solid. A good knowledge of particle size, particle residence time, heat transfer coefficient, drag coefficient, flow rate, moisture content, angle of repose and rotary dryer geometry and operating conditions are required to undertake successful simulations of flighted rotary dryers [10-12]. There is a large body of literature describing models of flighted rotary dryers where estimation of curtain properties is important.

2.4. Particle Properties

2.4.1. *Particle size*

Different definitions of average particle diameter have been used to characterise an assemblage of particles. These include arithmetic mean, surface mean, volume mean, volume surface mean and weight mean [13]. Among these, volume mean and volume surface mean are widely used in various industries. The volume mean diameter is the diameter of the hypothetical spherical particle whose volume, when multiplied by the total number of the particles in the assemblage, would be equal to the total volume of the assemblage. Volume surface mean defines the average particle size based on the specific surface area per unit volume or per unit weight. It is widely accepted that the most appropriate mean to use in modelling or characterising a fluid-particle system is the volume-

surface mean. Different methods for particle size analysis are applicable to different size ranges of the particles. These include sieving, laser diffraction, dynamic light scattering, sedimentation, imaging particle analysis and acoustic spectroscopy. Among these techniques, laser diffraction and imaging particle analysis are widely used because they are fast and accurate.

2.5. Flighted Rotary Dryers (FRD's) Models

In this section a brief review of FRD modelling is provided. The focus of the review is placed on mechanistic or physically based modelling approaches, because of their predictive capability. The importance of the particle curtains are emphasised and the approaches that have been to model and integrate curtain properties are also discussed. More comprehensive reviews of dryer modelling in the literature can be found elsewhere [10, 14-17].

2.5.1. *Empirical models*

The relationship between flow rate, hold up and residence time of rotary dryers is shown in the Equation 2.1. In this equation m^o is flow rate, \mathcal{H} is hold up and $\bar{\tau}$ is the mean residence time which describes the average time a particle spends within the curtain.

$$\bar{\tau} = \frac{\mathcal{H}}{m^o} \quad 2.1$$

Friedman and Marshall [18] developed one of the first empirical models to determine τ for flighted rotary dryers that is still widely used [11, 19, 20]. The Friedman and Marshall correlation

is shown in Equation 2.2, in which \hat{K} is an empirical constant, m_g^o and m_s^o are mass flow rate of gas and particles respectively, α is the dryer slope, D and L are diameter and length of dryer respectively.

$$\tau = \frac{0.23L}{\omega^{0.9}D\alpha} + \hat{K} \frac{m_g^o}{m_s^o} \quad 2.2$$

Numerous authors [7, 12, 21, 22] have noted that empirical models are insufficient to predict the dryers' behaviours accurately and are inadequate for predicting dynamic effects. Residence time is one of the key factors and many studies focus on calculation of this property. However, residence time alone is insufficient in fully describing the dispersion of particles in the dryer which is strongly affected by the drag on particles, by the gas. The residence time distribution is a better measure of the physical behaviour of a dryer because it describes the dispersion of particles throughout the dryers. Figure 2.2 shows the residence time distribution for a typical industrial sugar dryer [7]. The extended tail of distribution is common to flighted rotary dryers across a wide range of industries, and indicates that there is significant backwards dispersion of material, presumed to be due to the effects of the counter-current airflow driving material back-up the dryer [16].

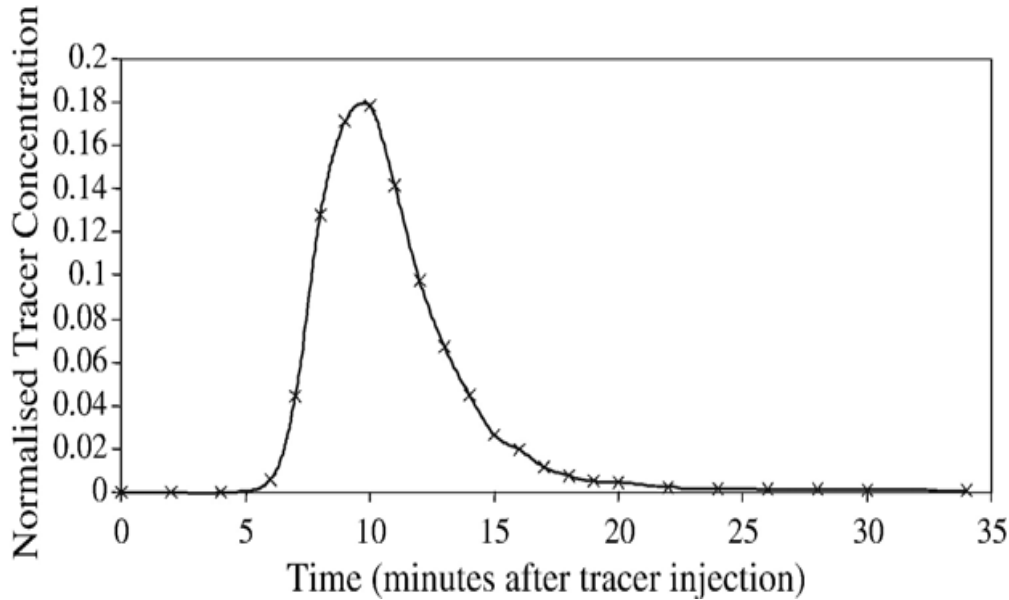


Figure 2.2: Residence time distribution data for the flighted rotary sugar dryer (Reported from Britton et al. 2006 [7])

Numerous researchers have taken a mechanistic approach to calculate residence time [14, 23, 24]. This has involved predicting residence time based on assuming a single particle is sufficient to represent curtain behaviours. For example, Schofield and Glikin [25] developed a residence time model for flighted rotary dryers in which drag and heat transfer were considered. In their model it was assumed that the behaviour of particles in curtains is the same as isolated single particles. They calculated the surface area of all of the particles in contact with the air and used this to calculate the heat transfer between the particles and air. Comparison of numerical results to experiment showed that the predicted heat transfer was overestimated.

The effect of drag on particle curtains was investigated by Baker [26]. Baker compared experimental data for falling curtains to both a single particle and to a double-sided flat plate models. It was found that the flat plate model more accurately predicted the behaviour of particle

curtains, while the single particle model predicts 1 to 2 orders of magnitude greater than experimental residence times results. However, the real behaviours of the particle curtain lies between these two extremes. Thus, there is a need to assess sophisticated models of curtain behaviour.

2.5.2. Compartment models

A comprehensive review of compartment models can be found in Lee [16]. In this section the important developments in incorporating curtain behaviour into dryer model is highlighted. An improved description of particle motion in flighted rotary dryer was described in Matchett and Baker [27]. In this research, two phases termed the active and passive phases were defined. The active phase was defined to be only the particles that fall under gravity within the curtain. The passive phase was defined to be the particles in the flights and on the base of the drum. This is important because the curtains were now differentiated from the other solids, creating the potential to model this phase in detail. Aspects such as drag and heat transfer can now be considered in context.

Duchesne et al. [28] developed a compartment model consisting of a series of well-mixed tanks which described the RTD well. Sheehan et al. [8] and Britton et al. [7] combined these approaches and developed a physical description of solid transport within dryers, in which dryer geometry was accounted for in the prediction of residence time distributions. They called this pseudo-physical compartment model. It has been applied to sugar dryers [16], mineral ore dryers [29] and fertilizer dryers [30]. The general structure of this model is shown in Figure 2.3.

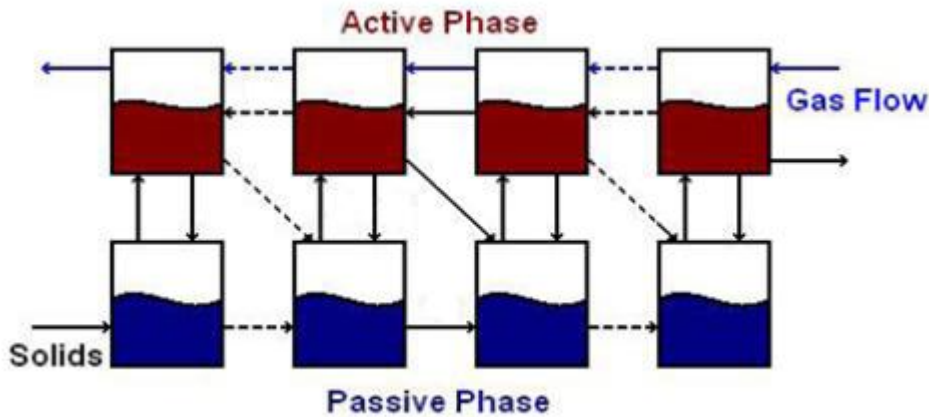


Figure 2.3: Compartment model developed by Sheehan et al. (2005) (Reported from Lee 2008 [16])

The model shows the movement of solids in and out of the active and passive phases. The effect of drag on the curtains is taken into account. The curtain is explicitly defined. However, in these models the active phase was still represented by using a single particle model. The fundamental assumption was that the particle curtains behave like isolated falling spheres, which is an inadequate representation. Therefore, more realistic models of particle curtain behaviour (heat transfer and drag) are essential in order to accurately model flighted rotary dryers. In recent years, Computational fluid dynamics (CFD) has emerged as a powerful tool to model multiphase particle-gas systems.

2.6. Computational Modelling of Multiphase Systems

Multiphase flow describes the interactive flow of two (or more) immiscible fluids, or a fluid and a solid component. Examples include a dispersed phase (droplets/particles/bubbles) intermingled in a continuous phase (gas/liquid). Particle curtains which are a focus of this thesis are a typical example of multiphase flow. In recent years due to the increase of computational capacity,

Computational Fluid Dynamics (CFD) has been applied extensively to model multi-phase systems. Navier-Stokes equations play an important role in CFD problems and it is a set of non-linear partial differential equations consist of continuity equation, conservation of momentum equation and conservation of energy equation and closure equations of drag, turbulence and buoyancy. Two different approaches are used to model multiphase systems: Eulerian-Eulerian and Eulerian-Lagrangian. Eulerian-Eulerian also called the two-fluid model is a useful technique for modelling low solids volume fraction particle-gas systems. Whereas, Eulerian-Lagrangian is more suitable for system with limited number of particles, because it is for more computationally expensive. A comprehensive review of the application of Computational Fluid Dynamics to multiphase drying, and the comparison of both Eulerian-Eulerian and Eulerian-Lagrangian techniques can be found in Jamaleddine and Ray [4].

2.6.1. Eulerian-Eulerian approach

The Eulerian-Eulerian approach treats two phases (fluid, solid) as interpenetrating continua and averages the properties of the fluid and solid phases within each “control volume”. The Eulerian model equations are applied to both phases (gas or solid). In this approach, continuity, momentum and energy equations are solved for each phase. Eulerian-Eulerian approach cannot predict the trajectories of the discrete particles, hence this approach has been extensively used to model particle suspensions such as, circulating fluidised beds, risers and bubble columns. Therefore, Eulerian-Eulerian appears to a very suitable approach for modelling particle curtains. This approach is regarded as the only feasible approach to model large systems. One of the shortcomings of the Eulerian models is the assumption of monosized particles. Another

shortcoming is using the averaged equations of motion by the Eulerian models to represent field variables such as particle volume fraction, velocity and temperature [4].

In what follows, the common defining equations in the Eulerian-Eulerian approach are presented. Equations 2.3 to 2.6 describe conservation equations of mass, momentum and energy for both phases of gas and solid.

2.6.1.1. Defining equations

Continuity equations for both phases are described in Equation 2.3 and 2.4:

Continuity equation for gas phase is described in Equation 2.3:

$$\frac{\partial(\alpha_g \rho_g)}{\partial t} + \nabla \cdot (\alpha_g \rho_g \vec{v}_g) = 0 \quad 2.3$$

Continuity equation for solid phase is described in Equation 2.4:

$$\frac{\partial(\alpha_s \rho_s)}{\partial t} + \nabla \cdot (\alpha_s \rho_s \vec{v}_s) = 0 \quad 2.4$$

Momentum equations for both phases are described in Equation 2.5 and 2.6:

Gas phase-Momentum is described in Equation 2.5:

$$\frac{\partial}{\partial t} (\alpha_g \rho_g \vec{v}_g) + \nabla \cdot (\alpha_g \rho_g \vec{v}_g \vec{v}_g) = \nabla \cdot \bar{\tau}_g - \alpha_g \nabla P - \alpha_g \rho_g \vec{g} + \beta(\vec{v}_s - \vec{v}_g) \quad 2.5$$

Solid phase-Momentum is described in Equation 2.6:

$$\frac{\partial}{\partial t} (\alpha_s \rho_s \vec{v}_s) + \nabla \cdot (\alpha_s \rho_s \vec{v}_s \vec{v}_s) = \nabla \cdot \bar{\tau}_s - \alpha_s \nabla P - \nabla P_s - \alpha_s \rho_s \vec{g} + \beta (\vec{v}_g - \vec{v}_s) \quad 2.6$$

In the gas and solid momentum equations the first term on the right hand side represents the gas and solid stress tensor respectively. The stress tensors are described in Equations 2.7 and 2.8, and are expressed in terms of the solids pressure (P_s), bulk solids viscosity (λ_s), and solids dynamic viscosity (μ_s).

Gas phase-stress tensor is described in Equation 2.7:

$$\bar{\tau}_g = \alpha_g \mu_g (\nabla \vec{v}_g + \nabla \vec{v}_g^T) + \alpha_g \left(\lambda_g + \frac{2}{3} \mu_g \right) \nabla \cdot \vec{v}_g \bar{\mathbb{I}} \quad 2.7$$

Solid phase-stress tensor is described in Equation 2.8:

$$\bar{\tau}_s = \alpha_s \mu_s (\nabla \vec{v}_s + \nabla \vec{v}_s^T) + \alpha_s \left(\lambda_s + \frac{2}{3} \mu_s \right) \nabla \cdot \vec{v}_s \bar{\mathbb{I}} \quad 2.8$$

The solid pressure is described in Equation 2.9 using the Gidaspow model [31].

$$P_s = \alpha_s \rho_s \quad s (1 + 2g_0 \alpha_s (1 + e_s)) \quad 2.9$$

Bulk viscosity is described in Equation 2.10 [32]:

$$\lambda_s = \frac{4}{3} \alpha_s^2 \rho_s d_s g_0 (1 + e_s) \sqrt{\frac{s}{\pi}} \quad 2.10$$

Shear viscosity is described in Equation 2.11 [31]:

$$\mu_s = \frac{4}{5} \alpha_s \rho_s d_s g_0 (1 + e_s) \sqrt{\left(\frac{\Theta_s}{\pi}\right)} + \frac{5\sqrt{\pi}}{48} \frac{\rho_s d_s}{(1+e_s)\alpha_s g_0} [1 + \frac{4}{5}(1 + e_s)g_0\alpha_s]^2 \sqrt{\Theta_s} \quad 2.11$$

Energy balance for the gas phase is described in Equation 2.12:

$$\alpha_g (\rho C_p)_g \frac{\partial T_g}{\partial t} + (\rho C_p)_g v_g \cdot \nabla T_g = \nabla \cdot (\alpha_g k_g \nabla T_g) + Ah(T_s - T_g) \quad 2.12$$

Energy balance for the solid phase is described in Equation 2.13:

$$\alpha_s (\rho C_p)_s \frac{\partial T_s}{\partial t} + (\rho C_p)_s v_s \cdot \nabla T_s = \nabla \cdot (\alpha_s k_s \nabla T_s) + Ah(T_g - T_s) \quad 2.13$$

In multiphase systems, the Eulerian-Eulerian approach requires constitutive equations to describe the rheology of the solid phase. The kinetic theory of granular materials is commonly used to describe the effective stresses in the solid phase resulting from particle-particle interactions. In this theory, the viscous forces and the solid pressure of the particle phase are described as a function of the so-called granular temperature (Θ_s). Analogous to the thermodynamic temperature for gases, the granular temperature is introduced as a measure for the energy of the fluctuating velocity of the particles (Equation 2.14).

$$_s = \frac{1}{3} \overline{\dot{v}_s \dot{v}_s} \quad 2.14$$

where \dot{v}_s is the particle fluctuating velocity. This equation represents conservation of solids fluctuating energy [31].

The granular kinetic theory as derived by Gidaspow [31] is presented in Equation 2.15.

$$\frac{3}{2} \left[\frac{\partial}{\partial t} (\alpha_s \rho_s \Theta_s) + \nabla \cdot (\alpha_s \rho_s \Theta_s) v_s \right] = (- \nabla \rho_s \bar{\bar{\tau}}_s + \bar{\bar{\tau}}_s) : \nabla v_s + \nabla \cdot (k_{\Theta_s} \nabla \Theta_s) - \gamma_{\Theta_s} + \emptyset_{gs} \quad 2.15$$

where k_{Θ_s} is the granular energy diffusion coefficient, γ_{Θ_s} is the collisional dissipation of energy and \emptyset_{gs} is the exchange of fluctuating energy between phases.

The granular energy diffusion coefficient is described in Equation 2.16 [31]:

$$k_{\Theta_s} = \frac{150 \rho_s d_s \sqrt{\Theta_s \pi}}{384 \times (1+e_s) g_{0s}} \left[1 + \frac{6}{5} \alpha_s g_{0s} (1+e_s) \right]^2 + 2 \rho_s d_s \alpha_s^2 g_{0s} (1+e_s) \sqrt{\frac{\Theta_s}{\pi}} \quad 2.16$$

The collisional dissipation of energy is described in Equation 2.17 [31]:

$$\gamma_{\Theta_s} = \frac{12(1-e_s^2)g_{0s}}{d_s \sqrt{\pi}} \rho_s \alpha_s^2 \Theta_s^{3/2} \quad 2.17$$

where e_s is the restitution coefficient of particles and g_{0s} is the radial distribution function. The radial distribution function, g_{0s} , can be seen as a measure for the probability of inter-particle contact [31]:

$$g_{0s} = \left[\frac{3}{5} \left[1 - \left(\frac{\alpha_s}{\alpha_{s,max}} \right)^{\frac{1}{3}} \right]^{-1} \right]^{2.18}$$

where $\alpha_{s,max} = 0.65$

The transfer of the kinetic energy of random fluctuations in particle velocity from the s^{th} solids phase to the g^{th} fluid or solid phase is represented in Equation 2.19 [31]:

$$\phi_{gs} = 3\beta\Theta_s \quad 2.19$$

where β is the interphase momentum exchange coefficient, and will be described in Section 2.7.1. Equations 2.16 to 2.19 describe kinetic theory. The use of these equations is well validated in the literature [33, 34]. Huilin et al. [34] used a 2-D Eulerian-Eulerian approach to model a gas-solid flow system in a riser. The results of granular temperature distributions agreed well with experimental data. Xiaofang et al. [33] used a 3-D Eulerian-Eulerian approach to model a gas-solid flow injector (pneumatic conveying systems), and a good agreement was found between their model and experiments. There are two possible mechanisms inducing the fluctuations of particle velocity: inter-particle collisions and particle interactions with turbulent fluctuations in the gas phase.

2.7. Critical Properties and Relations in Multiphase Systems

When modelling multiphase systems, the use of drag and turbulence relations remains uncertain. Drag is affected by solids volume fraction, inter-particle distances and temperature. Turbulence

models affect convergence, and are usually selected based on simplicity and the match between model and experiment. In this section the most common required closure equations such as drag and turbulence are described in detail. In particular, their application in two phase solid-gas is emphasized.

2.7.1. Drag models

The interphase momentum exchange coefficient (β) is formally defined as a friction factor between gas and particles. Several correlations are reported in the literature for the momentum exchange coefficient. Table 2.2 provides the most commonly used correlations in multiphase system for characterising β . In the literature there are hundreds of different drag coefficient models that have been introduced. Stokes [35] developed an analytical expression for the stationary drag coefficient on isolated sphere for $Re \ll 1$. For particles smaller than about 20 μm in diameter, Stokes' law (Equation 2.20) is an accurate formula for the drag coefficient.

$$C_D = \frac{24}{Re} \quad 2.20$$

Many empirical correlations have been derived as modifications of Stokes' law. For example, Schiller-Naumann equation for single particle is often used (Equation 2.21).

$$C_D = \begin{cases} \frac{24}{Re_p} (1 + 0.15 Re_p^{0.687}), & Re \leq 1000 \\ 0.44, & Re > 1000 \end{cases} \quad 2.21$$

A number of researchers have tried to measure the influence on the drag force of single particle in the presence of other particles. A review of drag models and their modification for multi-particle systems can be found in Lundberg's work [36]. Wen and Yu [37] have shown that for a multi-particle system the drag coefficient for a single particle model should include the influence of the solid volume fraction. The Schiller-Naumann equation, modified to account for a multi-particle system is as follows:

$$C_D = \begin{cases} \frac{24}{\alpha_g Re} \left[1 + 0.15(\alpha_g Re)^{0.687} \right] & Re < 1000 \\ 0.44 & Re \geq 1000 \end{cases} \quad 2.22$$

Kuan and Schwartz [38] found that reducing the drag coefficient to 65% of standard C_D , predicted particle velocities better matched those of the validating experimental results of a vertical gas-particle flow. The average solid volume fraction in their system was 1.5×10^{-4} . Although this is considered as a dilute system, the interactions between particles cannot be ignored.

Table 2.1: Solid-fluid momentum exchange coefficient correlations

Author	Correlation
Richardson and Zaki [39]	$\beta = \frac{3\rho_s \alpha_g \alpha_s}{4d_s v_r^2} C_D \vec{v}_g - \vec{v}_s $ $v_r = \alpha_g^{n-1}$ $Re_m = \frac{Re}{v_r}$ $n = \begin{cases} 4.65, & Re_m < 0.2 \\ 4.4Re_m^{-0.33} & 0.2 > Re_m < 1 \\ 4.4Re_m^{-0.1} & 1 > Re_m < 500 \\ 2.4 & Re_m > 500 \end{cases}$ $Re = \frac{\rho_g d_s \vec{v}_g - \vec{v}_s }{\mu_g}$

Wen and Yu [37]	<p>This model is actually an extension of Richardson and Zaki [39] adopted for high void fraction.</p> $\beta = \frac{3}{4} C_D \frac{\alpha_s \rho_g}{d_s} \vec{v}_g - \vec{v}_s \alpha_g^{-2.65} \quad \alpha_g \geq 0.8 \quad 2.24$ <p>The drag coefficient is a modification of the single particle Schiller-Naumann model [40] and extended to represent multi-particle systems.</p> $C_D = \frac{24}{\alpha_g Re} \left[1 + 0.15 (\alpha_g Re)^{0.687} \right]$ $Re = \frac{\rho_g d_s \vec{v}_g - \vec{v}_s }{\mu_g}$
Syamlal and O'Brien [41]	$\beta = \frac{c_D}{f^2} \frac{\alpha_s \rho_g \vec{v}_g - \vec{v}_s }{d_s} \alpha_s \alpha_g \quad 2.25$ <p>The drag coefficient is a modification of the single particle Dalla Valle model [42] and extended to represent multi-particle systems.</p> $C_D = (0.63 + 4.8 \sqrt{\frac{f}{Re_t}})^2$ $f = 0.5 \left(A - 0.06 Re + \sqrt{0.06 Re^2 + 0.12 Re(2B - A) - A^2} \right)$ $A = \alpha_g^{4.14}$ $B = \begin{cases} \alpha_g^{2.65} & \alpha_s < 0.15 \\ 0.8 \alpha_g^{1.28} & \alpha_s \geq 0.15 \end{cases}$
Di Felice [43]	$\beta = \frac{3}{4} C_D \frac{\alpha_s \rho_g \vec{v}_g - \vec{v}_s }{d_s} f(\alpha_s) \quad 2.26$ $f(\alpha_s) = (1 - \alpha_s)^{-x}$ $x = p - q \cdot \exp \left[\frac{-(1.5 - \theta)^2}{2} \right]$

	$\theta = (Re_s)$ $p = 3.7$ and $q = 0.65$	
Gidaspow [31]	$\beta = (1 - \varphi_{gs})\beta_{Ergun} + \varphi_{gs}\beta_{Wen-Yu}$ $\varphi_{gs} = \frac{\arctan [150 \times 1.75(0.2 - \alpha_s)]}{\pi} + 0.5$ $\beta_{Ergun} = 150 \frac{\alpha_s^2 \mu_g}{\alpha_g d_s^2} + 1.75 \frac{\alpha_s \rho_g \vec{v}_g - \vec{v}_s }{d_s} \quad \alpha_g < 0.8$ $\beta_{Wen-Yu} = \frac{3}{4} C_D \frac{\alpha_s \rho_g}{d_s} \vec{v}_g - \vec{v}_s \alpha_g^{-2.65} \quad \alpha_g \geq 0.8$ $C_D = \begin{cases} \frac{24}{\alpha_g Re} [1 + 0.15(\alpha_g Re)^{0.687}] & Re < 1000 \\ 0.44 & Re \geq 1000 \end{cases}$ $Re = \frac{\rho_g d_s \vec{v}_g - \vec{v}_s }{\mu_g}$	2.27

Among these correlations, the Gidaspow model, which combines Wen-Yu and Ergun models has been extensively used in modelling multiphase system. For example, in recent studies, Papadikis et al. [44] used the Gidaspow correlation to investigate the effect of particle size on the heat transfer coefficient in a fluidised bed, using Eulerian-Eulerian approach. Ma et al. [45] used the Gidaspow correlation in a Eulerian-Eulerian simulation to investigate the effect of pressure in pneumatic conveyors. They validated their model with experimental data, and a reasonable agreement was found between the model and experimental results. Zhang et al. [46] used the same correlation in a Eulerian-Eulerian simulation to investigate hydrodynamics in a fluidised bed. The CFD results were in good agreement with experiments. In modelling of particle curtains, Wardjiman et al. [47, 48] used Schiller-Naumann drag correlation in a Eulerian-Eulerian CFD model to predict the shape of the particles in curtain in isothermal conditions. Their model was well matched with experimental results. Hurby et al. [49] used Schiller Naumann correlation in Eulerian-Lagrangian

approach to model hot particles in curtain. Good agreement was found between CFD and their experiments. Furthermore, Papadikis et al. (2010) used Schiller-Naumann in Eulerian-Eulerian approach to investigate the effect on particle size on heat transfer coefficient.

2.7.2. Effect of temperature on drag coefficient

The temperature effect on drag in particle curtains was considered by Hurby et al. [49] who simulated hot particle curtains using the Eulerian-Lagrangian approach. The rate of heat loss in the simulations was less than the experimental results. They stated that by using a larger drag coefficient, the prediction of air and particles temperatures were in better agreement with experimental results [49].

Very little information is available in the literature on the effect of surface-gas temperature difference on the particle drag coefficient. An analytical study by Kassoy et al. [50] predicted the drag coefficient of an isolated particle in the Stokes flow regime would increase surface temperature. Some experimental studies have been reported in the Russian literature on the effect of particle surface temperature on particle drag coefficient. Babiy and Ivonova [51] stated that the increased drag coefficient of hot particle is due to the increased surface temperature of the particle. They correlated an empirical equation on the motion of hot coal particles. They used irregular particles with diameters of $50\mu m$ to $400\mu m$. The empirical drag correlation that was suggested is shown in Equation 2.28:

$$C_D = \begin{cases} \frac{52}{Re} & 0 < Re < 50 \\ \frac{2}{Re^{0.2}} & Re > 50 \end{cases} \quad 2.28$$

They proposed that drag coefficient should be correlated with a Reynolds number based on the fluid properties at the surface temperature not the average film temperature. They also stated that the kinematic viscosity of air in Reynolds numbers for hot particles should be calculated at particle surface temperatures. Basian and Maksimov [52] pointed out that the increased drag coefficient in Babiy and Ivonova [51] study might be due to the irregular shape of particles, therefore they carried out an experimental study to compare the drag force of hot and cold isolated spherical particle (2500μm). However, in their work the isothermal conditions are not well-described.

2.7.3. *Turbulence correlations*

Recent advances in large-scale scientific computing have made possible direct numerical simulations (DNS) of the Navier-Stokes equations under turbulent conditions. In other words, for simulations performed on the world's largest supercomputers, no closure or subgrid approximations are used to simplify the flow, but rather the simulated flow follows all the twisting turning and stretching-folding motions of the full-blown Navier-Stokes equations at effective large-scale Reynolds numbers of about 10^5 . These simulations render available for analysis the entire 3-D velocity field down to the dissipation scale. With these numerically generated data, one can study the structures of the flow and correlate them with turbulent transfer

processes, the nonlinear processes that carry energy from large to small scales. The major drawback of this method is the excessive amount of computational capacity. Furthermore, in this method a high order of numerical method is required for more accuracy [53]. For less computationally demanding simulations, an alternative approach is to use RANS (i.e. Reynolds-Averaged Navier-Stokes) modelling which includes the average turbulence of the system.

A turbulent flow field is characterised by velocity fluctuations in all directions and has an infinite number of scales (degrees of freedom). A turbulence model is defined as a set of equations (algebraic or differential) which determine the turbulent transport terms in the mean flow equations and thus close the system of equations. Solving the Navier Stokes equations for a turbulent flow is impossible because the equations are elliptic, non-linear, coupled (pressure-velocity, temperature-velocity). Since all turbulent flows are transient and three-dimensional, the engineer is generally forced to develop methods for averaged quantities to extract any useful information. The most popular method for dealing with turbulent flows is Reynolds averaging which provides information about the overall mean flow properties. The main idea behind Reynolds time-averaging is to express any variable, $\phi(x, t)$, which is a function of time and space, as the sum of a mean and a fluctuating component as given by:

$$\phi(x, t) = \bar{\phi}(x, t) + \hat{\phi}(x, t) \quad 2.29$$

Of course, this decomposition will yield a set of equations governing the average flow field. However, by using the Reynolds decomposition, there are new unknowns that are introduced, such as the turbulent stresses and turbulent fluxes. The need for additional

equations to solve for the new unknowns is satisfied by including a turbulence model. The classical turbulent models based on RANS equations, in the order of increasing complexity are as follows [54]:

- Algebraic (Zero equations models): mixing length (first order model)
- One equation models: k -model, μ_t -model (first order model)
- Two equation models: $k-\varepsilon$ style models (standard, RNG (i.e. Re-Normalisation Group), realizable, $k-\omega$ model and RSM (first order model))
- Seven equation models: Reynolds stress models

Some advantages of using the Zero-equations models are that they are easy to implement, offer fast calculation times and good predictability for simple flows. The Zero-Equation turbulence model is described in Equation 2.30:

$$tr,s = \frac{\rho_s}{\rho_g} \quad tr,g \quad 2.30$$

The one equation models are accurate for attached-wall bounded flows, flows with mild separation and recirculation and unstructured codes in the aerospace industry. The $k-\varepsilon$ style models are relatively simple to implement and using them leads to stable calculations that converge relatively easily. Their prediction is reasonable for many flows. Reynolds Stress Model is good for accurately predicting complex flows such as cyclone flows, secondary flows swirling combustor flows, rotating flow passages and flows involving separation.

Among two equation models, the $k-\varepsilon$ model has been extensively used in the literature. Wardjiman et al. [47, 48] used the $k-\varepsilon$ model to model particle curtains in isothermal conditions. Hurby et al.

[49] also used the k - ε model to model hot particle curtains. Kuang et al. [55] used the k - ε model to model a pneumatic conveying system. In all of these studies good agreement was found between CFD model and experiment. The defining equations for the k - ε model are shown in Equations 2.31 to 2.35

The k - ε model is described in Equation 2.31:

$$\mu_{tr,g} = 0.09 \frac{\rho K_g^2}{\varepsilon_g} \quad 2.31$$

Turbulent kinetic energy (K_g) is described in Equation 2.32:

$$\frac{\partial}{\partial t} (\alpha_g \rho_g K_g) + \nabla \cdot \left(\alpha_g (\rho_g \vec{v}_g K_g - (\mu_g + \frac{\mu_{tr,g}}{\sigma_k}) \nabla K_g) \right) = \alpha_g (G_{k,g} - \rho_g \varepsilon_g) \quad 2.32$$

Turbulent dissipation rate (ε_g) is described in Equation 2.33:

$$\frac{\partial}{\partial t} (\alpha_g \rho_g \varepsilon_g) + \nabla \cdot \left(\alpha_g \rho_g \vec{v}_g \varepsilon_g - (\mu_g + \frac{\mu_{tr,g}}{\sigma_k}) \nabla \varepsilon_g \right) = \alpha_g \frac{\varepsilon_g}{K_g} (C_{\varepsilon 1} G_{k,g} - C_{\varepsilon 2} \rho_g \varepsilon_g) \quad 2.33$$

where $C_{\varepsilon 1} = 1.44$, $C_{\varepsilon 2} = 1.92$, $\sigma_k = 1.0$ and $\sigma_\varepsilon = 1.3$ are constants.

$$G_{k,g} = \mu_{tr,g} \nabla \vec{v}_g \cdot (\nabla \vec{v}_g + \nabla \vec{v}_g^T) - \frac{2}{3} \nabla \cdot \vec{v}_g + (3\mu_{tr,g} \nabla \cdot \vec{v}_g + \rho_g K_g) + G_{kb,g} \quad 2.34$$

Buoyancy turbulence is described in Equation 2.35:

$$G_{kb,g} = -\frac{tr,g}{\rho_g} g \cdot \nabla \rho_g \quad 2.35$$

2.7.4. Heat transfer

Whenever a temperature gradient exists within a system, or when two systems at different temperatures are brought into contact, energy is transferred. The process by which the energy transport takes place is known as heat transfer. The following sections describe the standard equations used to quantify three mechanisms of heat transfer in multiphase and particulate systems.

2.7.4.1. Convective heat transfer

Convection heat transfer is comprised of two mechanisms. In addition to energy transfer and due to random molecular motion (diffusion), energy is also transferred by the bulk or macroscopic motion of the fluid. In this research, the focus is on the convection heat transfer which occurs between a fluid in motion and a bounding surface, when the two are at different temperatures. The convective heat transfer can be described via Newton's cooling law (Equation 2.36):

$$Q_{convective} = hA(T_s - T_g) \quad 2.36$$

In Equation 2.36, “ h ” is convection heat transfer coefficient and “ A ” is the surface area of contact between the hot and cold bodies. The heat transfer coefficient is a critical variable and most of

convection heat transfer studies focus on estimating the value for “ h ”. The heat transfer coefficient for a sphere particle is described in Equation 2.37:

$$h = \frac{Nu \times k_g}{d_s} \quad 2.37$$

where “ Nu ” is Nusselt number. Most empirical correlations for calculating convective heat transfer coefficient take the Nusselt form. The most commonly used correlations are Ranz-Marshall [56] (Equation 2.38) and Hughmark (Equation 2.39) correlation:

$$Nu = 2 + 0.6Re^{0.5}Pr^{0.3} \quad 2.38$$

where

$$Pr = \frac{C_{pg}\mu_g}{k_g}$$

$$Re = \frac{\rho_g d_s |\vec{v}_g - \vec{v}_s|}{\mu_g}$$

The Ranz-Marshall correlation is originally developed for water droplets when they are dispersed in the air.

$$Nu = 2 + 0.6Re^{0.5}Pr^{0.3} \quad Re < 776.06, \quad 0 \leq Pr < 250 \quad 2.39$$

$$Nu = 2 + 0.27Re^{0.5}Pr^{0.3} \quad 776.06 \leq Re, \quad 0 \leq Pr < 250$$

The Hughmark Correlation is originally developed for solid spheres when they are dispersed in the water.

Between these two correlations Ranz-Marshall correlation is the most extensively used equation to calculate the heat transfer coefficient. This is particularly so in the modelling of gas-particle systems and the Ranz-Marshall correlation is widely used in CFD codes. A comprehensive review of heat transfer coefficients is summarised in Issa [57]. For example, both Hurby et al. [49] and Chen et al. [58] used the Ranz-Marshall correlation when modelling hot particle curtains and solid particle receivers.

2.7.4.2. *Conductive heat transfer*

The conduction heat transfer is the transfer of heat energy by microscopic diffusion and collisions of particles or quasi-particles within a solid body due to a temperature gradient. Conduction heat transfer through solids is due to molecular vibration. This is also known as *Fourier law* (Equation 2.40). Fourier determined that $\frac{Q}{A}$, the heat transfer per unit area ($\frac{W}{m^2}$) is proportional to the temperature gradient $\frac{dT}{dr}$. Where k ($\frac{W}{m \cdot K}$) is the thermal conductivity of material and it provides measure of material's ability to conduct heat. Equation 2.40 shows steady-state heat conduction through a sphere.

$$\frac{Q}{A} = -k \frac{dT}{dr} \quad 2.40$$

Many materials involved in industrial processes such as catalysts materials, waste, wood or other raw materials have low heat conductivities and diameters above several millimetres. Heat dispersion in these materials is slow and the particles develop considerably large temperature gradients between the particle centre and exposed surface. Therefore a uniform internal temperature within a particle often cannot be justified.

The Biot number gives a direct indication of the relative importance of conduction and convection. Internal conduction is usually neglected or ignored. In fact, in Eulerian-Eulerian CFD simulation internal conduction is not able to be involved, and in Eulerian-Lagrangian simulation is rarely considered. The effect of Biot number was taken into account in work by Ricklet et al. [59]. They used Eulerian-Lagrangian CFD to model the interaction of particles and air in a packed bed. A visual comparison of the heat-up of the particles within the bed showed good agreement between simulations and experiments.

2.7.4.2.1. *Biot number*

Biot number (Bi) is a dimensionless number used in conductive heat transfer calculations [60]. Biot number is the ratio of convection to conductive thermal processes. The Biot number approaches zero when the conductivity of the solid is so large that the solid is practically isothermal and the temperature change is mostly in the fluid at the interface (Figure 2.4 (a)). Conversely, the Biot number approaches infinity when conduction is small in comparison to convection; in this case thermal resistance in the solid predominates and there is a significant temperature gradient within the particle (Figure 2.4(c)). $Bi \ll 0.1$ is a suitable criterion for determining if the body has a uniform temperature. Equation 2.41 shows the Biot number for spherical particles.

$$Bi = \frac{hL_c}{k_s}$$

2.41

where L_c is the characteristic length of the system and it depends on the shape of the system. It is commonly defined as the volume of the body divided by the surface area of the body. The characteristic length of the sphere is defined in Equation 2.42:

$$L_{c_{sphere}} = \frac{V_{body}}{A_{surface}} = \frac{d_s}{6} \quad 2.42$$

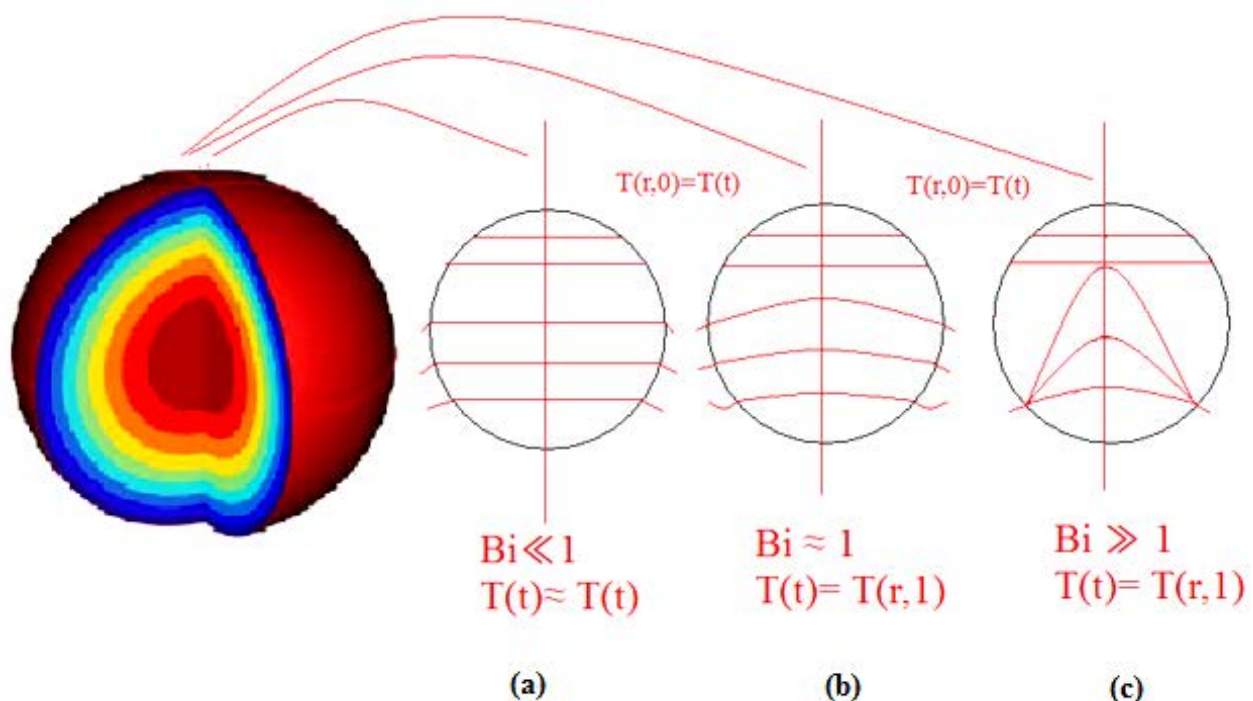


Figure 2.4: Temperature distribution for different Biot numbers

2.7.4.3. *Radiation heat transfer*

Heat transfer through radiation takes place in form of electromagnetic waves mainly in the infrared region. Radiation emitted by a body is a consequence of thermal agitation of its composing molecules. Radiation heat transfer can be described by a reference to the so-called “black body”. A black body is a hypothetic body that completely absorbs all wavelengths of thermal radiation incident on it [61]. Radiant intensity can be calculated using Stefan-Boltzman law (Equation 2.43):

$$Q = \sigma e A (T_s^4 - T_g^4) \quad 2.43$$

where σ is the Stefan Boltzmann constant ($\sigma = 5.67 \times 10^{-8} \frac{W}{m^2.K^4}$) and $0 \leq e \leq 1$ is the emissivity of the object and A is the surface area of body.

2.7.5. *Other modelling approaches*

As was explained in section 2.6.1, Eulerian-Eulerian approaches average solid phase characteristics such as temperature and solid volume fraction, and treat the particulate phase like a homogenous fluid. These approaches neglect internal heat conduction and make approximation for inter-particle forces. There are a variety of alternative modelling approaches that have been used to address these shortcomings. In the following section the application of CFD (including Eulerian-Lagrangian) and CFD hybrid models to particle curtains is summarised.

In the Eulerian-Lagrangian approach the fluid phase (continuous phase) is modelled using Eulerian approach and the solid phase (discrete particles) is modelled using Lagrangian approach, in which particles are tracked individually. Newton’s equations of motion and inter-particle force relations (cohesive or van der waals, electrostatic, and capillary) are used [4]. The Eulerian-Lagrangian

approach is more suitable for dense systems with solid volume fraction of the order of 10^{-2} or more, and when the particle numbers are low [62]. With this approach, the particle-particle collision mechanism can be described by either soft-sphere or hard-sphere models. In the soft-sphere model, particles are permitted to suffer minute deformations, which can be used to calculate the elastic, plastic, and frictional forces between particles. In the hard-sphere model, the coefficients of restitution and friction are used to describe the particle-particle collisions. This hard-sphere method is more useful in the study of rapid granular flows [63, 64]. Lagrangian models are more appropriate for flows with large particle velocity gradients and are well-suited to study the phenomena of segregation, fragmentation, or agglomeration. Eulerian-Lagrangian models have been extensively used in a variety of different applications such as spray dryers, fluidised beds, solid particle receivers and pneumatic conveyers. Some of the drawbacks of the Lagrangian approach are the large memory requirements and long computation times that require powerful high speed computers [4, 46].

Although possible to calculate computationally, the internal heat conduction within particles is commonly not included in Eulerian-Lagrangian simulation. There are a few examples of multi-phase simulations where internal heat conduction is accounted for. The most relevant is the study by Grena [65], who modelled falling particle properties within a solid particle receiver and calculated the internal temperature distribution within a single particle . In this model, properties of gas phase such as density, velocity and viscosity were obtained from Eulerian-Lagrangian CFD simulations reported in Chen et. al. [58]. A number of assumptions were made including that the air temperature was constant (300°C). Using these CFD derived properties, the 3D internal heat equation was solved as a function of time and position. They calculated the average, minimum and maximum temperature of the particles at different sizes. They concluded that the final temperature

distribution depended on particle size. Grena, suggested that the single particle simulation was useful in quantifying internal temperature distribution.

Recently internal heat conduction was combined with a Eulerian-Eulerian simulation of a fluidised bed. Papadikis et al. [66-68] used Eulerian-Eulerian approach to model the bubbling behaviour of a sand bed and the bed to surface heat transfer. In their model, biomass with two different particle sizes ($350\mu\text{m}$ and $550\mu\text{m}$) was injected into the fluidised bed and the internal heat conduction was modelled. The additional model was used to calculate the heat conduction along the radius of the particle by solving the heat diffusion equation for an isotropic particle. The Eulerian-Eulerian model and the conduction model were solved simultaneously, by including user-defined functions within the code. The inclusion of the heat conduction model had a major impact on the computational time in the 3-D simulation. This is because the time step used for the solving radial heat conduction was in the order of 10^{-5}s , whereas for Eulerian approach it was 10^{-1}s . Both Eulerian-Eulerian and heat conduction models have to converge in a synchronous way. They noted that the computational cost of such simulation is high.

In conclusion, combining the single particle model with the CFD model is an alternative way to account for the internal heat conduction of the particles, however, the computational cost of such simulation is high when they are performed simultaneously. In addition, including the internal heat conduction of particles will lead to a more precise heat loss calculation from the particles.

2.7.6. Particle curtains modelling

There are relatively few references in the literature in which the characteristics of curtains, particularly heat transfer, are studied. In this section, the modelling approaches are described, first with an emphasis on drag and isothermal studies, then focusing on thermal effects. The match

between the model and the experimental observations are discussed, and the reasons for any discrepancy are also described. Furthermore, the experimental methodology used to measure particle temperatures is also emphasised.

Wardjiman et al. [47, 48] studied the shape of falling particle curtains with a mean particle diameter of 204 μm through both stagnant and cross flow air streams in isothermal conditions. It was observed that varying initial curtain widths at the top of the curtain where they discharge from the duct outlet can lead to both diverging and converging curtain behaviour. It was found that for small initial curtain widths (i.e. 2cm) the shape of the falling curtain diverged or expanded during the fall, whereas at larger curtain widths (i.e. 8cm) the curtain converged or contracted during the fall. The convexity behaviour was attributed to variation in air pressure between the outside and inside of the curtain arising from gas entrainment within the curtains. The 3D Eulerian-Eulerian CFD reported in these papers was found to be well-matched with experimental results (using visible photography) for curtain shape under both stagnant and cross flow air conditions (Figure 2.5(a-d)). However, these simulations were under isothermal conditions when heat transfer did not occur, and the validity of Eulerian-Eulerian modelling of curtains undergoing heat transfer is not yet confirmed.

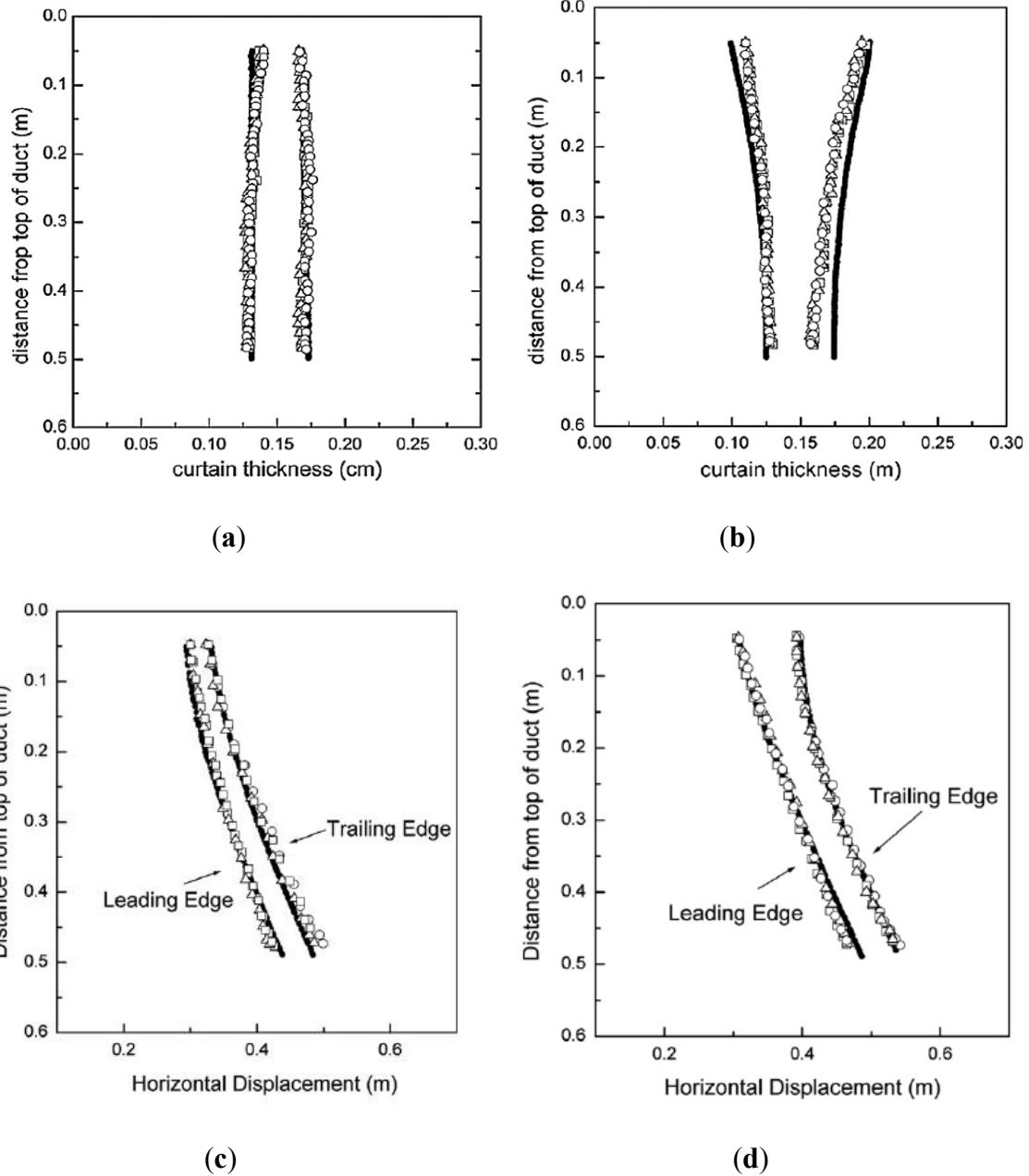


Figure 2.5: Effect of initial curtain width on the shape of the particle curtain; at $m^0 = 0.04\text{kg/s}$ and initial curtain width (a) 20mm, (b) 100mm, (c) 20mm, (d) 100mm. Air velocity in cross-flow conditions (c,d) was 0.9m/s (○Run 1, □Run 2, △Run 3, —CFDmodel). (Reported from Wardjiman et al. [47, 48])

Hurby et al. [49] studied the behaviour of freely falling curtains of spherical Norton Master BeadsTM with an averaged diameter of 650μm in both isothermal and non-isothermal conditions, in

a pilot scale solid particle receiver. The hot particles cooled as they fell through ambient air. Flow rates examined were between 0.02 and 0.04 kg/s and particles were initially heated in an oven. Two types of thermocouples for particles and air were used in order to measure discrete temperatures. A sampling cup, in which the particles accumulated, was fitted with a type K thermocouple and manually adjusted to measure the particle temperatures throughout the falling distance. The experimental results showed that the particles cooled more slowly at high flow rate when compared to low mass flow rate. A 2D-Eulerian-Lagrangian approach was compared to validate experimental results. Excellent agreement was found between CFD and experiments in isothermal conditions. However, the results of particle velocity, particle and air temperature were less well-matched, but did exhibit similar trends to the experimental data. The simulated results for both the temperature of air and particles were found to be higher than the experimental results. They suggested that using higher drag coefficient in non-isothermal conditions would result in better agreement between simulations and experiments.

Ogata et al. [69] compared the behaviour of free falling curtains and single particles in a particle jet. In line with other studies of particle curtains, both Hurby et al. [49] and Ogata et al. [69] observed that the velocity of particles within curtains was higher than the velocity of comparable single particles. Hurby et al. [49] also reported that both the temperature of air entrained within the particle curtain and the temperature of the particles themselves were higher at higher mass flow rates. Compounding this effect, at higher mass flow rates the time available for heat transfer between air and particles is reduced.

Wardjiman et al. [70] also studied heat transfer within a cold freely falling particle curtains with a mean particle diameter of 204 μ m exposed to hot cross-flowing air (40-50°C). Mass flow of particles was varied between 0.031 to 0.04kg/s. They measured the temperature profiles of both

particles and air at discrete points using a similar technique to Hurby et al. [49]. Wardjiman et al. [70] compared their experiments to a heat transfer model originally developed by McGaw [71, 72]. In their 2-D model the particle curtains were divided into two-dimensional arrays of elements with equal size. In each element, the numbers of particles were assumed to be constant, and individual particles were assumed to fall vertically within the curtain with constant velocity. Their equations and boundary conditions of the heat diffusion model are expressed as follows:

$$\frac{\partial T}{\partial t} = D \frac{\partial^2 T}{\partial r^2} \quad 2.44$$

where $D = \frac{k_s}{\rho_s C_{ps}}$

Internal heat conduction was included but the details were not provided. The boundary conditions at the surface of the particle included heat transferred by convection only:

$$k_s \frac{\partial T}{\partial r} = h(T_g - T_{sR}) \quad \text{at } r = R \quad 2.45$$

The heat transfer coefficient was calculated using the Ranz-Marshall correlation, and the mean particle temperature in each element was obtained by calculating the volume weighted average of the particle temperatures.

Their model was in good agreement with experiments. However, the model predictions of gas temperature were less satisfactory, particularly in the upper regions of the particle curtain where they assumed uniform gas flow across the curtain.

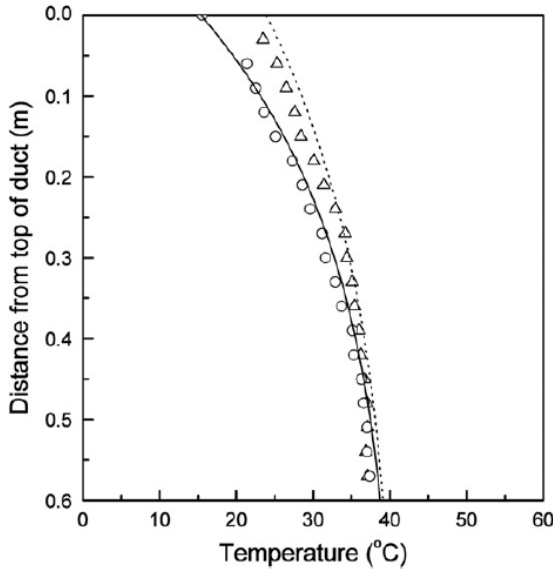


Figure 2.6: Model prediction and experimental data of gas and solid temperature for particle curtain with gas velocity of 0.9 m/s, initial curtain width of 10 cm, and solid mass flow rate of 0.040 kg/s. Inlet solid temperature=15.5°C and inlet gas temperature=41.3°C. (○ Solid (exp), △ Gas (exp), Gas model and — Solid Model). (Reported from Wardjiman et al. 2009 [70].)

Frain et al. [73] also investigated the heat transfer of cold free falling particle curtain with mean diameter of 700 μ m exposed to hot air in a vertical column of a heat exchanger. The aim of their study was to quantify the heat transfer effectiveness of the heat exchanger. The particles were discharged from a hopper at the top of the column, and the mass flow rate of the particles (ranging from 0 to 1.5kg/s) controlled using a gate valve. The mass flow rate of the particles was determined by measurements of the mass of the hopper, using two load cells. The mass flow rate of the air was measured with an orifice flow meter. They measured temperatures of gas and particles at various positions with the same discrete sampling method as Hurby et al.[49] and Wardjiman el. [70]. They used a uniform mixing model in which the overall heat exchanger coefficient was approximated from the heat transfer coefficient of a falling particle at terminal

velocity. The heat exchange surface area was assumed equal to the total surface area of the spherical particles suspended by drag within the column. It was observed that their model generally overpredicted the measured heat transfer rates of particles and gas. They suggested that the use of CFD would permit the modelling of turbulence and viscosity and lead to more realistic predictions.

Chen et al. [58] used 3-D Eulerian-Lagrangian approach in a solid particle receiver to model the behaviour of particle curtains with mean diameters ranging from 200-800 μm in a system similar to that investigated in Hurby et al. [49]. A total of 400 particles were tracked. In their studies the effect of mass flow rate (1-5kg/s) and particle size was included. They compared their simulations to experimental results of Hurby et al. [49]. The particle velocities and particle temperatures were in good agreement with Hurby et al.'s experimental study. The boundary conditions used in their simulations were found to make a significant difference to the efficiency of the solar particle receiver. Decreasing the particle size and increasing the mass flow rate increased the cavity efficiency of the receiver.

Kim et al. [74] used a 2-D Eulerian-Lagrangian approach to study the behaviour of particle curtains with mean diameter of 697 μm in terms of particles velocity, opacity and thickness, in a pilot scale solid particle receiver. It was found that increasing the initial thickness of the particle curtain and mass flow rate, resulted in converging particle curtains. Curtain shape (divergence and convergence) showed large deviation between the simulation and the experimental results. They suggested that this is due to the large size of mesh cell used in their simulations (4cm in curtain height).

Although there is consistency in approach, it is not obvious as to what model approach works best in modelling particle curtains. Both Eulerian-Eulerian and Eulerian-Lagrangian appear reasonable. However, all models to date, have been limited to 2-D and there is an opportunity to extend the modelling to 3D. Visible imaging has been shown to be an effective tool for characterising curtain shape, but measuring temperature of curtain remains a challenge. Trends in temperature appear to be measured with sufficient accuracy, but absolute temperatures are not readily obtainable. There is an opportunity to evaluate the effectiveness of other imaging techniques such as thermal imagery.

2.8. Summary of Literature Review

The literature review has summarised the different approaches used to model flighted rotary dryers, in order to emphasise the importance of determining average properties of particle curtains in these models. The important physical properties of particles and their application in modelling of flighted rotary dryers were also emphasised. The literature review has shown that there is limited information on modelling heat transfer in particle curtains, particularly the calculation of average properties of hot particle curtains, necessary to develop multi-scale models of flighted rotary dryers.

Computational Fluid Dynamics (CFD) is introduced and its potential as a powerful technique to model multi-phase systems such as particle curtains as found in flighted rotary dryers and solid particle receivers. Various different approaches in CFD are described and emphasis is placed on the Eulerian-Eulerian approach of CFD. This is because, when compared to Eulerian-Lagrangian, the Eulerian-Eulerian approach is more computationally efficient, thus it would be more cost-effective for integrating with multi-scale models involving large and dilute gas-particle systems

(i.e. particle curtains with low solid volume fractions). Given this emphasis, the most commonly used closure equations in Eulerian-Eulerian approach of CFD such as interphase momentum exchange coefficient, drag models, heat transfer coefficient and turbulence models are introduced and discussed.

In the Eulerian-Eulerian approach, the drag model was found to be one of the most critical properties. Among several correlations, the Schiller-Naumann equation was found to be the most suitable. Although the effect of temperature has been investigated by a few researchers, there are still uncertainties in defining temperature effects on drag.

Three mechanisms of heat transfer including convection, conduction and radiation were described using standard equations. Furthermore, the Biot number plays an important role in particle-gas heat transfer processes, particularly when there is internal heat conduction within the solid body. However, one of the identified shortcomings of the Eulerian-Eulerian approach is the difficulty of including internal heat conduction. As such, the use of hybrid or coupled modelling that combines internal heat conduction with Eulerian-Eulerian approaches is described. A variety of alternative modelling approaches including both CFD Eulerian-Lagrangian and CFD Eulerian-Eulerian models are introduced to address this issue. It was concluded that the decoupled Eulerian-Eulerian model used by Grena [65] offers lower computational cost, but neglected important mechanisms. In comparison, the coupled Eulerian-Eulerian model described in Papadikis [66-68] was very comprehensive but the computational cost of simulation is very high.

In this literature review, specific examples of modelling particle curtains are described. It was observed that both Eulerian-Eulerian and Eulerian-Lagrangian are suitable approaches to model particle curtains. However, in these simulations the effect of heat transfer has not been included in

the Eulerian-Eulerian models, and all Eulerian-Lagrangian models have been 2D. In this thesis, 3D Eulerian-Eulerian models will be developed and evaluated. Experimental particle curtains studies have all been based on discrete sampling of particle temperatures, and there is no data presented for temperature profiles that cover the entire area of the particle curtains. Therefore, there is capacity to improve the experimental methods for temperature measurement. Drawing on the value of visible imagery, in this thesis, I intend to evaluate the potential of infrared thermography of hot particle curtains.

Chapter 3 Model Development

In this chapter, a 3-D Eulerian-Eulerian base model is developed to simulate hot particle curtains falling through still air and undergoing convective heat transfer. The equations, geometry, material properties, boundary conditions and mesh considerations are described. A single particle model in the absence of internal heat conduction is also presented. Centreline particle temperature profiles from CFD simulations are compared to those derived using the single particle model. The base CFD model is used to derive Reduced Order Models (ROM) that are suitable for implementation in larger scale process models. Average properties such as the mean residence time, solids volume fraction and curtain area are calculated as they are convenient characteristics that can be used in larger-scale process models. Furthermore, the effects of particle mass flow, particle size, and particle slot width, on temperature profiles and heat loss are investigated using analysis of variance techniques. Conditions leading to maximum heat transfer in particle curtains are also examined.

In order to facilitate comparison of CFD simulation and thermal image results, a range of post-processing image analysis techniques for identifying curtain edges from CFD data are introduced and compared.

Substantial sections of this chapter are adapted directly from the published paper: Sepideh Afshar, Madoc Sheehan and Amir Fazlollahi, (2015), Using CFD to derive reduced order models for heat transfer in particle curtains. 15(2):71-80, Progress in Computational Fluid Dynamics.

3.1. Model Equations

A 3-D Eulerian–Eulerian model was used to simulate gas-particle interactions in falling particle curtains. The simulations were performed using ANSYS CFX V14.5.7 CFD software. The model equations in Eulerian-Eulerian approach are based on the continuity, momentum, energy conservation principles at steady state. In the interests of brevity, I refer the reader to Equations 2.3-2.19 of the literature review, where the complete set of mass, momentum and energy relations that were used in this study are provided. In Section 3.1.4, the single particle model equations in the absence of internal heat conduction are provided.

3.1.1. Heat transfer equations

Equations for the rate of convective heat transfer between particle curtain and air are written as follows:

$$Q_{sg} = hA(T_s - T_g) \quad 3.1$$

where h is convective heat transfer coefficient and A is the total interfacial surface area of particles in the curtain.

$$h = \frac{Nu \cdot k_g}{d_s} \quad 3.2$$

The Ranz-Marshall correlation [56] was used to describe the heat transfer coefficient characterising convective heat transfer between air and the particles:

$$Nu = 2 + 0.6Re^{0.5}Pr^{0.3} \quad 3.3$$

$$Pr = \frac{C_{pg}\mu_g}{k_g} \quad 3.4$$

$$Re = \frac{\alpha_s \rho_g d_s |\vec{v}_g - \vec{v}_s|}{\mu_g} \quad 3.5$$

3.1.2. Drag model

Interphase drag (β) is an important characteristic and has been the subject of numerous investigations [75]. The common approach to modelling dilute two-phase systems is the Gidaspow model [31] which is a combination of two older models developed by Wen-Yu and Ergun.

$$\beta = (1 - \varphi_{gs})\beta_{Ergun} + \varphi_{gs}\beta_{Wen-Yu} \quad 3.6$$

$$\varphi_{gs} = \frac{\arctan [150 \times 1.75(0.2 - \alpha_s)]}{\pi} + 0.5 \quad 3.7$$

$$\beta_{Ergun} = 150 \frac{\alpha_s^2 \mu_g}{\alpha_g d_s^2} + 1.75 \frac{\alpha_s \rho_g |\vec{v}_g - \vec{v}_s|}{d_s} \quad \alpha_g < 0.8 \quad 3.8$$

$$\beta_{Wen-Yu} = \frac{3}{4} C_D \frac{\alpha_s \rho_g}{d_s} |\vec{v}_g - \vec{v}_s| \alpha_g^{-2.65} \quad \alpha_g \geq 0.8 \quad 3.9$$

The particle drag model (C_D) was evaluated using the widely used Schiller-Naumann equation:

$$C_D = \begin{cases} \frac{24}{\alpha_g Re} [1 + 0.15(\alpha_g Re)^{0.687}] & Re < 1000 \\ 0.44 & Re \geq 1000 \end{cases} \quad 3.10$$

where:

$$Re = \frac{\rho_g d_s |\vec{v}_g - \vec{v}_s|}{\mu_g} \quad 3.11$$

3.1.3. *Turbulence model*

The $k - \varepsilon$ turbulence model has been frequently used for multi-phase simulation and has been shown to provide close agreement between experiments and simulations [47, 48, 68]. In the interests of brevity I refer the reader to Equations 2.31-2.35 of the literature review, where the complete set of relations are provided.

3.1.4. *Single particle model (SPM)*

Drag (F_D) and gravitational forces (F_G) are the most important forces acting on a single particle. The general equations of motion for a single particle with velocity (v_s) and displacement (Y) are written:

$$F_{net} = F_G - F_D \quad 3.12$$

$$m_s \frac{dv_s}{dt} = F_G - F_D \quad 3.13$$

$$v_s = \frac{dy}{dt} \quad 3.14$$

where

$$F_G = m_s g \quad 3.15$$

$$F_D = C_D A_{xs} \frac{1}{2} \rho_g v_s^2 \quad 3.16$$

where A_{xs} is cross-sectional area of the particle exposed to drag.

$$A_{xs} = \pi \frac{D_s^2}{4} \quad 3.17$$

Thus:

$$m_s \frac{dv_s}{dt} = m_s g - C_D A_{xs} \frac{1}{2} \rho_g v_s^2 \quad 3.18$$

The energy balance on the particle assumed to be undergoing convective heat transfer was described using Equation 3.19. The temperature of the particle was assumed to be uniform throughout (T_s).

$$m_s C_p \frac{dT_s}{dt} = h A_s (T_g - T_s) \quad 3.19$$

where A_s is the total area of the surface spherical particle as described in Equation 3.20:

$$A_s = \pi D_s^2 \quad 3.20$$

3.1.4.1. Numerical details (SPM)

The SPM set of ordering and algebraic equations was solved using Engineering Equation Solver [76] with standard inbuilt integration solvers. The equations were solved to track both location in y direction and particle temperature (T_s). In the single particle model, the gas temperature was taken as ambient (300K) and constant. The drag coefficient (C_D) used in single particle model was calculated using the same relations as the CFD simulation (Equation 3.10, where $\alpha_g = 1$). Typical time steps were 0.00025 seconds, for interval times between 0 to 0.6 seconds, which covered the fall distances monitored.

3.2. CFD Computational Set-up

In this section, a single curtain is generated within a fixed box using two different geometries and meshing scenarios. Scenario A was used to enable direct comparison with previous CFD simulation approaches [48]. Scenario A simulation results are presented in Sections 3.3 to 3.5.1. This means single particle model results are compared to scenario A simulations results. In addition, the Reduced Order Model results are based on scenario A simulations. In these simulations, the solid volume fraction is constant ($\alpha_s=0.52$), and the values of initial velocities are calculated using Equation 3.21 in which A_{slot} is the area of the slot. The initial velocity of the single particle was assigned the same initial velocity as the curtaining particles at the spreader box exit. In scenario A, the mass flow rate was varied between 0.041-0.1kg/s.

$$m^o = \rho_s v_s \alpha_s A_{slot} \quad 3.21$$

Scenario B was used to replicate the experimental conditions, and the results are presented in Sections 3.5.2 and 3.5.3, and Section 6.2 where there is comparison to experimental results. Mean residence times, curtain edge, mean solid volume fractions and curtain area results are calculated using scenario B simulations. In these simulations, the solid volume fraction values were calculated using Equation 3.21 in which the initial velocity was taken constant as $v_0=1.44\text{m/s}$. In scenario B, the mass flow rate was investigated at 0.041kg/s and 0.1kg/s . Note that the initial velocities used in Chapter 6 for comparison to experimental results are calculated experimentally in Section 4.3.4.4.

3.2.1. Geometry

The geometries consisted of rectangular boxes with varying slot width in the x direction from 10 to 80mm and constant slot length in the z direction of 150mm. A sketch of the geometries of the calculation domains for scenarios A and B are given in Figure 3.1(a) and (b) respectively. In scenario A, there are three faces bounding the calculation domain: the sand inlet and the two air openings. In scenario B, there are four faces bounding the calculation domain: the sand inlet and the three air openings. In both scenarios, the remaining walls were governed by no-slip boundary conditions.

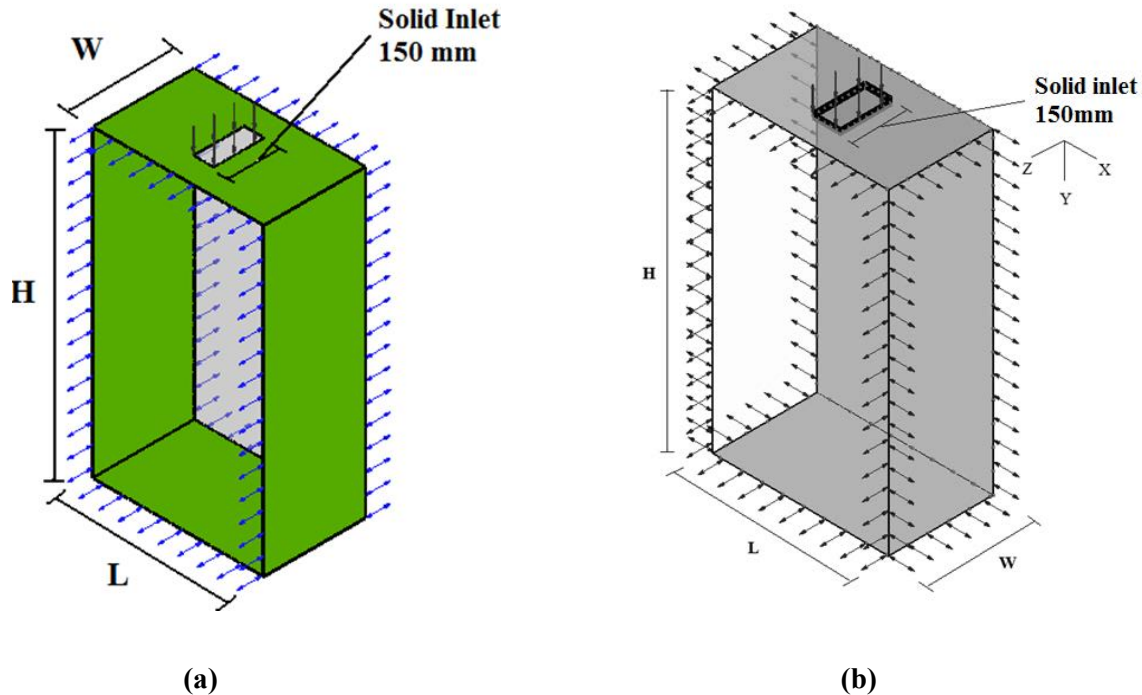


Figure 3.1: Schematic diagram of simulation domain (a) scenario A: L=450mm, H=900mm and W=225mm (b) scenario B: L=505mm, H=900mm and W=300mm

All simulations were run until steady-state conditions were reached and the RMS normalised residual values of the calculated variables (i.e., mass, velocity, turbulent kinetic energies, turbulent dissipation energies and volume fraction) in the three fundamental equations of continuity, momentum and energy, were stable. A high resolution scheme was used to ensure accurate numerical solutions. The first order upwind scheme was selected for solving the turbulence equations.

The model was solved on a 2.27 GHz CPU processor (96.0 GB memory) until all normalised residuals were less than 10^{-4} . The number of iterations required to achieve convergence was dependent on the particle size. For example, scenario B simulations with smaller particle sizes of 200 μm require approximately 36 to 62 iterations to converge. Simulations with 600 μm particles

ranged from 421 to 619 iterations. The details of mesh dependency for the two scenarios will be described further in Section 3.2.3.

3.2.2. Initial conditions

The simulation initial conditions for the results and analysis presented in this chapter, for both scenarios, are given in Table 3.1. In later comparisons between infrared thermography experimental data and CFD predictions (Chapter 6), measured values for these properties were utilised.

Table 3.1: Initial conditions of simulation domain in scenario A

Solid volume fraction at solid inlet in scenario A	0.52
Solid volume fraction at solid inlet in scenario B	Calculated using Equation 3.20
Sand inlet temperature	400 K
Initial gas temperature	300 K
Air velocity at solid inlet	0 m/s
Solid mass flow rate at solid inlet	0.041,0.1,0.2kg/s
Sand inlet velocity in scenario A	Calculated using Equation 3.20
Sand inlet velocity in scenario B	1.44(m/s)
Slot widths	10 - 80(mm)

In scenario B, sand inlet velocity (1.44m/s), taken from that reference [70], was used. As mass flow rates and slot widths change in those simulations, the initial inlet solid volume fraction was calculated via Equation 3.21.

Silica sand particles were used in all simulations. Table 3.2 presents the average properties of silica particles and air. These average properties were used in simulations presented in this chapter. In the simulation comparing infrared thermography and CFD modelling (Chapter 6), air properties (ρ_g , k_g and μ_g) were taken as function of temperature and relative humidity. Correlations for these properties were developed from references Kreith and Bohn [60] and Melling et al. [77] respectively.

Table 3.2: Physical and thermal properties of air and particle

Particle diameter	200,400,600(μm)
Particle density	2634(kg/m^3)
Molecular weight of sand (SiO ₂) at 25°C	60.0843 (g/mol)
Specific heat capacity of sand	0.9125T+522.5(J/kg.K) [61]
Thermal conductivity of sand	$5 \times 10^{-7}T^{-2} + 17 \times 10^{-2}T + 0.6545(\text{W}/\text{m.K})$ [61]
Restitution coefficient of sand	0.9
Specific heat capacity of air	1.0044×10^3 (J/kg.K) [78]
Thermal conductivity of air	2.61×10^2 (W/m.K) [78]
Dynamic viscosity of air	1.831×10^{-5} (kg/m.s) [78]

3.2.3. Mesh considerations

3.2.3.1. Average heat loss in particle curtain

In order to perform mesh analysis and assess simulation convergence, a bulk curtain property describing heat loss was defined. The heat loss was characterised as the total heat loss per unit mass of the falling particles evaluated from the spreader box exit to the landing zone (in this case, 0.8m down from the exit).

Equation 3.22 was used to determine the total heat loss per unit mass.

$$\hat{Q} = \bar{C}_p \bar{\Delta T} \quad 3.22$$

\bar{C}_p is the average heat capacity across the temperature range of interest of sand and $\bar{\Delta T}$ is the average temperature difference across the falling height ($\bar{T}_2 - T_{inlet}$). \bar{T}_2 is the average temperature of the particle curtain in a ZX plane 0.8 m down from the exit. Figure 3.2 describes the geometric location of this plane whilst the inlet temperature (T_{inlet}) is well-defined (Table 3.1). The outlet temperature requires integration techniques to calculate the average temperature at 0.8m down. The temperature of the particle curtain at the defined plane is described by numerical integration of the data, using mass flow rate as a weight function (Equation 3.23):

$$\bar{T}_2 = \frac{\int_{x=0}^{x=W} \int_{z=0}^{z=L} m_{xz}^o T_{xz} dz dx}{\int_{x=0}^{x=W} \int_{z=0}^{z=L} m_{xz}^o dz dx} \quad 3.23$$

In Equations 3.23, m_{xz}^o and T_{xz} are mass flow rate and temperature of sand at each node of simulation in the defined ZX plane. In each node of the ZX plane, particularly the outside edges, negative and positive values of mass flow rate occur (Figure 3.2). Only mass flow values for the downward particles (i.e. negative values) were included.

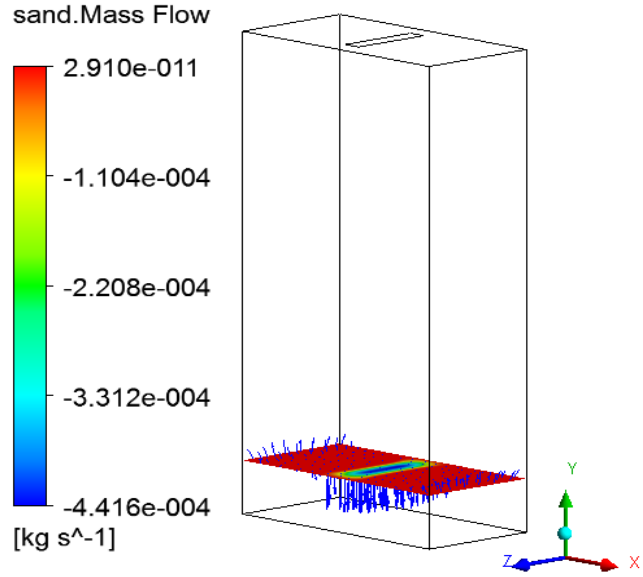


Figure 3.2: Sand mass flow rate vectors at ZX plane, 0.8m down from the entrance

3.2.3.2. *Approach*

The accuracy of results depends on the quality of mesh size used in simulations. Kim et al. [74] investigated mesh dependency in their modelling of a pilot scale solid particle receiver. It was found that mesh size in the CFD simulation has an important effect on determining the thickness of the curtain. In this research, the multizone method in CFX was selected for generating mesh within the domain. In other examples from the literature [47, 48], the tetrahedral method has been used. However, in our simulations using the multizone method facilitates systematic analysis of the data and post-processing on alternative software (Matlab). Furthermore, comparison to visible and thermal images, which are also defined as fixed element matrices, can be more easily undertaken. These advantages are particularly relevant to curtain edge detection processes.

3.2.3.3. Mesh analysis

In this research, mesh dependency was carried out on the described geometries at different mesh sizes (3mm, 4mm, 5mm, 6mm, 7mm and 8mm) with a mass flow rate of 0.041kg/s. Different slot widths (10mm, 60mm and 80mm) were investigated. Figure 3.3 shows mesh dependency analysis for scenario A simulations. Average heat loss per unit mass (Equation 3.22), was used as the convergence criteria. A mesh size of 4mm with 1,449,225 elements was utilised in scenario A simulations.

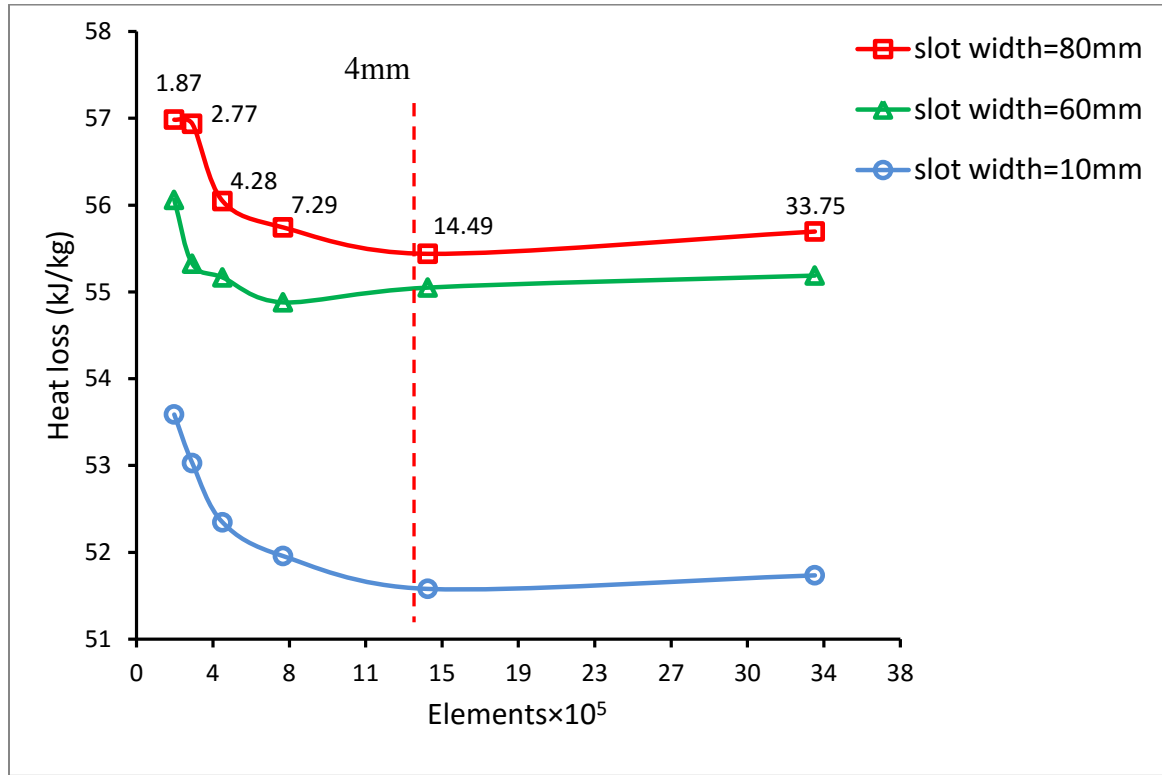


Figure 3.3: Heat loss predictions using the indicated element numbers

In the slightly larger scenario B simulations, the total change in average heat loss for each simulation (10mm, 30mm, 80mm slot widths) across the entire range of mesh sizes considered (3mm to 8mm) was 1%. The difference between the heat loss for the selected mesh sizes (5mm)

and the smallest mesh size was only 0.05%. The mesh size of 5mm, used in the scenario B simulations corresponded to element number of 1,096,200 to 1,099,980.

3.3. Significance of Process Parameters on Average Heat Loss

In the following section, the effects of slot width, mass flow rate and particle size, on heat loss, are investigated using Analysis of Variance techniques. Figure 3.4 shows a selection of results comparing CFD calculated heat losses per unit mass at different slot widths (10mm, 30mm, 60mm and 80mm), mass flow rates (0.041kg/s, 0.1kg/s and 0.2 kg/s) and particle size (200 μm , 400 μm and 600 μm).

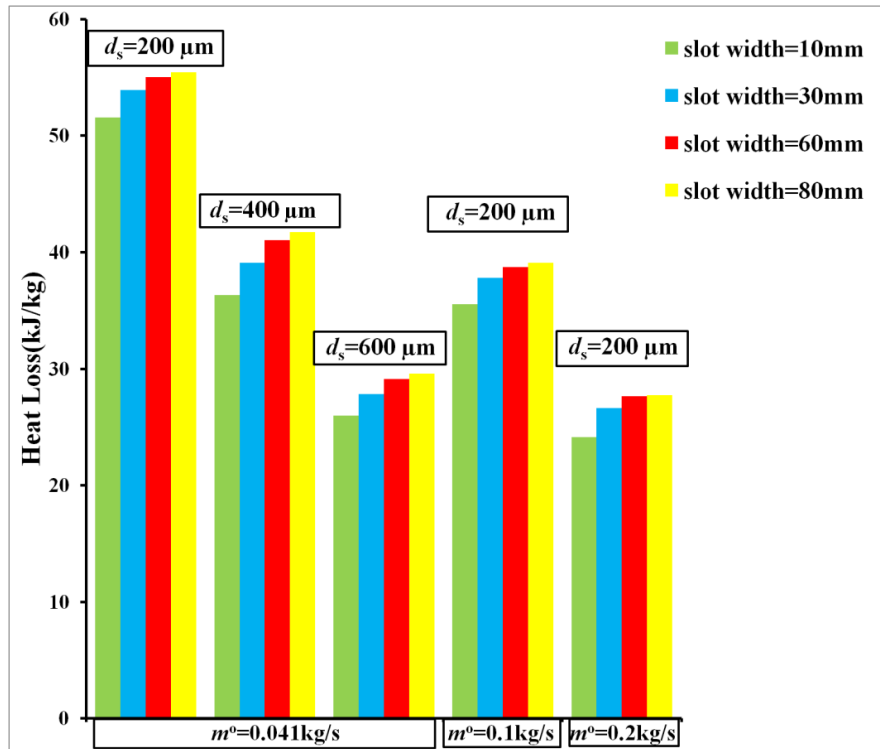


Figure 3.4: Heat loss comparison at slot widths of 10mm, 30mm, 60mm, 80mm, particle sizes of 200 μm , 400 μm and 600 μm and mass flow rates of 0.041kg/s, 0.1kg/s and 0.2kg/s. Similar trends in the effect of particle size (0.041kg/s) were observed at higher mass flow rates of 0.1kg/s and 0.2kg/s

A three way ANOVA (Analysis of Variance) was used to evaluate the effect of particle size (at three levels of 200 μm , 400 μm and 600 μm), mass flow rate (at three levels of 0.041kg/s, 0.1kg/s , 0.2kg/s) and slot width (at four levels of 10mm, 30mm, 60mm and 80mm) on heat loss. ANOVA results were generated using SPSS 19.0 (Table 3.3). The analysis of variance is required in order to better understand the interaction of variables and the relative significance of the independent variables. ANOVA analysis of CFD results also provides a valuable methodology for deriving ROM and determining the key parameters to be used in these models.

Table 3.3: Summary of results obtained by ANOVA

Source	Sum of Squares	Mean Square	F	Sig.
Slot width	8.964×10^7	2.988×10^7	1405.447	0
d_s	1.831×10^9	9.157×10^8	43070	0
m^o	2.199×10^9	1.099×10^9	51700	0
$d_s \times m^o$	2.546×10^8	6.364×10^7	2993	0
Slot width $\times m^o$	1.833×10^5	3.056×10^4	1.437	0.279
Slot width $\times d_s$	2.271×10^6	3.785×10^5	17.80	0
Error	2.551×10^5	2.126×10^4		
Total	3.783×10^{10}			

The results showed that all three variables of slot width, particle size and mass flow rate have significant effect on heat loss, as P values (Sig.) are less than 0.05. The statistical analysis also showed that mass flow rate, particle size and the interaction of mass flow rate and particle size had the highest influence on heat loss. As an example, Figure 3.5 shows the interaction effect between mass flow rate and particle size. It also shows the highest effect is at lowest mass flow rate and smallest particle size (200 μm).

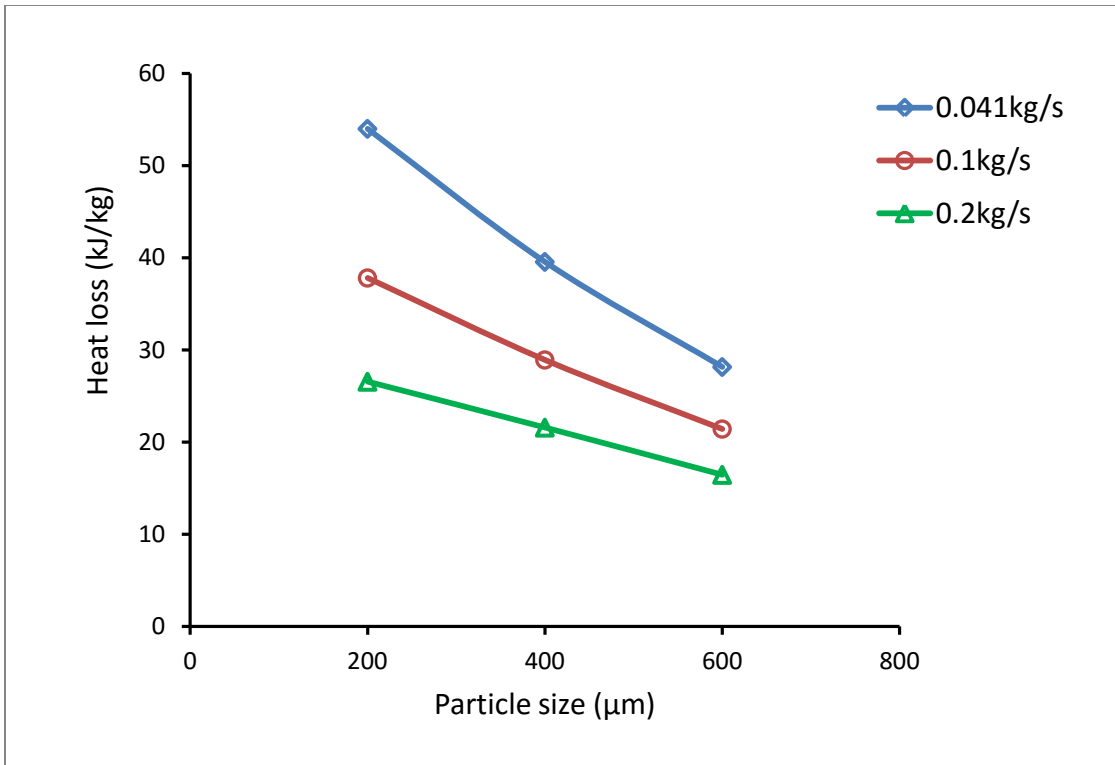


Figure 3.5: Average heat loss for interaction effect of particle size and mass flow rates

Figure 3.6 shows a comparison of heat loss per unit mass versus slot widths at the different mass flow rates for particle size of $200\mu\text{m}$. It was observed that there is a gradual decrease in the influence of slot width as slot width increases. It can be seen that heat loss is higher at lower mass flow rate (0.041kg/s), however heat loss is almost independent of slot width at larger slot widths of 60mm and 80mm for the same mass flow rate. This can be attributed to the rapid convergence of the curtain, as observed experimentally [48].

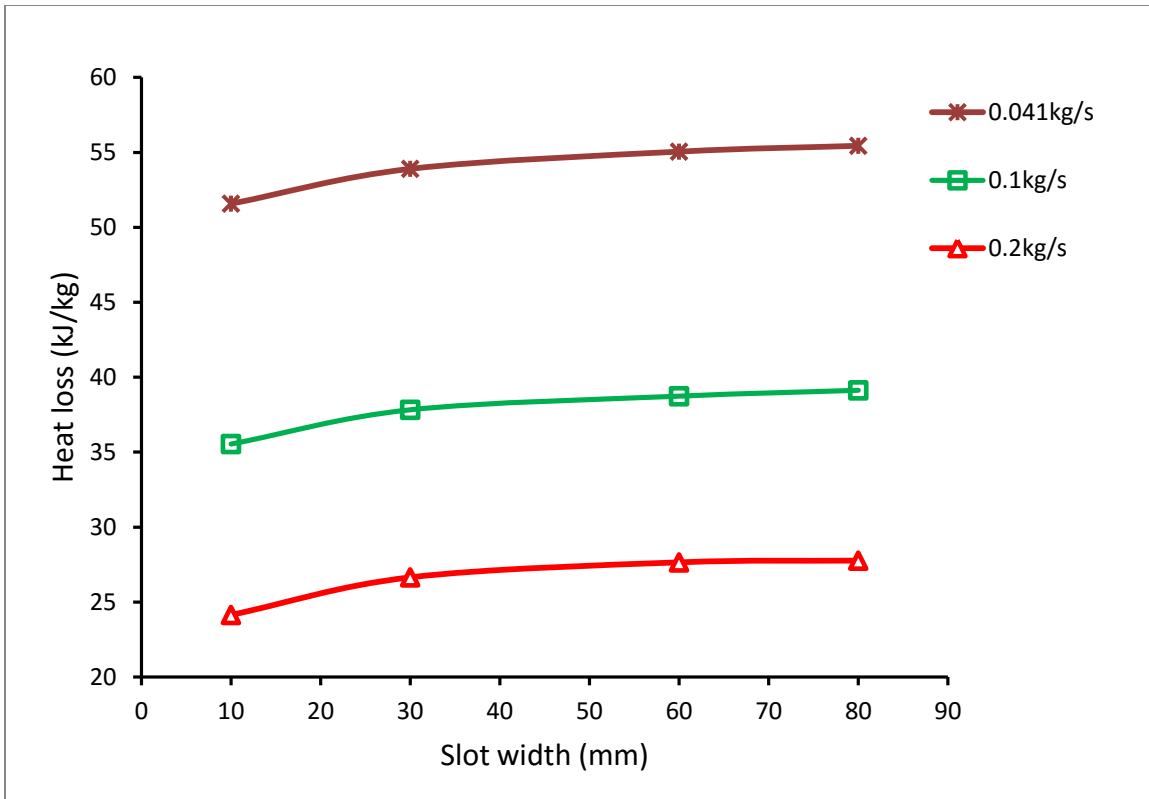


Figure 3.6: Heat loss per unit mass for different slot widths at mass flow rates of 0.041kg/s, 0.1kg/s and 0.2kg/s for particle size of 200 μ m

3.4. CFD and SPM Centreline Temperature Profiles Comparison

The change in particle temperature over falling distance is an important characteristic in curtain thermal behaviour. Both the single particle model and CFD simulations can be used to generate such profiles, although it is well known that the single particle models have deficiencies. In this research, I make the reasonable assumption that the CFD simulation results are a better approximation to the real system than modelling the curtain as a single particle model, even though the single particle model is commonly used.

Figures 3.7-3.9 show a selection of temperature profile comparisons between single particle simulations and CFD simulation results for the geometric centreline temperature of particles in the curtains. For the single particle model at constant particle size and constant slot width, only the initial velocity changes at different mass flow rates. I choose to present the data in this way to remain consistent with the assumption that CFD is the better approximation. The temperature of the single particle and the centreline temperature of the particles in curtain has been non-dimensionalized: $T^* = \frac{T - T_{f-CFD}}{T_0 - T_{f-CFD}}$, in which T_{f-CFD} is the final temperature of particles in curtain after 0.8m falling distance and T_0 is (400 K) the particle initial temperature.

It was found that the heat loss of particles in the simulated curtain is less (i.e. higher final temperature) than the single particle, particularly at higher mass flow rates (0.1kg/s and 0.2kg/s) and there are smaller differences in the simulated results comparing single particle simulations and CFD simulations at low mass flow rate (0.041kg/s).

It can be seen that for narrow slots (10mm), in all cases the single particle loses heat faster than its equivalent curtain. As the slot width widens or mass flow rate decreases this effect is less pronounced. In fact, in the low mass flow rate (0.041kg/s) and wide slot (60mm and 80mm) simulations this effect is reversed and the single particle loses heat at a slower rate. Under these low flow, wide slot conditions the curtain shape is convergent (narrows as it falls) rather than divergent, which is a significant factor in defining convection heat transfer behaviour.

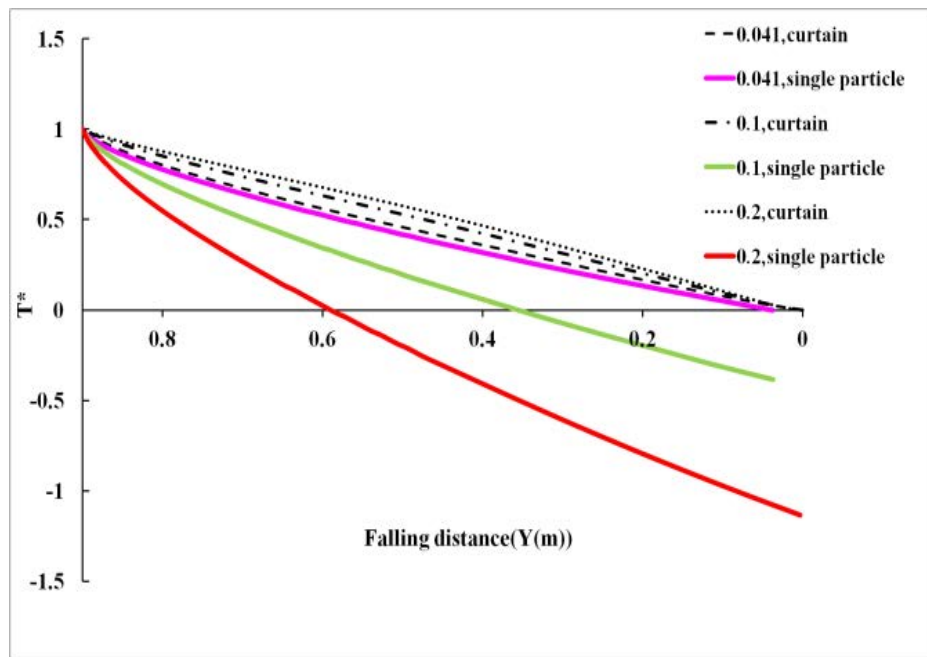


Figure 3.7: Temperature comparison between single particle and particles in curtain in 10mm slot at three 0.041, 0.1 and 0.2kg/s mass flow rates and particle size of 200 μm

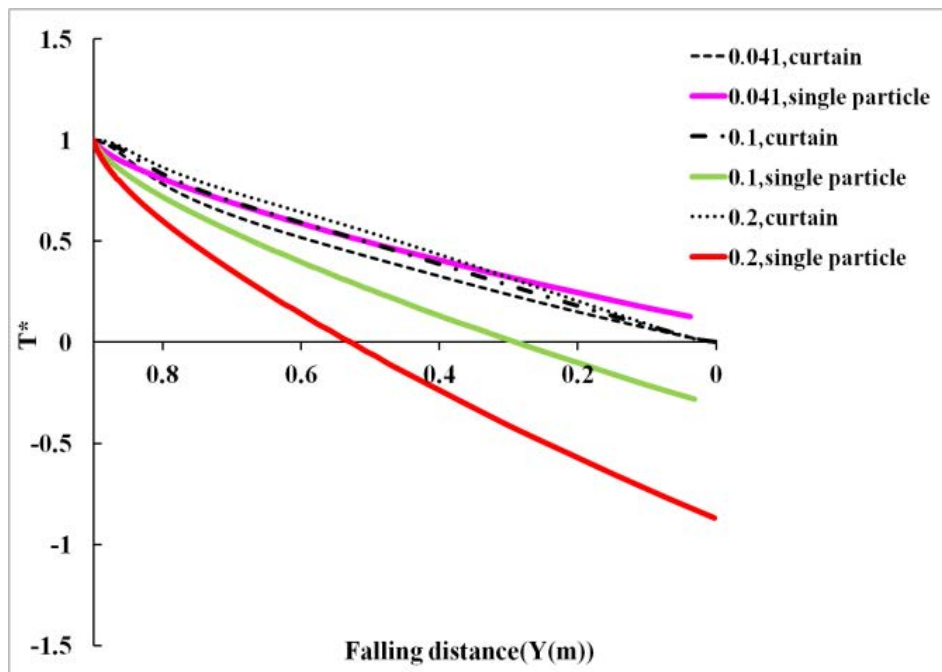


Figure 3.8: Temperature comparison between single particle and particles in curtain in 60mm slot at three 0.041, 0.1 and 0.2kg/s mass flow rates and particle size of 200 μm

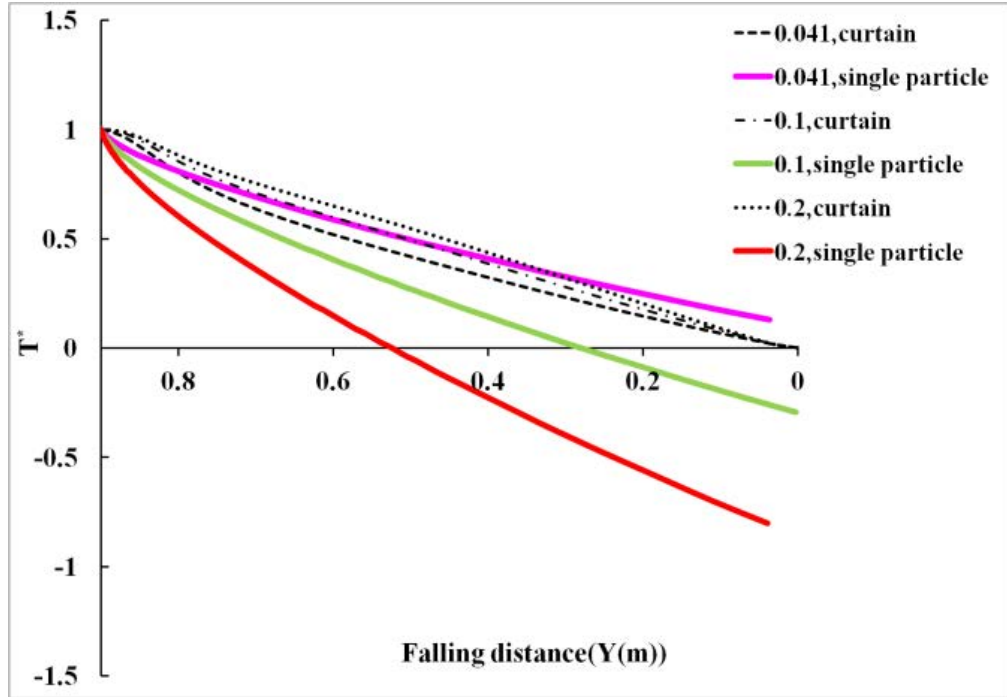


Figure 3.9: Temperature comparison between single particle and particles in curtain in 80mm slot at three 0.041, 0.1 and 0.2kg/s mass flow rates and particle size of 200 μm

3.5. Model Application: Reduced Order Modelling

To the authors best knowledge, all examples of geometric modelling of flighted rotary dryers have utilised the single particle model to represent curtain behaviour (see for example Britton et al. [7]). This has been the case for both drag (i.e. fall time) as well as mass and heat transfer. Fall times from curtains cascading off flights has been essential to modelling solids transport (mean residence times). Baker [26] demonstrated that the single particle model overestimated the drag experienced by the particles within the curtains in cross flowing situations. To improve predictions of particle movement using the single particle model, Baker modified the magnitude of the drag coefficient and assumed the curtains behaved as flat plates. This led to improved

results, but calculations were complicated by a lack of data characterising the curtain bulk properties (voidage and thickness). Baker's work demonstrated that CFD modelling has potential for use in developing Reduced Order Models to represent bulk curtain behaviour. In mass and heat transfer applications, there has been no work to date to account for bulk curtain behaviour. However, it is obvious that the same conclusions regarding SPM applications will apply. Methods to determine these average properties are not widely described in the literature. Reduced Order Models (ROM) have been used in modelling particulate systems such as fluidised beds [79]. The purpose of this research is to describe a methodology for using 3-D Eulerian-Eulerian CFD models to determine the average properties of particle curtains. These properties include frontal area, average solids volume fraction, and mean residence time. For properties such as the frontal area of the curtain and average volume fraction it is essential to define the extent of coverage of the curtain (i.e. to define the edges). In this research, a new technique for precise determination of the location of the curtain edges is introduced. The mean residence time of particle curtains is also determined using alternative techniques.

3.5.1. Temperature profiles

As illustrated in Figures 3.7-3.9, the modelled temperature behaviour of a single particle is different to that of particles in the curtain. It is assumed that CFD results are better than single particle results. This assumption was confirmed in Section 6.2.2. In That section, CFD modelling was found to provide better estimate than single particle modelling when compared to experimental thermographic data. The aim of this section is to modify the SPM so as to match the CFD curtain temperature profile. The CFD models are used as the basis from which the ROM is

derived. The first step in developing a ROM is to identify the controlling factors and identify the variables of the single particle model that are most suitable to modify in order to reproduce the thermal behaviour of particles in curtains. As described in Section 5.3, mass flow rate and particle size were identified to have the highest influence on heat loss. The contribution of these two parameters were considered significant enough for developing the ROM, and therefore the lesser significant parameters were ignored. In terms of the single particle model parameters appropriate to modify, Baker (1992) suggested that the particle drag coefficient was an appropriate parameter to vary. Furthermore, Hruby et al. (1988) also suggested that for hot particles in curtains, the magnitude of drag is different to that of cold particles. From a practical perspective, because air is entrained within the curtain as it falls there is a difference between the drag experienced by a single particle and that in a particle curtain.

In the ROM, the magnitude of the drag coefficient is altered by introducing the parameter B into the drag coefficient correlation (Equation 3.24):

$$C_D|_{ROM} = B \times \frac{24}{Re} [1 + 0.15(Re)^{0.687}] \quad 3.24$$

In order to obtain initial estimates of the value of B, a trial and error study was carried out using the observed temperature profiles for different particle sizes and mass flow rates for the slot size of 10mm. Figures 3.10 and 3.11 show the comparison to CFD profile and effect of changing the magnitude of B on the non-dimensionalised temperature profiles obtained using the single particle model.

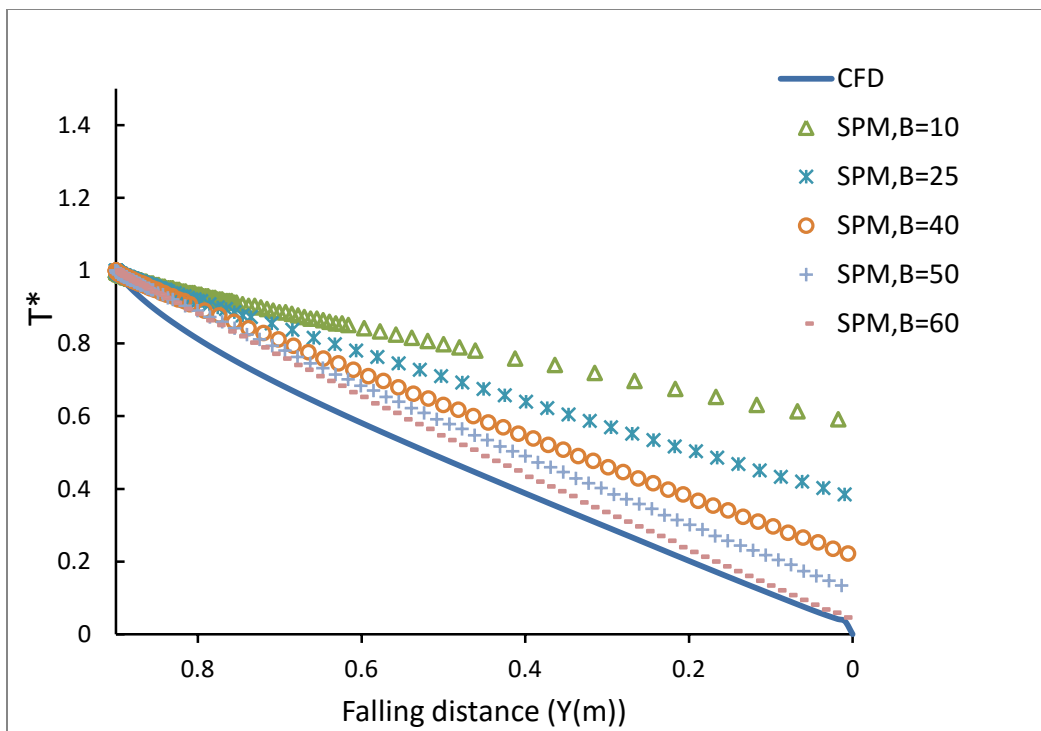


Figure 3.10: Temperature profiles comparing single particle model to CFD simulation, $d_s=600\mu\text{m}$, $m^0=0.041\text{kg/s}$ and slot width=10mm

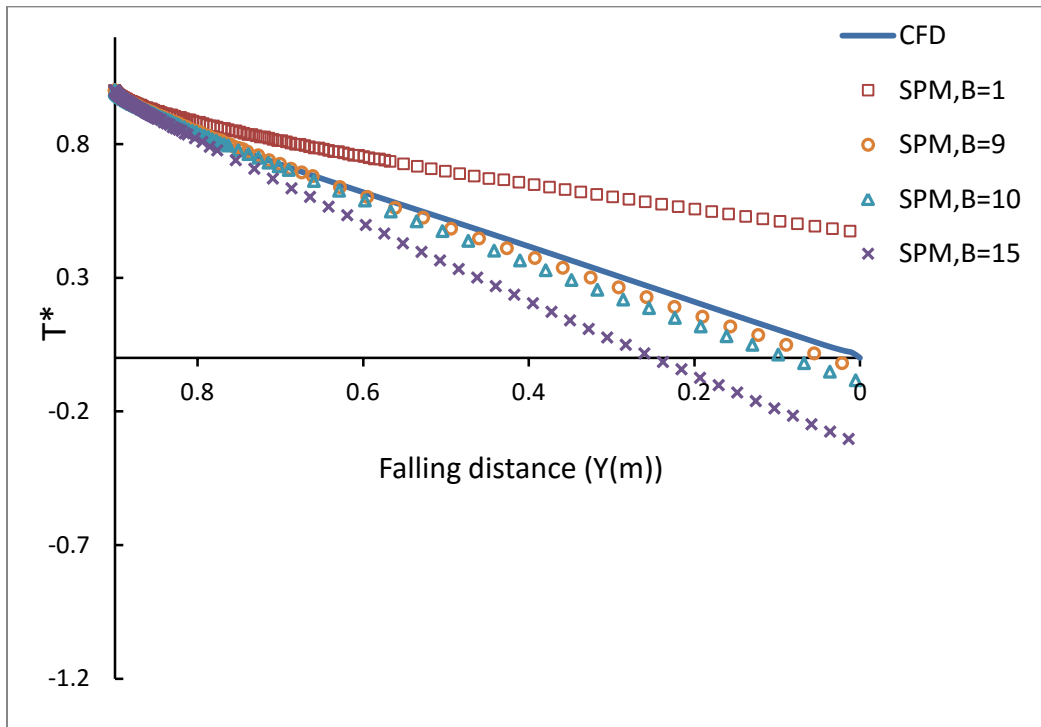


Figure 3.11: Temperature profiles comparing single particle model to CFD simulation, $d_s=400\mu\text{m}$, $m^0=0.1\text{kg/s}$ and slot width=10mm

Using the most promising initial estimates as starting guesses, B values were optimised by adopting a Matlab routine in which a derivative-free search procedure was employed. The objective function was defined as the sum of the absolute differences between the non-dimensionalised centreline temperatures obtained using the ROM (single particle model) and that obtained from the CFD simulation (Equation 3.25).

$$\text{objective function} = \sum |T^*_{CFD} - T^*_{SingleParticle}| \quad 3.25$$

To minimise the difference between the two temperature profiles, the same number of discrete temperature data points was required at equivalent falling distances. 100 discrete CFD data points were extracted for each profile. The single particle model results were interpolated to provide the same number of data points at the required distances. Figure 3.12 shows the estimated values of B for best match between the ROM and the CFD profiles.

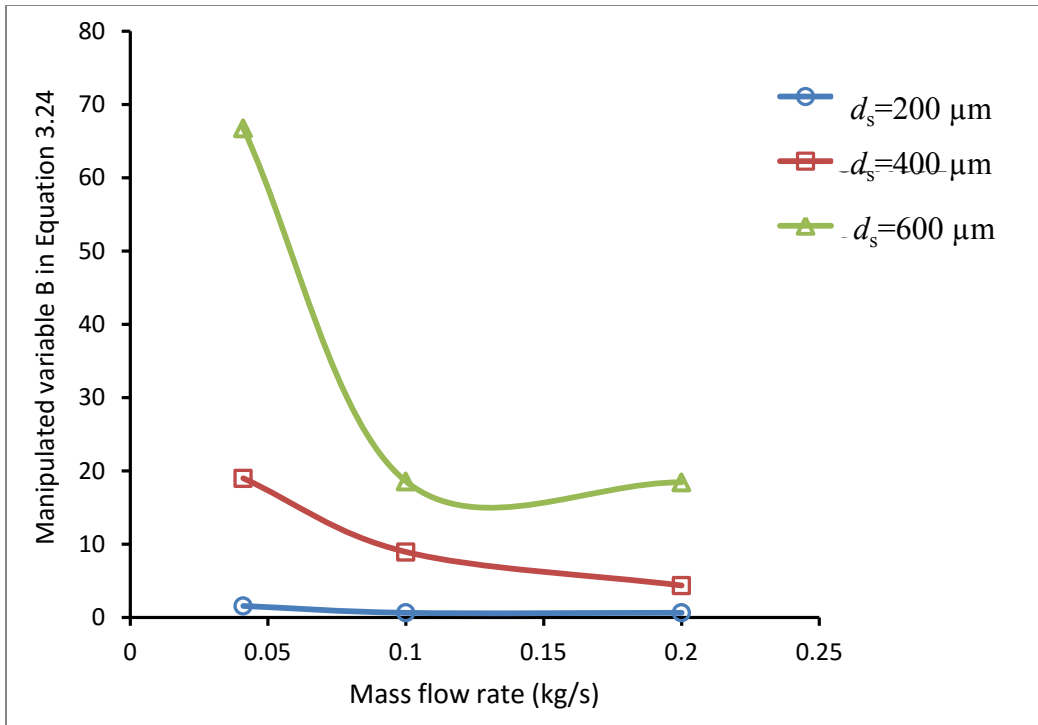


Figure 3.12: Parameter estimation for B values using Equation 3.24, slot width=10mm

Figure 3.12 demonstrates that there is less change in drag coefficient of single particle at lowest particle size, as expected from the match between models shown in Figure 3.7 from before. As the particle size is increased the drag coefficient is increased. At low mass flow rate a higher drag coefficient is required, independent of particle size.

The CurveExpert Professional software [80] was used to extract a correlation for B from the data used in Figure 3.12. In this correlation, B dependant on mass flow rate and particle size (Equation 3.26).

$$B = \frac{-20.19 + 65.254m^\circ + 90175.1d_s}{1 + 22.045m^\circ - 2257.49d_s} \quad 3.26$$

Equation 3.26 is an empirical correlation valid only in the ranges investigated. The intention was not to use the equation to explain fundamental phenomena, but to provide a correlation that can be used in ROM, based on single particle behaviour.

3.5.2. Mean residence time

Mean residence time (Equation 2.1) plays an important role in multi-scale modelling of flighted rotary dryers. It has been assumed in all previous modelling that the falling behaviour of particles in these devices can be represented by assuming isolated single particles. In this section, CFD simulation is used to calculate mean residence time in particle curtain systems. In what follows, the methodology used to calculate the bulk curtain mean residence time using CFD data is described. Two alternative techniques are outlined.

3.5.2.1. Curtain hold-up

The curtain holdup was determined by multiplying total solids volume by solids density where the total solids volume was determined via volume integration of solid volume fraction across the entire domain. Equation 3.27 was used to calculate mean residence time of the particle curtain.

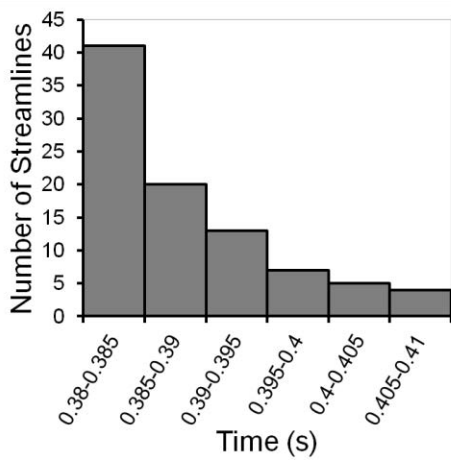
$$\mathcal{H} = \rho_s \int_{x=0}^{x=L} \int_{y=0}^{y=H} \int_{z=0}^{z=W} \alpha_s dx dy dz \quad 3.27$$

3.5.2.2. Residence time distributions

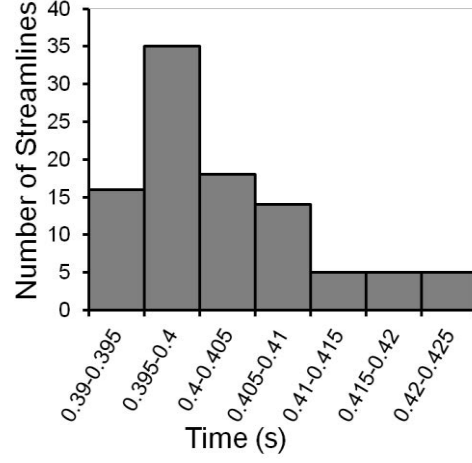
An alternative technique to calculate the mean residence time distributions involved the generation of distribution of streamlines. In each particle curtain, 100 streamlines for the mean flow field were generated, from the sand inlet to the base of the box. In this technique, the final time on each streamline was extracted and the frequency distributions of times were generated. The mean residence time was calculated using the distributions, via numerical integration (Equation 3.28).

$$\bar{\tau} = \frac{\sum(\text{frequency} \times \text{midpoint of time group})}{\text{total number of streamlines}} \quad 3.28$$

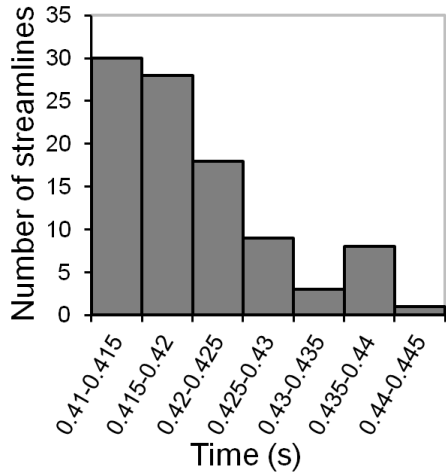
where *frequency* is the number of streamlines that have the same residence times within the selected time intervals (i.e. time group). Examples of the frequency distributions generated from simulations at constant initial velocity, mass flow rate and particle size with varying slot width are shown in Figure 3.13(a-d).



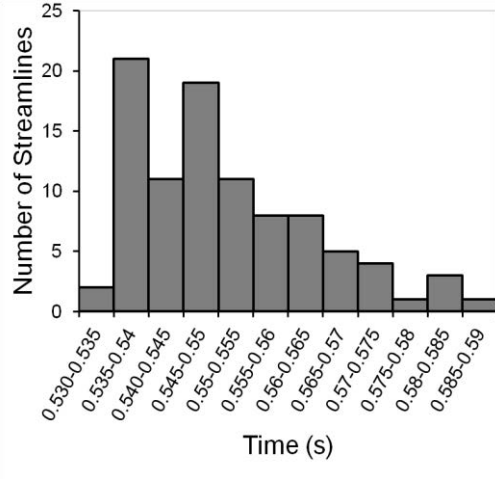
(a)



(b)



(c)



(d)

Figure 3.13: Residence time frequency distribution based on streamline ($d_s=200\mu\text{m}$, $m^o=0.041\text{kg/s}$ and $v_0=1.44\text{m/s}$) (a) slot width =10mm (b) slot width =30mm (c) slot width =60mm (d) slot width =80mm

Figure 3.13 shows that at larger slot widths the distribution of streamlines is broader. Particles experience varying pathways which effects the drag experienced, and larger inter-particle distances associated with the wider slot widths lead to longer mean residence times.

3.5.2.3. Results and discussion

Figure 3.14 shows a comparison of two techniques for calculation of mean residence time. The difference in mean residence times between the two techniques is relatively small and they follow the same trend. The prediction of residence time by the volume integral requires less manual data manipulation and has been chosen as a more convenient technique to present comparative analysis of mean residence times in different simulations. Mean residence time results across a variety of particle size, mass flow rates and slot widths are shown in Figure 3.15.

In previous studies of particle curtains, Ogata et al. [5] Hurby et al. [6] both postulated that the falling particles entrained gas as they fell. This led to increased particle velocities compared to an isolated single particle's velocity, as a result of the reduced drag. In Figure 3.14, the mean residence time increases with increasing slot width. Furthermore, as expressed in Equation 3.21, the solid volume fraction at the inlet is inversely proportional to the slot area. These results indicate that when the particle concentration is higher (i.e. narrow slots and high mass flow rate), the gas phase within the curtain is more easily entrained along with the particles, parallel to the direction of the particle phase. The reason for air entrainment may due to the effect of solid pressure generated within the particle curtain. Equation 2.9 is the critical equation, in this regard. Given that particle density, restitution coefficient and radial distribution are all constant, solid pressure is mainly influenced by solid volume fraction and granular temperature. At higher solid volume fractions the solid pressure is higher inside the curtain, acting to push particles apart and creating pressure differentials between the outside and inside of the curtain. Referring to Figure 3.15, this effect is more pronounced as particle size increased. Higher mass flow rates (for 200 μm particles) reduce the effect of increasing slot width, via the same mechanism.

It follows that the residence time for a single particle should represent the theoretical maximum residence time as the slot width increases.

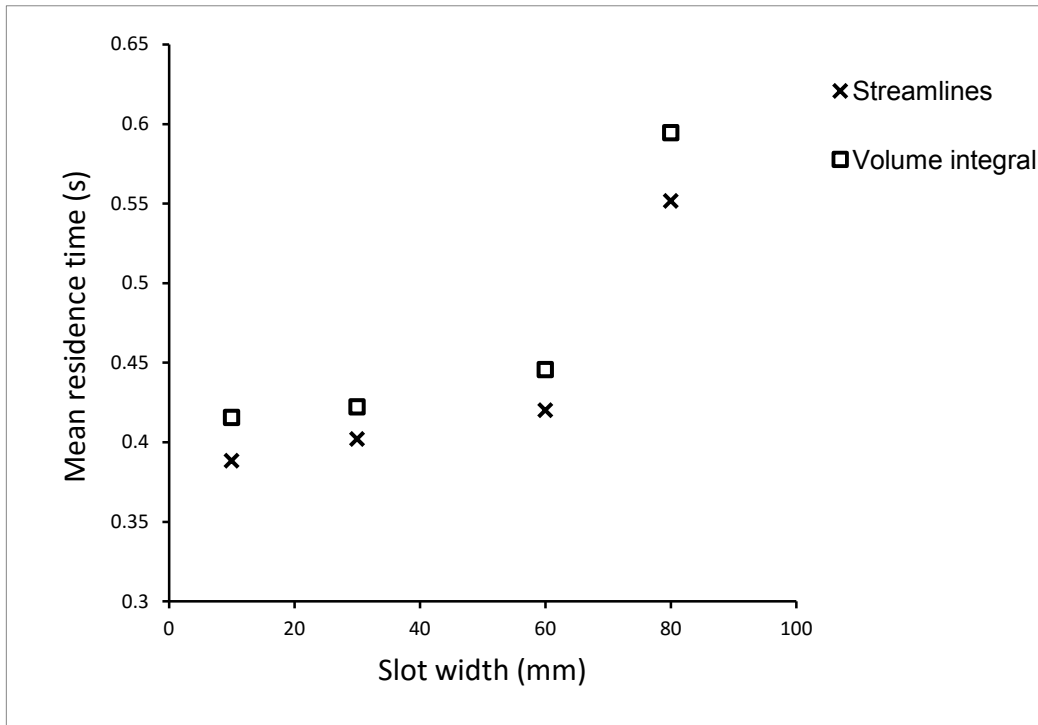


Figure 3.14: Mean residence time comparison of streamlines and volume integral techniques at different slot widths ($d_s = 200\mu\text{m}$, $m^o = 0.041\text{kg/s}$)

Referring again to Figure 3.15, for constant mass flow rate, across all slot widths, larger particle sizes lead to longer mean residence times. This is in direct contrast to the behaviour of isolated spheres, where larger particle sizes show reduced mean residence times. Fundamentally, there appears to be deficiency in the drag correlation (i.e. Equation 2.21) and the emphasis on solids volume fraction as the dominant influence. Alternatively, the inter-particle distance, or absolute distances between the falling particles, appears to be a greater influence on drag. Similar observations have been made by Dodds and Naser [81]. Take for example, the case where both

mass flow rate and slot width are held constant in Equation 3.21, but the particle size varies. In this case, solids volume fraction is constant, but the inter-particle distances, as calculated using Equation 3.29, are greater for larger particle sizes compared to smaller particle sizes (Table 3.4).

Table 3.4: Inter-particle distances (slot width=10mm, $m^0=0.041\text{kg/s}$)

Particle size (μm)	Solid volume fraction	Inter-particle distances (mm)
200	7.2×10^{-3}	0.634
400	7.2×10^{-3}	1.27
600	7.2×10^{-3}	1.9

$$\frac{X + d_s}{d_s} = \sqrt[3]{\frac{\pi}{6\alpha_s}} \quad 3.29$$

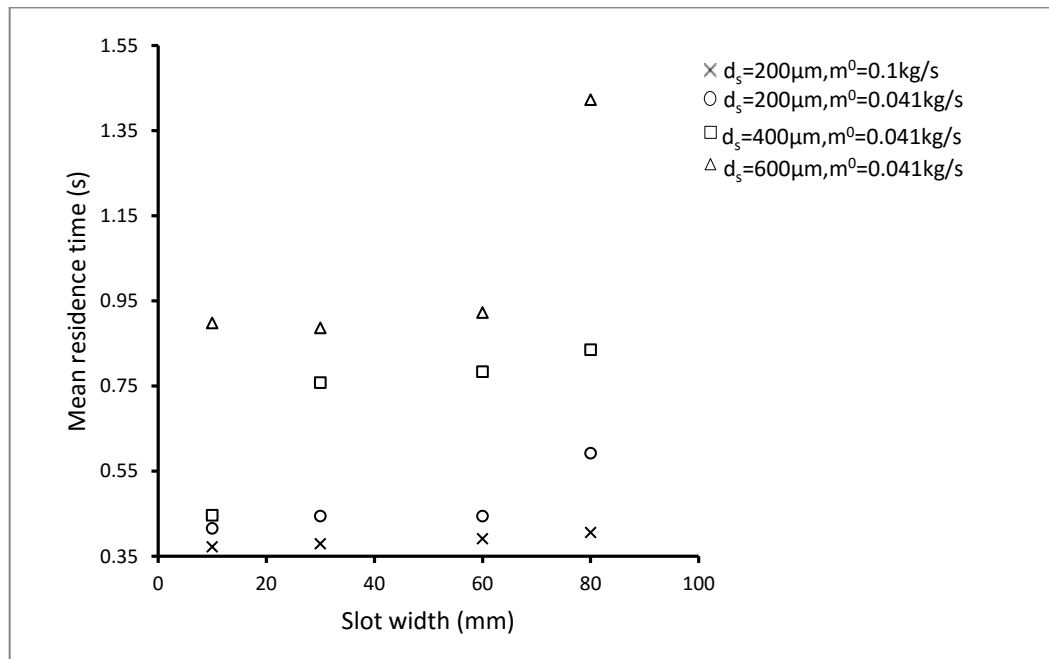


Figure 3.15: Effect of particle size on mean residence time at different slot widths (mm), 3D volume integral method

3.5.3. *Curtain edges*

The extend of convergence of a particle curtain as defined by the precise location of the edges is useful in defining drag [26]. It has also been used as a measure to assess quality of match between experimental visible images and CFD data [47, 48].

In the following section a range of techniques to calculate the edges of the particle curtains are compared.

In previous studies, an arbitrary solid volume fraction has been selected to define the curtain edge. Under similar inlet conditions, Wardjiman et al. [47, 48] and Lee [16] used this technique for edge detection of isothermal particle curtains falling through both flowing and stagnant gas using a solid volume fraction of 5.6×10^{-4} and 6×10^{-4} respectively. Results were compared to visible image experimental data and showed qualitative agreement. This technique was simple to implement by generating a polyline corresponding to the defined solid volume fraction and is used here for comparison. However, our simulations (see for example, Figure 3.16) and the simulations of Chen et al. [58] show that the solids volume fraction decreases with increasing distance from the inlet. It follows that the solids volume fraction at the curtain edge will also vary with height. Furthermore, in the absence of comparative experimental data, it is necessary to guess the critical volume fraction corresponding to the curtain edge. The variation in the selected volume fraction in the literature emphasises the uncertainty in this determination [47, 48]. The purpose of this work is to demonstrate a methodology which is based on image analysis, but it is applied to CFD data (and later thermal imagery), to determine curtain edge locations without recourse to experimental data.

3.5.3.1. Methodology

In order to visualise the variation in solid volume fraction within the curtain, consider an XY plane located at the middle of the geometry box, as shown in Figure 3.16. The contour qualitatively indicates an expanding curtain in the y and x directions. The solid volume fraction is higher at the discharge point and progressively decreases as the curtain falls.

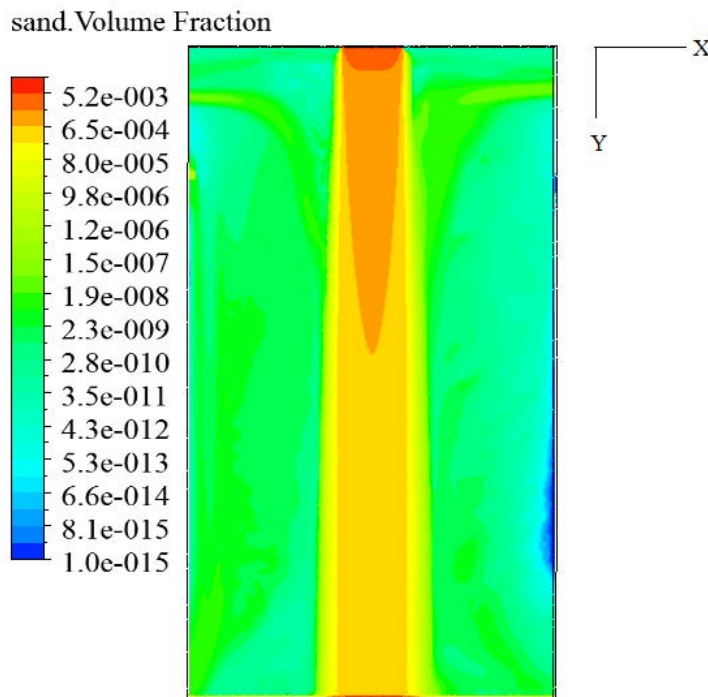


Figure 3.16: Solid volume fraction contour at XY plane ($Z=0.15\text{m}$, $d_s=200\mu\text{m}$, $m^o = 0.041\text{kg/s}$ and slot width=80mm)

Figure 3.17 shows the equivalent data as the variation of solid volume fraction in the x direction at different heights (ranging from 0.1m to 0.8m). Looking across the curtain at a constant height, the solids volume fraction is highest at the centre and decreases towards the edges. As the height

increases, away from the solids inlet, the solids volume fraction profile decreases, but shows the same trends in the overall solids volume fraction gradient towards the edges.

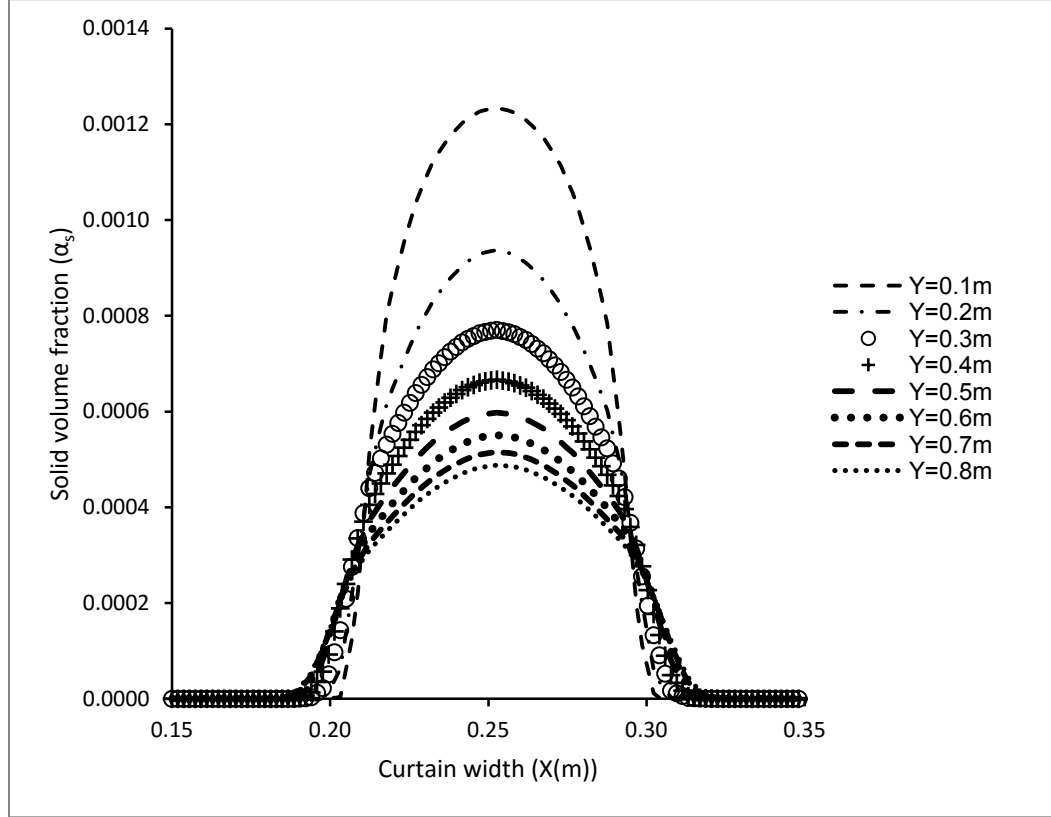


Figure 3.17: Solid volume fraction at different heights of the middle plane ($d_s = 200\mu\text{m}$, $m^o = 0.041\text{kg/s}$ and slot width=80mm). The sand inlet corresponds to $Y=0\text{m}$, and the base of the domain corresponds to $Y=0.9\text{m}$.

Using an approach widely adopted in image analysis for edge determination [28], the variation in solids volume fraction gradient at various heights $\left(\frac{\partial \alpha_s}{\partial x}\right|_y\right)$ is plotted (Figure 3.18). The two maxima that describe the sudden change in solid volume fraction between the particles and the surrounding gas phase correspond to the location of the edge. The values for the solid volume fraction at these maxima are used to define the curtain edge and are referred to as the critical volume fraction ($\alpha_c = f(Y)$).

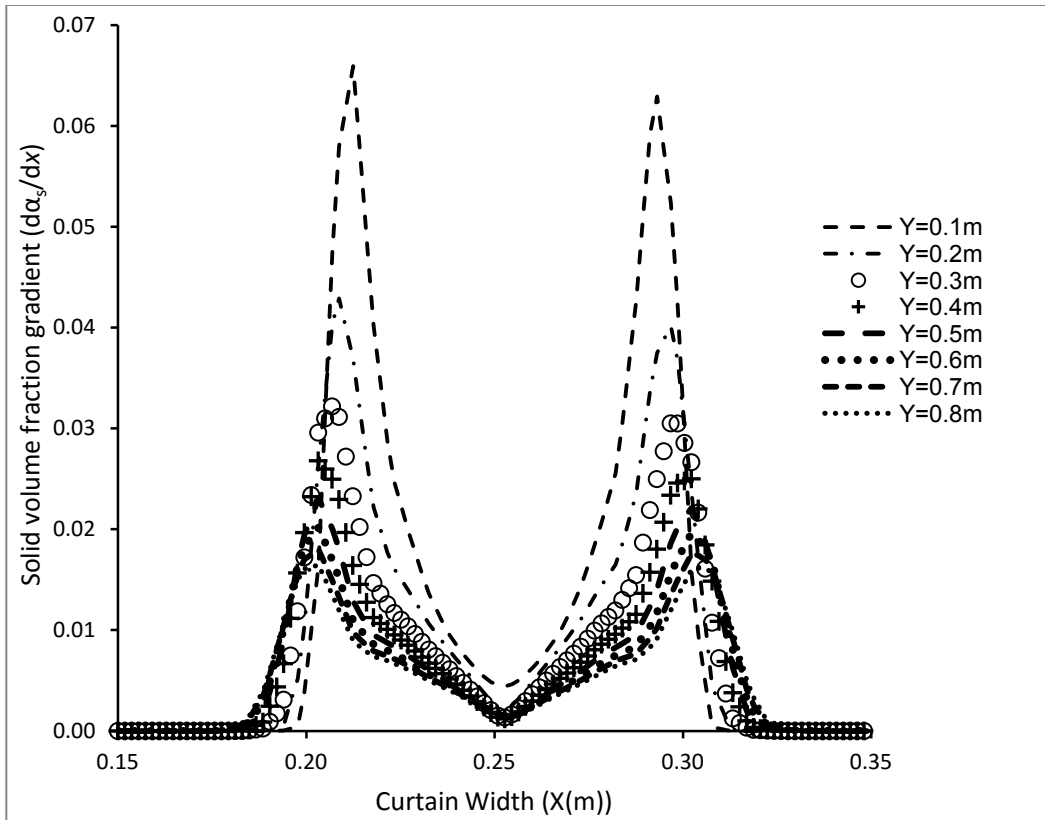


Figure 3.18: Solid volume fraction gradeint at different heights of the middle plane ($d_s = 200\mu\text{m}$, $m^o = 0.041\text{kg/s}$ and slot width=80mm). The sand inlet corresponds to $Y=0\text{m}$, and the base of the domain corresponds to $Y=0.9\text{m}$.

Since the mesh size is predefined, identification of these maxima values requires the extraction of a fitted quadratic polynomial around each maximum for both the gradient and solids volume fraction data (similar to filtering in image analysis). Differentiation of quadratic polynomial allows determination of the maxima in the solid volume fraction gradients and also the position of this maximum, and corresponding critical solid volume fraction.

3.5.3.2. Results and discussion

The critical solid volume fraction as a function of height for curtains falling from different slot widths is shown in Figure 3.19. Figure 3.19 shows that the critical solid volume fraction is highest at the inlet and reduces with falling distance. Reduction in α_c is more pronounced at small slot widths (10mm) because of expanding curtains. It can be seen that α_c is almost constant with respect to falling distance for larger slot widths (60 and 80mm). Furthermore, as the slot width increases, the critical solids volume fraction decreases.

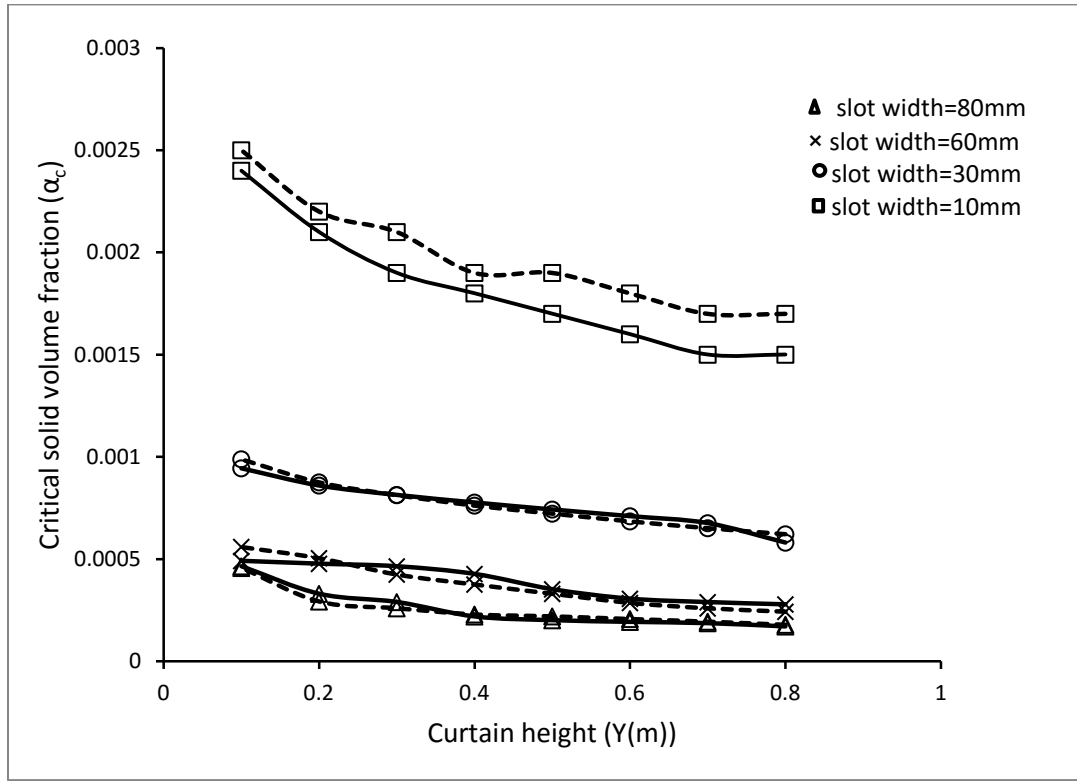


Figure 3.19: Critical solid volume fraction at different slot widths, $d_s=200\mu\text{m}$, $m^o=0.041\text{kg/s}$ (Dashed line and solid line represent critical solid volume fraction for the left and right edges of the curtain, respectively). The sand inlet corresponds to $Y=0\text{m}$, and the base of the domain corresponds to $Y=0.9\text{m}$

In addition to the constant solid volume fraction (6×10^{-4}), 500 streamlines evenly distributed across the sand inlet are compared to the gradient methodology. Figure 3.20(a-d) shows calculation of the edge of the curtain at different slot widths (10mm, 30mm, 60mm and 80mm). The gray area represents the frontal area of the curtain as shown by streamlines. The solid and dashed lines represent the constant solid volume fraction and gradient techniques respectively.

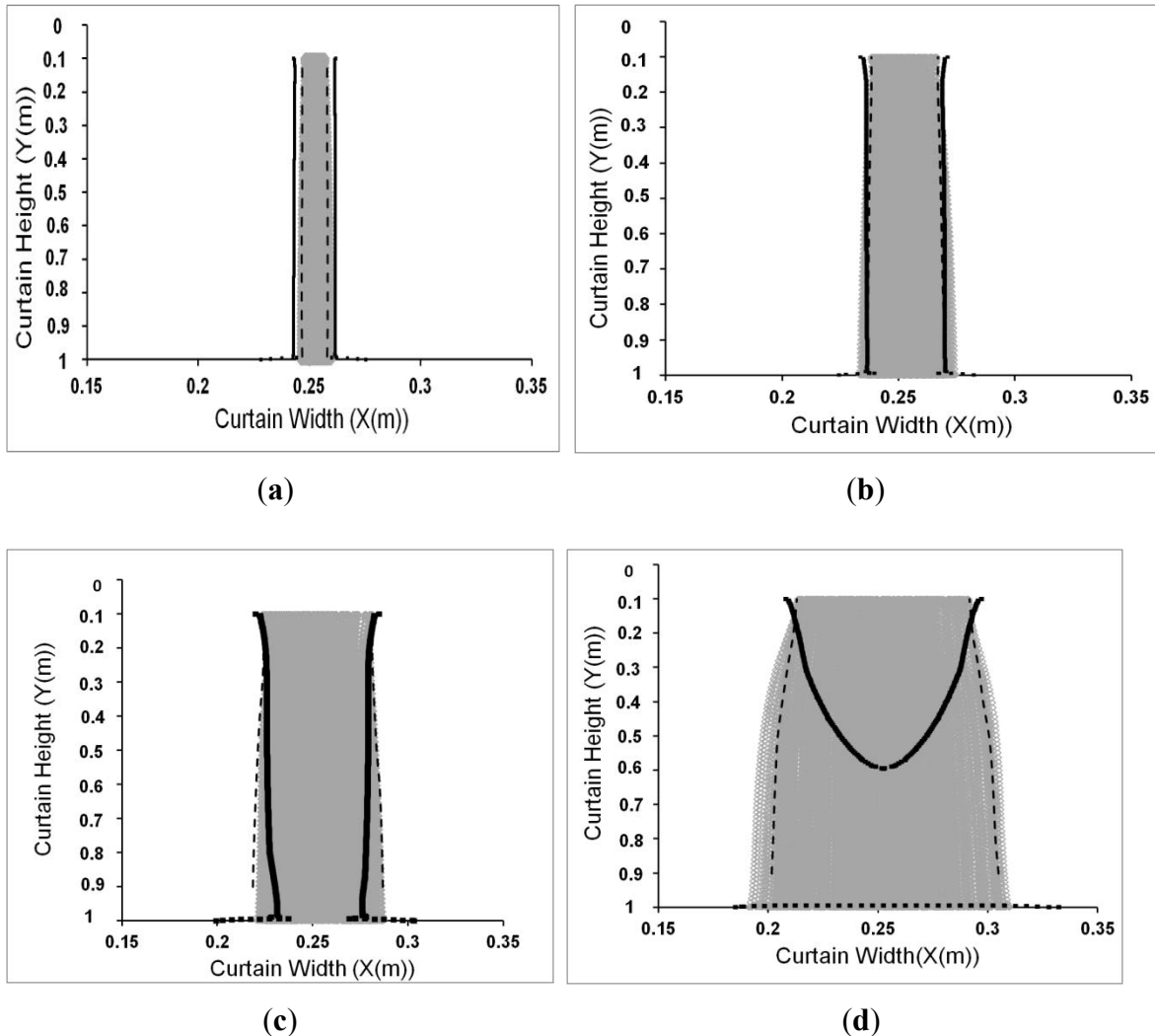


Figure 3.20: Edge identifying comparison techniques: a) slot width= 10mm, b) slot width= 30mm, c) slot width= 60mm, d) slot width=80mm ($d_s=200\mu\text{m}$, $m^o=0.041\text{kg/s}$, $T_s=400\text{K}$, $T_g=300\text{K}$ and initial velocity=1.44m/s). The sand inlet corresponds to Y=0m, and the base of the domain corresponds to Y=0.9m. Gray area, dashed lines and solid lines represent the streamlines, rate of change and constant solid volume fraction techniques respectively

The gradient technique shows excellent agreement with the streamlines, whilst the chosen constant solid volume fraction technique is not able to predict the edge of the curtain as the slot width is increased. Although streamlines provide a good representation of the curtain shape, care must be taken because the accuracy of prediction depends on the number of streamlines used. Higher numbers of streamlines allows the edges to be more precisely defined. Unfortunately, processing of the streamline data would be required to enable cross-correlation to the domain properties such as temperature, velocity and volume fraction. This is because streamlines follow the mean particle path and do not overlay the coordinate system making automated processing more difficult. Alternatively, the gradient technique is a direct manipulation of the raw CFX data, cross-correlated to temperature and the corresponding x and y coordinates. It is a more convenient method to quantify the edge of the curtain.

The frontal area of the curtain within the dashed lines (i.e. curtain edges), which were generated using the gradient technique, was calculated for two mass flow rates (0.041kg/s and 0.1kg/s) at different slot widths for 200 μm particles (Figure 3.21(a)). The frontal area of the curtain is relatively independent of mass flow rate and increases with slot width. Figure 3.21 (b) illustrates the average solid volume fraction in particle curtain, calculated using Equation 3.30 in which W corresponds to the longest dimension of the slot (0.15m) and A is the frontal area of the curtain. The calculation of the mean residence time ($\bar{\tau}$) was described earlier in section 6.

$$\bar{\alpha}_s = \frac{m^0 \times \bar{\tau}}{A \times W \times \rho_s} \quad 3.30$$

Increasing slot width decreases the average solid volume fraction and lower mass flow rate results in lower average solids volume fraction.

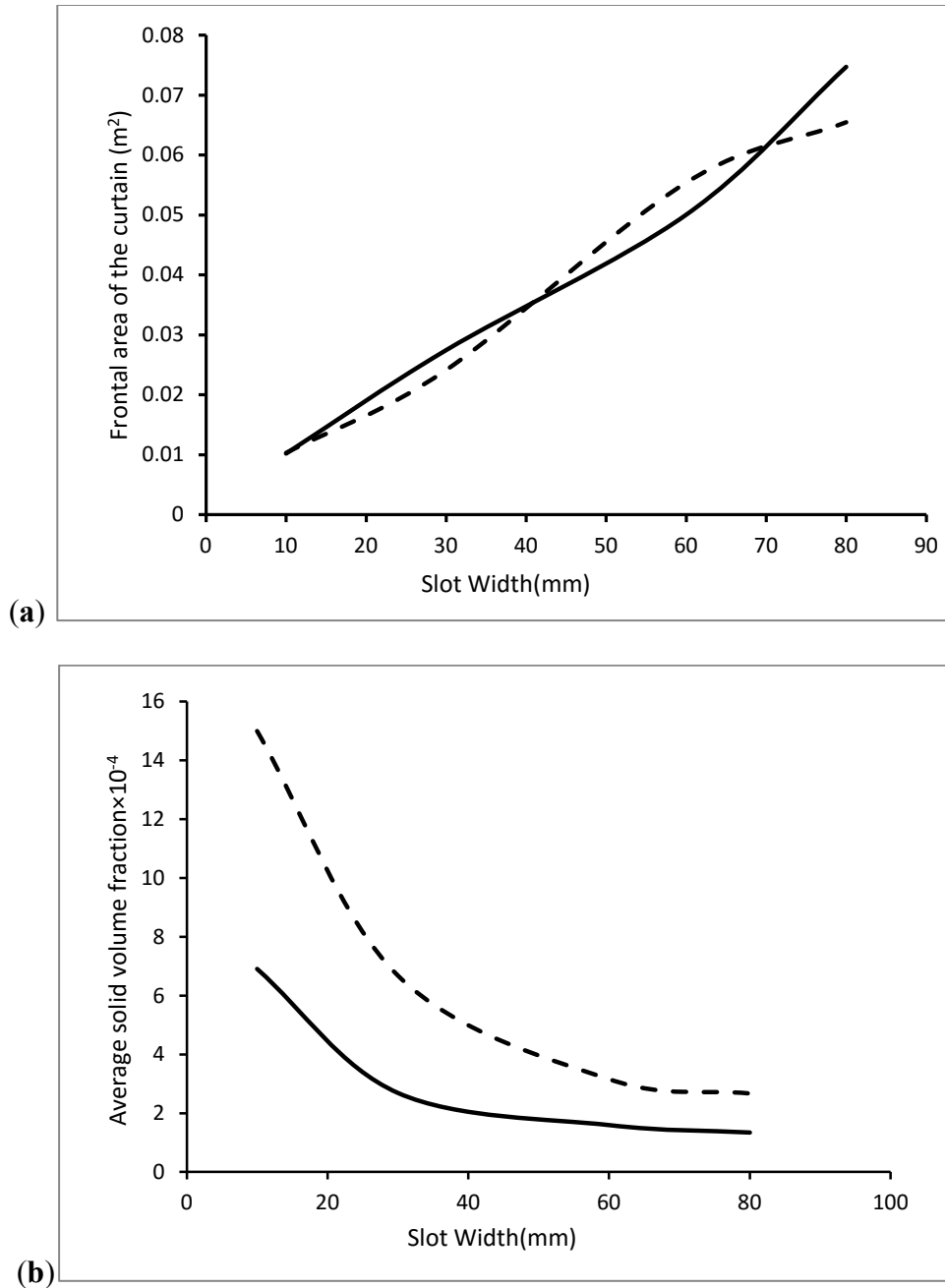


Figure 3.21: (a) Frontal area of the curtain at different slot widths (b) Average volume fraction of particle curtain at two mass flow rates of 0.041kg/s and 0.1kg/s ($d_s=200\mu\text{m}$) - The dashed line and solid line present the mass flow rate of 0.1kg/s and 0.041kg/s respectively

3.6. Conclusions

Eulerian-Eulerian CFD simulations of hot particle curtains falling through slots of varying widths were described. Two model variations are presented in order to be directly comparable to simulations in the literature and in order to replicate experimental conditions in this thesis. The CFD results for particle temperature in curtains have been compared to the temperature of single particle falling under equivalent conditions. It was found that the heat loss within the particle curtains is less than the equivalent single particle heat loss. As the mass flow rate of the particle curtains increases, the rate of heat loss decreases. Analysis of variance was used to identify the most significant effects on the rate of heat loss. The three top significant variables were mass flow rate and particle size, and the interaction of these variables. Temperature profiles using both CFD and single particle models were generated. CFD results were well matched with single particle at low mass flow rates and small particle sizes, but the single particle model was not able to predict the behaviour of particles in curtains at larger particle sizes and higher mass flow rates. A ROM correlation was developed to enable the single particle model to be used as a basis for predicting curtain behaviour.

New methodologies for generating bulk curtain characteristics and for later comparison to experimental thermal imagery were developed. Mean residence times, average solid volume fractions and the curtain areas were calculated at varying mass flow rates and particle sizes. Volume integral and frequency histograms constructed from streamlines were compared for their suitability in calculating mean residence time, and volume integral techniques were preferred. Three different techniques were compared for their suitability in determining the location of the edges of the curtains and corresponding solids volume fractions. The novel application of image analysis edge detection techniques to simulation data was successful in quantifying curtain areas

and average solids volume fractions. Maxima identification in the solids volume fraction gradient was preferred because it enables the definition of the properties of the edge without recourse to experimental data. The effects of slot width, mass flow rate and particle size on these average properties were investigated. Larger particle sizes, larger slot widths and lower mass flow rates result in longer mean residence times and lower solid volume fractions, reducing the influence of fluid entrainment and increasing particle drag. In terms of practical heat exchanger design, heat transfer can be maximised by designing equipment that provides longer mean residence times in which the interaction time between the fluid and particles is maximised.

Chapter 4 Experimental Methodology

This Chapter describes the materials and the experimental apparatus used to generate and characterise hot particle curtains cooling predominant via convection heat transfer. The experiments were carried out to investigate effects on temperature profiles of particles within the curtain across a range of particle sizes, mass flow rate, and curtain dimensions. The tools used to characterise both the thermal and physical attributes of the curtains are described. The primary apparatus consisted of a hopper, perforated plates, wire mesh screens, scale indicator, data logger and oven. High speed photography and the procedure used to calculate the initial velocity of particles exiting from the primary apparatus is explained. The infrared camera and the procedure used to perform the thermography is also explained. Visible imagery techniques are described because they were used to better understand and enhance the quality of the thermal images. Furthermore, direct thermocouple measurement procedures used to measure the hot particle curtain temperatures at discrete points are also presented.

4.1. Introduction

The predominant experimental tool used in this study was infrared thermography. This technique was used to infer the temperature of the hot particle curtains. To date, all curtain studies have utilised direct temperature measurement using discrete sampling points [49, 70]. An alternative approach, examined for the first time in this thesis, is to measure temperature in a dilute two-phase

system using infrared thermography. The objective of this approach is to provide a continuous temperature profile across the entire field of interest.

Infrared thermography is a powerful technique for surface temperature mapping and has applications in medicine [82], agriculture [83], pharmaceuticals [84] and thermo-fluid dynamics [85]. The thermography application has been mainly in surface and sub-surface defect detection [86, 87]. Subsurface defects cause abnormal thermal patterns, which indicate the presence of those defects. Infrared thermography has been extensively used in medicine [88] and building diagnosis [89]. However, there has been surprisingly little use in two phase particulate flow characterisation.

Infrared thermography offers advantages in comparison to standard sensors such as thermocouples, resistance temperature detectors and pyrometers. It allows measurement of the temperature of a solid-state body surface, including particles, and not that of the surrounding atmosphere. Compared to IR thermography, measuring temperature with thermocouples can disturb flow fields, because they are required to be attached to the object. As such IR thermography appears to show great promise for measuring bulk temperature in convective heat transfer applications. It is able to measure both high and low temperatures accurately. IR thermography measures temperature of a surface in a two dimensional plane rather than at a particular point, which makes it suitable for comparison to contours planes generated in CFD software, for example. Many industrial processes are carried out under high temperatures that potentially destroy the contacting sensors. In these cases, contactless infrared thermography would provide advantages over direct contact devices [90, 91].

The few examples of the use of applied infrared thermography to visualise temperature in the particulate systems include (Yamada et al. [92] Dang et al. [93] and Patil et. al.[94]). Yamada et al.

[92] used IR thermography to investigate conductive heat transfer in a fluidised bed. In their research, the temperature of fluidising particles and during contact with a solid heat transfer surface was visualised. Infrared thermography was used to measure the temperature of single particles including glass beads with average diameters of 400 μm and 600 μm and iron particles, 300 μm in diameter. Thermal images were taken every 1/30 of a second. The contact conductance between fluidizing particles and the heat transfer surface was estimated by an inverse analysis. In their study they benefited from being able to characterise the heat transfer at the microscopic level. Dang et al. [93] used infrared thermography to measure the concentration of CO₂ inside bubbles injected into a gas-particle fluidised bed.

The most relevant study is the recent contribution by Patil et al. [94]. They combined Infrared thermography with visible image/digital image analysis (DIA) to measure the temperature and infer solid volume fraction of particles in a small pseudo 2D fluidised bed (8cm wide, 20cm high and 1.5cm in depth). The fluidisation experiments were performed with glass particles of sizes 0.5mm and 1mm. The infrared camera (250×512 resolution) was sensitive in the 1.5-5.1 μm spectral range and placed in very close proximity to the bed surface. Individual hot particles were detectable from the background. In their research, they used threshold techniques to filter the effect of background and calculate the average temperature of individual particles.

4.2. Physical and Thermal Properties of Materials

The experiments were performed using Potters Industry® spherical glass beads with mean particle size (d_s) of 290 μm , 400 μm and 610 μm , density of 2500kg/m³, heat capacity of 0.83 (kJ/kg °C) and thermal conductivity of 0.18 (W/(m.K)). The mean particle sizes (d_s) quoted from Potters

Industry® were calculated using a Camsizer imaging system made by ©Retsch Technology GmbH. Independent particle size analysis was also used to confirm the quoted means and provide particle size distributions.

4.2.1. Particle size measurement techniques

Particle size and distribution analysis of a sample can be performed using a variety of techniques, each with advantages and disadvantages, depending on the sample properties and question at hand.

Sieving, microscopy, sedimentation and laser diffraction are the most commonly used techniques.

In this research, in addition of the reports from Potters Industry®, analysis using a

Malvern Mastersizer 3000 was also undertaken.

Malvern Mastersizer 3000 was used to calculate the volume diameter (D_V) of the particles. The Malvern Mastersizer uses laser diffraction to measure the angular variation in intensity of light scattered as a laser beam passes through a dispersed particulate sample. Large particles scatter light at small angles relative to the laser beam, and small particles scatter light at large angles. The angular scattering intensity data is then analyzed to calculate the size of the particles responsible for creating the scattering pattern, using the Mie Theory [95]. Figures 4.1 to 4.3 show the particle size distributions and the average volume diameters. The standard deviation and skewness of curves are presented in Table 4.1.

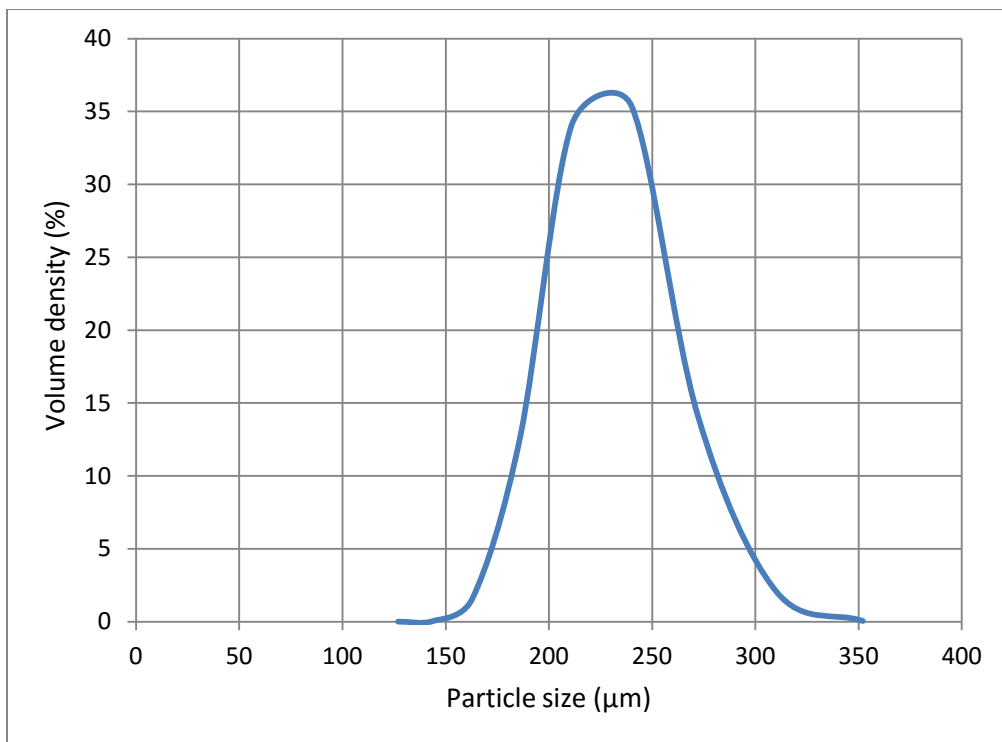


Figure 4.1: Malvern Mastersizer analysis for $d_s=290\mu\text{m}$, $D_v(50)=241\mu\text{m}$

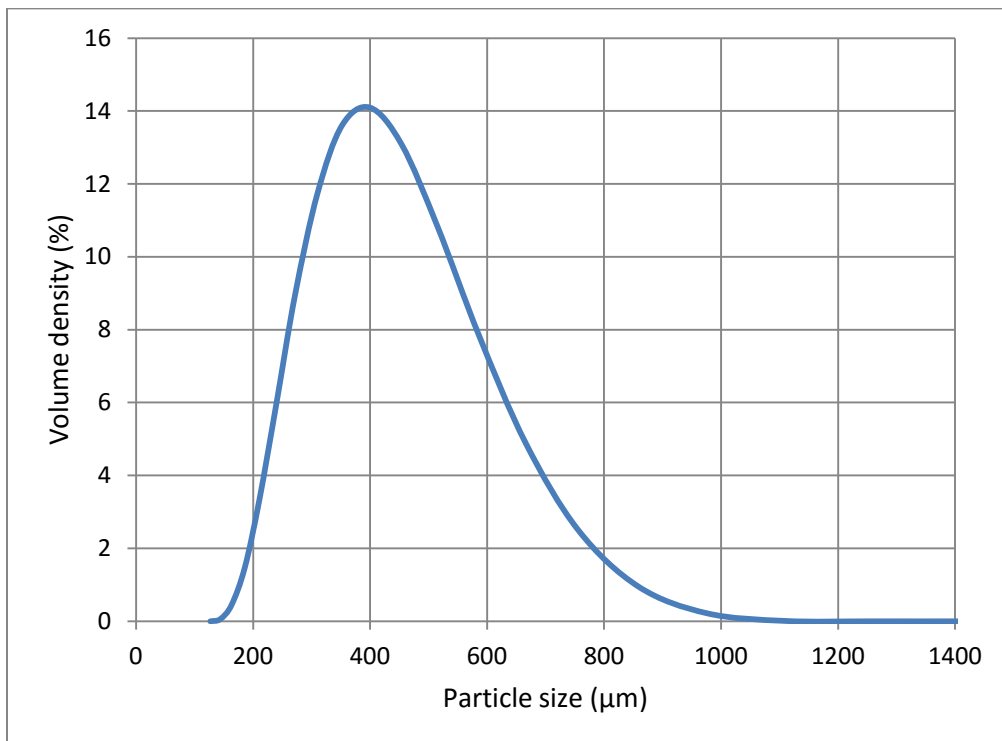


Figure 4.2: Malvern Mastersizer for $d_s=400\mu\text{m}$, $D_v(50)=416\mu\text{m}$

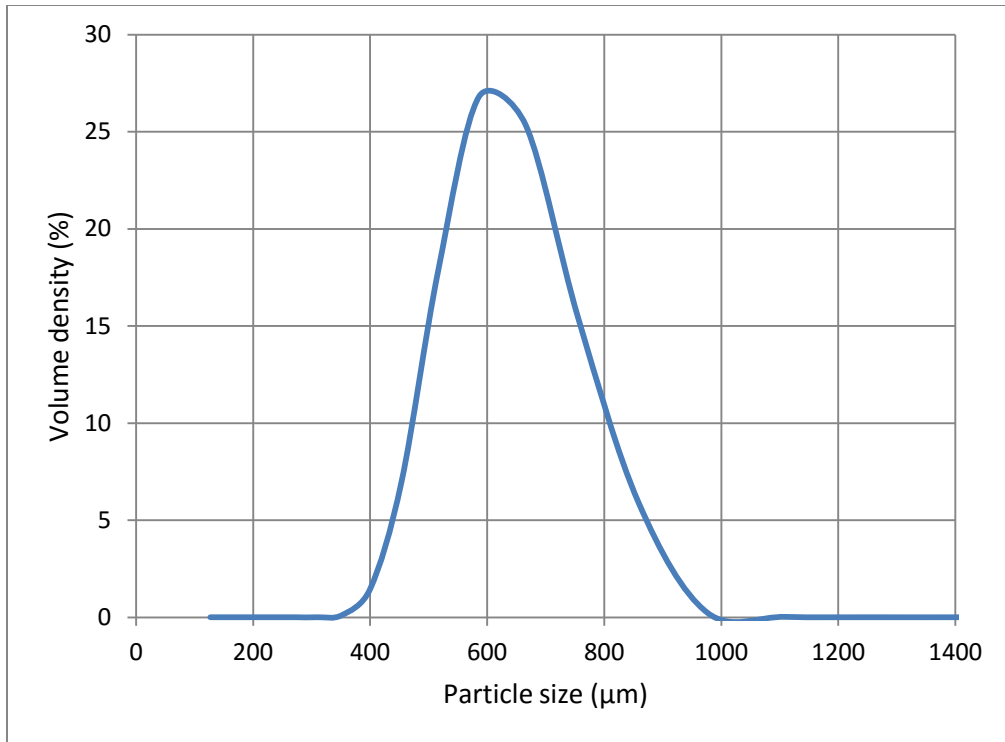


Figure 4.3: Malvern Mastersizer for $d_s=610\mu\text{m}$, $D_v(50)=656\mu\text{m}$

It was reported that the Camsizer provides a higher degree of accuracy compared to Malvern Mastersizer [96]. The Camsizer calculates the mean diameter of the particles based on the area of particle projection using automated image analysis. Therefore, the measured mean particle size reported by Potters Industry has been used in all further modelling simulations. Furthermore, particles were assumed to be uniformly sized in all simulations and distributions were only considered when interpreting results.

Table 4.1: Standard deviation and skewness of particle size distributions

Mean particle size (μm)	Standard Deviation	Skewness
		Standard Error
241	91.73	0.687
416	346.14	0.524
656	309.84	0.637

4.3. Experimental Apparatus

The entire experimental apparatus was designed and fabricated in house and was used to generate particle curtains. It is shown schematically in Figure 4.4. The experimental set-up consisted of an insulated wedge hopper, black background, spreader box, perforated plates and wire mesh screens, scale indicator, oven, infrared camera, high speed camera, visible image camera and laptop.

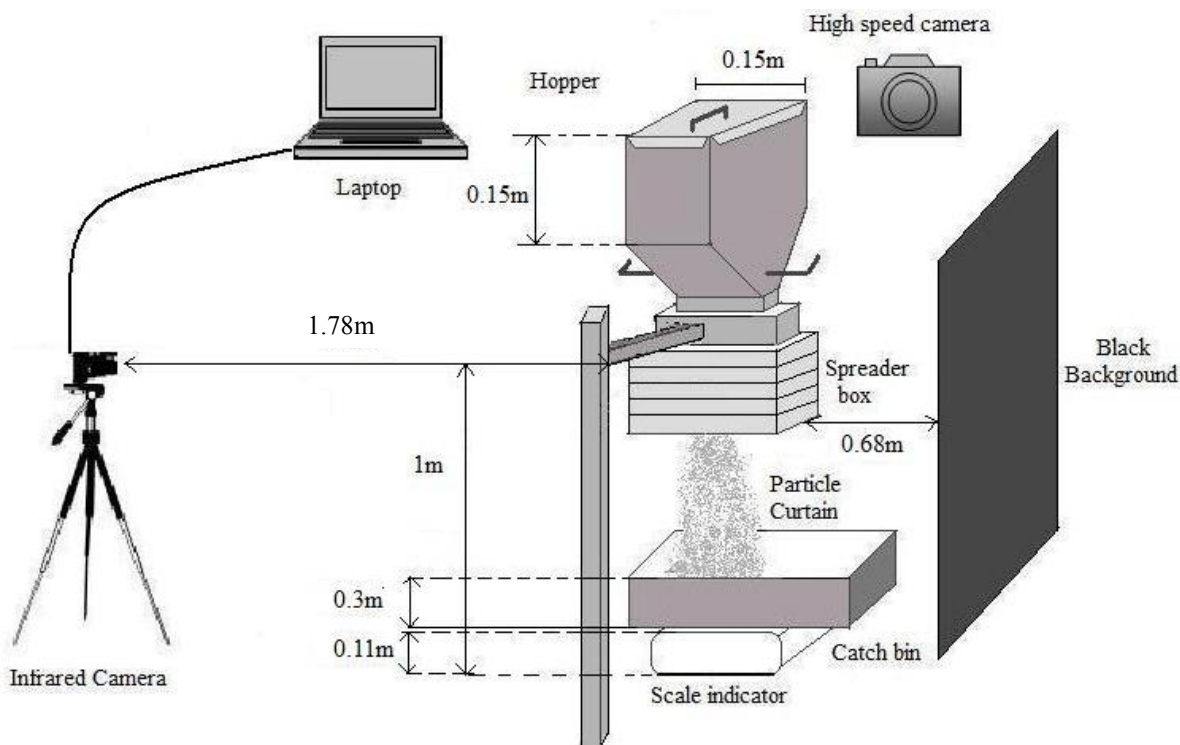


Figure 4.4: Experimental apparatus

The maximum capacity of the hopper was approximately 7kg of glass beads. The wedge hopper was coated with black paint to reduce light reflection. In order to improve the quality of images, a black background was located behind the hopper. This gave high level of contrast between white glass beads and the black background during thermal and visible photography. The hopper was fabricated with a valve to manually regulate the mass flow rate of the particle curtains. The mass flow rates generated using this type of valve varied between 0.04-0.155kg/s. Since the mass flow rate was generated using the manual valve it was not possible to precisely fix the desired mass flow rate. Although repeat runs were quite consistent, some minor variation occurred. The hopper was fit into the spreader box.

4.3.1. Spreader box

Two sizes of spreader box were designed in order to generate uniform particle curtains across two slot widths (20×150mm and 60×150mm).

Drawing on previous designs discussed in (Dawson et al. [97]) the spreader box consisted of a thick casing enclosing two perforated plates followed by two wire mesh screens. The perforated plates were specifically designed for the two different slot sizes (20mm and 60mm). Two types of perforated plates were designed in larger slot width of 60mm. The perforated plate for the 20mm slot had 40 holes with hole diameters of 5mm. The number of holes for the two 60mm slot designs was 40 and 119 with diameters of 5mm each. Figure 4.5 shows the designed perforated plates for the different slot widths. The specific dimensions of the apparatus design are presented in Appendix C. In addition to perforated plates, longitudinal rails were located on the top of the 60mm width spreader box in order to spread the particles from the narrow hopper exit, into the spreader box.

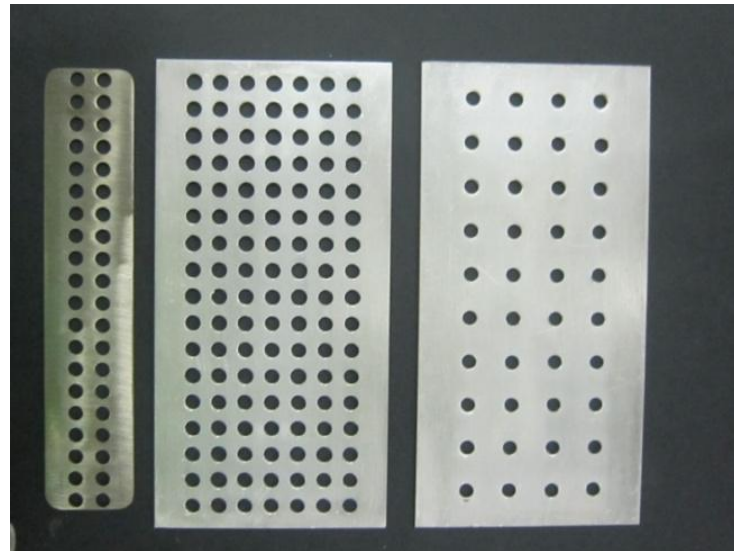


Figure 4.5: Perforated plates (hole diameter=5mm) for slot widths of 20mm and 60mm

4.3.2. Mass flow rate

Falling particles were collected in a catch bin which was placed on a digital scale indicator connected to a R400 viewer device. This device is able to accurately measure the mass of the falling particles over time. The R400 viewer device was connected to a laptop with a USB Rinlink cable and controlled by a software interface called RinstrumView400. RinstrumView400 displays the complete menu structure of the indicator on the laptop and detects the communications port that the Rinlink is connected too. A linear correlation was used to fit the mass versus time data over the duration of each experiment. Regression constants (R^2) varied between 0.99 to 1 across all runs and particle sizes, demonstrating a very consistent mass flow rate of particles leaving the spreader box. Examples of two mass flow rates (0.066 and 0.141 kg/s) are shown in Figure 4.6(a,b).

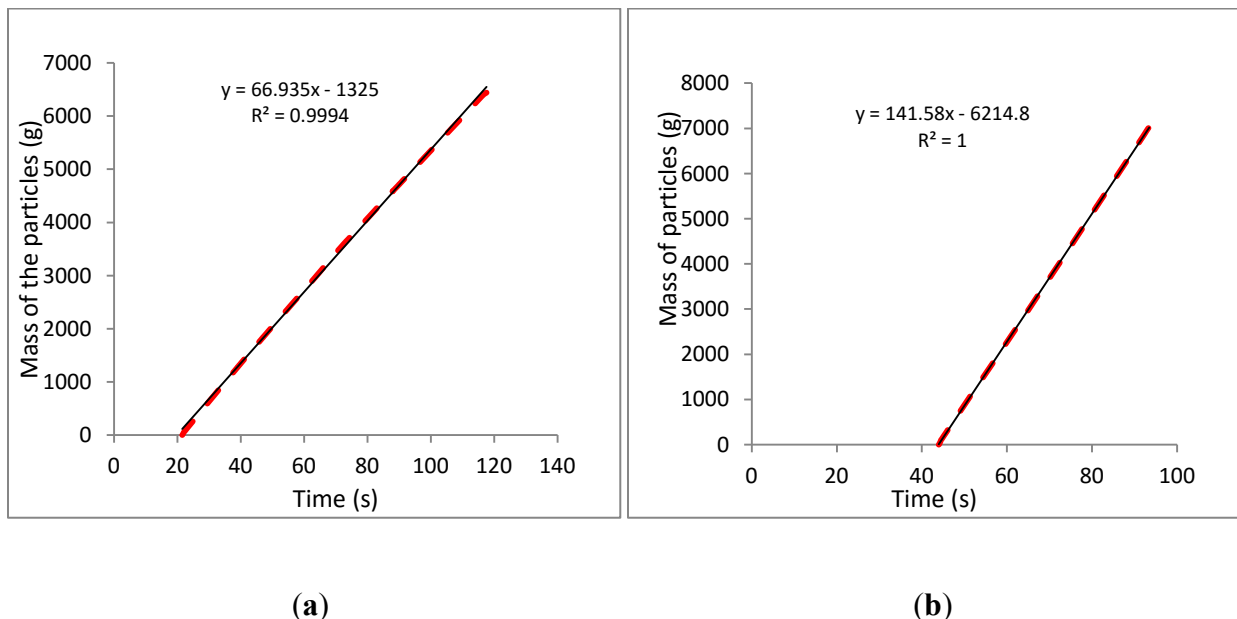


Figure 4.6: Examples of mass flow rate calculation using RinstrumView400 software, (a) $d_s=290\mu\text{m}$, $m^\circ=0.066\text{kg/s}$ and slot width=20mm (b) $d_s=400\mu\text{m}$, $m^\circ=0.141\text{kg/s}$ and slot width=60mm

4.3.3. Infrared thermography

4.3.3.1. Theory

Infrared (IR) Thermography is based on measuring the infrared radiation emitted from the surface of an object. Infrared radiation lies between the visible and microwave portions of the electromagnetic spectrum (Figure 4.7). The primary source of infrared radiation is heat or thermal radiation. Any object that has a temperature above absolute zero will emit radiation in the infrared region. The infrared portion of the electromagnetic spectrum is broken into two distinct categories: near infrared (700nm-2500nm) and far infrared ($2500\text{nm}-10^6\text{nm}$). This information is reproduced from the thermal imaging guidebook for industrial applications published by FLIR systems [98].

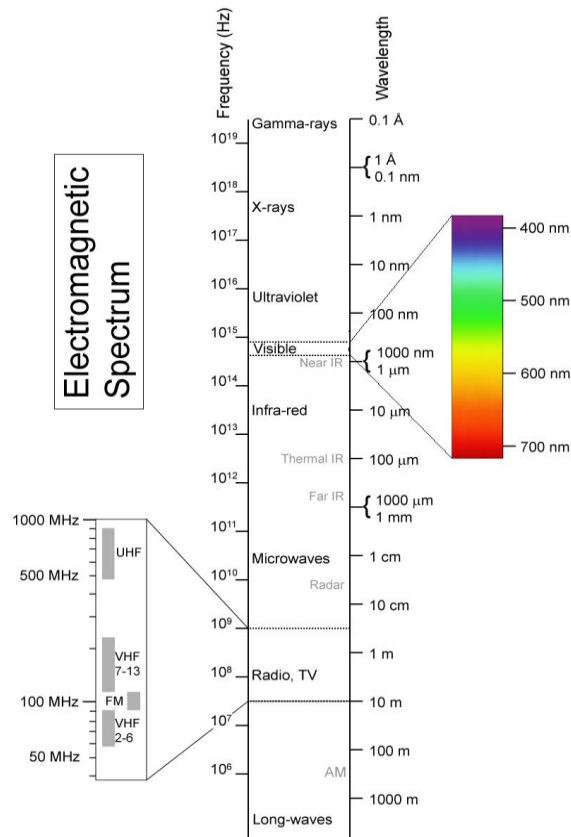


Figure 4.7: The electromagnetic spectrum [99]

4.3.3.2. Camera details

An infrared camera (NEC Avio, H2600 Series developed by FLIR Systems) with resolution of 640×480 pixels was used to capture thermal images of the particle curtains. The process of converting infrared radiation to an image is explained as follows (see Figure 4.8).

1. Infrared radiation coming from an object (A) is focused by a special lens (B)
2. The focused light is scanned by a phased array of infrared-detector elements (C). The detector elements create a very detailed temperature pattern (thermogram). It only takes about one-thirtieth of a second for the detector array to obtain the temperature information to make the thermogram. This information is obtained from three hundred thousand points in the field of view of the detector array.
3. The thermogram created by the detector elements is translated into electric impulses.
4. The impulses are sent to a signal-processing unit (D), a circuit board with a dedicated chip that translates the information from the elements into data for the display.
5. The signal-processing unit sends the information to the display, where it appears as various colours depending on the intensity of the infrared emission. The combination of all the impulses from all of the elements creates the image that can be viewed in the viewfinder or on a standard video monitor or LCD screen (E).

Each infrared frame is taken at 0.033s. The minimum detectable size (i.e. the size of each pixel) by the infrared camera is 1.5175mm (see Section 5.1.1). Therefore, individual particles in this research are not detectable. Consider an example in which $d_s=290\mu\text{m}$, $m^o=0.15\text{kg/s}$ and slot width=20mm. Initial velocity of particles are calculated experimentally in Section 4.3.4.4 as 0.23m/s and the velocity of particle at the distance of 62cm was 2.64m/s calculated using CFD simulations. Thus, the average velocity is 1.43m/s. The distance particles travel from spreader box

exit in 0.033s and between frames is 4.7cm. Thus, each image captured by the infrared camera is an amalgamation of many particles falling through each frame, noting that each image is also hundreds of particles deep. Since 10 frames over a time period of 0.033 seconds is averaged in image processing, a pseudo-steady state approximation is assumed. When volume fractions and mass flow rates are high it is a good assumption that the entire field is saturated with particles only.

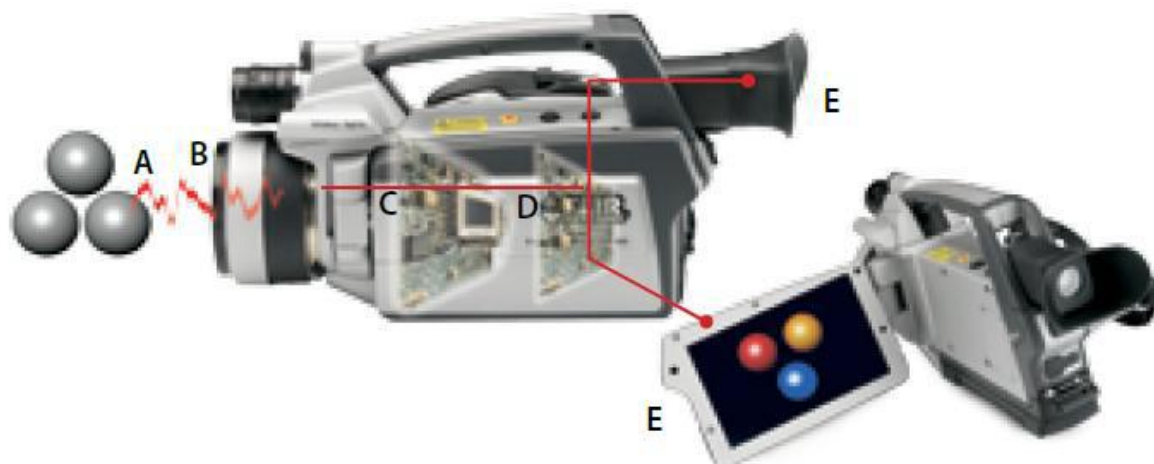


Figure 4.8: Infrared camera

4.3.3.3. *Image capture procedure*

The infrared camera was held perpendicular to the front of the spreader box, aligned with the narrow dimension of 20mm and 60mm (for the two slot widths) at a distance of 1.78m from the hopper. This distance is an optimised distance in which the thermal images appeared sharp and

crystal clear. The distance between the centre of camera lens to the floor was 1m. The distance between the hopper to the floor was 1m. Deducting the height of the scale indicator, catch bin and spreader box results in approximately 62cm of falling distance captured in the thermal photography.

After switching the camera on, reflection calibration was performed in order to eliminate reflections of other objects. Before performing the calibration, the lens protection cap is used to cover the lens of camera and thus act as a black body during reflection calibration. In order to connect the infrared camera to the laptop, an IEEE 1394 cable was connected from the camera via the IEEE1394 port in the laptop.

InfRec Analyzer NS9500 Professional software in snapshot format was used to record the thermal images. A range of 0 – +500°C of temperature was set to cover the range of expected experimental temperature variation. The focal position (0-1023) was adjusted via the camera software to 850, at which the images appeared most vivid. Infrared images were recorded every 1/30 seconds. The duration of image capture for small particles (290µm) was approximately 6 minutes (3300 frames), and 2422 frames (4.5 minutes) for the larger particle size (400µm and 610µm). The images were captured in the SVX format. This format of image was only visible in InfRec Analyzer NS9500 Professional software.

4.3.4. Visible imagery

Visible imaging of the particle curtain was used to obtain bulk characteristics such as pixel intensity. High Speed visible imaging was used to estimate the initial velocity of particles exiting the spreader box.

4.3.4.1. Visible camera details

Visible photography was used to capture the pixel intensities within the particle curtains over the entire falling distance. The images were taken in black and white using a Nikon D80 camera which was adjusted to manual focus settings with focal length of 18 mm and aperture size of 3.5. The shutter speed was 1/60 second. The images were taken using the continuous operation mode and in grayscale (3872×2592 pixels). Six 500 watt spotlights on tripod stands were placed in front of particle curtain at the distance of 1.4m. The location of lights was consistent during all visible photography.

4.3.4.2. Light intensity considerations

In order to ensure even light distribution and avoid undue influence of external factors on pixel intensity, light locations were adjusted until the mean pixel intensities on a fixed white cardboard area were uniform with regard to height (see Figure 4.9). Visible image intensity data was processed using Matlab.

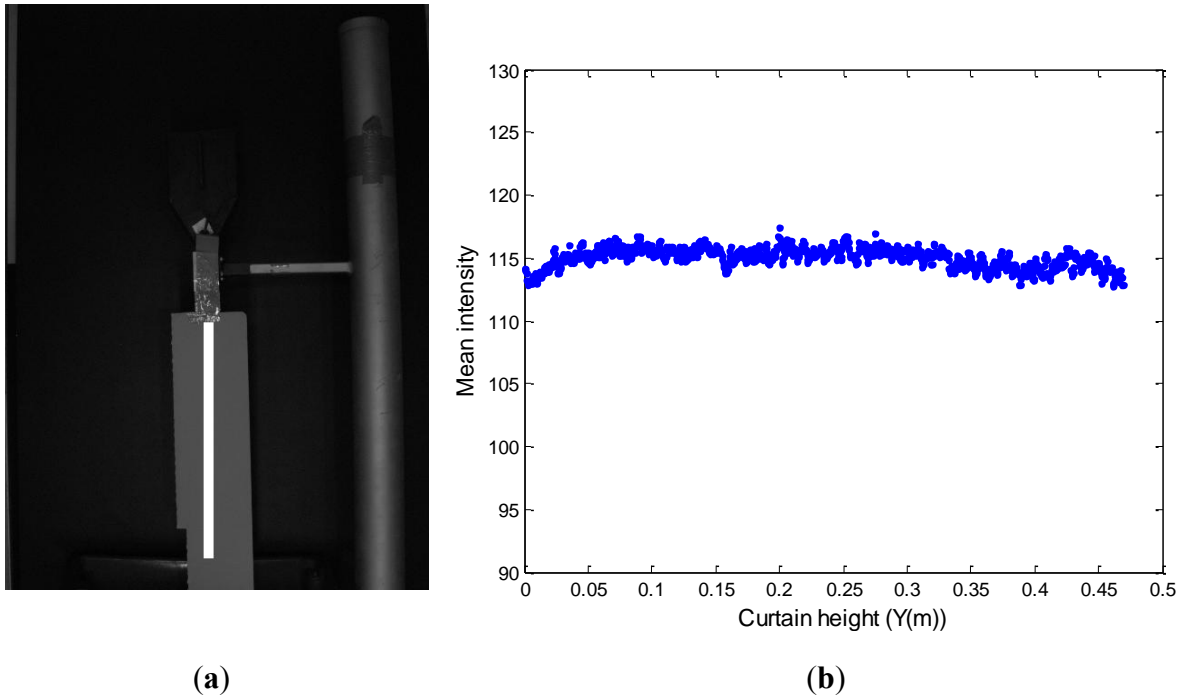


Figure 4.9: (a) Visible image of the experimental set-up in the absence of particle curtain (b) The graph of pixel intensities versus height for the bright white area in Figure 4.12 (a)

As can be seen from Figure 4.9, the uniformity of light on the cardboard placed in the spreader box is relatively constant. The visible image pixel intensities shown are averages of 3 pixels at the centre of the particle curtain. This is to create equivalent pixel dimensions in both visible and thermal imagery. The centreline width of three pixels in the visible image was approximately equal to the width of a single pixel in thermal imagery.

In order to expedite image capture and processing, the pixel intensities of hot and cold particle curtains were examined. Figure 4.10 shows that the differences between centreline visible image pixel intensities of hot (i.e. initial condition of 140°C) and cold particles (i.e. ambient conditions: 25°C) are negligible. The visible images in this comparison were carried out with cold particles at the same mass flow rate as the hot particle curtain images. Noting the link between pixel intensity

and volume fraction, it is interesting that hot and cold particle curtains exhibit the same pixel intensity distribution.

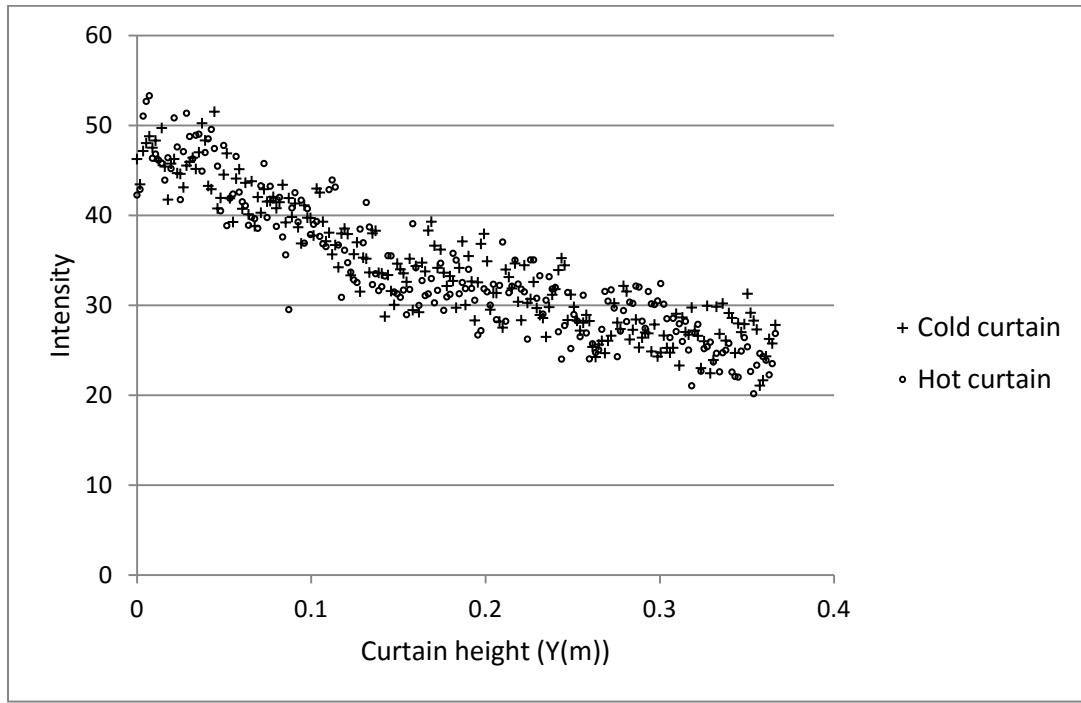


Figure 4.10: Pixel intensities in cold and hot particle curtains ($d_s=610\mu\text{m}$, $m^o=0.085\text{kg/s}$ and slot width=20mm)

4.3.4.3. *Visible high speed camera details*

A REDLAKE MotionXtra® HG-100K high speed camera (1504×1128 resolution) was used. The distance between camera lens and particles was approximately 20cm. In order to improve the quality of images, a black cardboard was used behind the spreader box. The high speed camera was located in front of particle curtain aligned with the wide dimension of 15cm.

4.3.4.4. *Image processing*

The initial velocity was calculated for all particle sizes ($290\mu\text{m}$, $400\mu\text{m}$ and $610\mu\text{m}$), all mass flow rates and through the two different slot widths. Figure 4.11 shows an example image in which the pathway of a particle is identified. The same particle is identified in sequential images. High speed visible images were taken every 0.001 seconds. All images were scaled using the spreader box dimensions and analysed using ImageJ software. Ten consequent frames of high speed photography were selected to record the falling distance of the particle. Particle locations (i.e. falling distance versus time) are processed by fitting to a single particle drag model. The initial particle velocity is extrapolated from the best fit model. The single particle model describes a particle motion in the fluid subjected to drag and gravity forces. This model was integrated using Engineering Equation Solver® (EES) software [76]. The single particle model is described in Section 3.1.4.

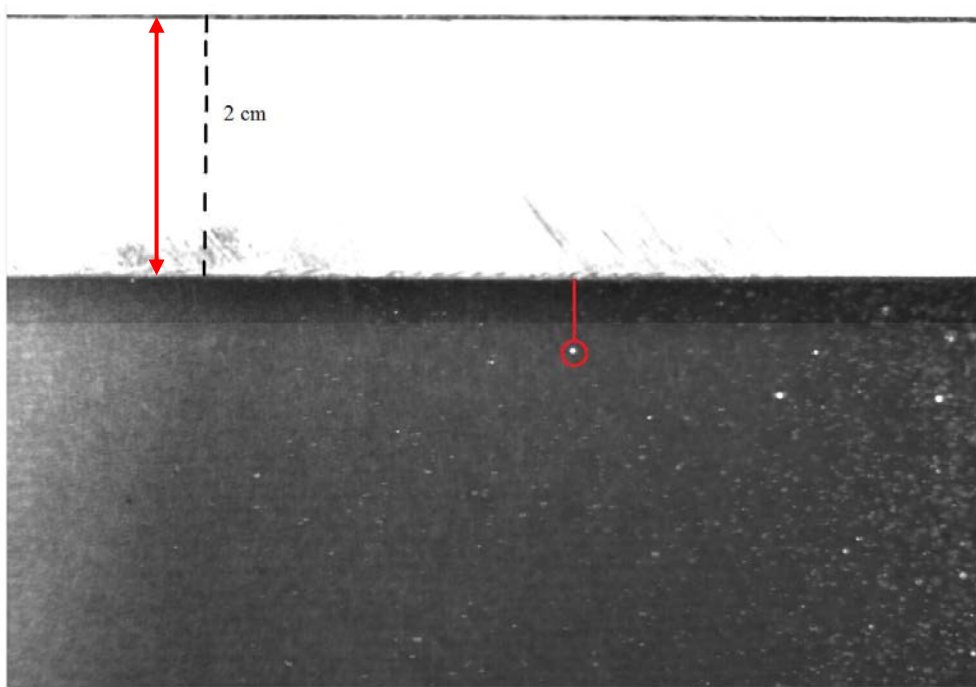


Figure 4.11: Particle pathway from inlet ($d_s=610\mu\text{m}$, $m^o=0.057\text{kg/s}$, slot width=20mm). The spreader box width (2cm) was used as known distance to scale and convert pixels to centimetres with the ImageJ software.

Figure 4.12 shows examples of plotted falling distance versus time. The regression constants between each model and experimental curve were calculated (Table 4.2) and the regression constants demonstrating the best fit were selected.

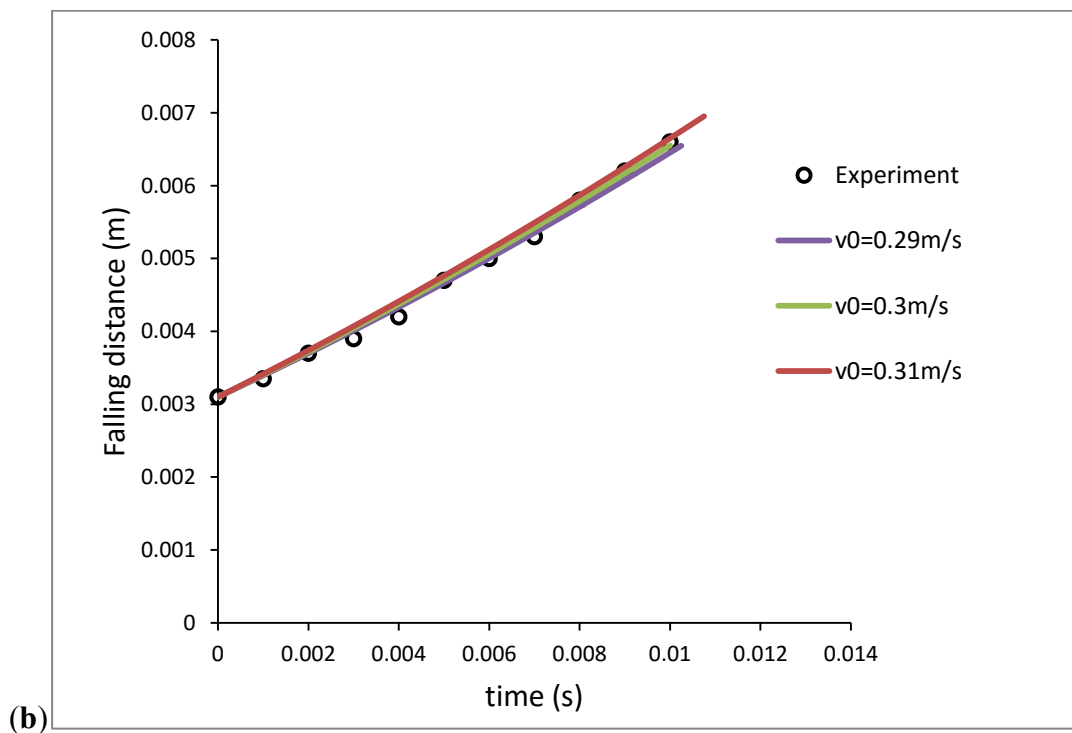
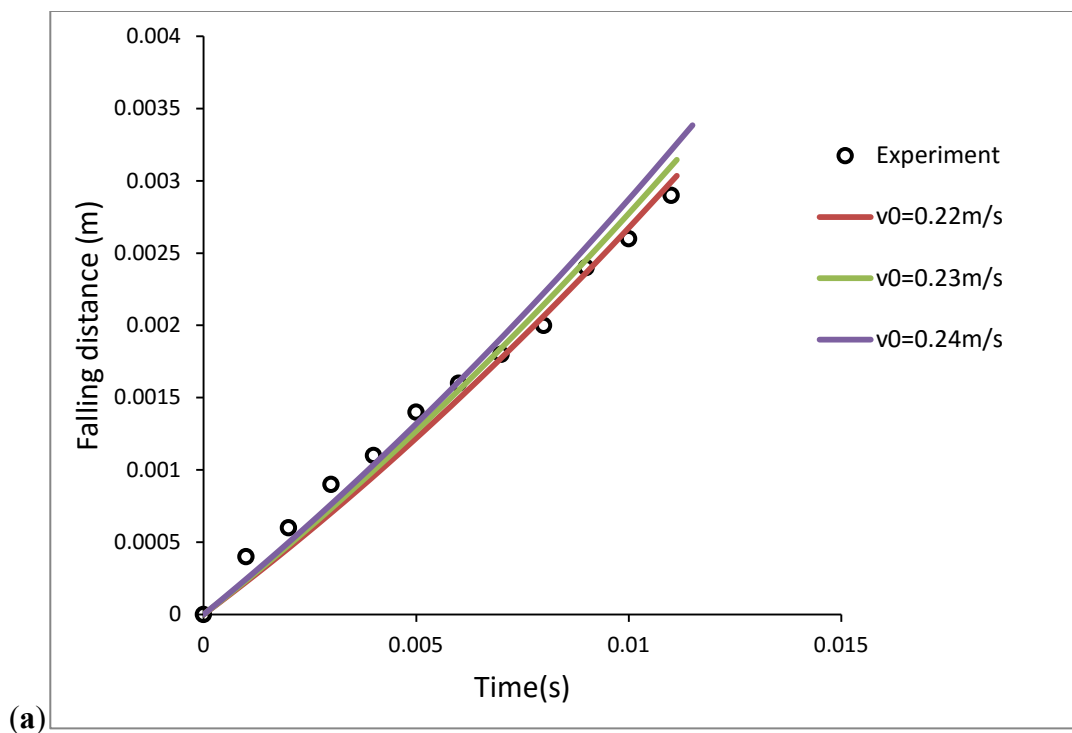


Figure 4.12: Comparison of travelled distance by an individual particle between the model and experiment (a) $d_s = 400\mu\text{m}$, $m^o = 0.101\text{kg/s}$, slot width=20mm, (b) $d_s = 290\mu\text{m}$, $m^o = 0.114\text{ kg/s}$, slot width = 60mm

From Table 4.2 it can be seen that the initial velocity of 0.23m/s and 0.3m/s shows the best fit to experimental results for slot width of 20mm and 60mm respectively. For the same slot width, the initial particle velocity was found to be independent of particle size. The initial velocity of the particles is controlled by the presence of the perforated plates, leading to constant initial velocities.

Table 4.2: Regression constant at different conditions

Initial velocity (m/s)	d_s (μm)	Slot width (mm)	m^o (kg/s)	Regression constant (R^2)
0.22	400	20	0.101	0.9
0.23				0.90905
0.24				0.90903
0.29	290	60	0.114	0.906
0.3				0.907
0.31				0.905

4.3.5. Direct thermocouple measurement

In order to assess the accuracy of the thermography data, the curtain was discretely sampled and temperatures were measured with direct contact thermocouples. The direct thermocouple measurement is used in Hurby et al. [49] and Wardjiman and Rhodes [70] study. The temperature of the particle curtain was measured at three distances below the discharge point (5cm, 30cm and 57cm down from the spreader box exit for the 20mm slot runs, and 5cm, 26.5cm and 53cm down for the 60mm slot runs). Each measurement was undertaken during separate experimental runs to

avoid disturbing the flow field. Only a selection of experimental runs were directly sampled using this technique.

A T type bead thermocouple with the accuracy of $\pm 0.1^{\circ}\text{C}$ was fitted into sampling cups (Figure 4.13) using a technique previously reported in the literature [49, 70]. The bare tip of the thermocouple was 1mm diameter and 2.5mm high and extended into the cup 17.5mm. The sampling cup consisted of a small, cylindrical aluminium cup (35mm in diameter and 20mm high).



Figure 4.13: The sampling cup fitted with a T type bead thermocouple

The size of the discharge hole in each cup was different for each position to account for varying flow rates. The cup hole size at 5cm down from the spreader box exit was 6mm, and for the cups at 30cm and 57cm down the spreader box were 4.5cm and 3mm respectively. This was to avoid accumulation of the particles inside the cup under conditions of higher solid volume fraction near the spreader box. The thermocouple probes were connected to data logger thermometer (SE-378) and logged on a laptop. The sampling rate of data logger was every second. The cup hole were

positioned at the centre of the frontal edge of the spreader box (Figure 4.14 (a)) where from the side view, the edge of the cup is aligned with the edge of the mesh screen where particles started to fall (Figure 4.14(b)).

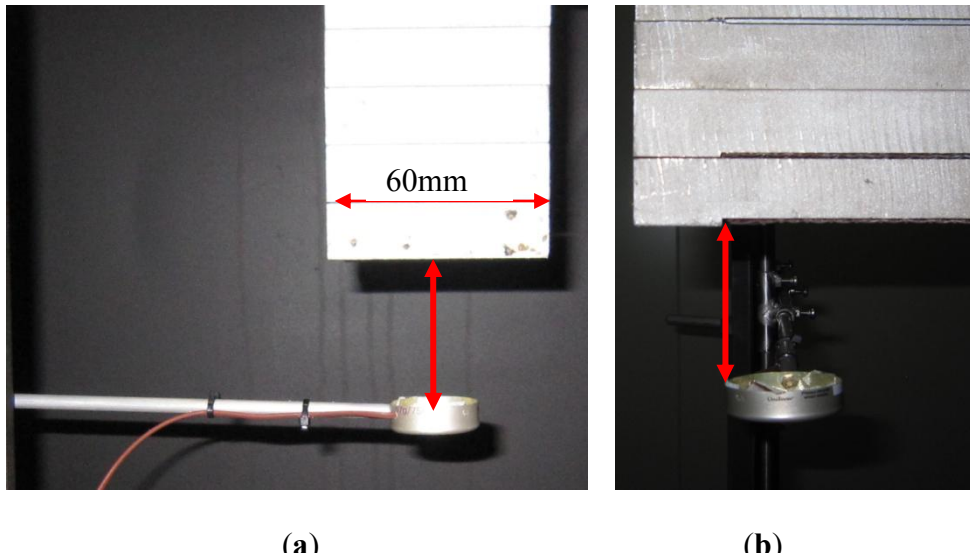


Figure 4.14: Location of cup in the experimental set-up (a) spreader box frontal view (b) spreader box side view. Note the edge of the cup aligned with the slot opening.

4.3.5.1. *Temperature stability*

Particle curtain temperatures were recorded during the entire time of particles falling (i.e. 50-150 seconds depending on mass flow rate). In order to report the thermocouple temperature at a certain location and account for delay in thermal response, the average temperature of recorded temperatures were calculated within a discrete time interval in which the temperature profiles were most stable. Generally, at high mass flow rates (Figure 4.15 (a)) the recording discrete time interval chosen for averaging was less than at low mass flow rates (Figure 4.15 (b)). Thus, at high

mass flow rates the time interval used to determine average temperature was 10 seconds between the 20th and 30th second, whereas the time interval for low mass flow rate was taken between 50th and 70th second for 20 seconds.

Figure 4.15 shows two examples of recorded thermocouple temperature data. In each graph the region chosen for temperature averaging is illustrated. The full set of thermocouple temperature data profiles are presented in Appendix D.

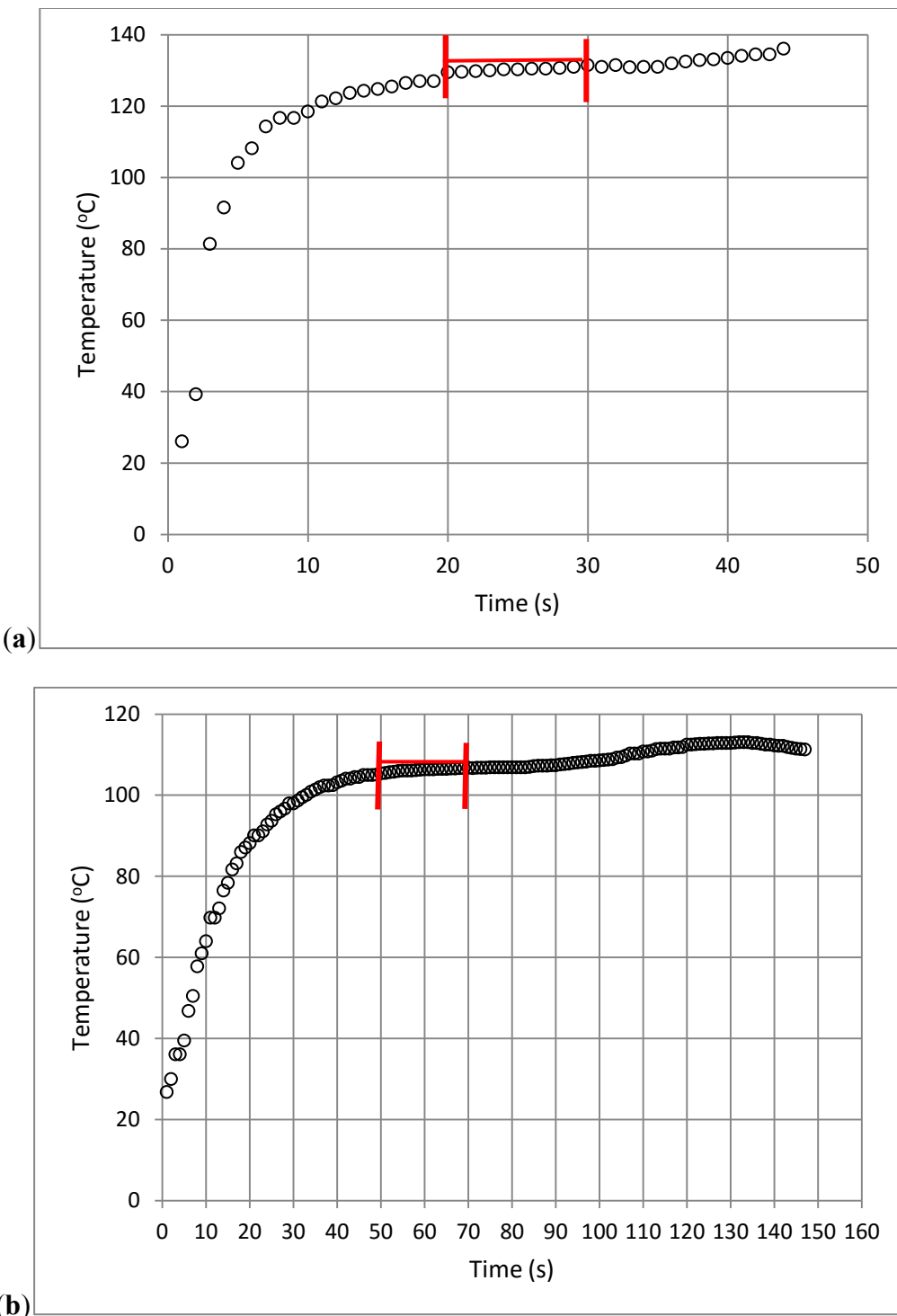


Figure 4.15: Direct thermocouple temperature measurements (a) $Y=0.05\text{m}$, $d_s=290\mu\text{m}$, $m^o=0.15\text{kg/s}$ and slot width= 20, (b) $Y=0.05\text{m}$, $d_s=610\mu\text{m}$, $m^o=0.045\text{kg/s}$ and slot width=60mm

In Figure 4.15, there is an increasing trend at the end of the temperature profiles. This may be due to the accumulation of particles in the cup and the associated rate of heat conduction. This effect is more pronounced for larger particles and could be reduced by designing tailor-made cups for each particle size and mass flow rate.

4.4. Experimental Procedure

Experiments were undertaken in an enclosed air conditioned room such that ambient air velocity was 0 m/s. The humidity and temperature of ambient air was recorded by humidity sensor (Testo 610 made in Germany) with accuracy of $\pm 2.5\%$ RH and $\pm 0.5^{\circ}\text{C}$. The experiments were carried out at three particle sizes (290, 400 and 610 μm), high and low mass flow rates (0.055-0.062kg/s) for two slot widths (20mm and 60mm).

The hopper was filled with glass beads and the entire apparatus (including spreader box) was heated in the oven for exactly three hours in order to obtain a sufficiently uniform temperature across the whole volume of hopper. The temperature of oven was kept between 160-165 $^{\circ}\text{C}$. Data recording with the camera and scale indicator were initiated before taking the hopper out of the oven. Immediately after heating, the hopper was placed in the spreader box.

The experimental conditions for different slot widths are summarised in Table 4.3. In this table, calculated properties include solid volume fraction and inter-particle distances. Initial solids volume fractions were calculated using Equation 3.21. Inter-particle distances were calculated using Equation 3.28, assuming that the spherical particles were evenly distributed.

Table 4.3: Experimental conditions

Slot width (mm)	Particle size (μm)	Mass flow rate (kg/s)	Relative humidity (%)	Air temperature ($^{\circ}\text{C}$)	Initial solid volume fraction	Inter-Particle distance (mm)
20	290	0.066	77	27	0.0382	0.403
20	290	0.14	60	23.6	0.0811	0.2499
20	290	0.15	84.1	25.9	0.086	0.2394
20	400	0.062	79	24.1	0.0359	0.577
20	400	0.129	64	23.7	0.0747	0.3654
20	400	0.132	70	24.3	0.0765	0.3593
20	400	0.138	50	23	0.08	0.3481
20	610	0.088	70	24	0.051	0.7156
60	290	0.063	70	22.6	0.0093	0.8213
60	290	0.086	73	22.7	0.0127	0.7117
60	290	0.138	83	24.5	0.02	0.571
60	290	0.548	45	22.2	0.0811	0.2499
60	290	0.55	45	22.1	0.0814	0.2492
60	400	0.071	46.2	25	0.0105	1.0721
60	400	0.141	67.3	24.6	0.02	0.7875
60	610	0.047	60	23	0.007	1.9597
60	610	0.075	70	22.5	0.011	4.152
60	610	0.096	65	23.1	0.0142	1.42
60	610	0.094	70	23	0.014	1.4296

The initial temperature of particles at the hopper exit was measured using a long probe thermocouple and compared to the temperature obtained by infrared thermography measurement at the spreader box exit. Table 4.4 shows the initial temperatures at the exit using the two different devices for particle sizes of $290\mu\text{m}$ and different mass flow rates. These measurements were repeated three times and the data are presented in Table 4.4. It can be seen that the temperatures are closely correlated as the calculated Root Mean Square Error (RMSE) is $\pm 0.56^\circ\text{C}$.

Table 4.4: Comparison of initial temperatures measurement at the hopper inlet using infrared camera and thermocouple

Initial temperature using infrared camera ($^\circ\text{C}$)	$d_s(\mu\text{m})$	$m^o (\text{kg/s})$	Initial temperature using thermocouple ($^\circ\text{C}$)
141.9	290	0.062	140
139.8	290	0.132	139.8
139.1	290	0.155	139.5

Chapter 5 Image and Data Processing

The broad objective of the image processing methods described in this chapter is to obtain the best quality and most reliable quantitative description of a hot particle curtain with varying characteristics. In this chapter, the methods used to process and analyse thermal and visible images which were generated using the approaches and methods described in the previous chapter, are described. The use of image processing software such as ImageJ and Matlab to manipulate and filter raw image data is emphasised. All images were scaled to normal length dimensions, and then aligned to achieve symmetry about the curtain centreline. The curtain centreline temperature profile (with respect to height) is the most important measure obtained from the data, and is used extensively in the comparative analysis described in later chapters. With respect to data reliability, the uniformity of temperatures at the spreader box exit is examined. Furthermore, repeatability of temperature profiles obtained using infrared thermography and thermocouple measurements in various examples is investigated. To better understand the limitations in infrared thermography, the effect of particle curtain depth on thermographic data is also investigated. The comparison of infrared and thermocouple temperature measurements is presented to better understand the influence of volume fraction on recorded temperature. Statistical tests are carried out to compare alternative measurement methods and to define procedures for adjusting recorded infrared temperatures. Finally, methods to identify the edges of the particle curtain from thermographic data are described.

5.1. Raw Image Data Processing

5.1.1. Infrared thermal image scaling

The bitmap formatted image thermal images were processed using ImageJ software [100]. Infrared image pixels were converted to length by scaling a known length of hot metal bar 23cm long. The hot metal bar was fixed at the edge of the catch bin (Figure 5.1). Figure 5.1(a) and (b) shows infrared and visible image of hot metal bar and spreader box showing the metal bar height and the particle curtain fall height. Figure 5.1(c) illustrates an example of the ImageJ pixel conversion function. The calculated scaling factor for all processed infrared images in ImageJ was 659 pixels/m.

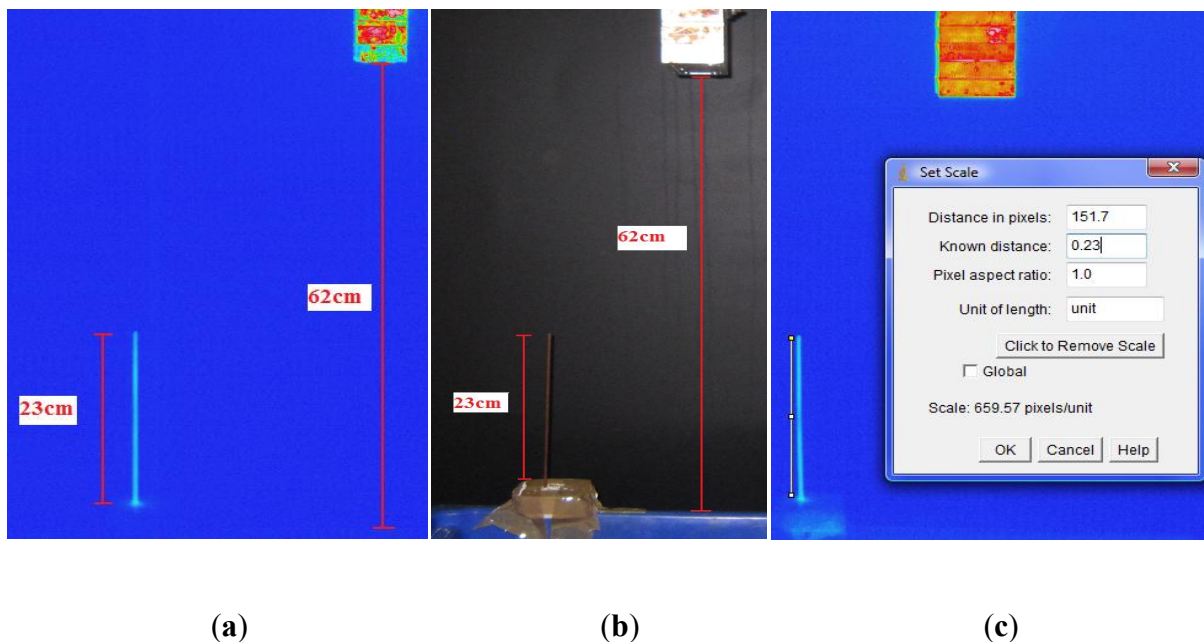


Figure 5.1: Hot metal bar and spreader box showing metal bar height and particle curtain height (a) infrared image (b) visible image (c) ImageJ pixel conversion function

Figure 5.2 shows a SVX infrared (a) and visible (b) photo of particles discharging from the spreader box. In the thermal images, a defined area was selected for temperature analysis and further processing. This data was exported to Excel as a matrix of pixels, and the corresponding temperatures distributed across the height and width of the selected area. See Figure 5.2(a) as an example of the area of thermal image selected for further processing. The matrix data shown in Figure 5.2(c) is the raw temperature data with corresponding x row and y column directions. In the matrix of raw temperature data, the first row includes the image pixels corresponding to the x direction. The first column of matrix data includes the image pixels corresponding to the y direction.

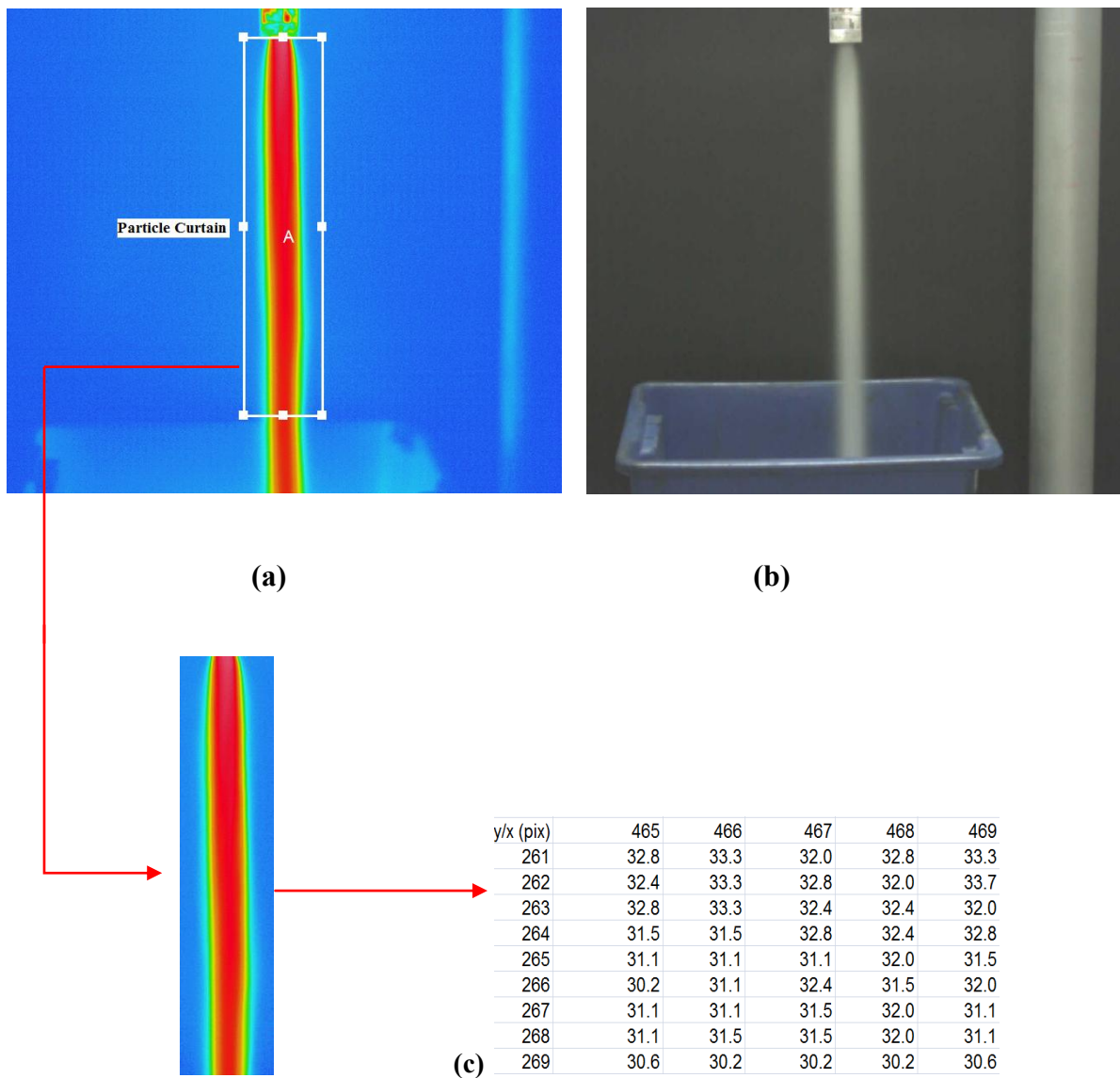


Figure 5.2: Experimental apparatus (a) infrared image (rectangular box (A) has an approximate area of $0.11 \times 0.62\text{m}^2$) (b) standard visible image (c) matrix of raw temperature data

5.1.2. *Visible image scaling*

Figure 5.3 shows an example of a particle curtain visible image. The height of the particle curtain from the spreader box exit to the edge of the catch bin (62cm) was used as a known distance to

convert pixels to centimetres, again using ImageJ software. The scaling factor in visible images was 1737.42 pixel/meter.

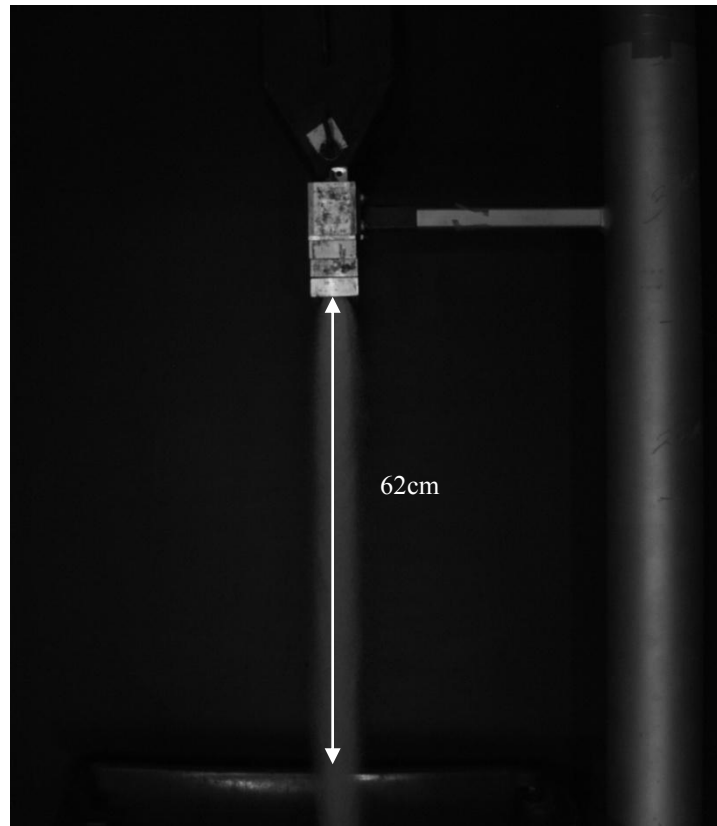


Figure 5.3: Visible image of particle curtain showing the curtain fall height

5.1.3. *Image Alignment*

The data manipulation was carried out because the centre of the curtain was not located at geometric centre of the image, which makes direct comparisons to CFD difficult. In addition, data manipulation improves methodologies to detect the edges of the curtain. Two sets of experiments

were carried. The first was in an open laboratory subject to external influences and not-air conditioned. In this setting, even minor air movement was observed to cause asymmetrical particle curtain profiles (see for example Figure 5.4 (a)). A second and more comprehensive set of experiments (see Table 4.3 in Section 4.4 for experimental conditions) were repeated in a completely closed and air-conditioned laboratory with no external openings and uniform wall and roof surface coating (dull grey). Figure 5.4 (b) shows the thermal image of the particle curtain in the closed laboratory. Even in the closed laboratory, the centreline temperatures were not always located at geometric centre of the image and more subtle forms of asymmetry were present, potentially a result of variation in initial velocity (at the spreader box exit). To force symmetry and precisely identify the centreline temperatures, the image data was manipulated. In the x direction, the centre of the curtain was assumed to exhibit the highest temperature, across the entire fall length.

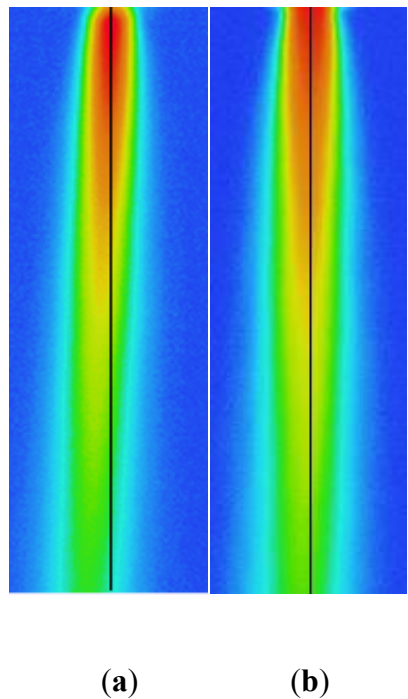
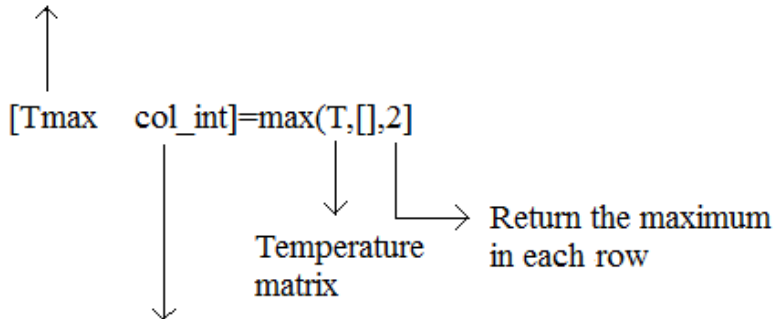


Figure 5.4: Thermal image of particle curtain in (a) an unclosed lab (b) closed lab

Matlab software was used to identify the maximum temperatures at each row (i.e. at various heights up and down the curtain) of the raw temperature matrix data, via Equation 5.1.

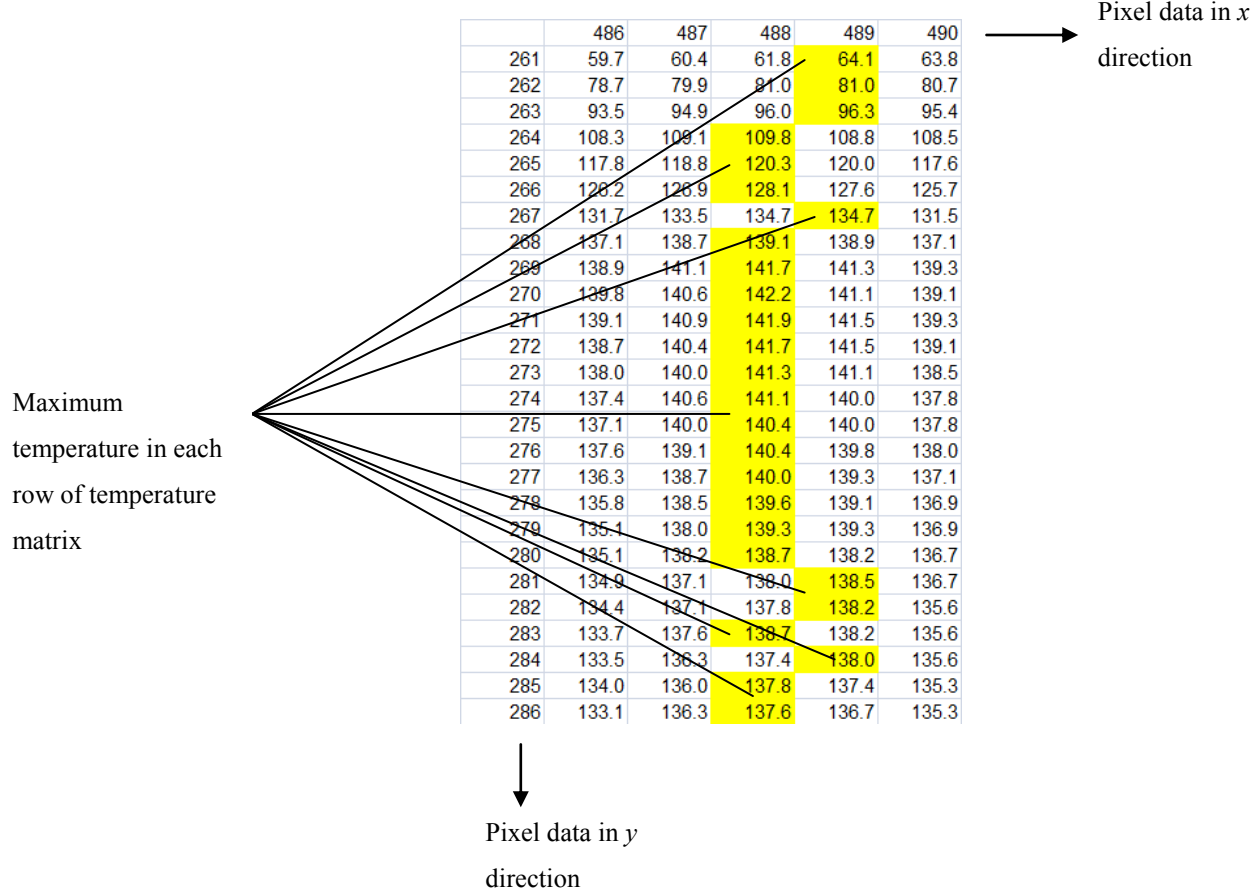
Maximum of
temperature value



5.1

The column number (col_int) in the temperature matrix at which the maximum value is located was used to precisely identify the corresponding x coordinate for the curtain centreline, as a function of height. Table 5.1 shows a selection of raw temperature data with the shaded entries corresponding to the maximum temperatures in each row.

Table 5.1: Matrix of raw temperature data showing maximum temperatures across each row with corresponding x and y direction



5.1.4. Initial conditions

The rectangular area (described in Section 5.1.1) defining the extent of the curtain was chosen to be larger than necessary, to ensure that the spreader box exit is included in the field of view. As such, the raw data temperature matrix includes a few pixels corresponding to the spreader box, rather than curtain. To identify the initial temperature of particles precisely at the spreader box exit, the row of data that displays the maximum centreline temperature is selected. Typically, this

leads to elimination of 1-9 pixels from the top of the image. Figure 5.5 (a) and (b) show the raw data and corresponding thermal image (white rectangular box).

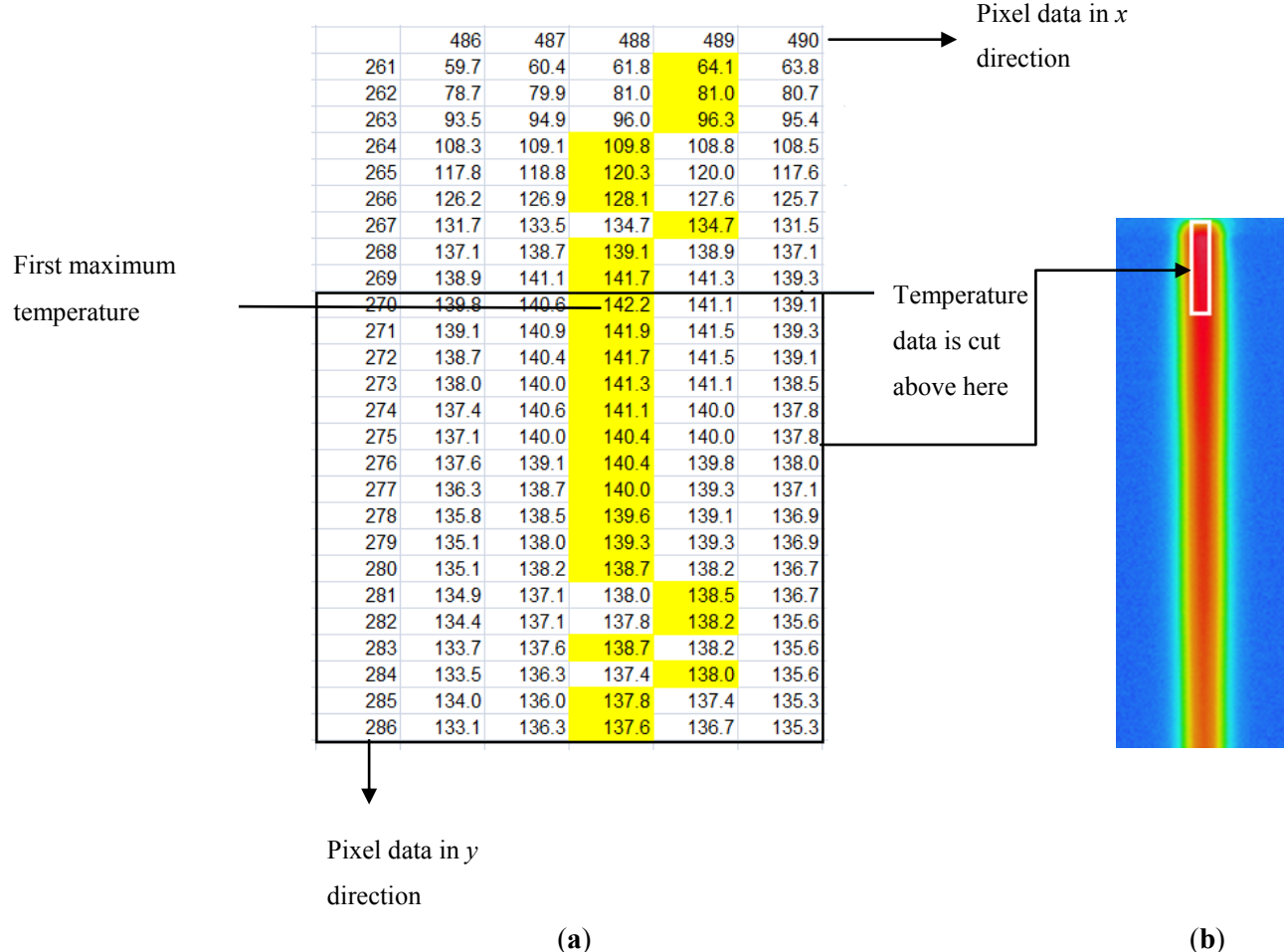


Figure 5.5: (a) Raw temperature matrix and (b) corresponding thermal image illustrating the identification of the spreader box exit

Figure 5.6 illustrates the process for presenting centreline temperature data. Figure 5.6 (a) shows an example of the centreline temperature profile versus height for the example temperature matrix shown in Figure 5.5. Figure 5.6 (b) shows the centreline temperature shifted left after identifying the first maximum temperature. Figure 5.6 (c) shows the same centreline temperature but includes temperature profiles located at 2 pixels (approximately 5mm), and 6 pixels (approximately 10mm)

on the right side of the centreline. The temperature profiles on either side of the centreline show increased fluctuations in comparison to the centreline.

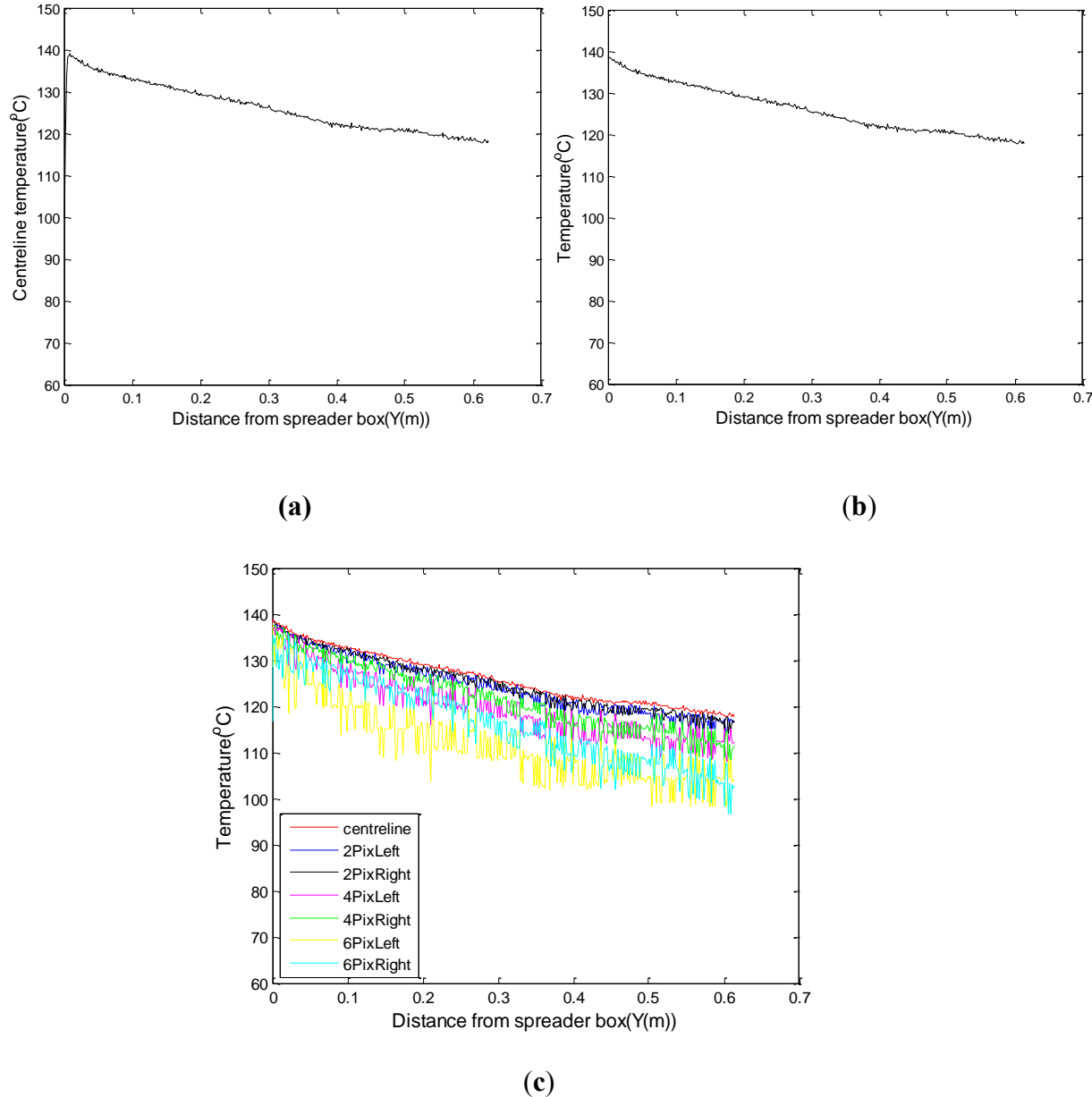


Figure 5.6: Centreline temperatures ($d_s=290\mu\text{m}$, $m^o = 0.066\text{kg/s}$ and slot width=20mm) (a) before identifying the initial temperature of particle curtain (b) after indentifying the initial temperature of the particle curtain (c) Temperature dispersion about the centreline

5.1.5. Profile filtering and smoothing

For each experimental run, approximately 2500-3000 frames over 1 to 5 minutes were captured. In all centreline temperature profiles presented in this thesis the data were smoothed to decrease the profile fluctuations by averaging over sequential frames (over a period of 0.33s seconds) and applying a Gaussian smoothing function (Sigma=2) [101]. Typical differences in measured initial temperature across the 10 frames were 1-3°C. The first frame in the set of 10 frames was selected only after the curtain was fully developed after exiting the spreader box exit. The curtain was defined as fully developed when it extended all the way from the spreader box exit to the catch bin. Figure 5.7 from left to right shows the process of curtain development. The last image on the right shows that the entire curtain height can be seen in the thermal image.

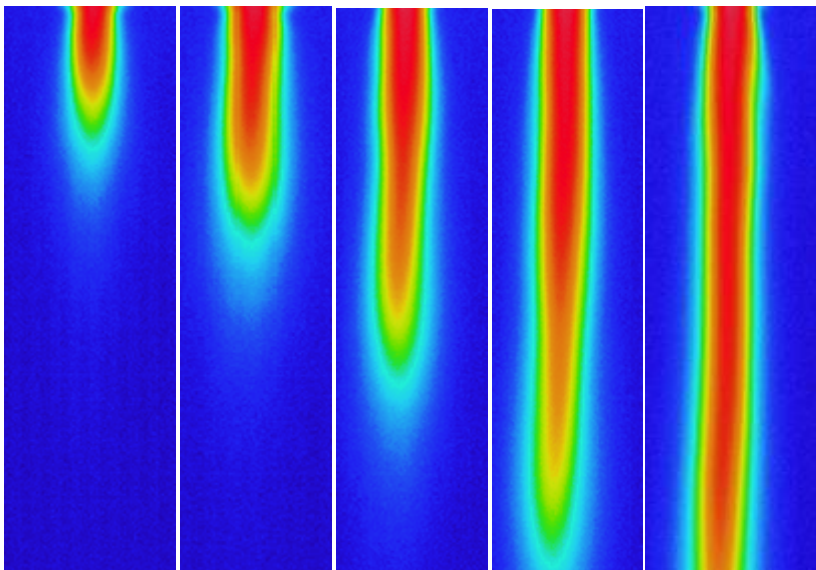


Figure 5.7: Developing particle curtain profile, with fully developed profile in the far right image (from left to right)

5.1.6. Temperature uniformity

The uniformity of temperature across the entire slot width was examined for different particle sizes, slot widths and mass flow rates. Temperature profiles across the frontal face (i.e. 20mm) were extracted from a line (i.e. the white line A in Figure 5.8) inserted at the spreader box exit. Figure 5.9(a-d) shows examples of temperature profiles corresponding to line A. In these figures, the spreader box width (i.e. 20mm/60mm) is illustrated with a dashed line. An example of a side view particle curtain thermal image taken from experimental results carried out by Dare [102] using identical methods and apparatus is shown in Figure 5.10(a). The corresponding temperature profile at the spreader box exit is shown in Figure 5.10(b). The temperature profiles at the spreader box exit in the short dimension (width) are relatively uniform. In the long direction, temperature is uniform for most of its length but reduces at the edges. The uniformity of temperatures across the spreader box exit in Figures 5.9 and 5.10 is an evidence for even-distribution of particles across the spreader box exit.

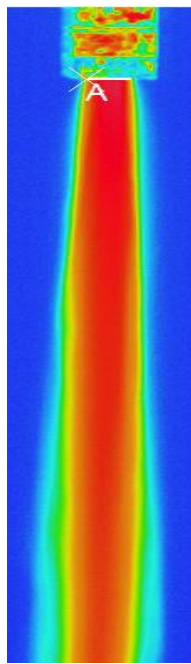


Figure 5.8: Thermal image of the particle curtain showing line A at the spreader box exit

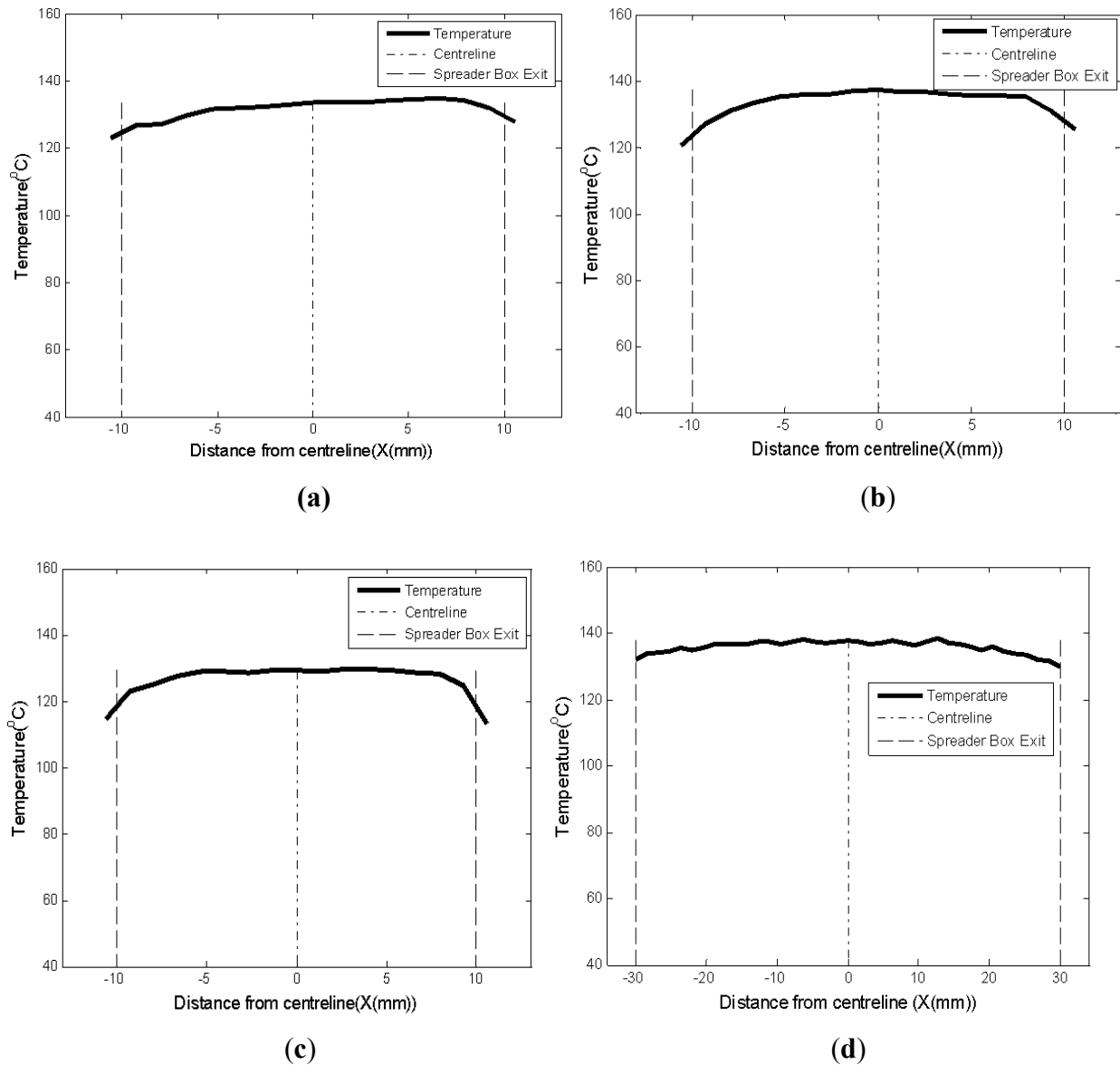
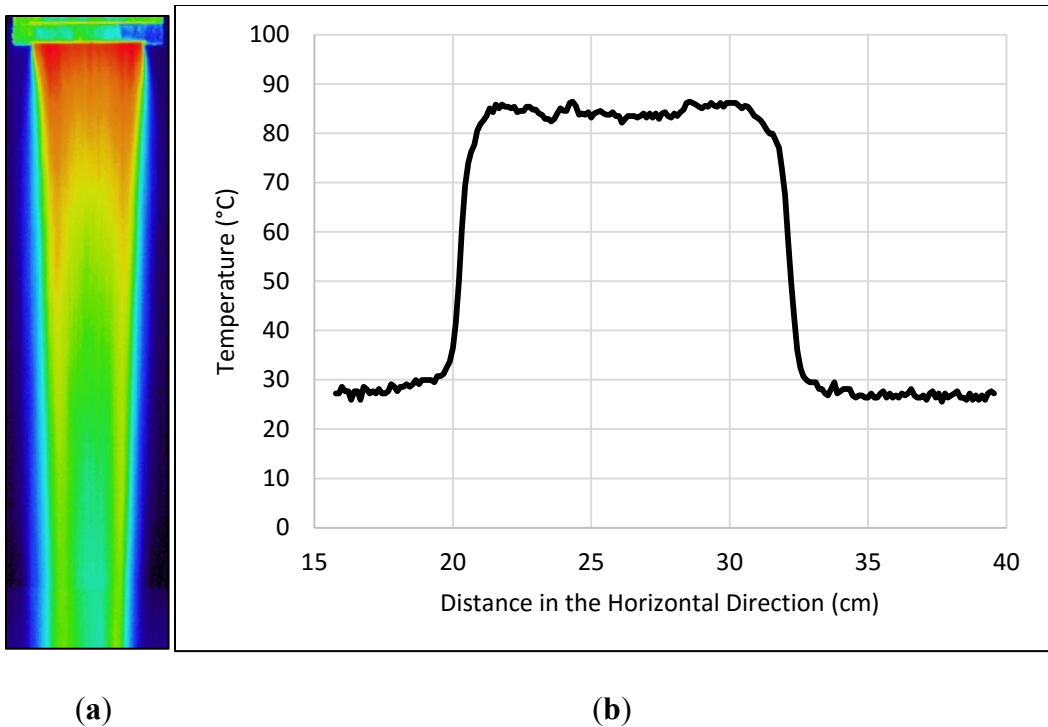


Figure 5.9: Temperature profiles at the spreader box exit (a) $d_s = 290\mu\text{m}$, $m^o = 0.14\text{kg/s}$ and slot width=20mm (b) $d_s = 400\mu\text{m}$, $m^o = 0.129\text{kg/s}$ and slot width=20mm (c) $d_s = 610\mu\text{m}$, $m^o = 0.088\text{kg/s}$ and slot width=20mm (d) $d_s = 290\mu\text{m}$, $m^o = 0.55\text{kg/s}$ and slot width=60mm



(a)

(b)

Figure 5.10: (a) Side view thermal image (i.e. 150mm) of the particle curtain (b) The graph of the temperature profile across the spreader box exit from the side view (150mm) (Reported from Dare 2014 [102])

5.1.7. Data repeatability

To test the repeatability of experimental results with regard to mass flow rate and ambient temperature variations, a number of repeat infrared and thermocouple experiments were separately performed. Repeat experiments were performed for different particle sizes, mass flow rates and slot widths. The repeatability of visible imagery data was discussed in Section 4.3.4.2. Repeatability is assessed here in terms of the centreline temperature profiles. Figure 5.11(a-c) represents repeat experiments for centreline temperatures obtained from thermal images.

Figure 5.11(a-c) shows there is relatively good repeatability in the experimental data for these conditions. The average of sum of square error between two temperature profiles was calculated for the above examples to represent the deviation of infrared repeat experiments. The calculated average of sum of squares in the above examples was 3.8°C, 1.4 °C and 1.2 °C for Figure 5.11(a), (b) and (c) respectively. These values contribute to 2%, 1% and 0.9% errors respectively. The repeatability of the direct thermocouple measurements was also evaluated using repeat experimental runs.

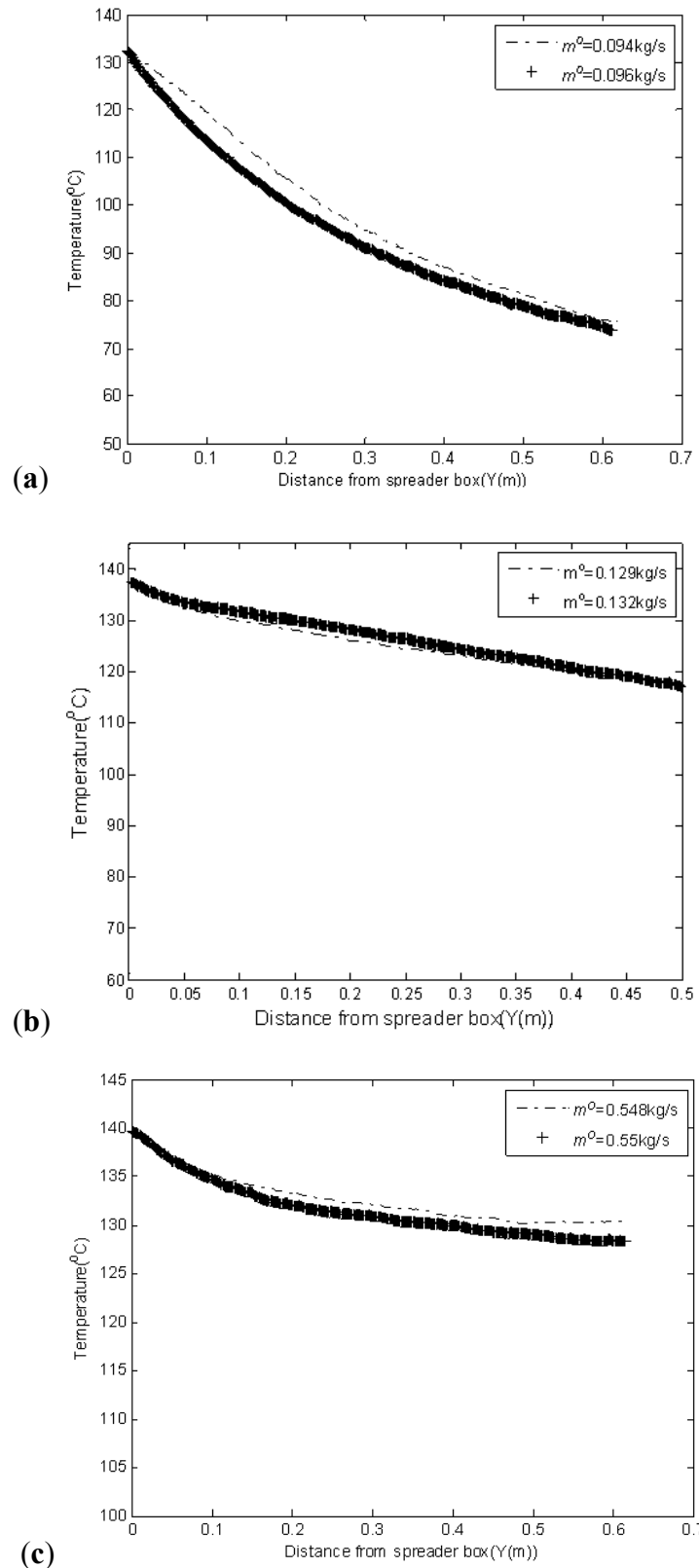


Figure 5.11: Infrared centreline temperature profiles (a) $d_s=610\mu\text{m}$, slot width=20mm (b) $d_s=400\mu\text{m}$, slot width=20mm (c) $d_s=290\mu\text{m}$, slot width=60mm

Figure 5.12(a-c) illustrates thermocouple profiles (sampled every 45-150 seconds) for repeat experiments. As can be seen in Figure 5.12, there is good repeatability in the thermocouple measurement profiles.

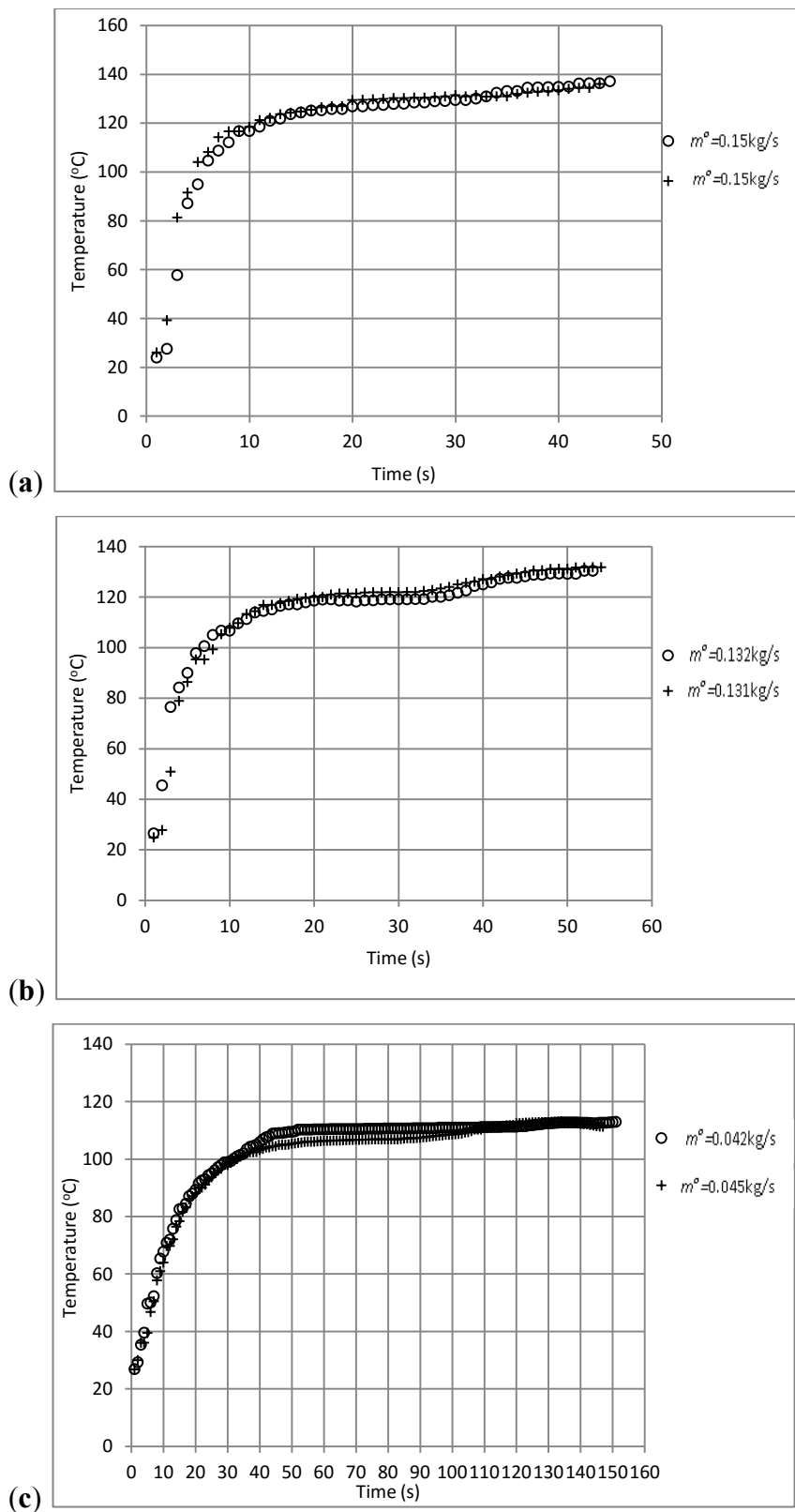


Figure 5.12: Discrete thermocouple temperature profiles (a) $Y=0.05\text{m}$, $d_s=290\mu\text{m}$ and slot width= 20mm (b) $Y=0.3\text{m}$, $d_s=400\mu\text{m}$ and slot width= 20mm (c) $Y=0.05\text{m}$, $d_s=610\mu\text{m}$ and slot width= 60mm

5.2. Data Reliability

Infrared thermography is fraught with challenges in dilute two-phase systems. Almost all previous examples of infrared thermography have been on opaque homogenous surfaces. In this research, the particle curtain has very low solids volume fractions (in the range 0.01-0.09). In low volume fraction situations, the camera's field of view may contain both particles and a high proportion of background, which can bias the recorded temperature. Two different sets of experiments were undertaken to examine this effect, and to better understand the limitations in applying infrared thermography to dilute two-phase systems. The first qualitative analysis examined the effect of curtain depth on recorded temperature. The second involved direct comparison to thermocouple data and the use of visible images in order to derive temperature correction methods. Note that the background in the field of view refers to wall surface, which is at ambient temperature. The infrared camera used in this work captures measures surface temperatures, and the infrared camera uses infrared radiation with a wavelength of $8\mu\text{m}$ to $15\mu\text{m}$ (see Figure 4.7). Air is totally transparent to this wavelength [93, 103]. In addition, emissivity is the ability of the object to emit thermal radiation, and the emissivity of the air is too low to be detected.

5.2.1. Curtain depth

In order to better visualise and quantify the influence of the background on thermographic recorded temperature at different mass flow rates and particle sizes, visible images of the particle curtains were collected. As an example, in Figure 5.13 white circles at the top and bottom of the curtain emphasise the differences in visible image pixel intensity (i.e. white). At small particle sizes the curtain pixel intensity is higher than for larger particle sizes, indicating a reduced

influence of the background even at the bottom of the curtain where the particle curtain is more dilute. At large particle sizes, the influence of background leads to darker curtains, especially at the bottom of the curtain where the solid volume fractions are lowest. To investigate the effect of curtain depth on recorded temperatures, experiments using two examples of particle sizes ($290\mu\text{m}$ and $610\mu\text{m}$) were conducted.



Figure 5.13: Visible images of the particle curtain showing the sparsity of particle at the top and bottom of the curtain (a) $d_s=290\mu\text{m}$, $m^o=0.14\text{kg/s}$ and slot width=20mm (b) $d_s=610\mu\text{m}$, $m^o=0.088\text{kg/s}$ and slot width=20mm

5.2.1.1. Methods

In these experiments thermal images were captured for hot particle curtains of varying depth. Short curtains were expected to show more influence from the background than longer curtains, because the field of view is less occupied by the particles. The depth of the curtain was changed using an adjustable black screen (Figure 5.14). The black screen was inserted to create various depths of curtain, from 1.5cm deep to and 15cm (full length).

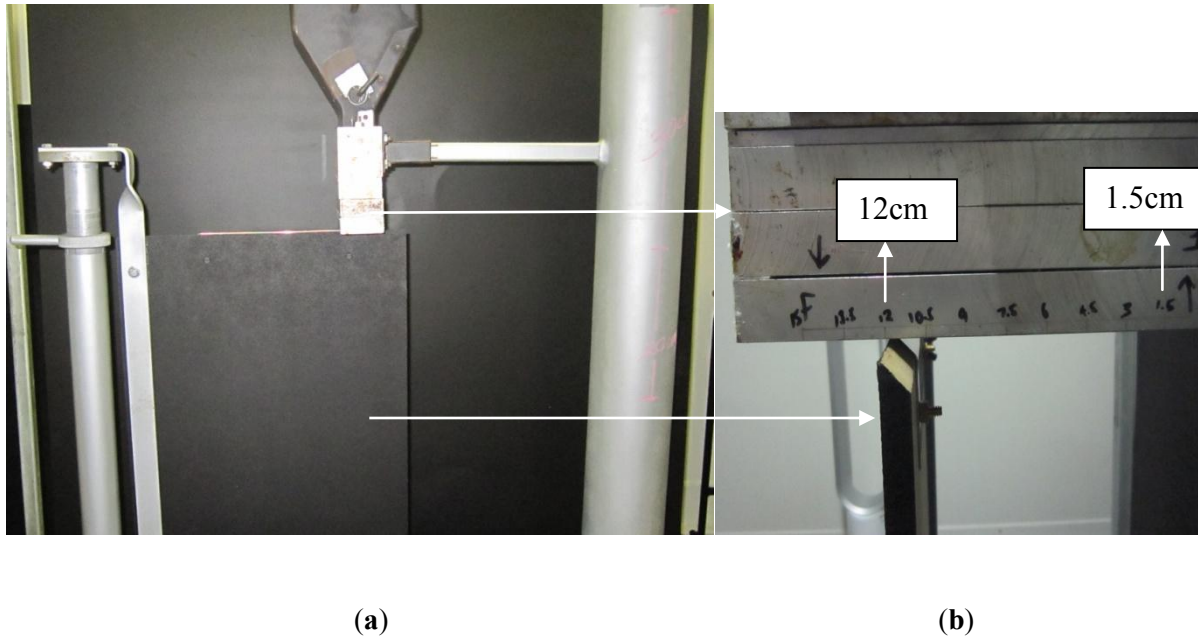


Figure 5.14: Experimental set-up for changing the depth of the curtain (a) frontal view (b) side view

Table 5.2 presents the experimental conditions for particle sizes of $290\mu\text{m}$ and $610\mu\text{m}$. In these experiments, the valve was fully opened to keep the mass flow rate as consistent as possible. Table 5.2 shows that the mass flow rates for particles of $290\mu\text{m}$ and a slot width of 20mm fluctuated

between 0.14kg/s and 0.154kg/s. For large particle sizes (610 μ m) the mass flow rates were between 0.1 and 0.082kg/s. The margin of error of mass flow rates at the 95% confidence interval was calculated as $\pm 0.0015\text{kg/s}$ and $\pm 0.0023\text{kg/s}$ for small and large particle sizes respectively.

Table 5.2: Experimental conditions for changing the depth of the particle curtain

Slot width (mm)	Particle size (μm)	Particle curtain depth (cm)	Mass flow rate (kg/s)	Initial solid volume fraction	Relative humidity (%)	Air temperature ($^{\circ}\text{C}$)	Inter-particle distance (mm)
20	290	1.5	0.147	0.085	17.6	20.9	0.0241
20	290	3	0.154	0.089	17.3	21	0.0233
20	290	4.5	0.140	0.081	18.1	21.7	0.025
20	290	6	0.147	0.085	18.2	21.3	0.0241
20	290	7.5	0.144	0.083	18	20.9	0.0245
20	290	9	0.144	0.083	17.9	21	0.0245
20	290	10.5	0.142	0.082	17.8	21.6	0.0247
20	290	12	0.153	0.088	17.4	21	0.0235
20	290	13.5	0.143	0.082	16.9	20.7	0.0247
20	290	15	0.144	0.083	17.6	20.8	0.0245
20	610	1.5	0.1	0.058	17.7	21	0.065
20	610	3	0.098	0.057	18.4	21.3	0.066
20	610	4.5	0.093	0.054	18.1	20.9	0.069
20	610	6	0.091	0.052	18	21.1	0.07
20	610	7.5	0.091	0.052	17.5	21.1	0.07
20	610	9	0.093	0.054	18.3	21.4	0.069
20	610	10.5	0.092	0.053	18	21.1	0.069
20	610	12	0.089	0.051	18.1	21	0.071
20	610	13.5	0.082	0.047	18.1	20.9	0.075
20	610	15	0.091	0.052	18.2	21	0.07

5.2.1.2. Results

Figure 5.15(a) and (b) show smoothed centreline temperature profiles for small and large particle sizes respectively. Profiles for depths from W=15cm to W=1.5cm are shown.

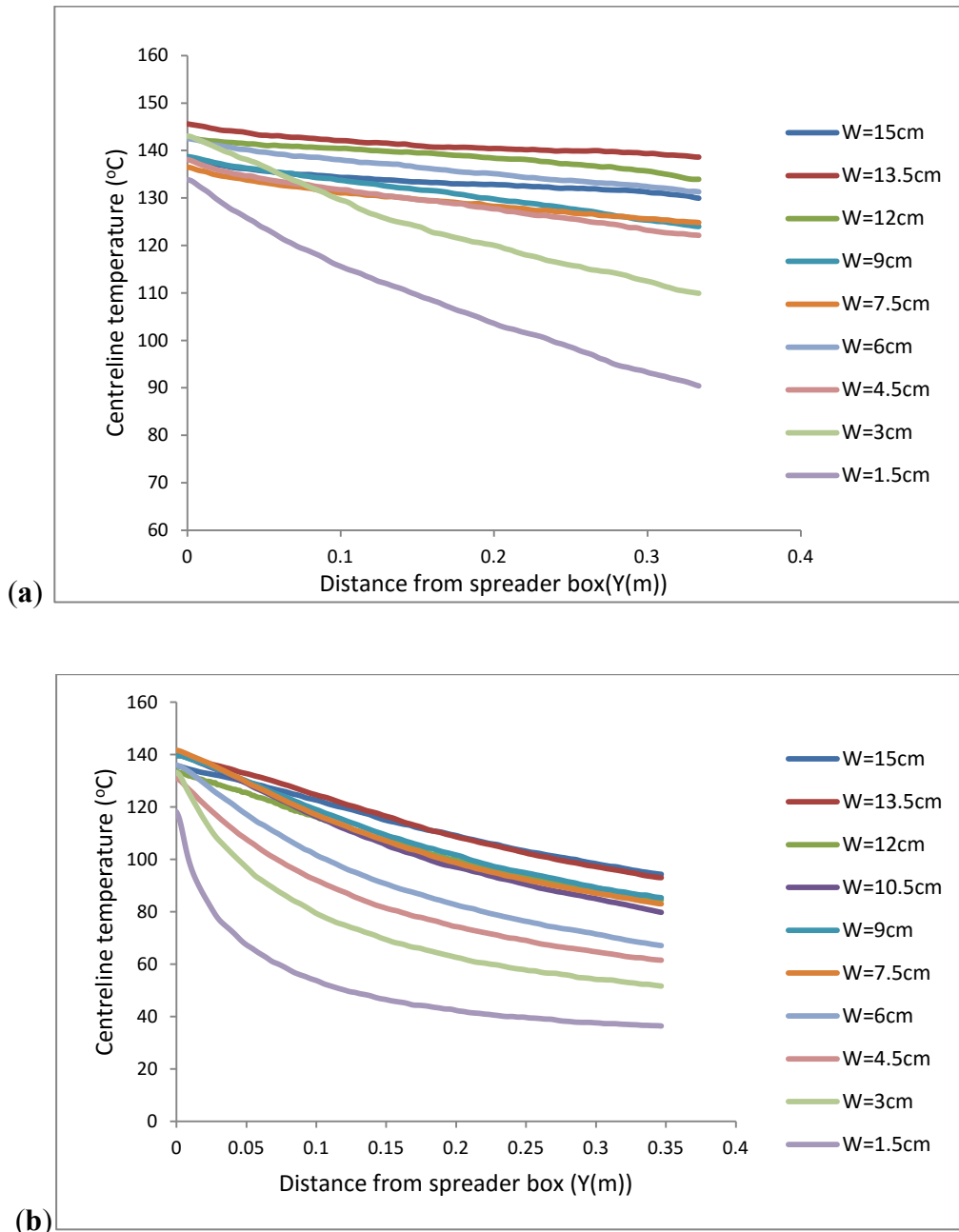


Figure 5.15: Centreline temperature profiles at varying curtain depth (a) $d_s = 290\mu\text{m}$, $m^o = 0.14\text{-}0.153\text{kg/s}$ and slot width=20mm (b) $d_s = 610\mu\text{m}$, $m^o = 0.082\text{-}0.1\text{kg/s}$ and slot width=20mm

Figure 5.15 shows that at greater depths (i.e. 15cm to 4.5cm for small particles and 15cm to 10.5cm for large particles) the centreline temperatures show universally higher temperatures, and there is consistency in the recorded temperature profiles. The critical depths at which temperature profiles begin to deviate away from a consistent profile was 3.5cm and 6cm for small and large particles respectively. The hypothesis is that at less than these critical depths, the background started to influence the recorded temperatures. Thus, it can be concluded that the particle curtains 3cm to 1.5cm deep for $290\mu\text{m}$, and 6cm to 1.5cm deep for $610\mu\text{m}$ are not sufficiently dense for the particle temperature to dominate the thermal image.

In order to eliminate the influence of background that would be associated with narrower curtains, the measured temperature at a fixed point (at the spreader box exit) was calculated. Figure 5.16(a) and (b) show this specific temperature versus the depth of the curtain for the two particle sizes: $290\mu\text{m}$ and $610\mu\text{m}$.

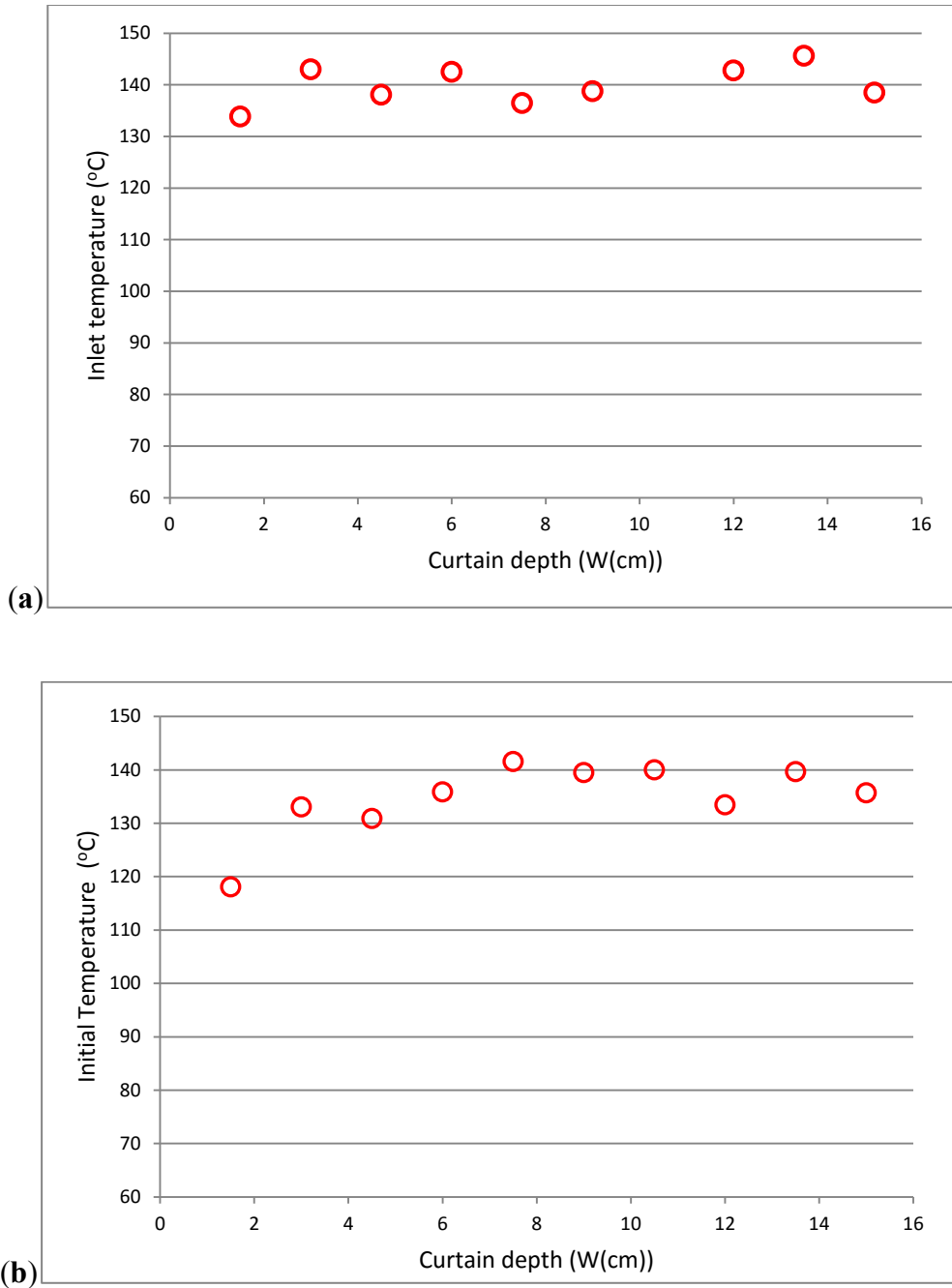
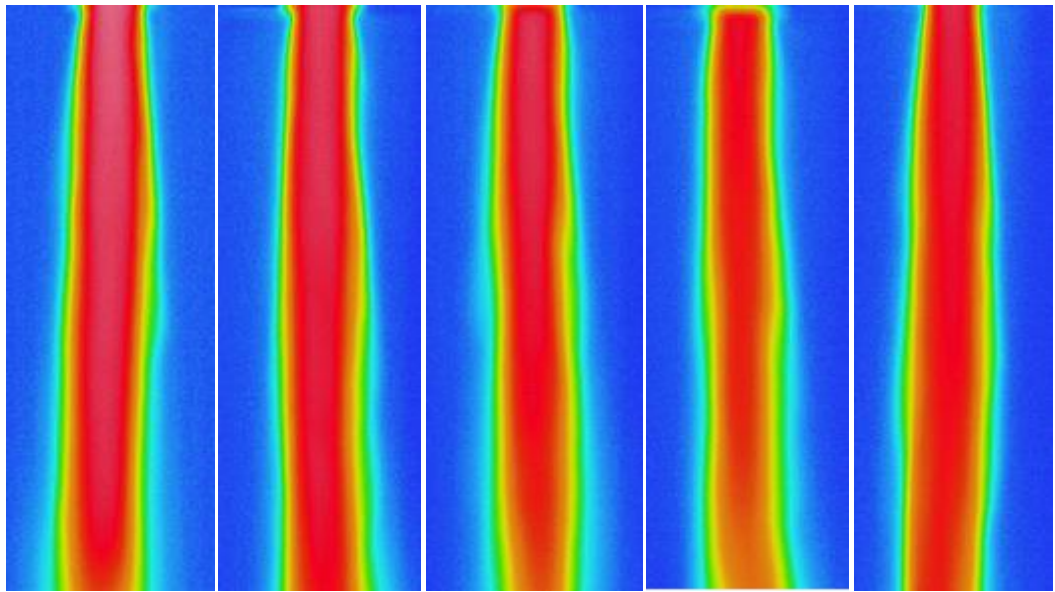


Figure 5.16: Effect of particle curtain depth on inlet temperatures (a) $d_s=290\mu\text{m}$, $m^o=0.14-0.153\text{kg/s}$ and slot width=20mm (b) $d_s=610\mu\text{m}$, $m^o=0.082-0.1\text{kg/s}$ and slot width=20mm

Figure 5.16(a) shows that despite small fluctuations in temperature at the spreader box exit for $290\mu\text{m}$ particles, there is deviation only for thin curtains (less than 3cm deep) and for large

particles ($610\mu\text{m}$), deviation occurs in thicker curtains (less than 6cm). These discrete temperature observations reinforce the conclusions drawn by comparing profiles.

In order to qualitatively evaluate the influence of curtain depth, 2-D thermal images of particle curtains ($290\mu\text{m}$ and $610\mu\text{m}$) at various depths are shown in Figures 5.17 and 5.18 respectively.



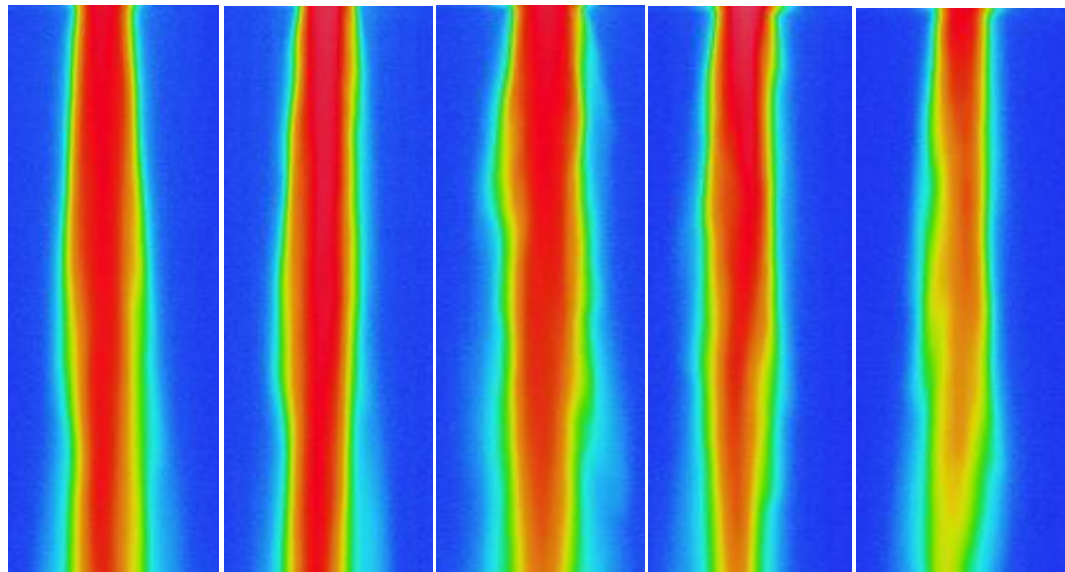
W=15cm

W = 13.5cm

W = 12cm

W=10.5cm

W= 9cm



W=7.5cm

W = 6cm

W = 4.5cm

W =3cm

W= 1.5cm

Figure 5.17: 2D thermal image of particle curtain with varying depths ($d_s=290\mu\text{m}$, $m^o=0.14-0.153\text{kg/s}$ and slot width=20mm)

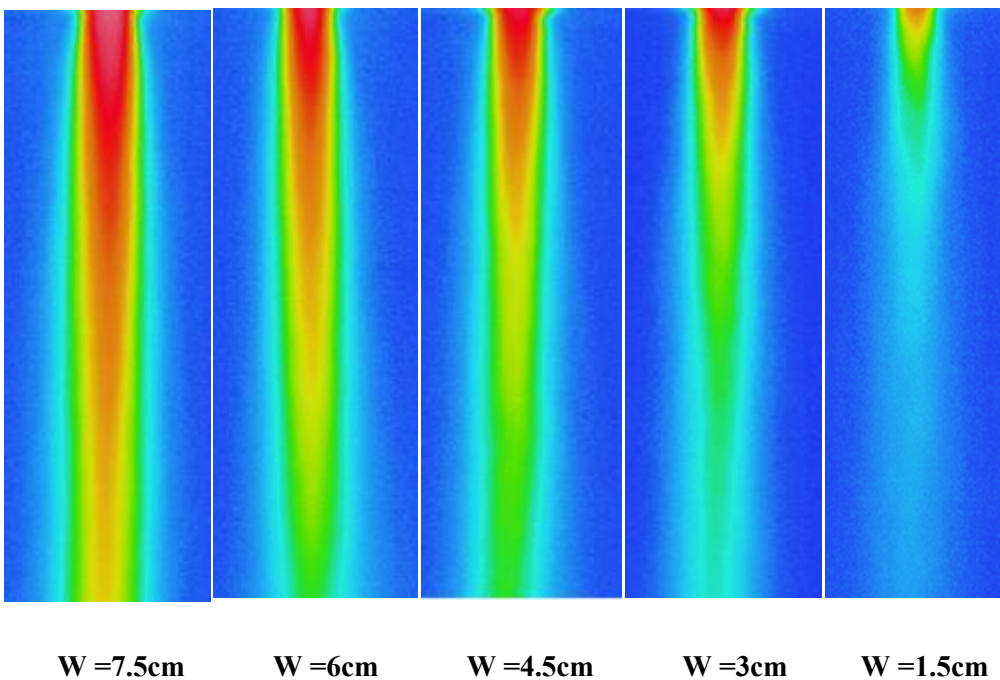
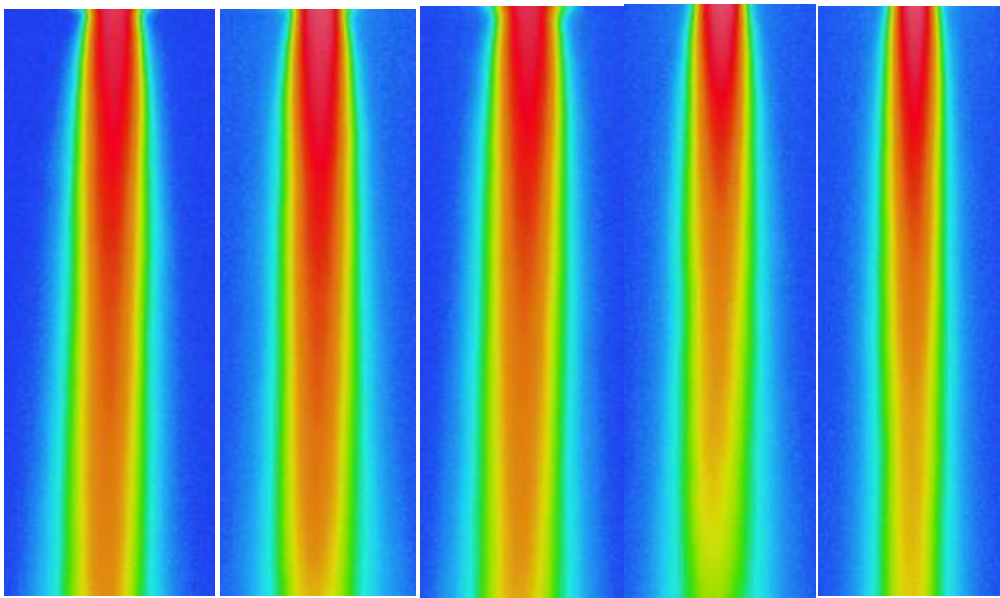


Figure 5.18: 2D thermal image of particle curtain with varying depths ($d_s = 610\mu\text{m}$, $m^o = 0.082\text{-}0.1\text{kg/s}$ and slot width=20mm)

Broadly, Figures 5.17 and 5.18 show that as curtain depth reduces, for both small and large particles, the hot particle region (i.e. dark in red) in the curtains becomes smaller and the extend in length and width is reduced. Qualitatively, there are no noticeable differences between curtains from 15cm to 6cm deep (290 μ m particles) and between 15 cm to 12cm deep. This effect particularly is observable at depths of 3cm-1.5cm and 6cm-1.5cm for 290 μ m and 610 μ m respectively. These results reinforce the results obtained from centreline observations and suggest the effect of background interference is important at low volume fraction and for large particle sizes.

In conclusion, the effect of particle curtain depth on recorded infrared temperatures depends on particle sizes and mass flow rates. For small particle sizes (i.e. 290 μ m) and higher mass flow rates, the field of view is more fully saturated with particles and recorded temperature is more reliable.

In order to account for the influence of the background in thinner curtains (i.e. large particles and low mass flow rates), there is a need to consider the combination of thermography and visible imagery, which provides a measure of solid volume fractions via pixel intensity.

5.2.2. Infrared thermography temperature reliability

Given the influence of background temperature on the recorded infrared thermal images, in this section direct comparison between infrared data and direct thermocouple temperature measurements are presented. A selection of experimental runs from Table 4.3 was directly sampled using a thermocouple measurement device. Conditions were chosen to encompass both high and low extends of particle saturation of the infrared field of view. The experimental conditions that were examined are provided in Table 5.3, and include four situations. Note that, each direct

measurement required an additional run to avoid the thermocouple apparatus disturbing the flow field. Minor variations in mass flow rate occur in these separate runs. Visible images were also collected.

Table 5.3: Experimental conditions chosen for direct comparison between infrared thermography and thermocouple measurements

d_s (μm)	m^o in thermocouple technique (kg/s)	m^o in thermography technique (kg/s)	Slot width (mm)	Y(m), Thermocouple distance down from the spreader box exit
290	0.15	0.15	20	0.05
290	0.15		20	0.3
290	0.151		20	0.57
290	0.068	0.066	20	0.05
290	0.066		20	0.3
290	0.071		20	0.57
400	0.137	0.132	20	0.05
400	0.131		20	0.3
400	0.127		20	0.57
610	0.045	0.047	60	0.05
610	0.045		60	0.265
610	0.045		60	0.535

Figure 5.19-5.22 shows centreline temperature comparison between infrared and thermocouple measurements. The thermal image data is presented as the average profile from an ensemble of profiles collected over the same time interval as the thermocouple sampling time (i.e. 10s for high

mass flow rates, and 20s for low mass flow rates (see Section 4.3.5.1)). Thermal images were recorded every 1/30s; thus, 10 second and 20 second time intervals are equivalent to 300 and 500 thermal image frames respectively. The red error bars represent the standard deviation across the sampling time for the temperatures measured using the thermocouples.

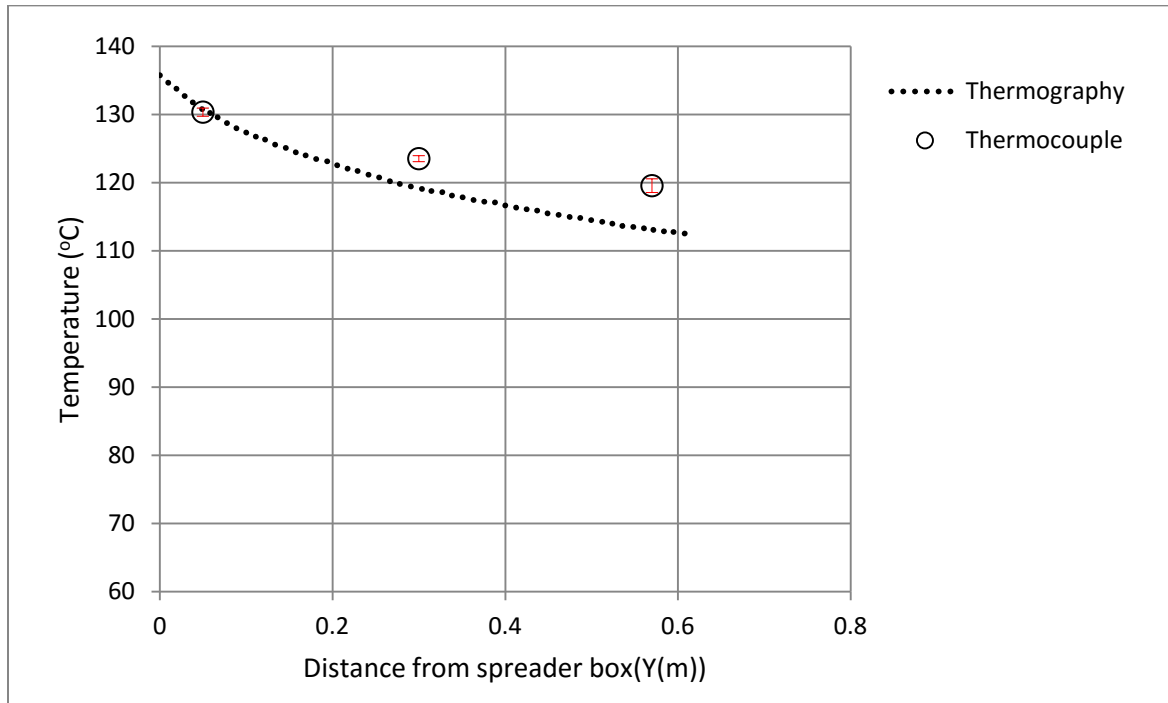


Figure 5.19: Infrared and thermocouple measurement comparison, $d_s=290\mu\text{m}$, $m^o_{infrared}=0.15\text{kg/s}$ and slot width=20mm

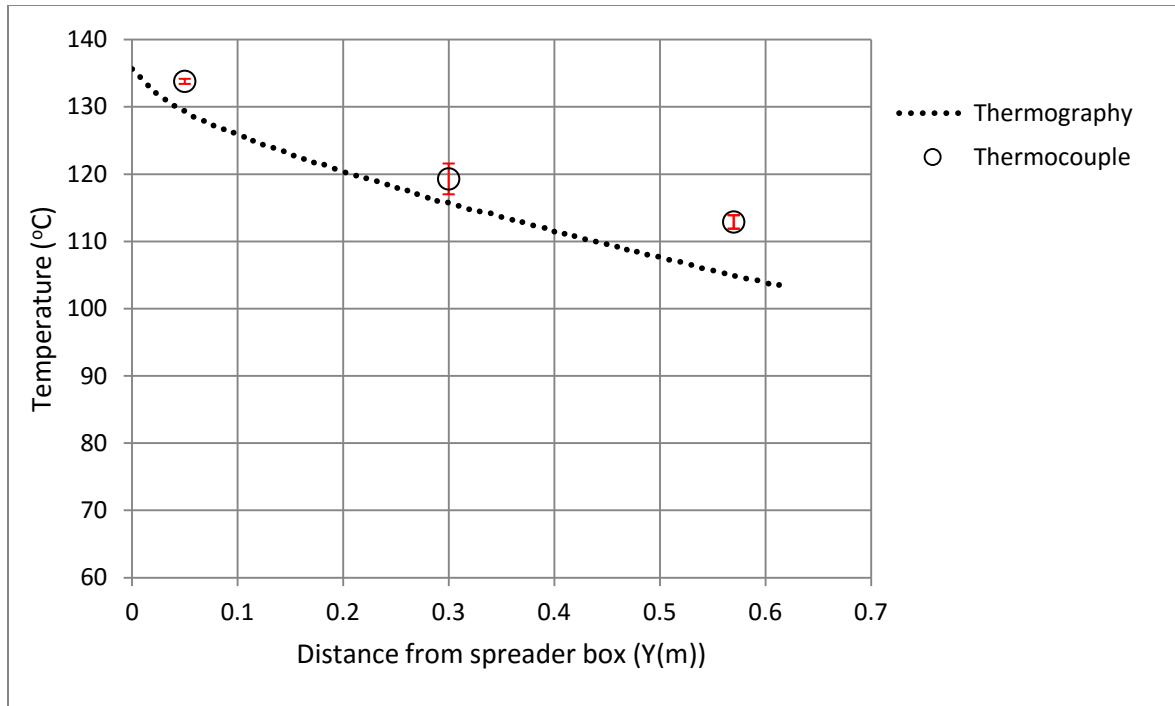


Figure 5.20: Infrared and thermocouple measurement comparison, $d_s=290\mu\text{m}$, $m^o_{infrared}=0.066\text{kg/s}$ and slot width=20mm

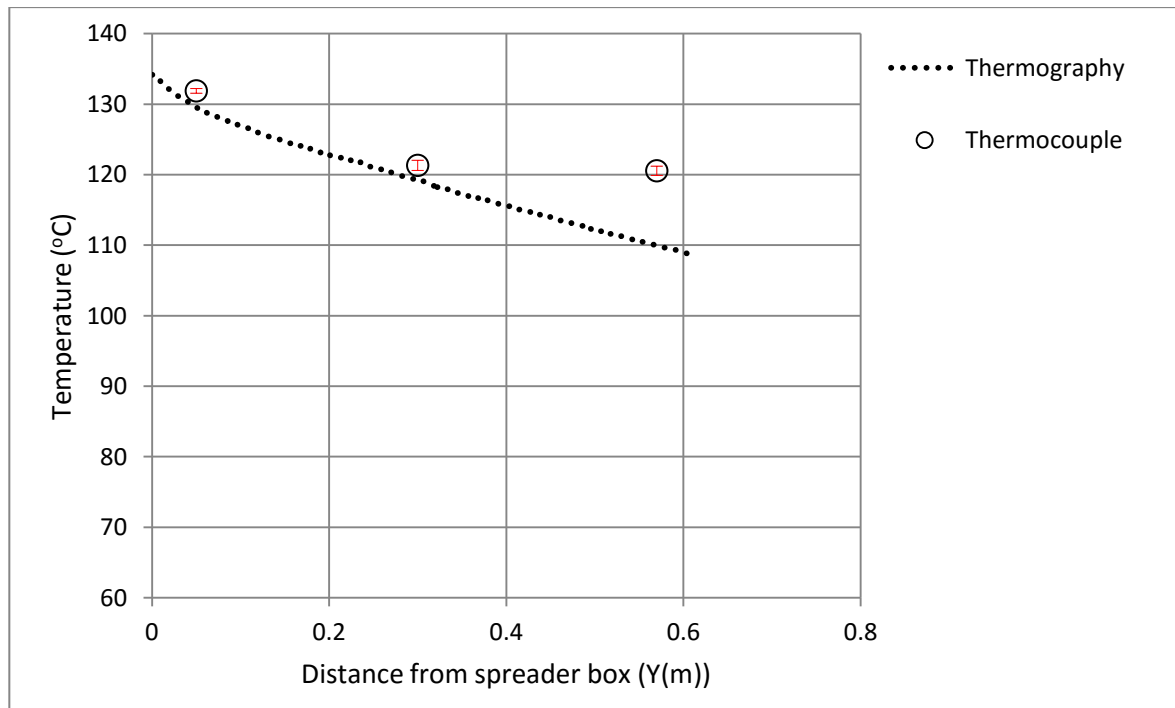


Figure 5.21: Infrared and thermocouple measurement comparison, $d_s=400\mu\text{m}$, $m^o_{infrared}=0.132\text{kg/s}$ and slot width=20mm

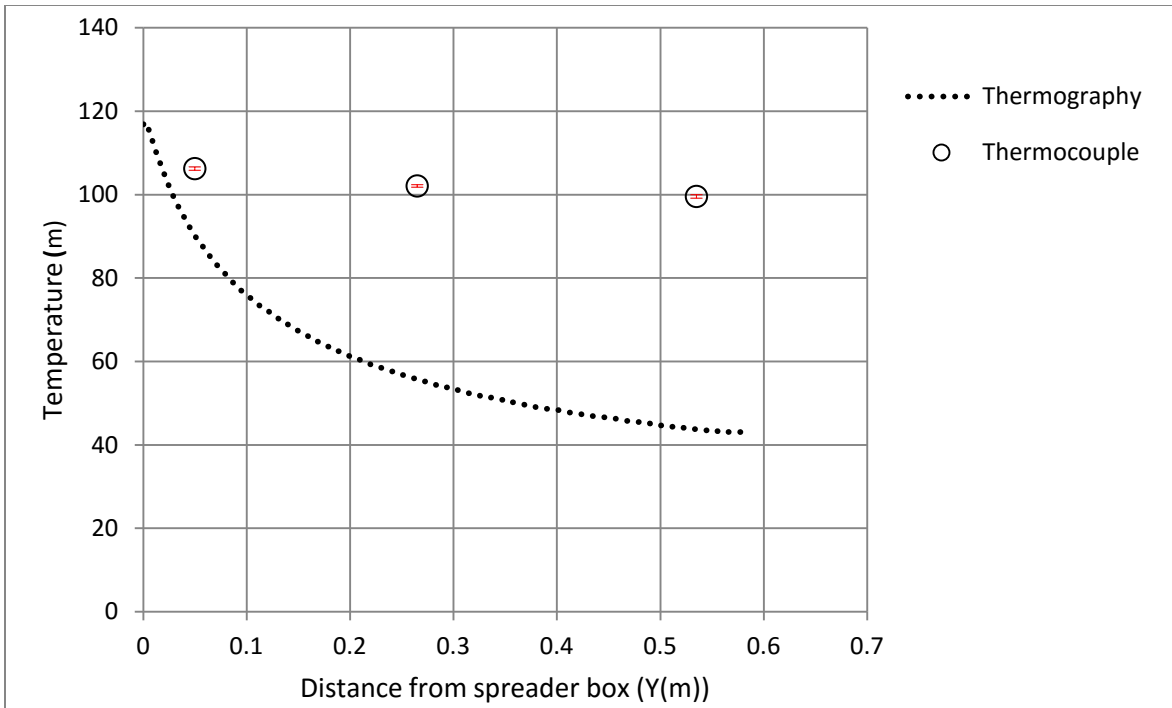


Figure 5.22: Infrared and thermocouple measurement comparison, $d_s=610\mu\text{m}$, $m^o_{infrared}=0.047\text{kg/s}$ and slot width=60mm

Figure 5.19 and 5.20 show consistent underestimation of the temperature using infrared thermography, despite there being a close agreement between infrared and thermocouple measurements for the smallest particles ($290\mu\text{m}$) at both high and low mass flow rates. Agreement between thermocouple and thermal imagery data deteriorates as particle size increases and solid volume fraction reduces. There is a substantial mismatch for the largest particles, at low mass flow rate and wide slot width. This situation expected to be the worst condition, and was anticipated to show the most influence of background temperature. This discrepancy suggests a deficiency in infrared measurements which is more pronounced for low solid volume fractions and large particle sizes. In the next section, a t-test analysis is carried out to examine the quality of match between thermocouple and infrared temperatures. The t-test is necessary to identify the location where the actual temperature and thermographic data do not match.

T-tests were carried out to compare the mean temperatures at the three locations (5cm, 30cm and 57cm). The null hypothesis in the t-test was that the mean temperatures calculated using the two techniques (infrared and direct thermocouple) were equal. The thermal images were exported to Matlab to calculate the averaged centreline temperature over the entire set of image frames. The bare tip of the thermocouple is 2.5mm which equals 3 pixels in the thermal image. The centreline temperatures from thermography, used to compare to direct thermocouple measurements, are the average of three pixels at about the centre of the curtain. Table 5.4 shows the results of the t-test (confidence interval=95%), calculated for averaged temperatures obtained from different conditions in Table 5.3.

Table 5.4: t-test results on infrared and thermocouple measurements

NO.	d_s (μm)	m^o in thermocouple technique (kg/s)	m^o in thermograph y technique (kg/s)	Slot width (mm)	Y(m), Distance down from the spreader box	Confidence interval	t – Stat	P-Two- tail	Is the null hypothesis rejected?
1	290	0.15	0.15	20	0.05	95%	2.14	2.2	No
2	290	0.15		20	0.3	95%	23.45	2.02	Yes
3	290	0.151		20	0.57	95%	12.38	2.17	Yes
4	290	0.068	0.066	20	0.05	95%	42.53	2.01	Yes
5	290	0.066		20	0.3	95%	6.94	2.07	Yes
6	290	0.071		20	0.57	95%	25.96	2.05	Yes
7	400	0.137	0.132	20	0.05	95%	18.46	2.06	Yes
8	400	0.131		20	0.3	95%	8.79	2.11	Yes
9	400	0.127		20	0.57	95%	10.77	2.07	Yes
10	610	0.045	0.047	60	0.05	95%	161.5	2.03	Yes
11	610	0.045		60	0.265	95%	587.23	2.01	Yes
12	610	0.045		60	0.535	95%	556.45	2.05	Yes

Table 5.4 shows that only in condition 1 are the thermocouple and infrared temperature means equal, because the null hypothesis is not rejected. In other conditions, there are significant deviations between infrared and thermocouple temperatures. Although this analysis likely underestimates the variance associated with obtaining repeat data at precise mass flow rates, which would result in improved match between measurement techniques. However, deviations are greatest in the large particle size (conditions 10-12) and low mass flow rate (conditions 4-6).

situations. It can be concluded that there is an apparent merging of the background temperature with the infrared temperature measurements. In the following section, a filtering process is derived in an attempt to improve the reliability of thermography as a tool to measure particles temperature in dilute two-phase systems.

5.3. Thermographic Filtering

At low solid volume fractions, and particularly for large particle sizes (i.e. $610\mu\text{m}$) where inter-particle distances are at their greatest, the (black) ambient background temperature occupies more spaces between the particles, reducing the captured temperatures. This is because at the same volume fraction, the visible surface area of small particles is higher than the visible surface area of large particles according to below calculations:

$$\alpha_{s1} = \alpha_{s2} \quad 5.2$$

$$n_1 V_1 = n_2 V_2 \quad 5.3$$

Given equivalent initial solid volume fractions for small (1) and large (2) particles, particle volumes are equivalent. Here, V_1 and n_1 are the volume and number of small particles and V_2 and n_2 are the volume and number of large particles.

Thus:

$$n_1 \times A_1 \times \frac{2}{3} \times D_1 = n_2 \times A_2 \times \frac{2}{3} \times D_2 \quad 5.4$$

where A_1 and A_2 are cross-sectional areas of each spherical particle.

If $D_2 > D_1$ then $n_1 A_1 > n_2 A_2$

Therefore, the cross-sectional area visible in a field occupied by small particles is greater than that occupied by large particles. In these situations, the (black) ambient background temperature occupies the spaces between the particles, influencing the captured temperatures. The background is merged with the particle temperature during the capturing and processing of the average temperature in each thermographic pixel. This will result in the particle temperature recorded with infrared thermography reading lower temperature than the particles actually experience, as illustrated in Figure 5.19 to 5.22.

Recent work by Patil et al. [94] on infrared thermography of narrow fluidised beds suggested that there is also a temperature blurring effect brought about by the hot particles themselves. In their research, undertaken at the micro-scale so as to precisely identify individual hot particles ($\sim 100^\circ\text{C}$), the researchers recognised a blurred region around each particle that showed an intermediate temperature between the particle and background temperatures. They filtered their raw data to remove the blurred regions around each particle, by introducing a threshold temperature between the background temperature and the assumed particle temperature. Any pixels less than the threshold temperature were reassigned to the background temperature. However, the blurred effect was more challenging to deal with in regions of low solid volume fraction. In these situations, they ignored the contribution of the particle, and reassigned the temperature to be that of the background.

A convenient model for each infrared thermographic pixel is illustrated in Figure 5.23, showing regions of true temperature, background temperature and blurred temperature surrounding each particle. In this work, a key assumption is that the visible image pixel intensity can be linearly correlated to the proportion of the total infrared image area occupied by the particles. Thus, when visible pixel intensity is high, the field of view is saturated with particles and when it is low the background dominates.

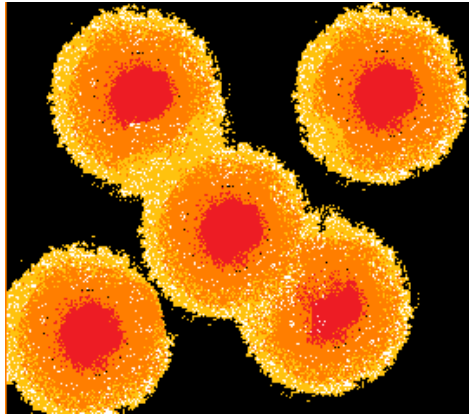


Figure 5.23: Illustration of the blurred temperature (T_{bl}) in orange, particle true temperature (T_t) in red and background temperature (T_b) in black in a single thermographic pixel

5.4. Visible Image Pixel Intensity

In the previous section it was mentioned that the influence of background is important in thermography. In order to quantify the proportion of background and particles, visible imagery is required. In combination with infrared thermography, visible photography can be used as a tool to quantify solids volume fraction. In the literature, visible image pixel intensities are often assumed to be directly proportional to solid volume fractions, particularly at low volume fractions and for short depths of field [104]. Figure 5.24 shows typical examples of thermocouple measurements, infrared temperature profiles as well as the corresponding visible image pixel intensity profiles for

small and large particle size examples. Figure 5.24(a) shows that for a proportion of the temperature profile there is a good match between thermocouple and infrared, and for those corresponding magnitudes of visible pixel intensity, there is no influence of the background. However, in the later stages of the profile, the infrared temperature profile deviates away from thermocouple data and the infrared thermographic temperature data reduces in comparison. In this work, the precise location (i.e. visible image intensity) where deviation begins, is defined as the *critical visible image pixel intensity*. Figure 5.24(b) shows an example of a situation where there is big discrepancy between the thermocouple and infrared thermography data ($610\mu\text{m}$, 0.047kg/s). Note that in this situation, the visible image pixel intensity is much lower and follows a different profile shape.

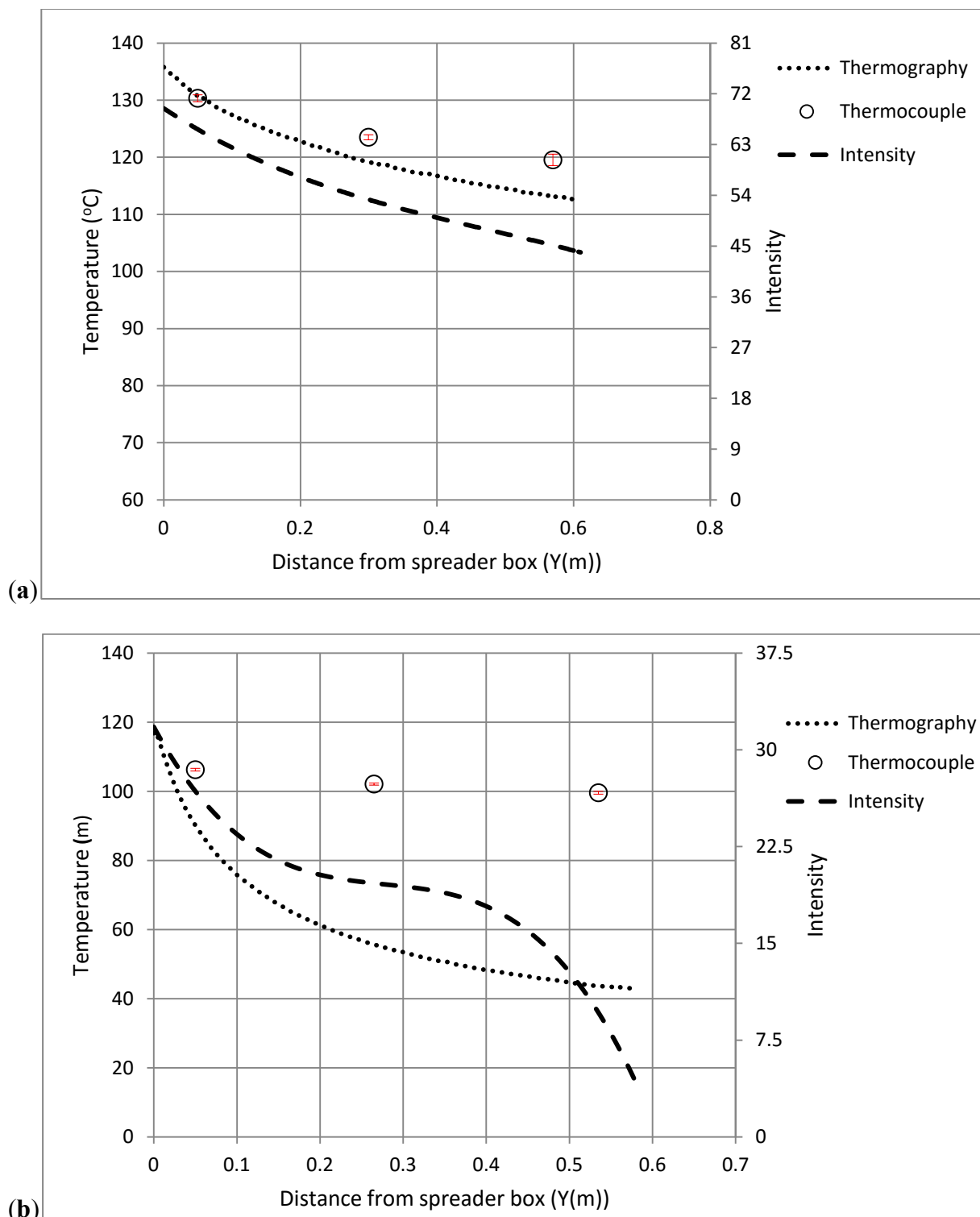


Figure 5.24: Thermocouple and infrared temperatures along with particle pixel intensities calculated from visible photography (a) $d_s=290\mu\text{m}$, $m^o_{infrared}=0.15\text{kg/s}$ and slot width=20mm (b) $d_s=610\mu\text{m}$, $m^o_{infrared}=0.047\text{kg/s}$ and slot width=20mm

5.5. Thermographic Models

In this research, a series of theoretical models have been developed and tested for their capability to decouple the effects of background and blurred temperature on the true particle temperature. In the most complex model, it was assumed that the temperatures recorded by the infrared camera are a linear combination of blurred temperature (T_{bl}), particle true temperature (T_t) and background temperature (T_b). Referring to Figure 5.23, in this model, conceptualisation temperature in each pixel, as recorded by the infrared camera, is an area weighted average of the three contributing temperatures (Equation 5.5).

$$T_{IR} = \frac{A_s \times T_t}{A_{total}} + \frac{A_{bl} \times T_{bl}}{A_{total}} + \frac{A_b \times T_b}{A_{total}} \quad 5.5$$

where A_s is the area of particle, A_{bl} is the blurred area around each particle, A_b is the area of background, and A_{total} is the area of each pixel.

Assuming that the visible image pixel intensity is linearly correlated to the proportion of the total infrared image area occupied by the particles, area relations are replaced by intensity.

$$\frac{A_s}{A_{total}} = \frac{I}{I_{critical}} \quad 5.6$$

where I is the pixel intensity of particles, and $I_{critical}$ is the critical pixel intensity where thermocouple and thermographic temperatures vary significantly.

To account for uncertainties in the model, description of the blur temperature, the blurred area around each particle was assumed to be a fixed proportion (γ) of the particle area (Equation 5.4):

$$A_{bl} = \gamma \times A_s$$

5.7

Furthermore, the blurred temperature was also assumed to be a fixed proportion (δ) of particle true temperature (Equation 5.8):

$$T_{bl} = \delta \times T_t \quad 5.8$$

The area of the background in each pixel is calculated via Equation 5.9:

$$A_b = A_{total} - A_s - A_{bl} \quad 5.9$$

By substitution, the recorded infrared temperature (T_{IR}) can be expressed as a function of the true or actual particle temperature (T_t) and the background temperature (Equation 5.10).

$$T_{IR} = \frac{A_s}{A_{total}} T_t + \frac{A_s}{A_{total}} \gamma \delta \times T_t + [1 - \frac{A_s}{A_{total}} (1 + \gamma)] \times T_b \quad 5.10$$

5.5.1. Model 1 verification

Eleven sets of comparative thermocouple and infrared data were modelled using Equation 5.10 to estimate the true particle temperature. In each data set, γ and δ are model parameter values. In order to estimate $\frac{A_s}{A_{total}}$, via Equation 5.6, it is necessary to define a value for $I_{critical}$.

Using the t-test results from Section 5.2.2, and noting that only condition 1 ($d_s=290\mu\text{m}$, $m^o_{infrared}=0.15\text{kg/s}$) statistically demonstrated mean temperatures from the two techniques being equal, a single value for $I_{critical}$ was established. To calculate this value, the discrete thermocouple temperatures were interpolated using Matlab. Figure 5.25 shows the comparison of interpolated thermocouple data and infrared profiles.

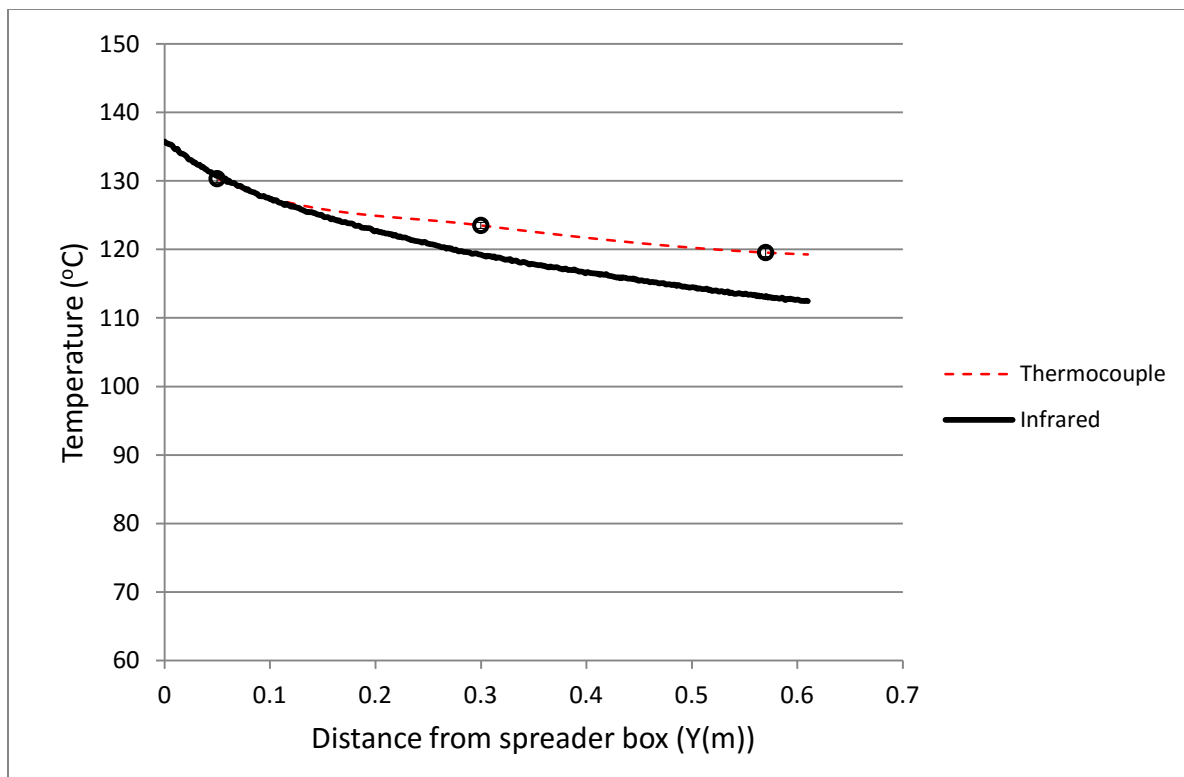


Figure 5.25: Interpolated thermocouple temperature in comparison to centreline infrared temperatures ($d_s=290\mu\text{m}$, $m^o_{infrared}=0.15\text{kg/s}$ and slot width=20mm)

The critical intensity was selected at the location where there was 1°C difference between two temperature profiles. 1°C temperature difference was based on the average margin of error for all three thermocouple data points.

Under these circumstances, the calculated visible critical pixel intensity was 59.6, 0.15m down from the spreader box exit. This value was utilised in model 1 for all 11 comparative data points (Table 5.4).

Substitution of known values (T_{IR} , T_t , $\frac{I}{I_{critical}}$ and T_b) into each data set via Equation 5.10, resulted in 11 equations shown in Table 5.5.

Table 5.5: Derived equations corresponding to Table 5.4 conditions

NO.	Equations
2	$6.5 - 109.92\gamma\delta + 22.25\gamma = 0$
3	$17.17 - 89.66\gamma\delta + 18.75\gamma = 0$
4	$9.764 - 116.4\gamma\delta + 21.75\gamma = 0$
5	$24.646 - 83.5\gamma\delta + 17.5\gamma = 0$
6	$24.6 - 71.12\gamma\delta + 15.75\gamma = 0$
7	$1.95 - 126.62\gamma\delta + 24\gamma = 0$
8	$21.85 - 91\gamma\delta + 18.75\gamma = 0$
9	$22.82 - 78.37\gamma\delta + 16.25\gamma = 0$
10	$29.4 - 46.75\gamma\delta + 11\gamma = 0$
11	$5.29 - 33.68\gamma\delta + 8.25\gamma = 0$
12	$-2.39 - 16.92\gamma\delta + 4.25\gamma = 0$

To test the validity of the conceptualised model, optimisations to estimate γ and δ were performed.

A Matlab procedure (Appendix B.3) was used to minimise the sum of squared errors for all the eleven equations. Optimal values for γ and δ parameters were pre-defined to be in the range 0 to 1, in agreement with the theoretical descriptions of γ and δ in Equation 5.10. The optimised values of γ and δ were 0 and 0.19 respectively, but illustrated a very poor fit to the data set.

To assess the model validity further, all possible pairwise sets of data were solved directly for γ and δ . The 55 pairs of equations were solved in Matlab without constraining the values of γ and δ . The distribution of γ and δ compared to their means is shown in Figure 5.26. Because of the

substantial inconsistency in the predicted model constants, a simplified model of the thermographic temperature (referred to as model 2) was developed.

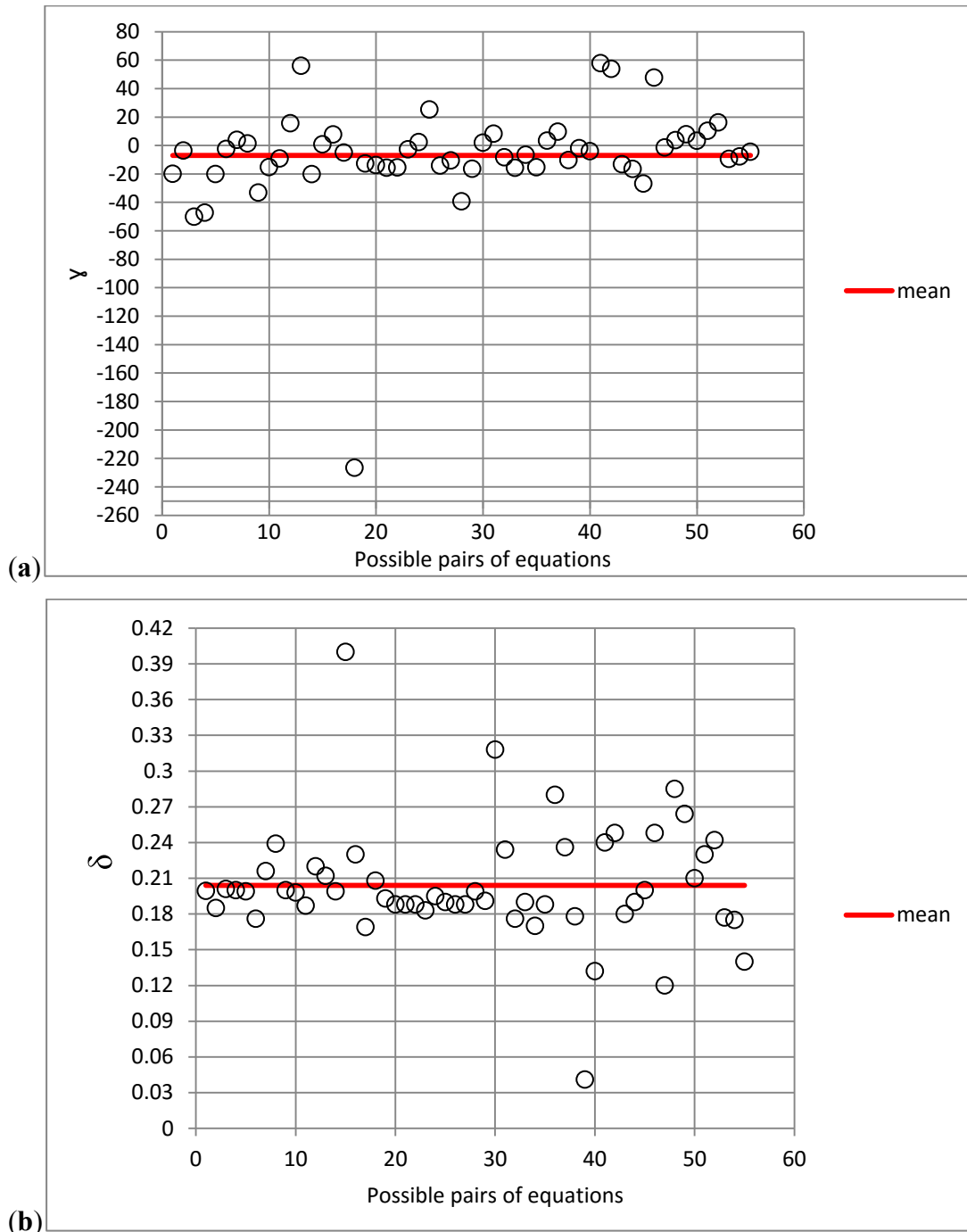


Figure 5.26: Distribution of γ and δ values compared to their mean values (a) γ values (b) δ values

5.5.2. Model 2

In model 2, the infrared thermal data is assumed to be only a blend of the particle temperature measured via thermocouple, and the background ambient temperature (i.e. ignores the blurred temperature contribution). These thermal influences were again assumed to vary in proportion to the visible image pixel intensity (Equation 5.11)

$$T_{IR} = \frac{A_s}{A_{total}} T_t + [1 - \frac{A_s}{A_{total}}] T_b \quad 5.11$$

where $\frac{A_s}{A_{total}}$ is approximated by visible image intensity ratio ($\frac{I}{I_{critical}}$).

In this model, there are two critical uncertainties. The first is the selection of $I_{critical}$ and whether this property is independent of system conditions such as particle size. The second uncertainty is whether there is a 1:1 correlation between $\frac{A_s}{A_{total}}$ and $\frac{I}{I_{critical}}$. Whilst it is clear that these two ratios are correlated, it is not clear that a decrease in $\frac{I}{I_{critical}}$ throughout particles fall would lead to precisely the same decrease in $\frac{A_s}{A_{total}}$. These issues are explained in the following section.

5.5.3. Model 2 verification

Figure 5.27 shows an example of modelled infrared temperature using Equation 5.11 with $I_{critical}$ defined as before (Section 5.5.1): $I_{critical}=59.6$.

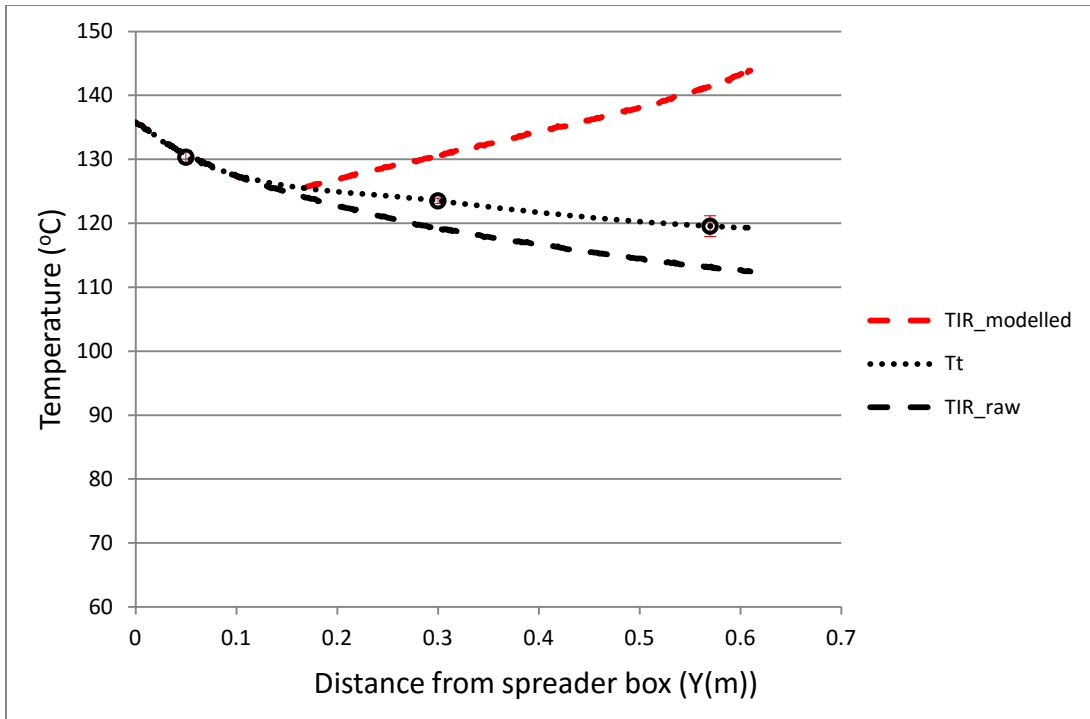


Figure 5.27: Comparison of modelled infrared, raw infrared and thermocouple temperature using Equation 5.8, $d_s=290\mu\text{m}$, $m^o_{infrared}=0.15\text{kg/s}$, slot width=20mm and and $I_{critical}=59.6$

Application of Equation 5.11 results in an increasing temperature trend which indicates that a 1:1 correlation between visible pixel intensity and area in Equation 5.11 is too strong. To reduce the relative influence of visible pixel intensity, the gradient of visible pixel intensity curve is scaled linearly as follows. Generally, the gradient at each point ($i+1$) on the visible pixel intensity curve can be defined in a piecewise manner via Equation 5.12, where Y is distance vertically down the spreader box exit.

$$\frac{dI}{dY} \Big|_{i+1} = \frac{I_{i+1} - I_i}{Y_{i+1} - Y_i} = I_{i+1} - I_i \quad 5.12$$

Note that, the difference between successive data points (i and $i+1$) in the Y direction is equal to 1 pixel. To reduce the influence of $\frac{I}{I_{critical}}$, the gradient of intensity curve is scaled using an adjustable parameter (x'), such that intensity values past $I_{critical}$ can be predicted. Figure 5.28 illustrates the effect of varying x' values on the intensity profile. When $x'=1$ is used, the profile is unchanged and when $x=0$ is used the profile remains flat at $I_{critical}$.

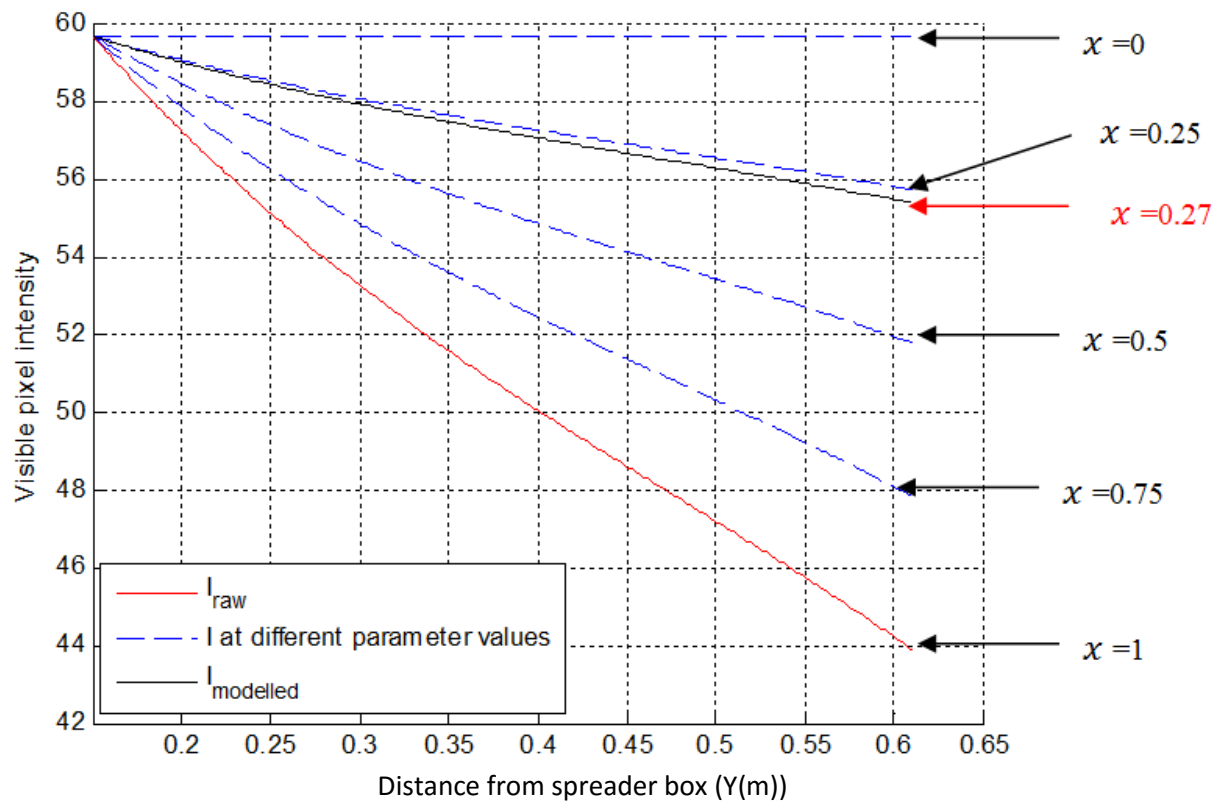


Figure 5.28: Visible pixel intensity calculated at different x parameter values, $d_s=290\mu\text{m}$, $m^o_{infrared}=0.15\text{kg/s}$, slot width=20mm, $I_{critical}=59.6$ and $Y=0.15\text{m}$

Figure 5.29 illustrates the effect on the predicted particle temperature, of varying the scaling parameter (x'). In this example ($I_{critical} = 59.6$), the best fit to thermocouple data occurs when the intensity is scaled to 27%.

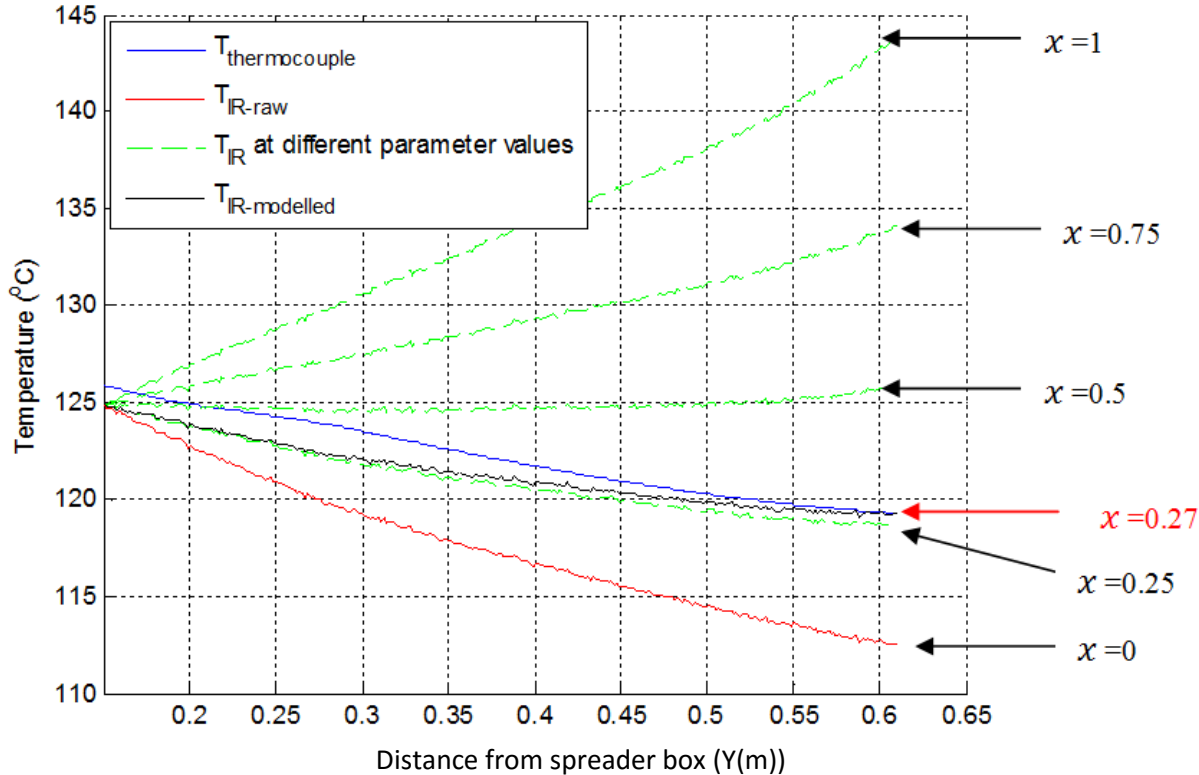


Figure 5.29: Infrared temperature at different x' parameter values compared to thermocouple temperature, $d_s=290\mu\text{m}$, $m^o_{infrared}=0.15\text{kg/s}$, slot width=20mm, $I_{critical}=59.6$ and $Y=0.15\text{m}$

Matlab was used (Appendix B.4) to parameter estimate for x' in order to obtain the best fit between the infrared and thermocouple measurements. The objective function minimised was defined as the average sum of squares differences between the discrete thermocouple data points and the predicted true temperature.

The critical visible pixel intensities ($I_{critical}$) and intensity scaling parameter (x') were calculated separately for each different particle size (290 μm , 400 μm and 610 μm). As a result of simulations in the intensity profiles for both runs at 290 μm particle size, an average $I_{critical}$ was applied across

all 290 μm data sets. Furthermore, both experimental runs at 290 μm particle size were used simultaneously to optimise for generic value for the scaling parameter.

For each experimental run, $I_{critical}$ was defined as the visible image intensity at the location where the thermocouple and thermography data were qualitatively observed to vary significantly. Figure 5.30 to 5.33 shows the infrared thermocouple profiles and thermocouple data and the selected $I_{critical}$ locations. Figure 5.34 to 5.37 show the predicted particle temperatures for these parameter values.

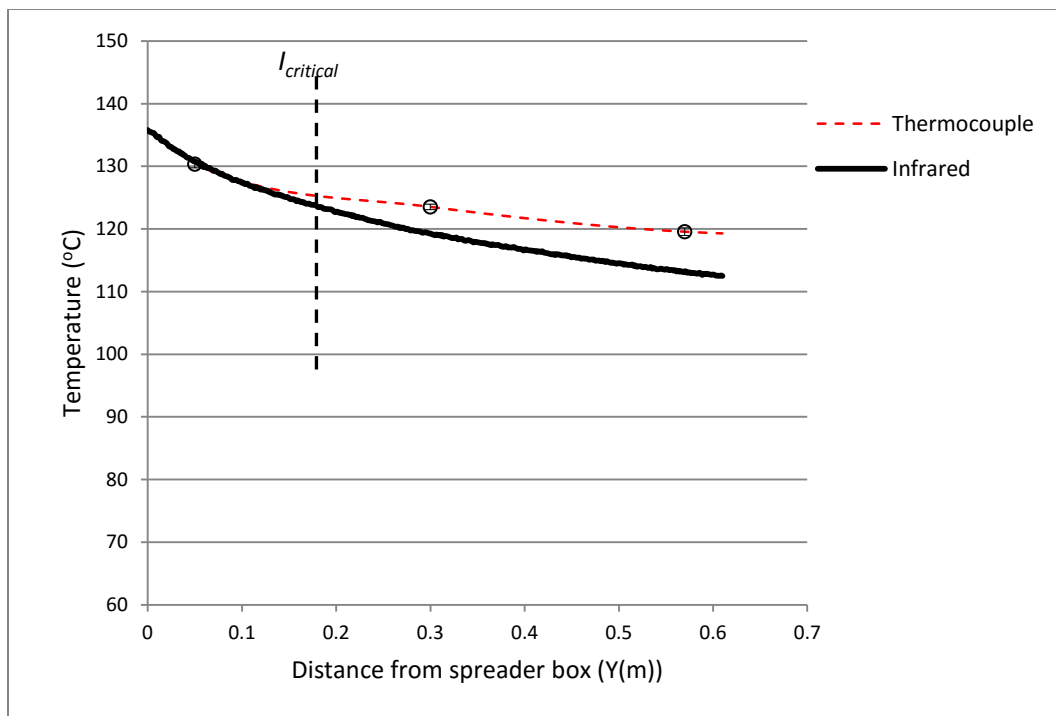


Figure 5.30: Comparison of thermocouple temperature and infrared temperature, $d_s=290\mu\text{m}$, $m^o_{infrared}=0.15\text{kg/s}$ and slot width=20mm

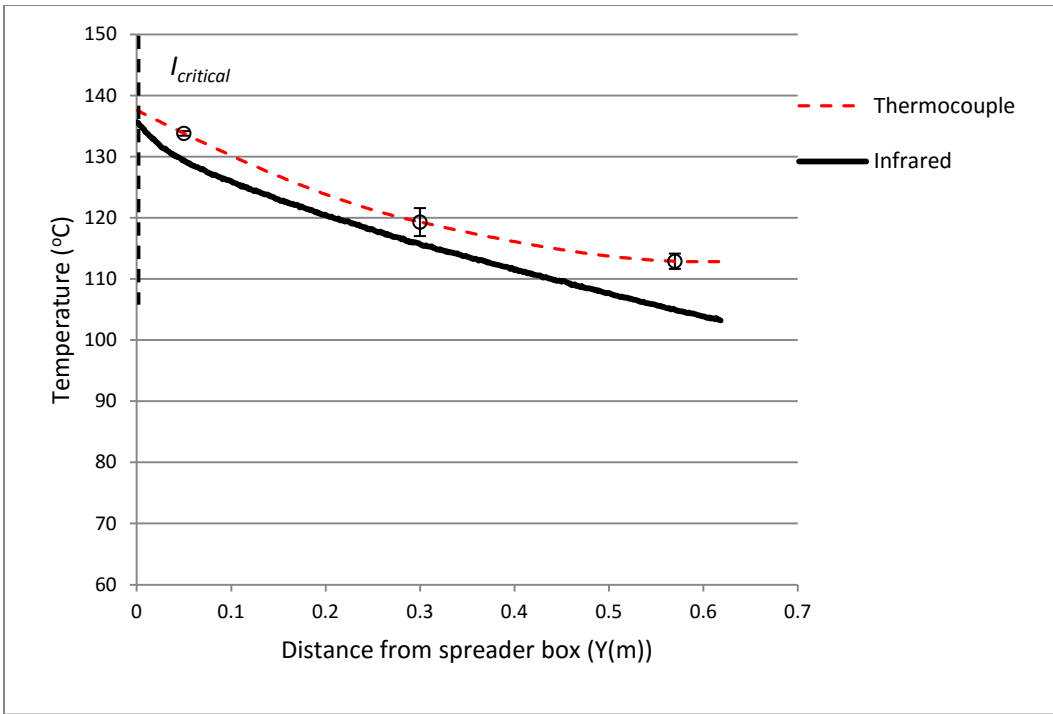


Figure 5.31: Comparison of thermocouple temperature and infrared temperature, $d_s=290\mu\text{m}$, $m^o_{infrared}=0.066\text{kg/s}$ and slot width=20mm

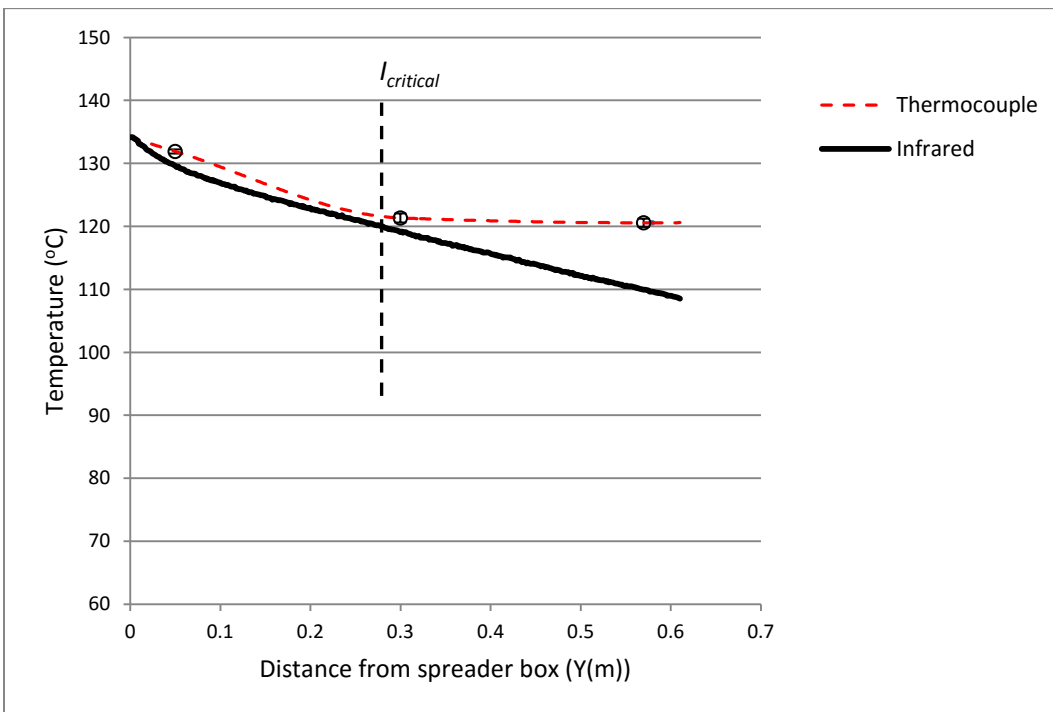


Figure 5.32: Comparison of thermocouple temperature and infrared temperature, $d_s=400\mu\text{m}$, $m^o_{infrared}=0.132\text{kg/s}$ and slot width=20mm

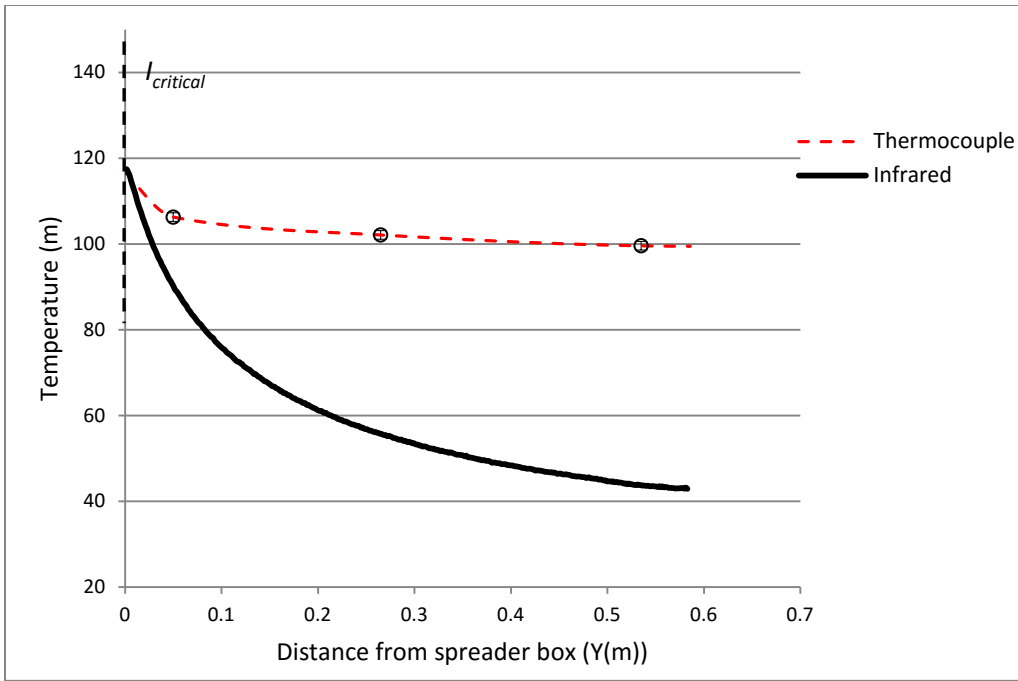


Figure 5.33: Comparison of thermocouple temperature and infrared temperature, $d_s=610\mu\text{m}$, $m^o_{infrared}=0.047\text{kg/s}$ and slot width=20mm

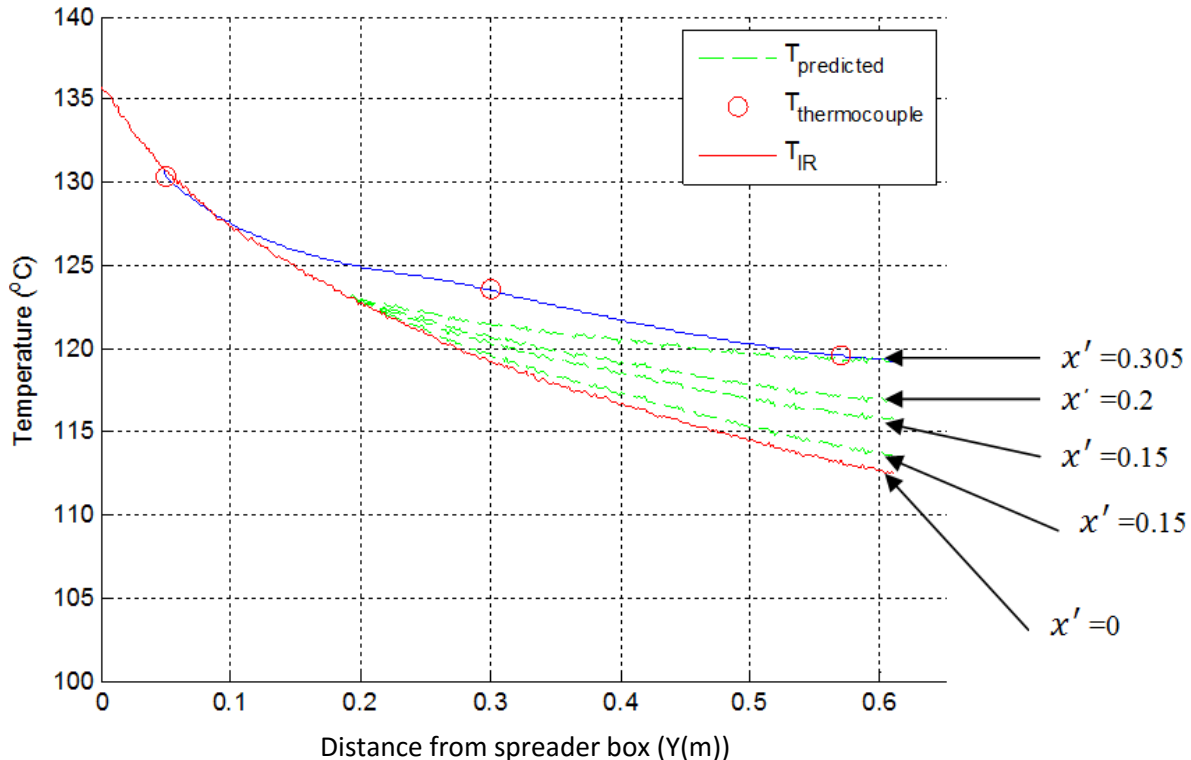


Figure 5.34: Infrared temperature at different x' parameter values compared to thermocouple, $d_s=290\mu\text{m}$, $m^o=0.15\text{kg/s}$ and slot width=20mm, $I_{critical}=57.6$ and $Y=0.19\text{m}$

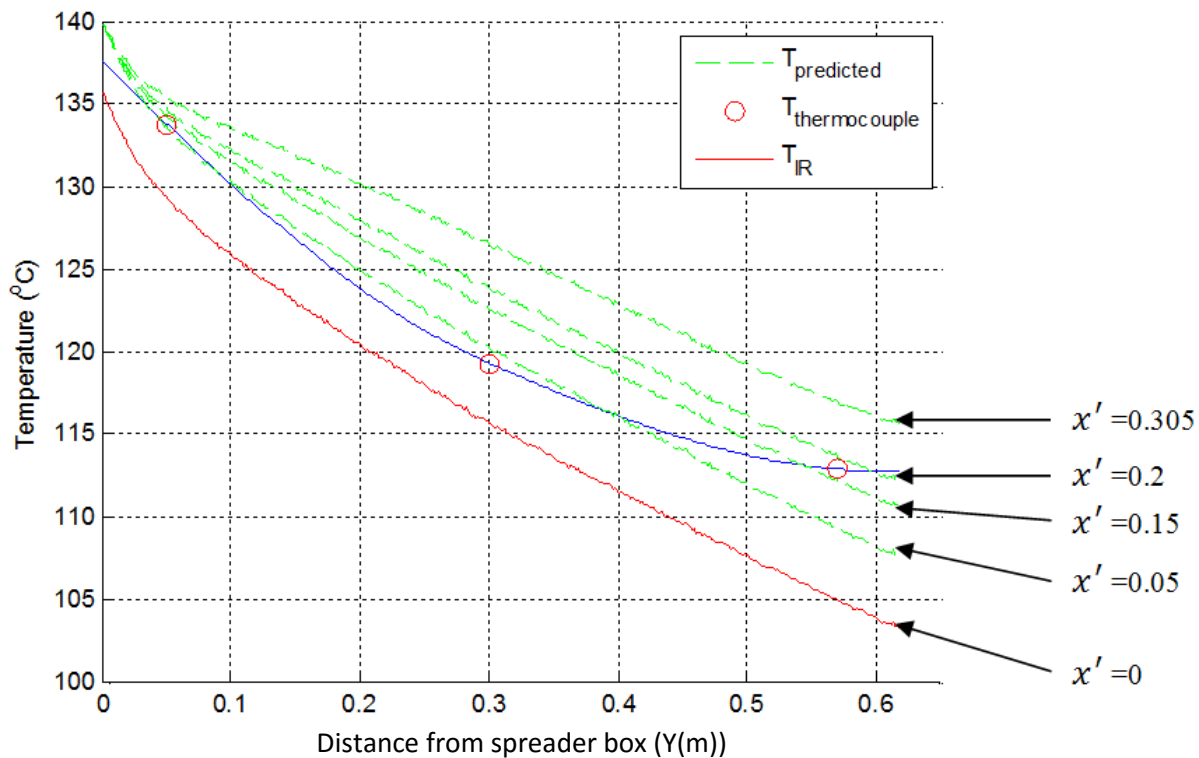


Figure 5.35: Infrared temperature at different x' parameter values compared to thermocouple, $d_s=290\mu\text{m}$, $m^o=0.066\text{kg/s}$ and slot width=20mm, $I_{critical}=57.6$ and $Y=0\text{m}$

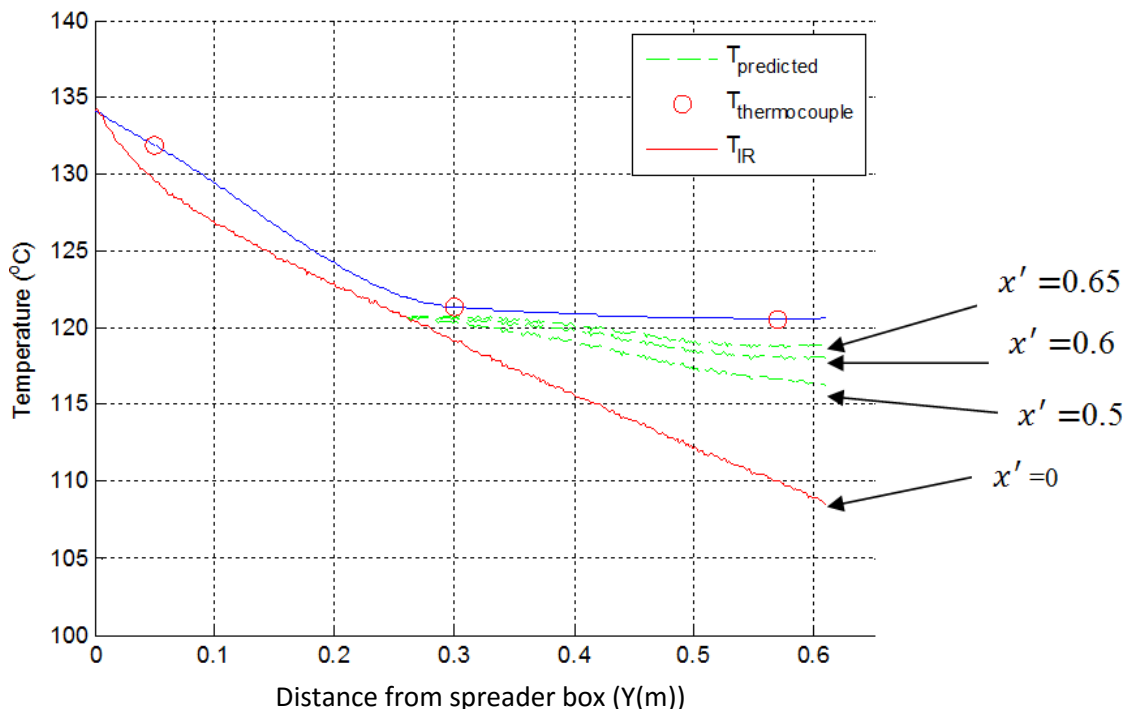


Figure 5.36: Infrared temperature at different x' parameter values compared to thermocouple, $d_s=400\mu\text{m}$, $m^o_{infrared}=0.132\text{kg/s}$ and slot width=20mm, $I_{critical}=45.9$ and $Y=0.26\text{m}$

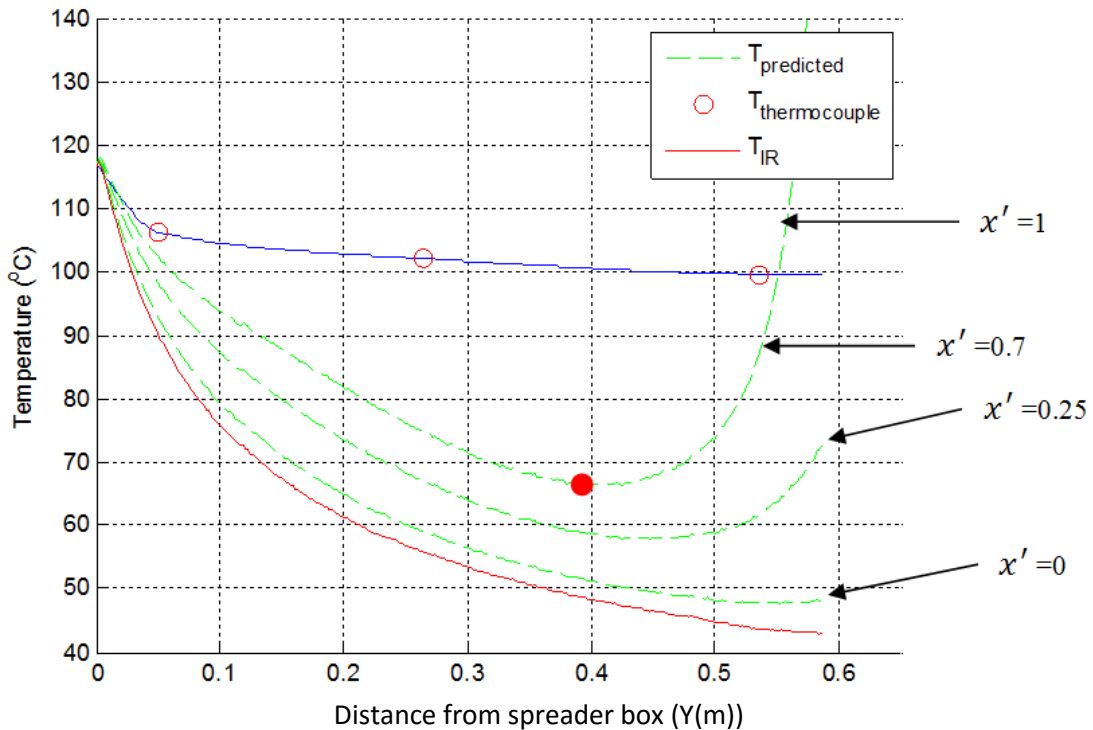


Figure 5.37 Infrared temperature at different x' parameter values compared to thermocouple, $d_s=610\mu\text{m}$, $m^o_{infrared}=0.047\text{kg/s}$ and slot width=60mm, $I_{critical}=45.9$ and $Y=0\text{m}$

Final optimised parameter values for $I_{critical}$ and x' are shown in Table 5.6 for each particle size.

These values are applied in Chapter 6 to adjust thermographic temperature profiles.

Table 5.6: Critical visible pixel intensities and x' parameters at different particle sizes

Particle size (d_s)	Critical pixel intensity ($I_{critical}$)	x' parameter	Average error
290 μm	57.6	0.20	2%
400 μm	45.9	0.65	1.3%
610 μm	31.8	1.00	3%

Figure 5.37 demonstrates the difficulty adjusting infrared thermographic data in situations of very low volume fractions ($y>0.4\text{m}$). This is assumed to be related to the very low visible image pixel intensities in this region. In addition, the visible image pixel intensity profile for the largest particle

size ($610\mu\text{m}$) is substantially different to that of the smaller particle sizes (see Figure 5.38). In the large particle size situations, there is a point past which the temperature profiles become unpredictable, primarily because of the lack of particles in the field of view.

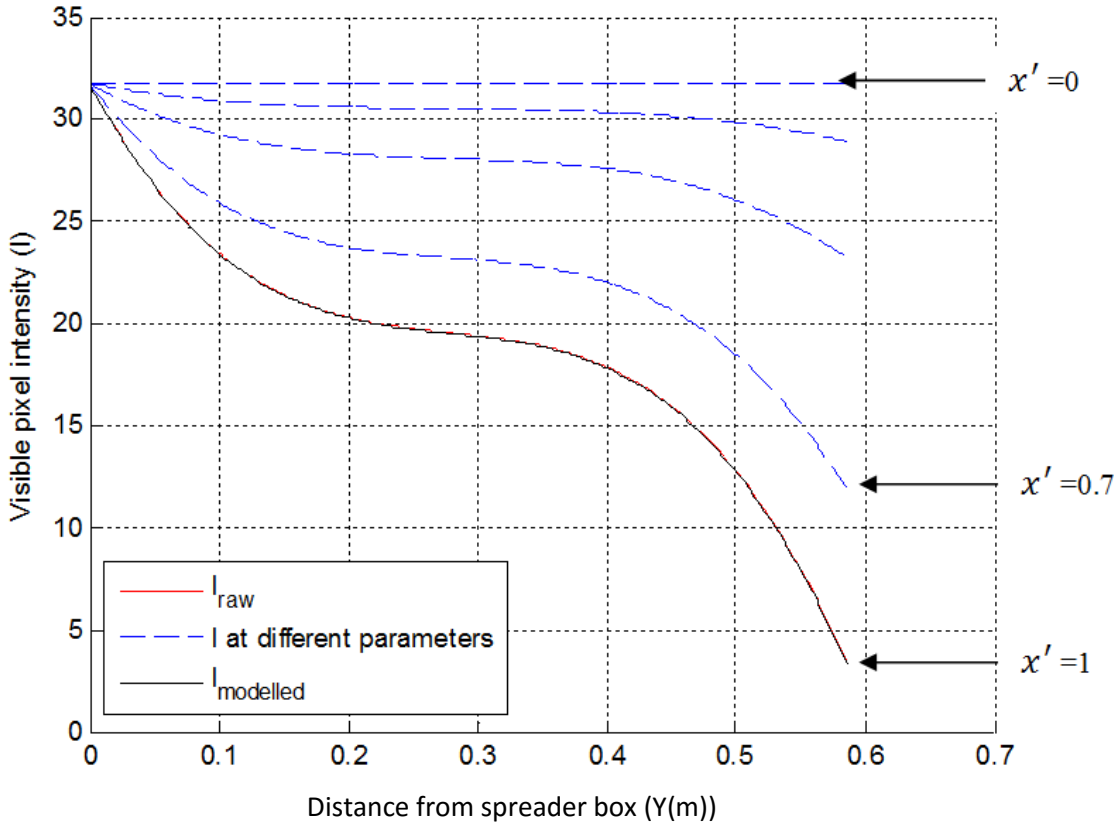


Figure 5.38: Visible pixel intensity at different x' parameter values, $d_s=610\mu\text{m}$, $m^o_{infrared}=0.047\text{kg/s}$, slot width=20mm, $I_{critical}=31.8$ and $Y=0\text{m}$

5.6. Data Processing for Curtain Edge Detection

In image analysis, an edge point is often defined as the location of a local intensity change, typically a change in visible image pixel intensity. The gradient based edge detection technique detects the edges by looking for the maximum in the first derivative of the image intensity [105]. The first derivative is computed based on the pixel intensity in one of the coordinate directions (typically x direction).

In Chapter 3, a gradient technique, based on the gradient of solid volume fraction was successfully used to identify the edges of the particle curtain generated using CFD simulations. In this section, a similar methodology is applied to the 2D infrared thermal images. However, in this methodology, edge detection is based on the gradient of temperature (in the x direction) in order to identify curtain edges from infrared thermography data.

5.6.1. Methodology

In this research, the temperatures of particles are very high (approximately 140°C) compared to the temperature of the ambient air (approximately 25°C). Thus, maxima in the temperature gradient are expected to occur at the edge the particle curtain where there is a sudden temperature change between the hot particle curtain and air temperature. Calculation of the location of the maxima leads to identification of particle curtain edges. The procedures for identifying the edge of the curtain in thermal images are described as follows. An example of the hot particle curtain thermal image is illustrated in Figure 5.39.

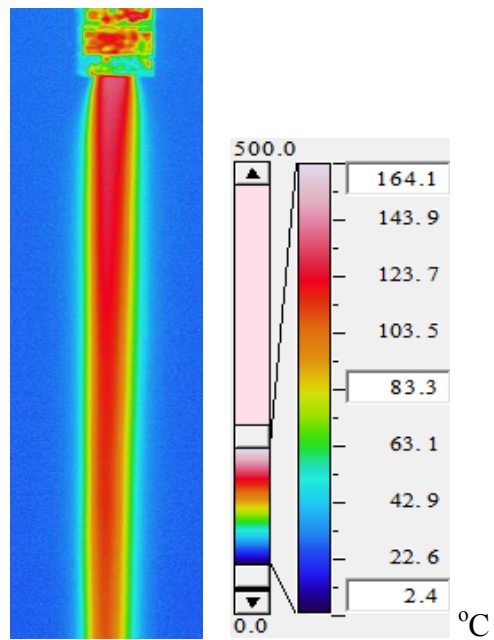


Figure 5.39: Thermal image of a hot particle curtain, $d_s=290\mu\text{m}$, $m^o=0.066\text{kg/s}$ and slot width=20mm

Figure 5.40 shows the corresponding particle curtain temperature profiles in the thermal image throughout the entire height of the particle curtain, plotted versus the width of the particle curtain. To facilitate numerical differentiation of this temperature data, a “Gaussian Kernel” function ($\text{Sigma}=1$ and $\text{Kernel size}=\text{Sigma}\times 6$) was used to smooth the raw temperature profiles.

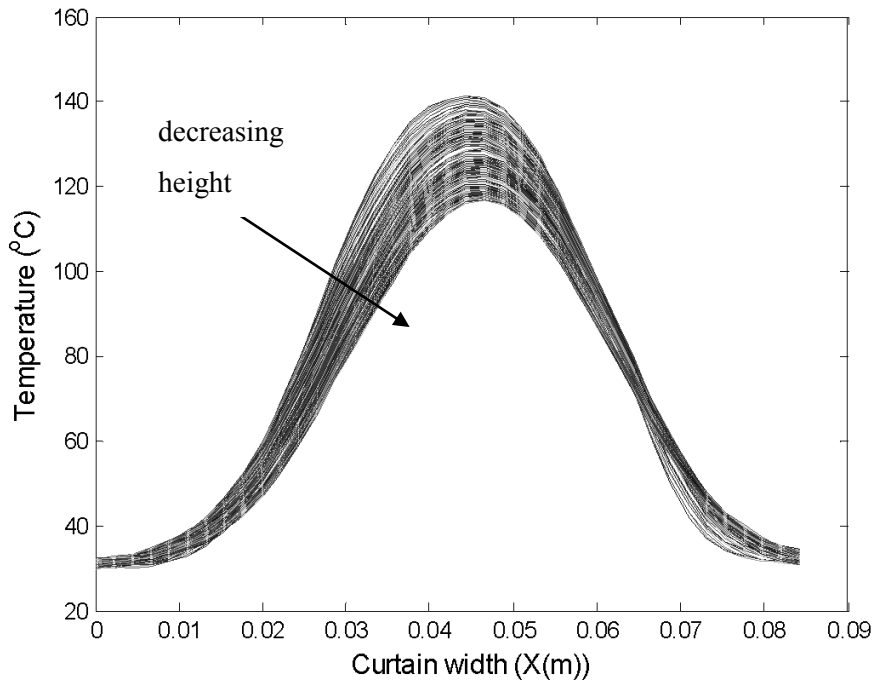


Figure 5.40: Raw data temperature profiles, $d_s=290\mu\text{m}$, $m^o=0.066\text{kg/s}$ and slot width=20mm

The smoothed temperature data was differentiated with respect to width using the “gradient” function in Matlab, which utilises a forward difference approach. Figure 5.41 shows the gradient profiles corresponding to raw temperature profiles in Figure 5.40.

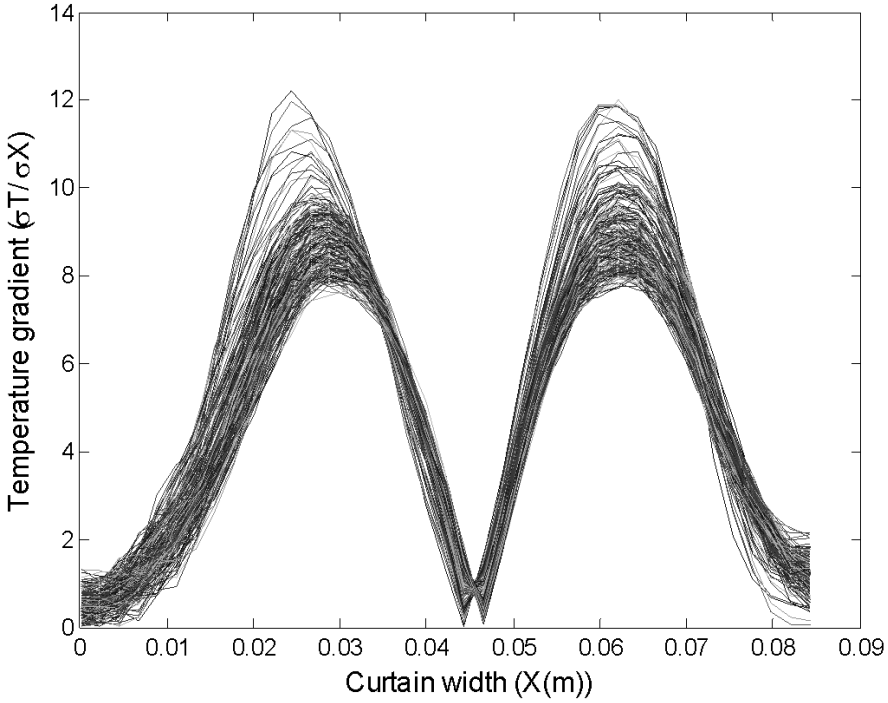


Figure 5.41: Temperature gradient profiles, $d_s=290\mu\text{m}$, $m^o=0.066\text{kg/s}$ and slot width=20mm

Figure 5.41 shows that the temperature gradients are not as smooth as the temperature profiles. This is because the temperature profiles are smoothed with low sigma values in the Gaussian function. Smoothing with higher sigma values attenuates the temperature gradient values and causes loss of data in the smoothing process. With low sigma values, the profiles are smoothed while retaining as much actual data as possible. In Figure 5.41, two maxima can be clearly seen, which correspond to the location of the curtain edges. A Matlab code was used to identify maxima at each height and their corresponding x locations. The details of the edge detection Matlab program can be found in Appendix B.2.

To obtain precise location of curtain edges, a quadratic polynomial was fitted to discrete temperature gradient data around each identified maximum. To generate the polynomial function, two extra points, one on the right side and one on the left side of the maxima, were included.

Figure 5.42 shows an example of the identification of the three points, including the maxima point and points on either side used to generate the polynomial.

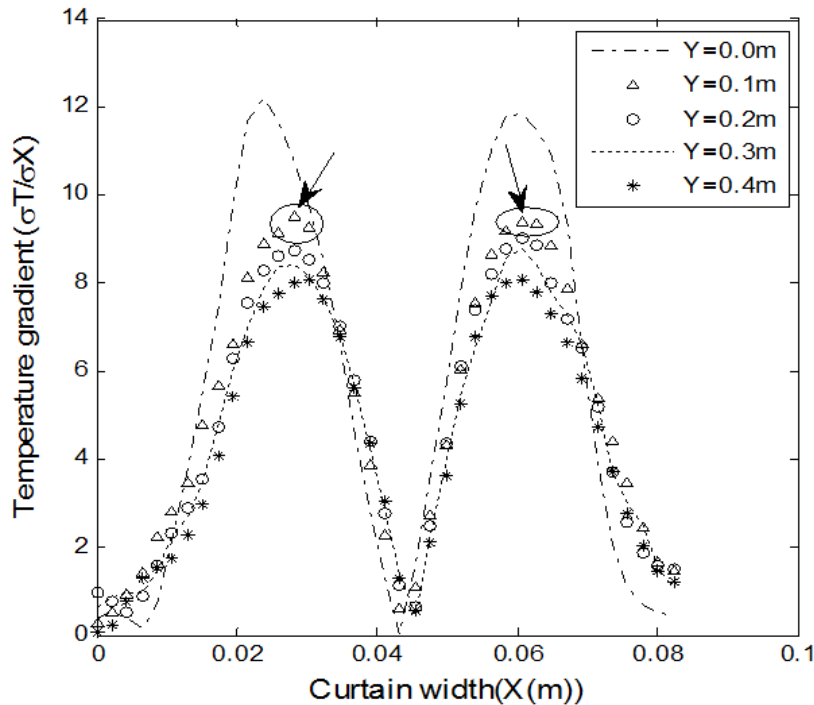
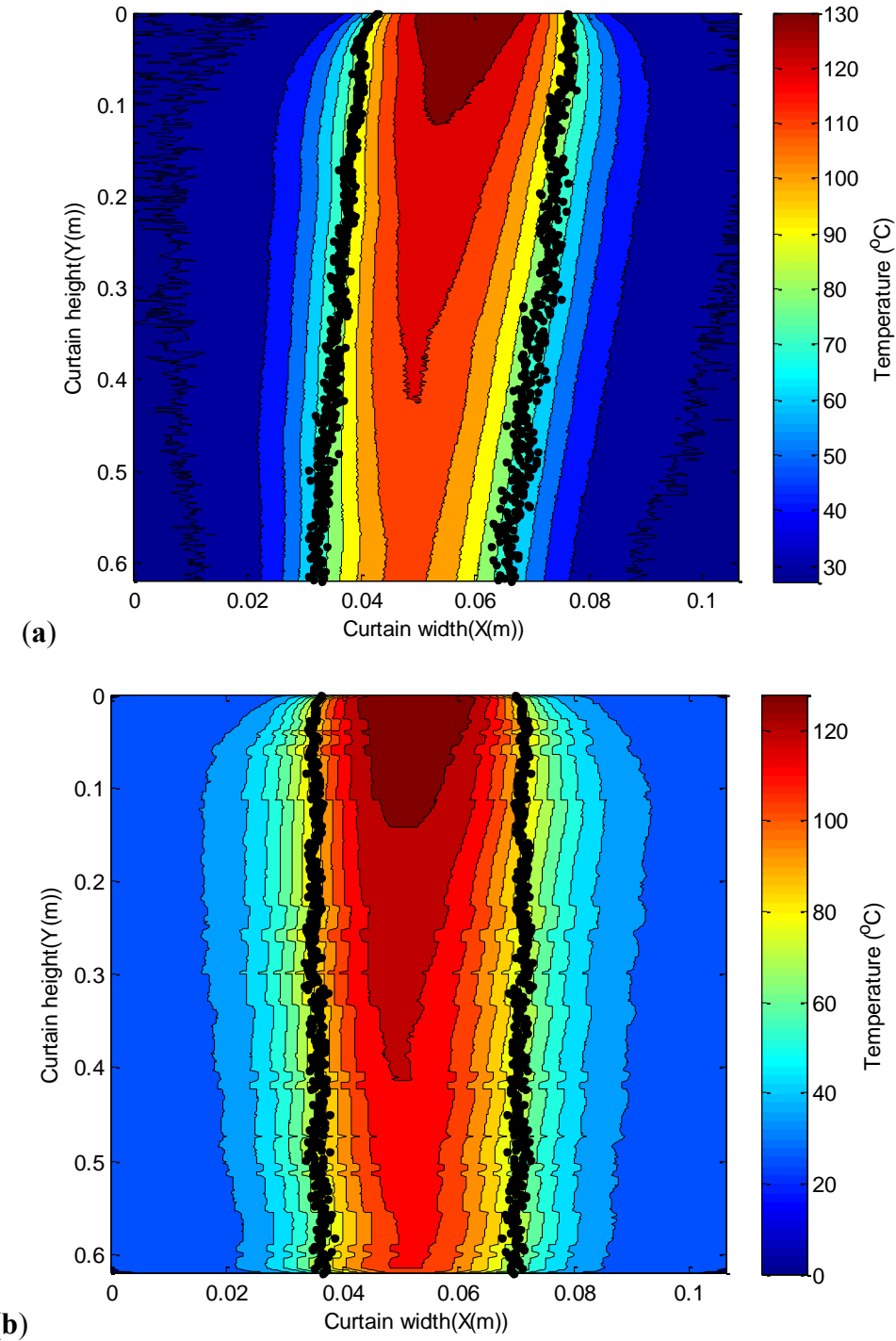


Figure 5.42: Maximum temperature gradient and two neighbour points

The “polifit” function in Matlab was used to generate a quadratic polynomial function with the three points and the “polyder” function was used to calculate the continuous derivative of polynomials. Finally, the “roots” function was used to return the roots of the polynomial, which are the precise locations of the two maxima corresponding to the edges.

5.6.2. Examples and symmetry adjustment

Figure 5.43(a) and Figure 5.44(a) show asymmetrical examples of 2D temperature profiles with edges located using the above methodology. For later comparison to CFD profiles, it is important to reduce asymmetry in the images. To enforce symmetry on the 2D thermal images, the edge locations are utilised. For each row of thermographic data, the midpoint between the two edges is determined. Each entire row of data is then shifted left or right, so that the midpoint corresponds to the geometric centreline (at $x=0.7\text{m}$). Figure 5.43(b) and Figure 5.44(b) show symmetrical examples of the mentioned figures.



**Figure 5.43: Overlaid edges on the thermal image, $d_s=290\mu\text{m}$, $m^o=0.066\text{kg/s}$ and slot width=20mm (a)
Unsymmetrical image (b) asymmetrical image**

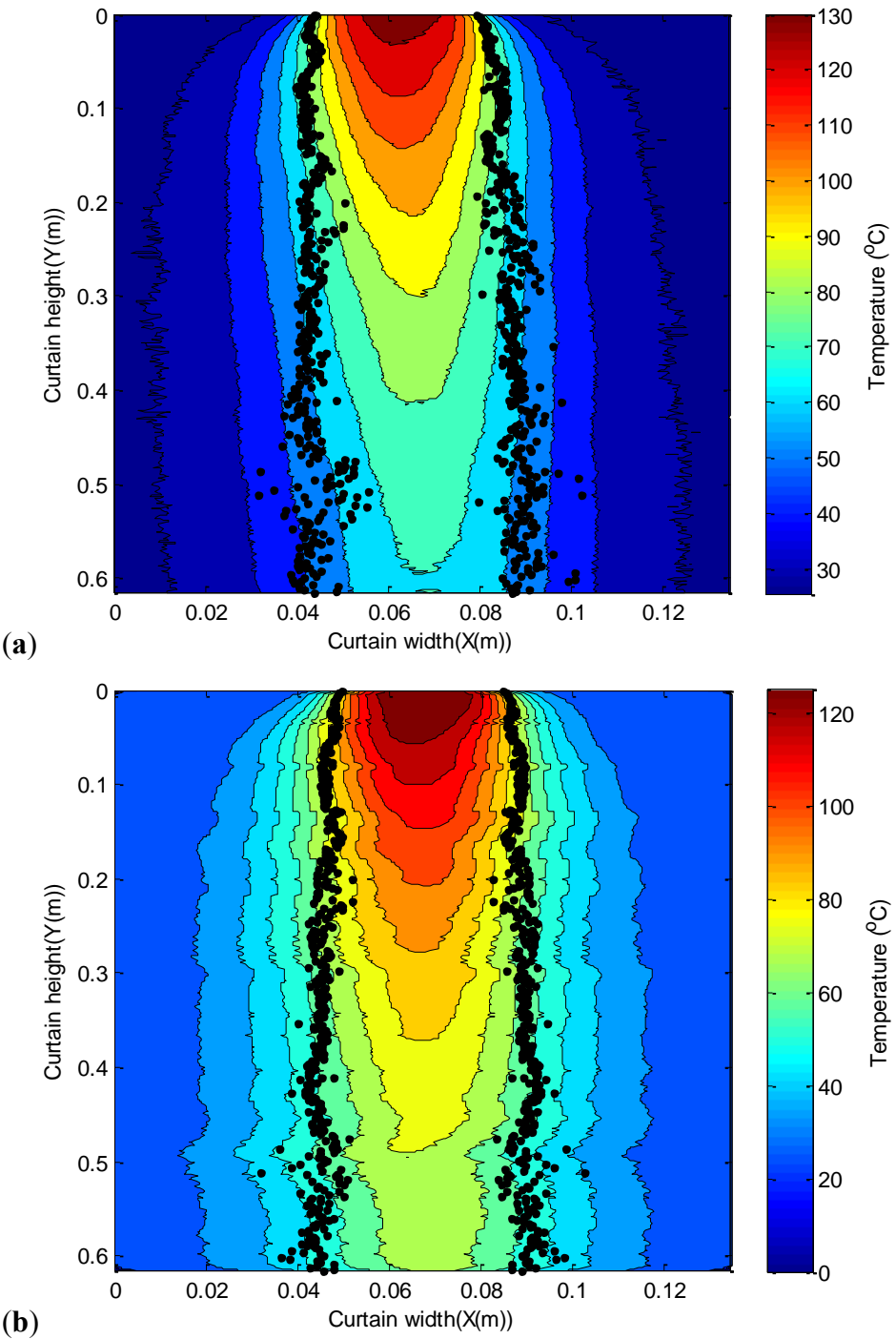


Figure 5.44: Overlaid edges on the thermal image, $d_s=290\mu\text{m}$, $m^o=0.062\text{kg/s}$ and slot width=20mm (a) Unsymmetrical image (b) asymmetrical image

5.7. Conclusion

A range of image processing tasks including image alignment and scaling were undertaken in this chapter to enforce symmetry, to identify key features (centreline temperature) and to enable comparison to CFD simulations. In addition, the locations of the particle curtain edges were identified in the thermal image using visible image analysis edge detection techniques (gradient technique). The reliability of thermographic temperature profiles was investigated, and it was observed that for low solid volume fractions, the thermographic data are less reliable due to the influence of background ambient temperature interference. A thermographic model was developed to adjust the infrared temperatures and reproduce the actual particle temperatures. In the selected model, the recorded infrared temperature was assumed to be a blend of the particle temperature and the background ambient temperature. It was found that visible photography is essential to calculate the influence of solid volume fraction on the thermal images. The model was found to be more successful for small and medium particle sizes.

Chapter 6 Results

In this chapter, all of the raw thermography results, such as centreline temperatures and 2D infrared images are presented. The effects of parameters such as particle size, mass flow rate and slot width on these profiles are investigated. One of the key objectives of this chapter is to assess the methodologies that have been developed in this thesis. This includes methods such as the gradient technique for edge detection for both CFD and thermography. Results are compared with previous methods to determine strengths and weaknesses. Furthermore, the effects of the particle size, mass flow rate and slot width on CFD centreline temperatures are presented to assess the CFD model trends. The location of curtain edges obtained from CFD simulations are compared to experimental results to assess the circumstances where CFD model predictions fail to identify curtain edge locations. The centreline temperature profiles from CFD are also compared to direct thermocouple measurements. Finally, the results of CFD, raw thermographic and filtered thermographic centreline temperatures are compared. In conditions where CFD modelling is unable to accurately predict the thermal characteristics of particle curtains (i.e. $610\mu\text{m}$), internal heat conduction is considered. A proposed CFD-Hybrid particle-heat-conduction model is used to investigate model deficiencies.

6.1. Raw Thermography Results

In this section, the effects of particle size, mass flow rate and slot width on raw infrared thermography centreline temperature profiles and 2D profiles are investigated. In addition, the shapes of the curtain obtained using the temperature gradient approach (Section 6.1.3) are

discussed in terms of convergence and divergence behaviours. The edges of the curtain obtained experimentally are compared with those obtained from CFD simulations.

6.1.1. Centreline temperature profiles

The calculation methodology for obtaining centreline temperature profiles from thermal images was described in Section 5.1.4. The effect of particle size, mass flow rate and slot width is presented through a selection of experimental results taken from the conditions outlined in Table 4.3, Section 4.4.

6.1.1.1. Effect of particle size

In the figures that follow, the effect of particle sizes is examined by presenting comparisons where slot size and mass flow rate are kept constant (Figure 6.1(a-c)). It is worth noting that in each comparison, the initial solids volume fractions are equal. In all graphs, the red circle and blue triangle symbols show the average of 10 raw centreline temperature profiles, and the black solid line indicates smoothed profiles. In all figures, the mass flow rates were not exactly identical but were as similar as possible given the experimental constraints.

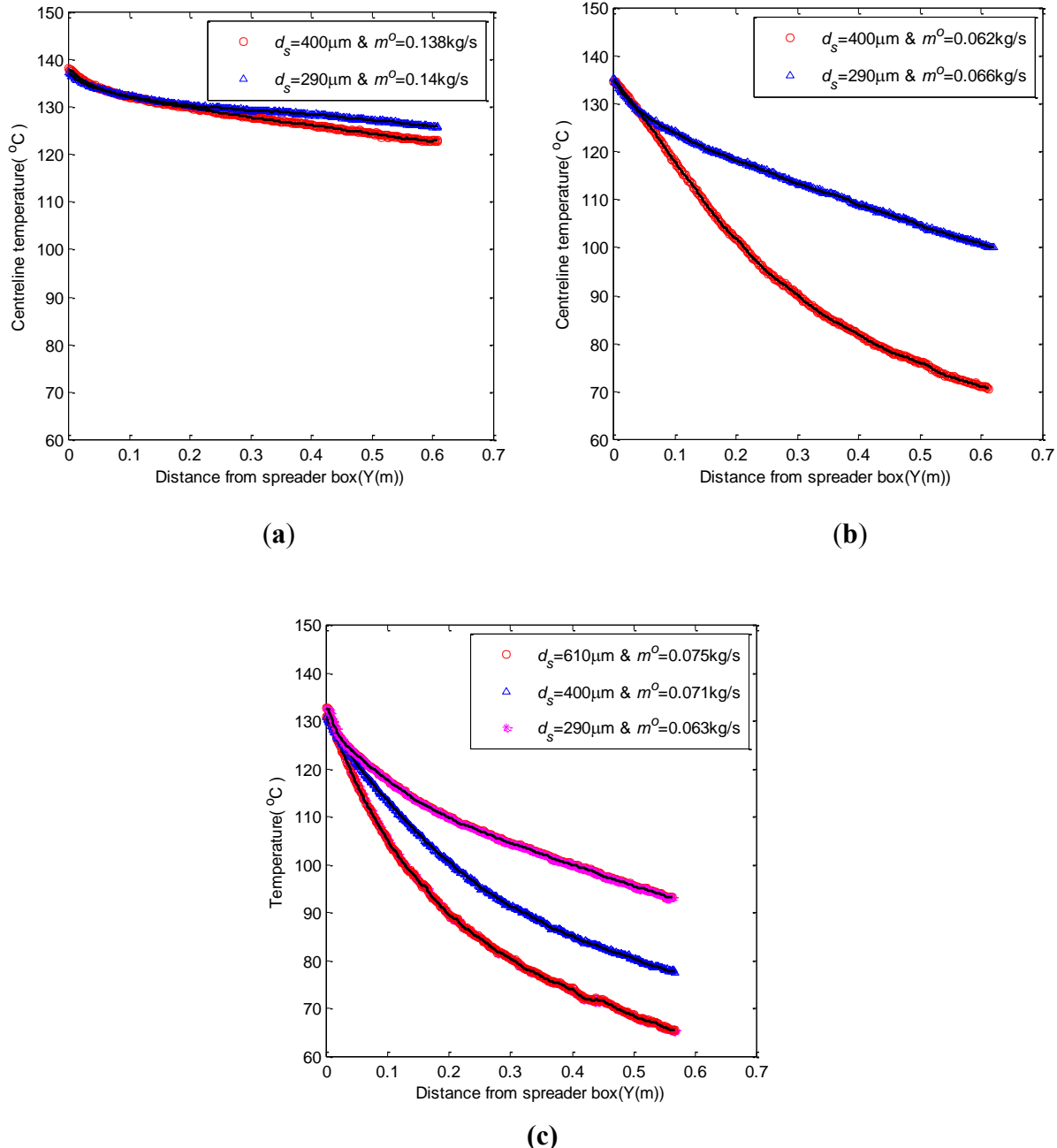


**Figure 6.1: Effect of particle size on raw infrared centreline temperatures at constant mass flow rate
(a) and (b) slot width=20mm (c) slot width=60mm**

In Figure 6.1(a), the mass flow rate is high and slot width narrow, leading to a high degree of confidence in the thermal data for both profiles. As particle size increases the heat loss experienced by the particles also increases. However, under these high mass flow rate and dense curtain

conditions, the effect of particle size on the temperature profiles is minimal. Furthermore, if the mass flow rates were identical, the temperature profiles would be even more close. When mass flow rate is reduced (Figure 6.1(b)) the trends remain consistent but the influence of particle size becomes more significant and substantial differences in temperature profiles are observed. Figure 6.1(c) shows the comparison of temperature profiles for three particle sizes at wider slot widths. Although, making judgments when there is low mass flow rate and wide slot width is difficult because of a lack of confidence in the thermal data. However, the temperature profiles are considered to be more reliable in the early stages of the profiles (i.e. $Y \leq 0.1\text{m}$) where the solid volume fractions are higher. In these wide slot width experiments, the effect of the background on the thermal image data can be more significant than the effect of particle size. In Figure 6.1(c), there are small variations in the mass flow rates for each particle size. If these runs had identical mass flow rates for each particle size, there would be more substantial differences in their profiles and the trends would be similar to Figure 6.1(b). Recalling the ANOVA results for the effects of mass flow rate, particle size and slot width on heat loss (Section 3.3), the most significant effect was mass flow rate then particle size, then the interaction of mass flow rate and particle size which is supported by the thermal data.

6.1.1.2. Effect of mass flow rate

In this section, the effects of mass flow rate are emphasised by comparing raw infrared thermal profiles for conditions of constant particle size and constant inlet slot width. Figure 6.2 shows profiles for particle flow through a 20mm slot, and Figure 6.3 shows profiles for particle flow through a 60mm slot. Figure 6.2 and 6.3 show that the rate of heat loss is much higher at low mass flow rates. This is because the mean residence times are greater at low mass flow rates compared

to high mass flow rates. Given constant particle size and equal initial particle velocities, the key physical difference in these situations is the initial voidage and inter-particle distances (see Table 4.3 in Section 4.4). For example, in Figure 6.2(a) there is an almost halving of inter-particle distance at high flow rate compared to low flow rate. For constant particle size, the high mass flow rate conditions lead to a reduction in the air space between the particles which results in higher localised air temperatures within the curtain. Given that heat loss is proportional to the localised temperature difference between the gas and solids, this leads to the lower rates of observed convective heat transfer at high flow rate. It was also observed that as particle size increases, the rate of heat loss also increases, particularly when comparing the 610 μm particles with the 290 μm and 400 μm particles in Figure 6.3(c). Unfortunately, at low mass flow rate, the infrared thermal data is more significantly influenced by background temperature and, thus the absolute values are less reliable. This makes drawing conclusions regarding the absolute temperature differences difficult. For example, it is difficult to state that the effects of mass flow rate on heat loss are more significant for larger particles than smaller particles, as Figure 6.2(a) and (b) suggest. CFD simulations (Figure 6.4) show that the effects of mass flow rate on heat loss are significant and follow the same trends. However, these effects are independent of particle size.

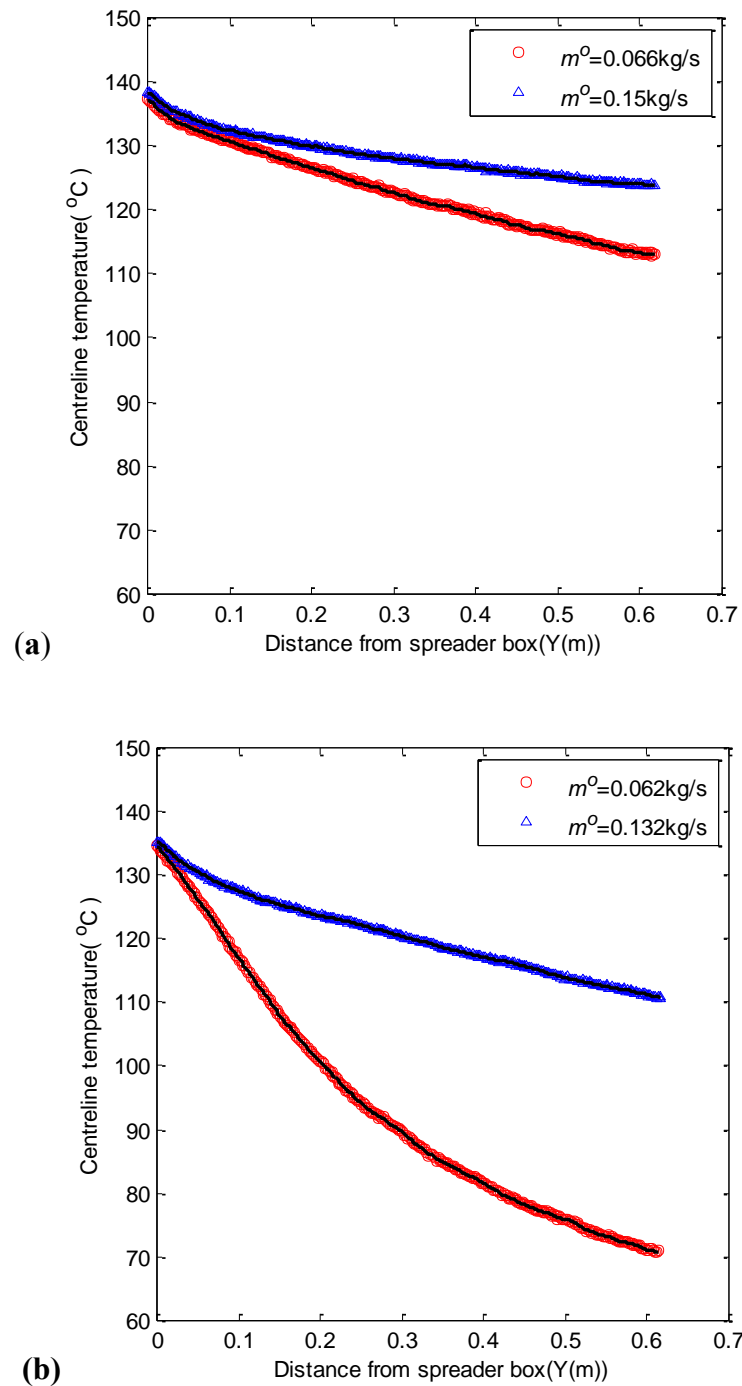


Figure 6.2: Effect of mass flow rate on raw infrared centreline temperatures at constant particle size and at slot width=20mm (a) $d_s=290\mu\text{m}$ (b) $d_s=400\mu\text{m}$

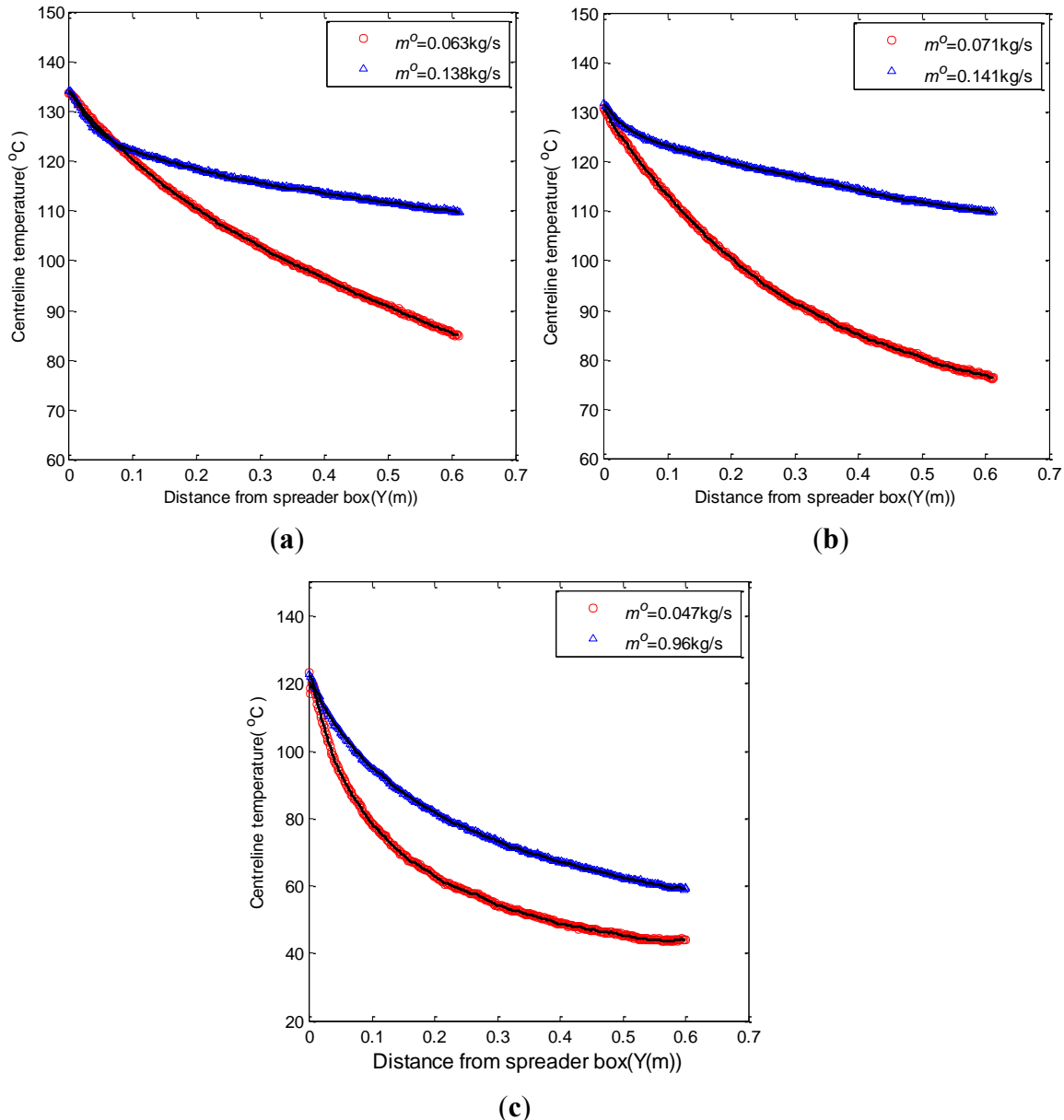
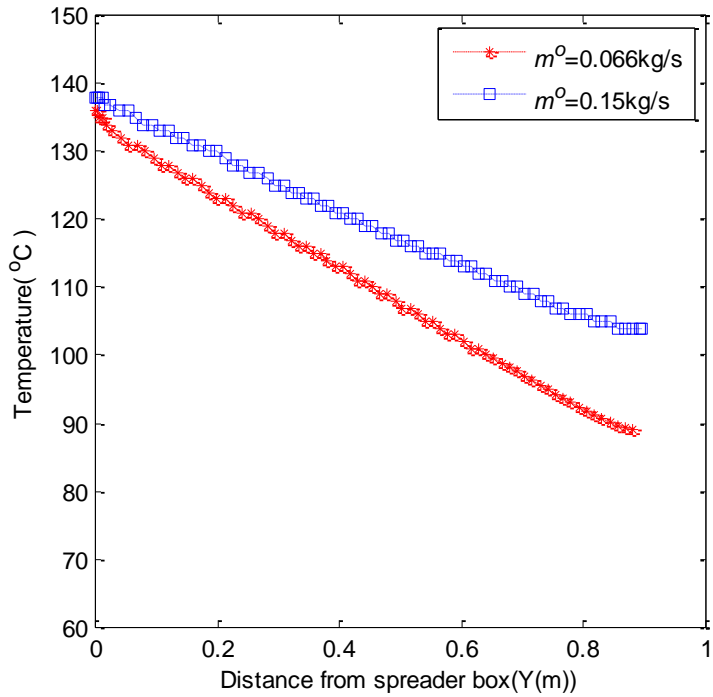
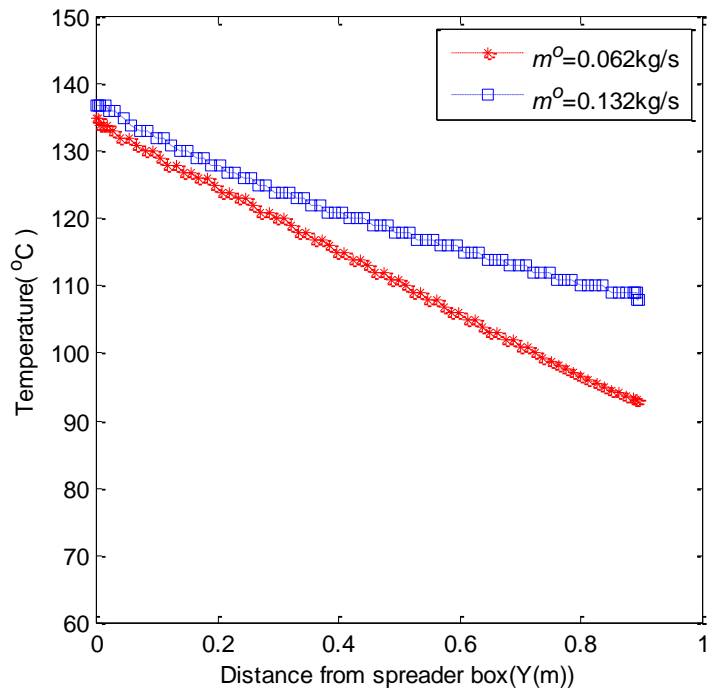


Figure 6.3: Effect of mass flow rate on raw infrared centreline temperatures at constant particle size and at slot width=60mm (a) $d_s=290\mu\text{m}$ (b) $d_s=400\mu\text{m}$ (c) $d_s=610\mu\text{m}$



(a)



(b)

Figure 6.4: Effect of mass flow rate on CFD centreline temperatures at constant particle size and at slot width=20mm (a) $d_s=290\mu\text{m}$ (b) $d_s=400\mu\text{m}$

6.1.1.3. *Effect of slot width*

Figure 6.5 shows the effect of slot width on raw infrared centreline temperature profiles under conditions of constant mass flow rate and constant particle size. Note that the initial velocities at two different slot widths are calculated in Section 4.3.4.3. The initial velocity for 20mm slot widths is 0.23m/s and for 60mm slot widths is 0.3m/s. The initial solid volume fractions for each of these experimental conditions are calculated in Table 4.3. It is interesting to note that these results are quite inconclusive, despite obvious qualitative differences in the 2D thermal profiles presented in Figure 6.6 and Figure 6.7 (Section 6.1.2). For example, under conditions of low mass flow rate in Figure 6.5(b) and (c), the centreline temperature drops more quickly for the larger slot width. However, the effect of minor variations in mass flow rate and the uncertainties of background interference would act to reduce these differences and two profiles might be very similar. At high mass flow rates where the profiles are more reliable and the influence of background is minimal (Figure 6.5(a)), there is no discernible difference between profiles for either slot width considering only the centreline temperature profiles leads to the conclusion that the temperature of the curtain, for the height of fall investigated remains the same in either situation. However, the 2D profiles presented in Section 6.1.2 suggested that the average or bulk temperature across the entire width of curtain are substantially different. Care must be taken not to infer bulk thermal effects from centreline temperature profiles, when comparing conditions with varying slot width. To illustrate this difference, the temperature distributions across the width of the curtains, for the conditions presented in Figure 6.5(a) are compared in Figure 6.6. In Figure 6.6, temperature profiles showing equal centreline temperatures are extracted across the x dimension. These temperatures are scaled with regard to curtain width. Despite equal centreline temperature the profile from the 60mm slot conditions has much lower temperatures at the curtain

edges. CFD simulations for bulk heat loss reinforce these differences (see Figure 3.4 in Section 3.3).

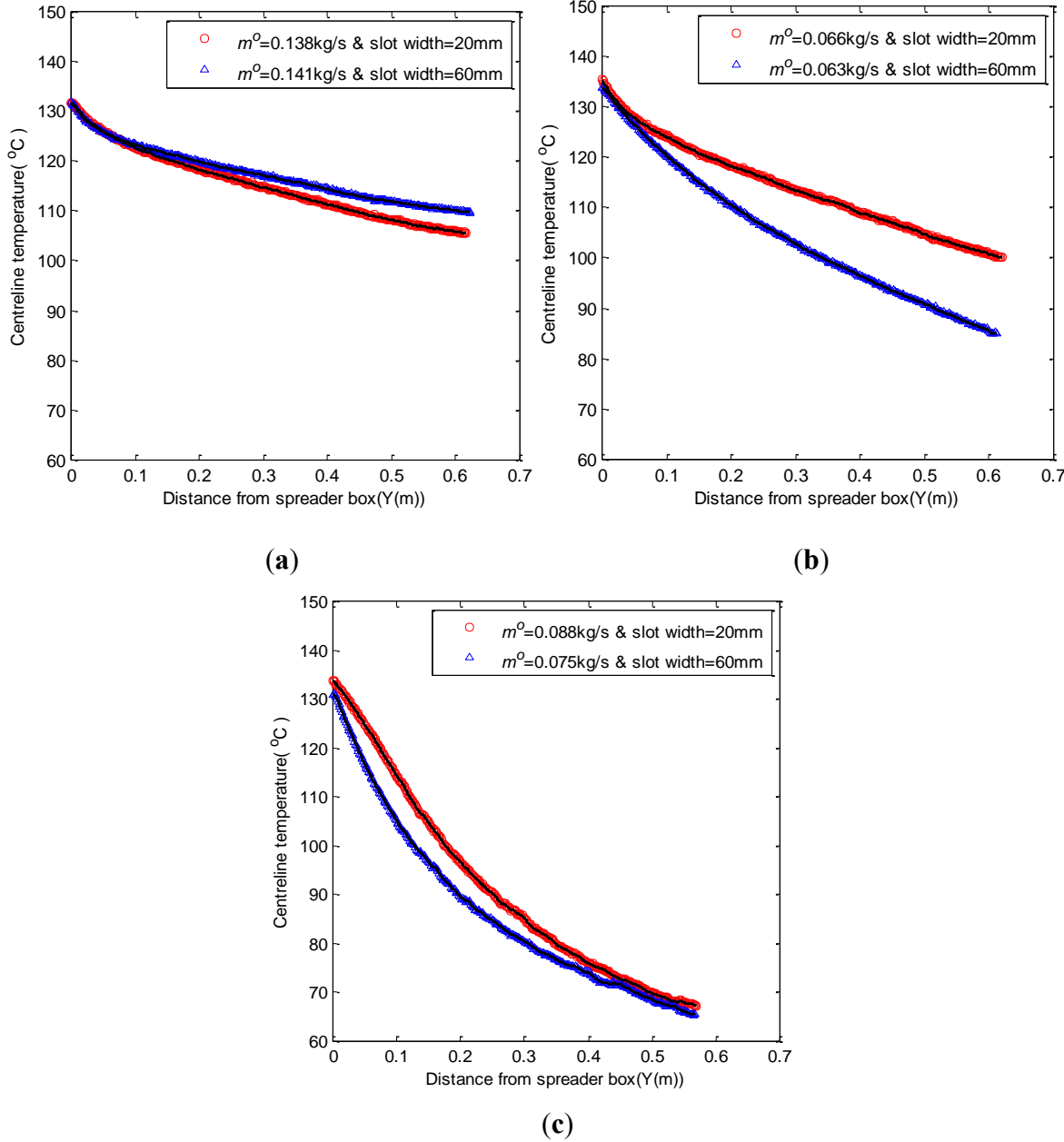


Figure 6.5: Effect of slot width on raw infrared centreline temperatures at constant particle size (a) $d_s=400\mu\text{m}$ (b) $d_s=290\mu\text{m}$ (c) $d_s=610\mu\text{m}$

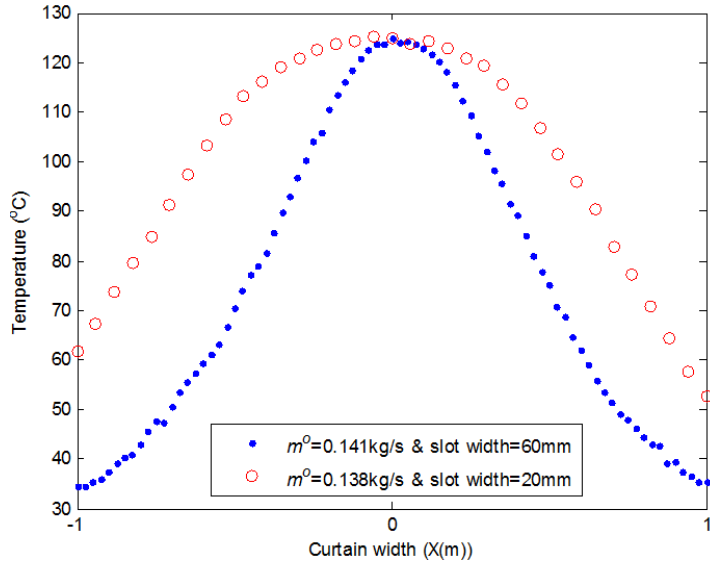


Figure 6.6: Temperature profiles in the x direction (scaled with regard to curtain width)

6.1.2. 2D Infrared thermal profiles

In this section, a selection of 2D thermal images are provided to show qualitatively the effect of particle size and slot width on the hot particle curtains. Figures 6.7 and 6.8 show profiles for varying particle size discharged from slot widths of 20mm and 60mm, respectively.

At constant mass flow rate and particle size, the temperature profiles are higher at small slot width (i.e. 20mm). The shapes of the 2D profiles are substantially different, and appear to be independent of particle sizes and strongly dependent on slot width. 60mm slot profiles all contract (converge) markedly as particles fall, and cool ambient air is able to penetrate into the curtain easily. This leads to curtains cooling quickly from the outside into the centre. In the narrow slot width situations, this penetration is less obvious and the curtains cool longitudinally and more gradually. Even at higher mass flow rates, the influence of slot width on the mechanism of cooling can be observed (see for example Figure 6.9). The visible images confirm this effect although image

contrast and thin curtains make edge detection difficult. These images are provided in Appendix E. In terms of practical heat exchanger design, heat transfer can be maximised by designing equipment that provides wide particle curtains which draws cool ambient air into the curtain.

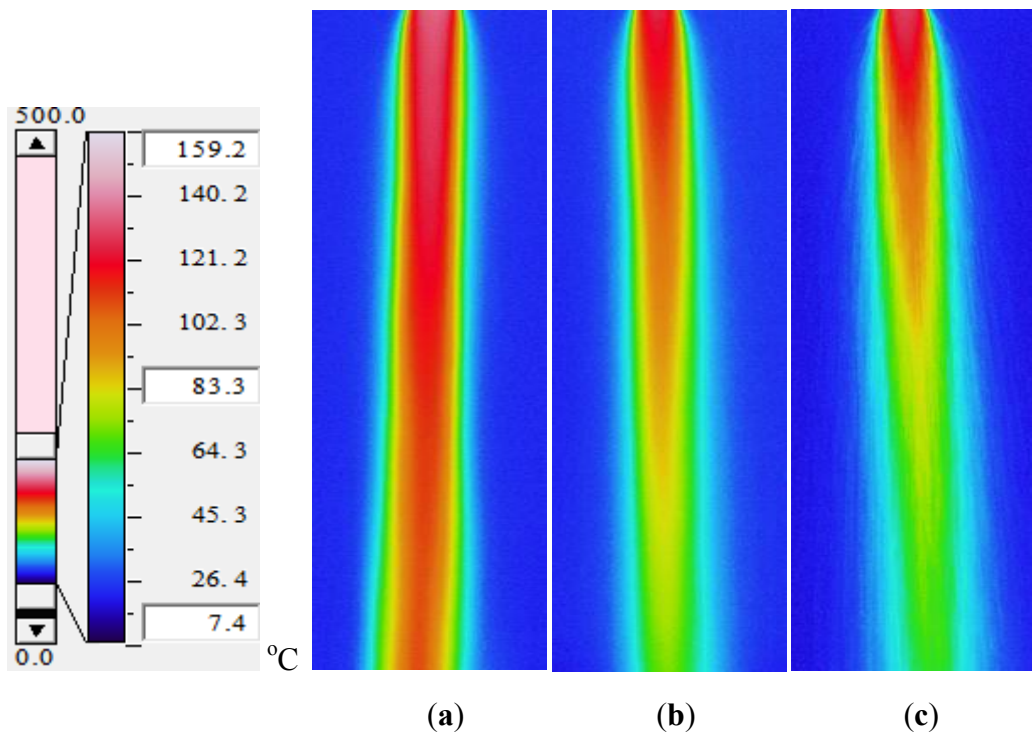


Figure 6.7: 2D thermal images of particle curtain at slot width=20mm (a) $d_s=290\mu\text{m}$, $m^o=0.066\text{kg/s}$ (b) $d_s=400\mu\text{m}$, $m^o=0.062\text{kg/s}$ (c) $d_s=610\mu\text{m}$, $m^o=0.088\text{kg/s}$

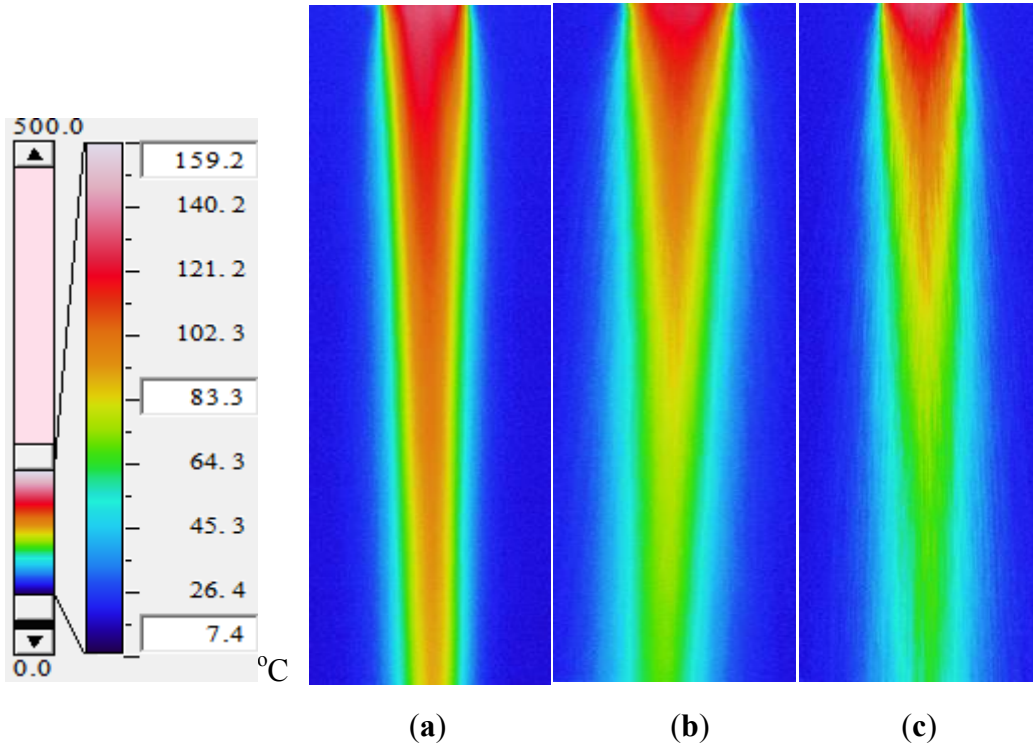


Figure 6.8: 2D thermal images of particle curtain at slot width=60mm (a) $d_s=290\mu\text{m}$, $m^o=0.063\text{kg/s}$ (b) $d_s=400\mu\text{m}$, $m^o=0.071\text{kg/s}$ (c) $d_s=610\mu\text{m}$, $m^o=0.075\text{kg/s}$

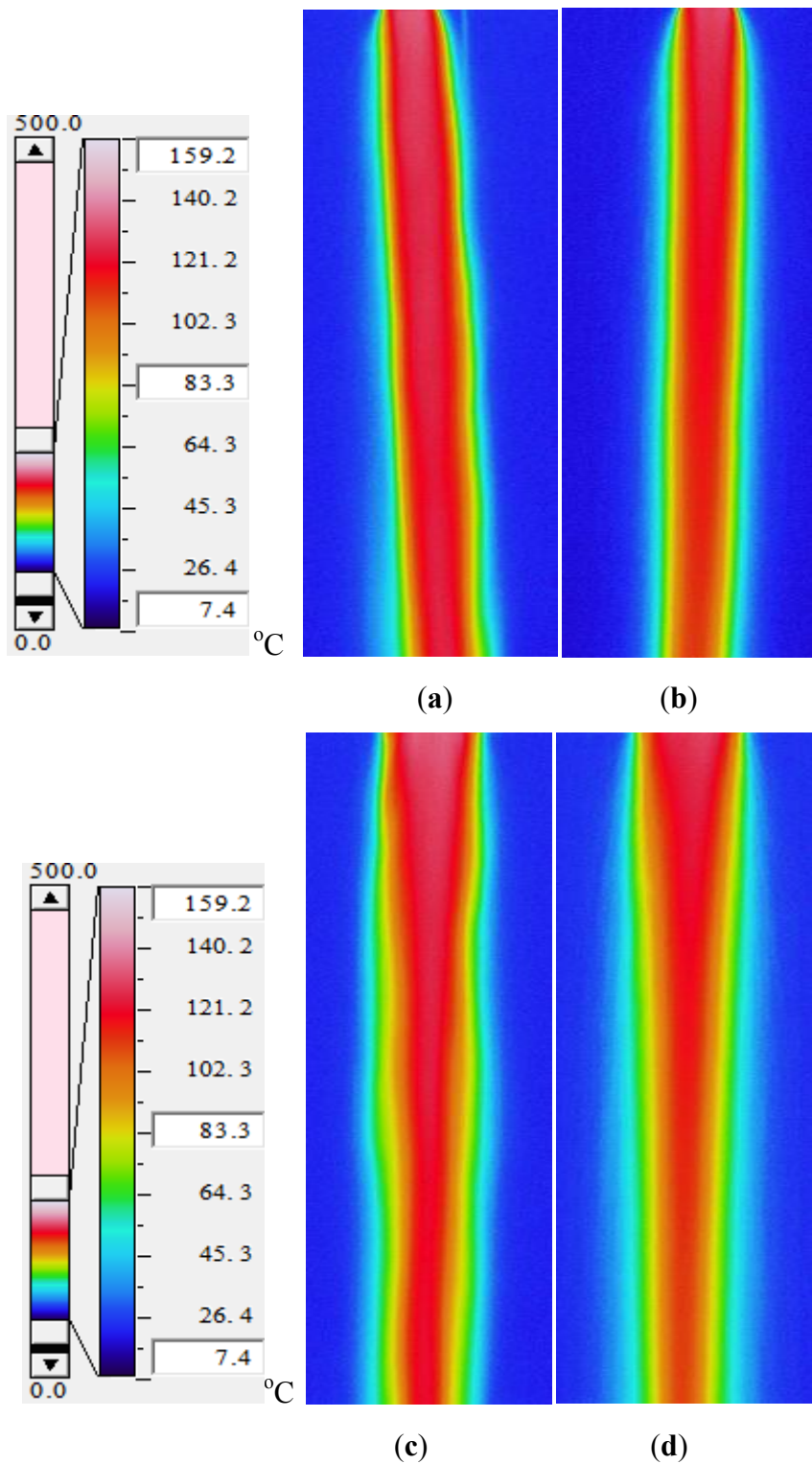


Figure 6.9: 2D thermal images of particle curtain at slot width=60mm (a) $d_s=290\mu\text{m}$, $m^o=0.14\text{kg/s}$ (b) $d_s=400\mu\text{m}$, $m^o=0.138\text{kg/s}$ (c) $d_s=290\mu\text{m}$, $m^o=0.138\text{kg/s}$ (d) $d_s=400\mu\text{m}$, $m^o=0.141\text{kg/s}$

6.1.3. Shape of the curtain

In this section, the shapes of the particle curtain as predicted by applying the gradient technique (Section 5.6) to 2D infrared thermographic images are investigated.

In Figures 6.10-6.14 which shows profiles for 20mm slot width conditions, the shape of the curtain shows almost consistently uniform curtain widths or curtains that expand slightly as they fall. This reinforces the view that ambient air is unable to penetrate these curtains. In these situations, the assumption is that the internal air pressure is greater than the external air pressure. Hot air between the particles is driven out instead of cool ambient air being drawn in. For the large slot width (i.e. 60mm) conditions (Figure 6.15-6.19), curtains consistently contract indicating a lower internal pressure and a situation that would result in ambient air being sucked into the curtain bulk, increasing convection cooling. To maximise heat transfer and particle cooling, conditions that result in profiles such as wide slot widths, are required.

The shapes derived from the 2D thermal images are well-matched to those observed for isothermal curtain experiments reported in the literature [48]. Thus, the gradient technique applied to the 2D thermal images is able to predict curtain shape successfully. When designing heat exchange equipment and seeking maximisation of heat transfer, isothermal experiments would be sufficient.

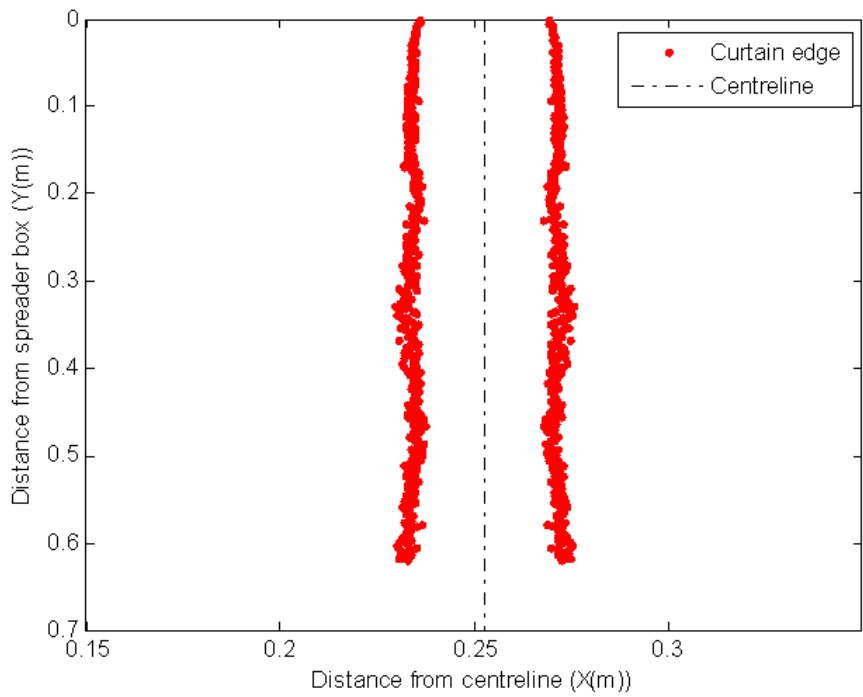


Figure 6.10: Particle curtain shape, $d_s=290\mu\text{m}$, $m^o=0.066\text{kg/s}$ and slot width=20mm

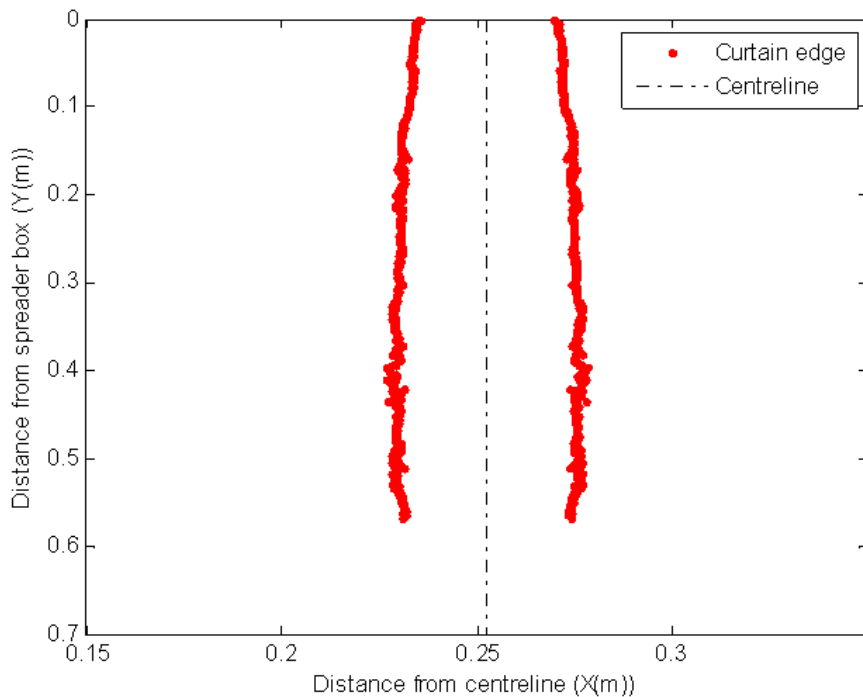


Figure 6.11: Particle curtain shape, $d_s=290\mu\text{m}$, $m^o=0.14\text{kg/s}$ and slot width=20mm

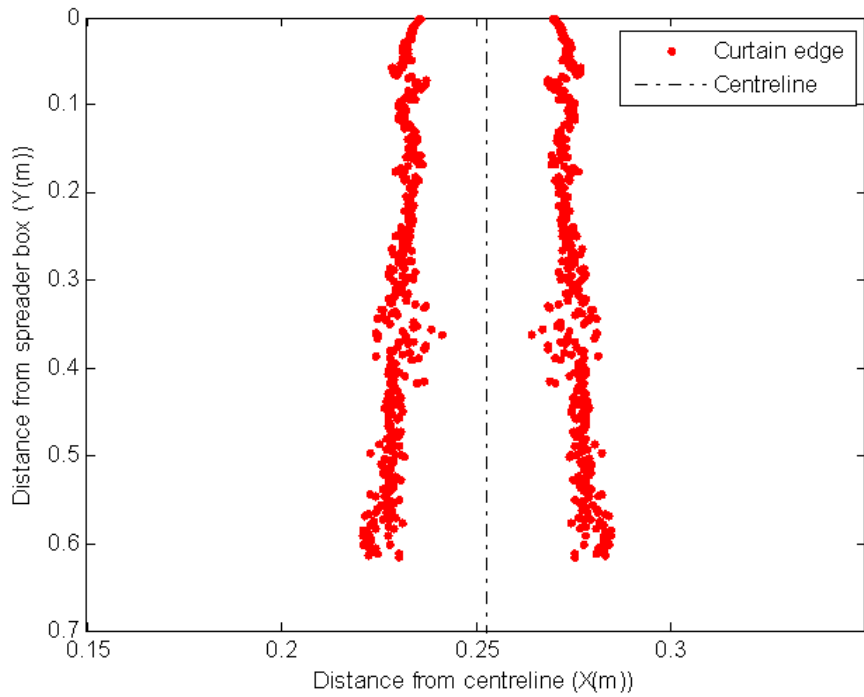


Figure 6.12: Particle curtain shape, $d_s=400\mu\text{m}$, $m^o=0.062\text{kg/s}$ and slot width=20mm

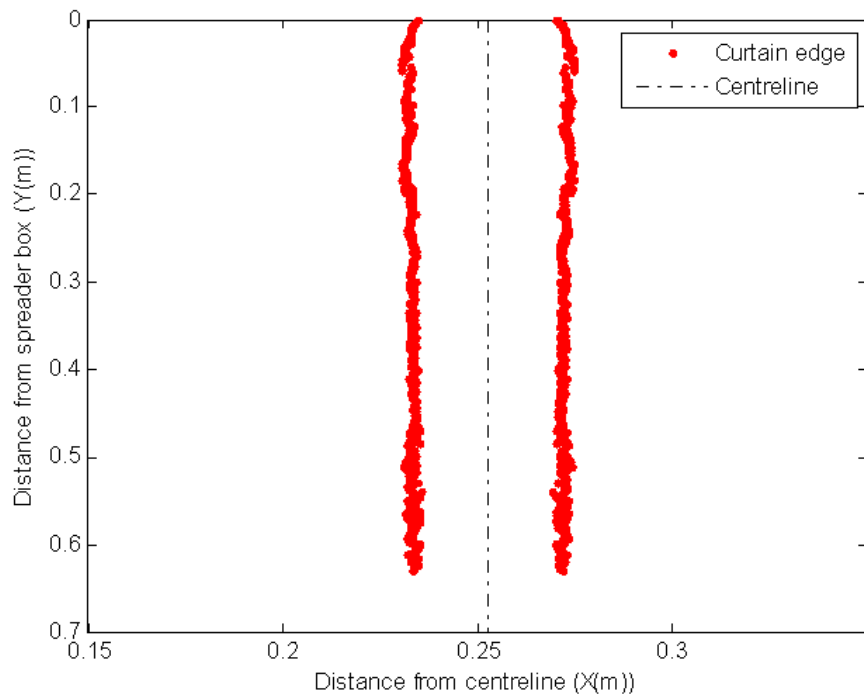


Figure 6.13: Particle curtain shape, $d_s=400\mu\text{m}$, $m^o=0.138\text{kg/s}$ and slot width=20mm

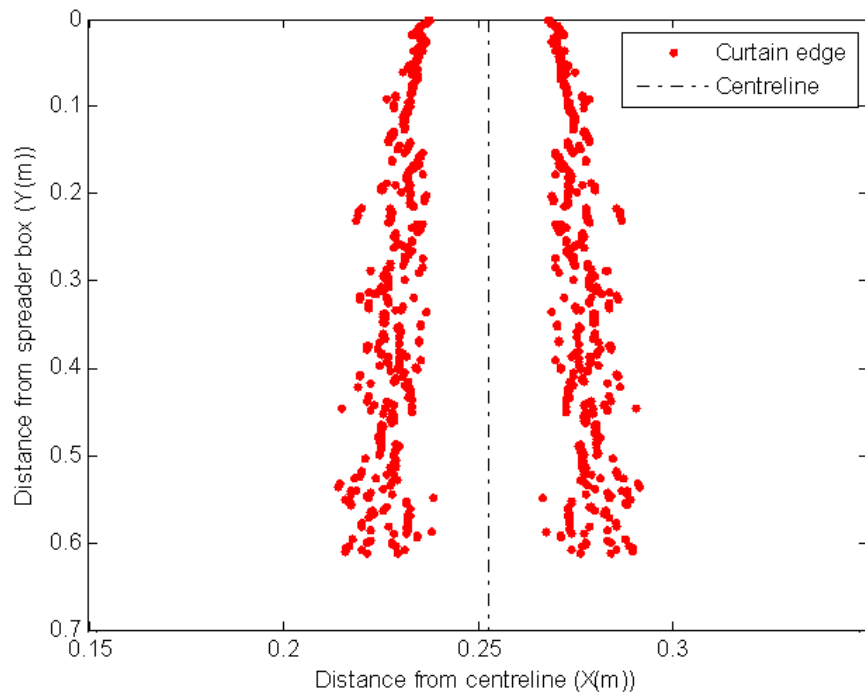


Figure 6.14: Particle curtain shape, $d_s=610\mu\text{m}$, $m^o=0.088\text{kg/s}$ and slot width=20mm

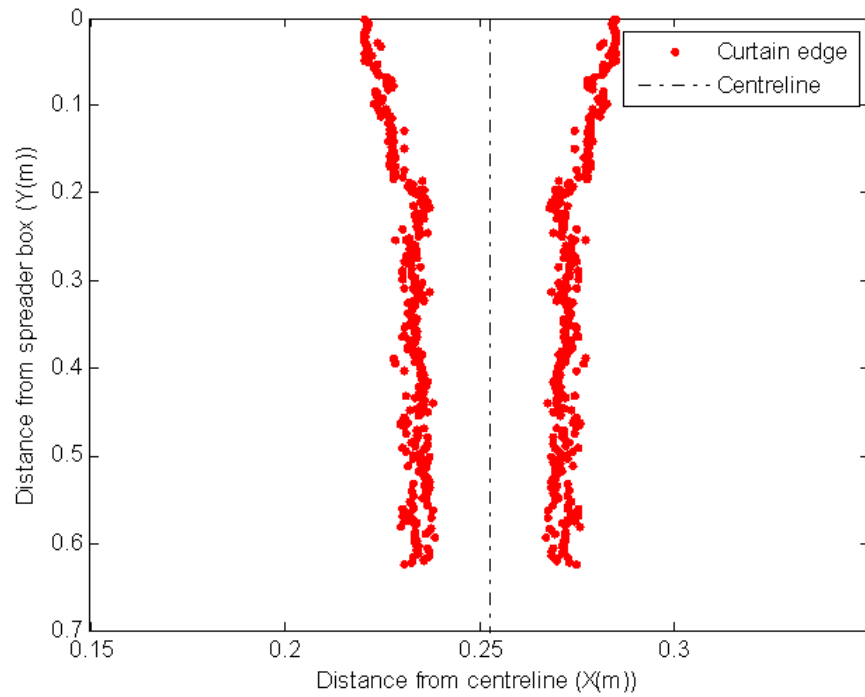


Figure 6.15: Particle curtain shape, $d_s=290\mu\text{m}$, $m^o=0.063\text{kg/s}$ and slot width=60mm

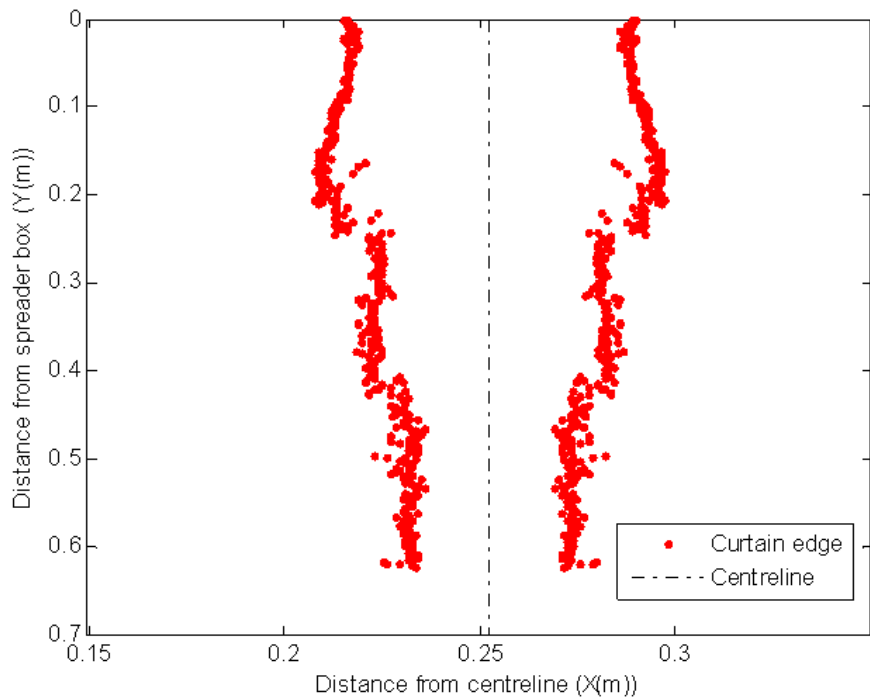


Figure 6.16: Particle curtain shape, $d_s=290\mu\text{m}$, $m^o=0.138\text{kg/s}$ and slot width=60mm

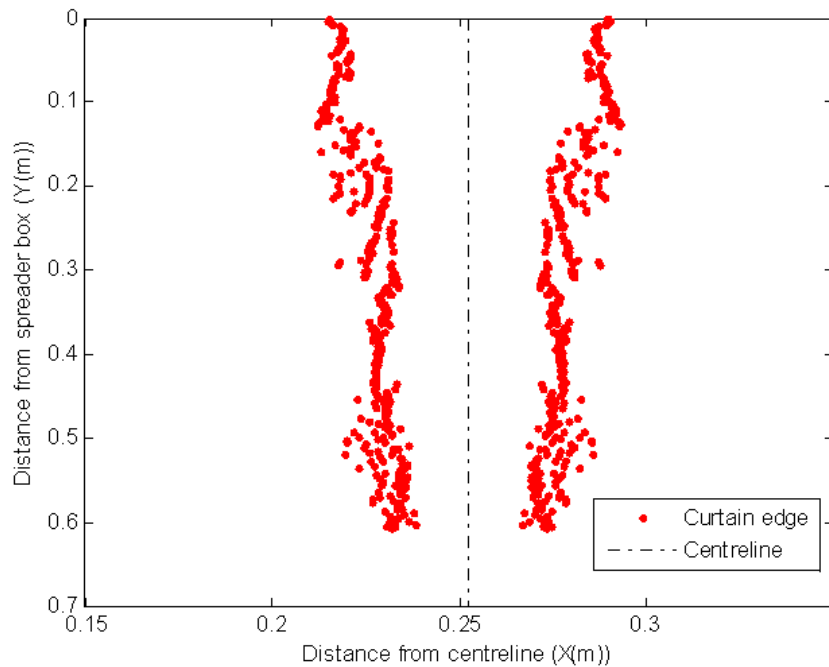


Figure 6.17: Particle curtain shape, $d_s=400\mu\text{m}$, $m^o=0.071\text{kg/s}$ and slot width=60mm

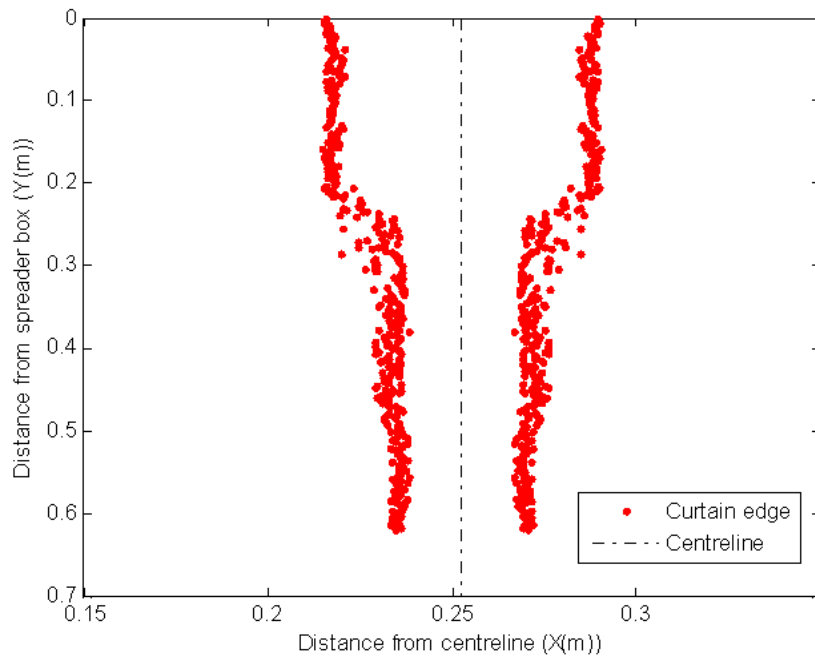


Figure 6.18: Particle curtain shape, $d_s=400\mu\text{m}$, $m^o=0.141\text{kg/s}$ and slot width=60mm

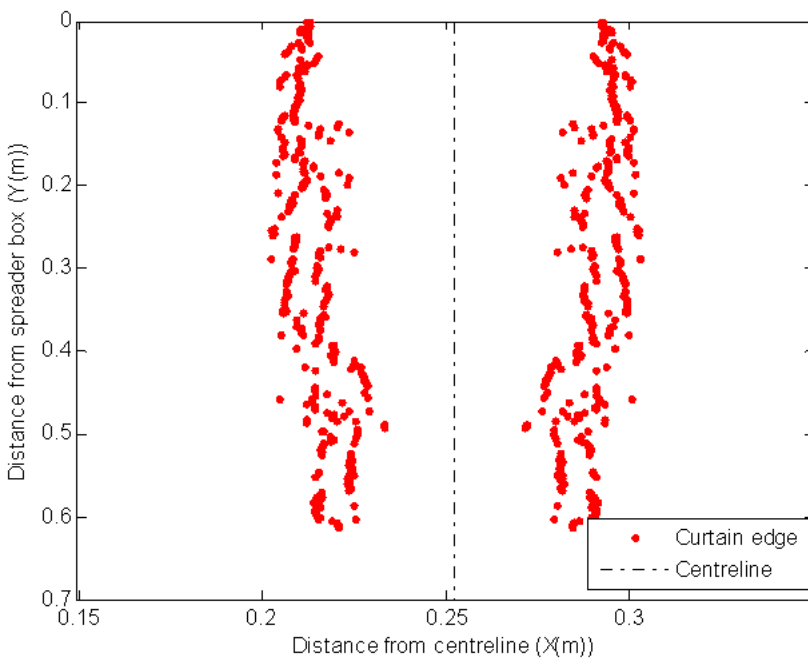


Figure 6.19: Particle curtain shape, $d_s=610\mu\text{m}$, $m^o=0.096\text{kg/s}$ and slot width=60mm

6.2. Comparison of CFD and Thermographic Data

In this section, CFD predictions are compared to infrared thermographic data. Direct thermocouple measurements are also included where available. Adjusted infrared thermographic data modelled via Equation 5.11 is also examined. All CFD data is generated using the model described in Section 3.2 using the exact matching experimental conditions for the corresponding infrared thermal image as outlined in Section 4.4.

Figure 6.20(a-e) shows 2D thermographic temperature profiles manipulated as per Section 5.6.2 to enforce symmetry. Edges obtained using the temperature gradient method applied to the infrared data and edges obtained using the solid volume fraction gradient applied to CFD data overlaid onto the 2D thermal images. In all figures, the black dotted points, and red dashed lines, show edges of the curtain from thermography data and CFD model predictions respectively. The edge comparisons are presented mainly to investigate the gradient method in thermographic results and CFD model.

In Figure 6.20, there is a better agreement between CFD and infrared thermographic edge predictions at small slot widths, 20mm, than at 60mm. If edge detection in the infrared data were based on a predicted temperature cut-off, such as ambient temperature (i.e. the outside line delineating the border between the ambient temperature darkest blue and next darkest blue in Figure 6.20), the location of the edges would be very different and clearly incorrect. In the infrared images, there is a cloudy area of higher temperature readings around the edges of the curtain. This is likely due to the blurred temperature around the curtain. Thus, traditional techniques for visible image edge detection based on threshold values, are unsuitable for infrared thermographic data. It may require further study to use the gradient technique on visible images where the solid volume fractions within the curtain are measured experimentally. However, calculation of solid volume

fractions is challenging and a proper technique does not exist. The recent studies are based on the calculation of particle pixel intensities and cannot predict the solid volume fraction directly.

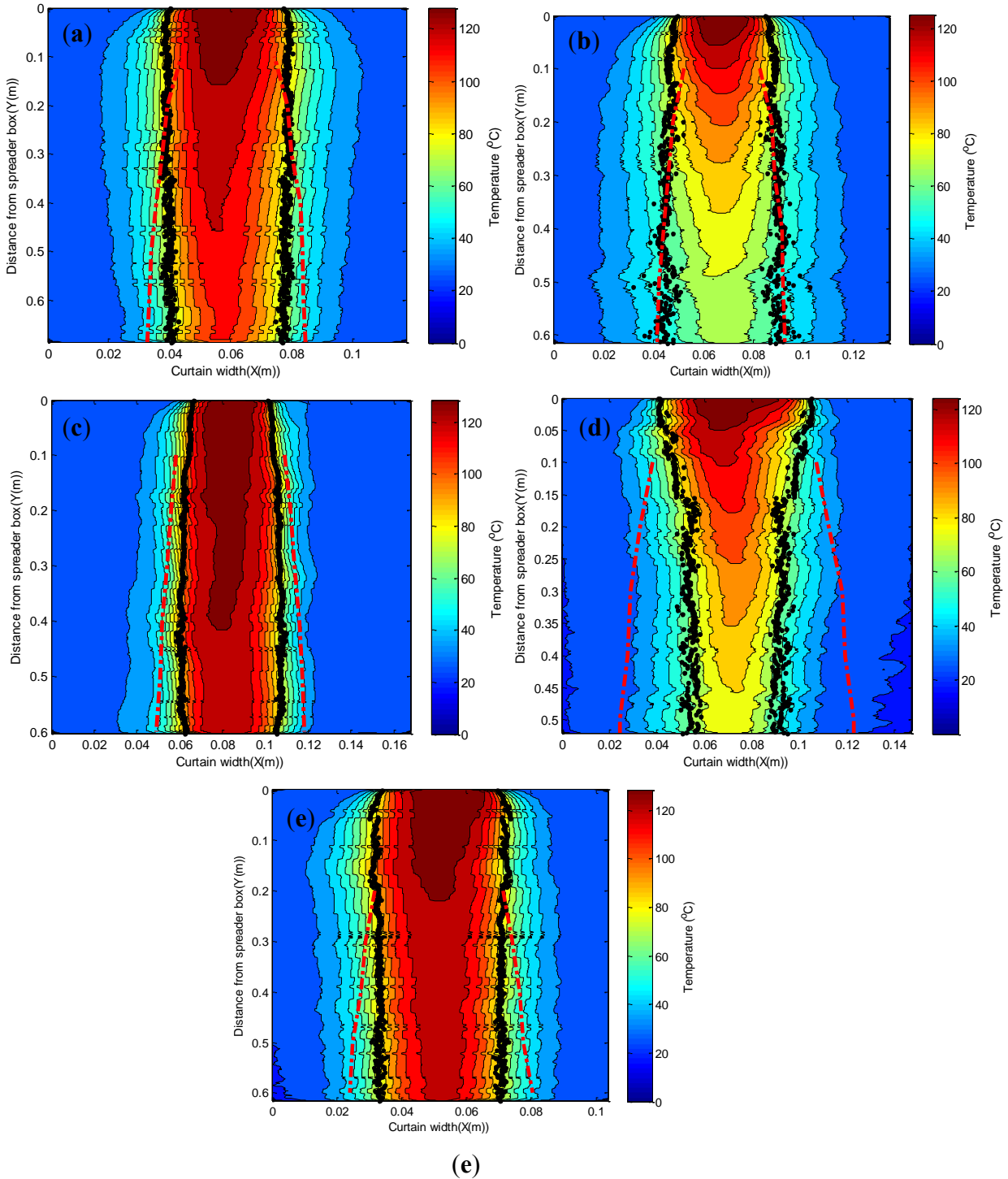


Figure 6.20: Edges of the particle curtain in CFD and experiment overlaid on the thermal image (a) $d_s=290\mu\text{m}$, $m^o=0.066\text{kg/s}$ and slot width=20mm (b) $d_s=400\mu\text{m}$, $m^o=0.062\text{kg/s}$ and slot width=20mm (c) $d_s=290\mu\text{m}$, $m^o=0.14\text{kg/s}$ and slot width=20mm (d) $d_s=290\mu\text{m}$, $m^o=0.063\text{kg/s}$ and slot width=60mm (e) $d_s=400\mu\text{m}$, $m^o=0.138\text{kg/s}$ and slot width=20mm

Figure 6.21 and Figure 6.22 show comparison of curtain edges at various particles sizes, mass flow rates and slot widths. In all graphs, the black dashed lines, the red dot symbols and black solid lines represent the curtain centreline, experimental curtain edges and CFD simulation curtain edges respectively.

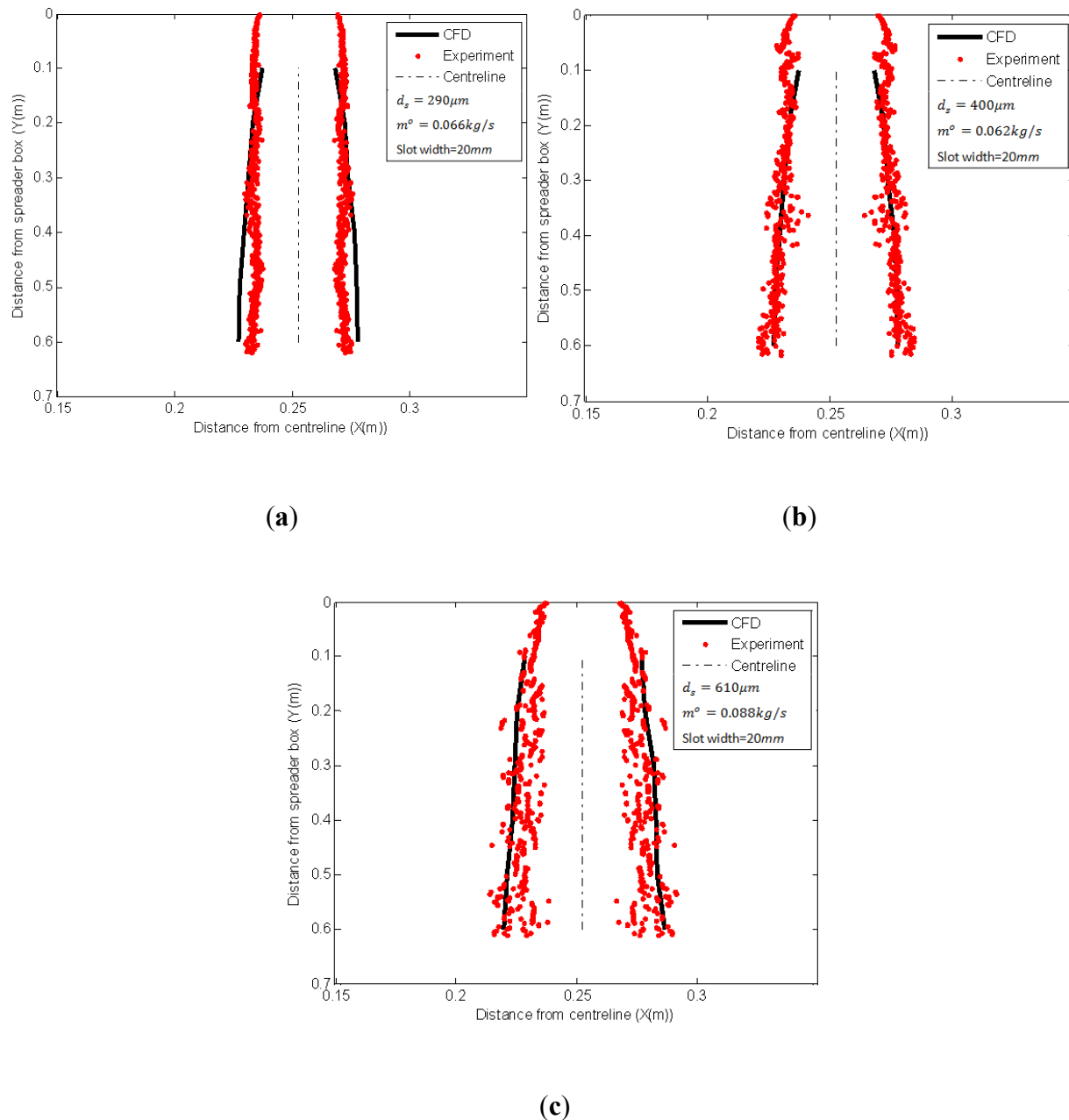


Figure 6.21: Particle curtain edges in CFD and experiments

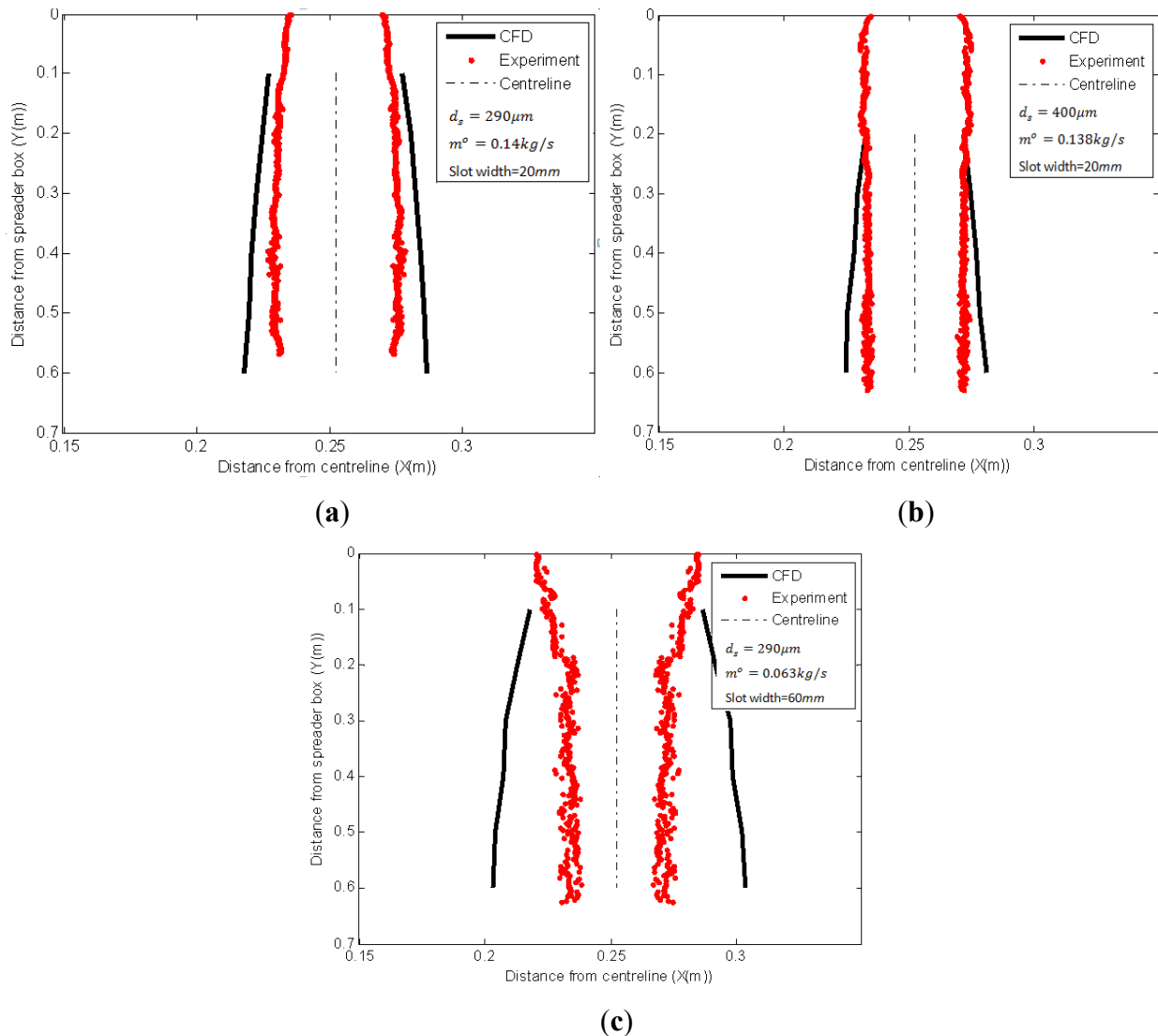


Figure 6.22: Particle curtain edges in CFD and experiments

Figure 6.21 shows good agreement between the results of CFD and experiments. These conditions are characterised by low mass flow rates and small slot width (20mm). However, at higher mass flow rates, and particularly at large slot widths (Figure 6.22) there is a greater discrepancy between the model predictions and experimental results. The CFD model was unable to predict the edges of the curtain at the larger slot width (60mm). This is because the dispersion of the particle curtain is high at the edges compared to the centre of the curtain in which the solid volume fractions are

higher. This remains a dilute region around this core that reduces the ability to use the gradient technique effectively. The only condition where CFD was capable of predicting the edge in 60mm slots occurred at $d_s=290\mu\text{m}$ and low mass flow rate (i.e. 0.063kg/s). Figure 6.23 shows the comparison of using various selected cut-off values of solid volume fraction (α_c) to define the edges in the CFD simulations, and that obtained via the gradient technique. The critical constant solid volume fractions of 6×10^{-4} (used in [48]) and 4.5×10^{-4} were applied to the CFD data. Although still failing to accurately match the infrared edge predictions, there is a minor improvement in predictability. These problems were observed in the majority of 60mm slot width simulations.

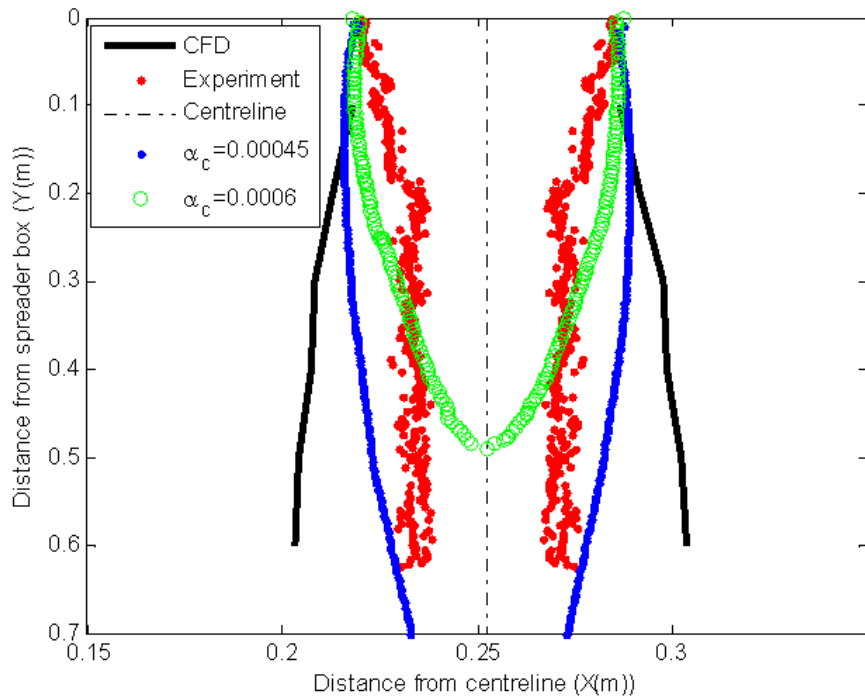


Figure 6.23: Edges of the curtain in CFD and experiment using both constant solid volume fraction and gradient technique, $d_s=290\mu\text{m}$, $m^o=0.063\text{kg/s}$ and slot width=60mm

6.2.1. 2D temperature profiles

Figure 6.24 shows a 2D temperature profile comparison under conditions of greatest confidence in the thermography profiles (i.e. small particle size and high mass flow rate). Note that the comparisons shown in Figure 6.24 only provide the qualitative description of the temperature profile and are not intended for quantitative comparison. The temperature drop over the entire falling distance is more pronounced in the CFD model. However, direct comparison is challenging because the CFD contours are extracted from a single plane positioned at the front edge of the slot. In the thermal image, the recorded temperatures are the result of an amalgamation of numerous layers of the particle curtain. This may cause higher temperatures to be observed in the thermal image, in comparison.

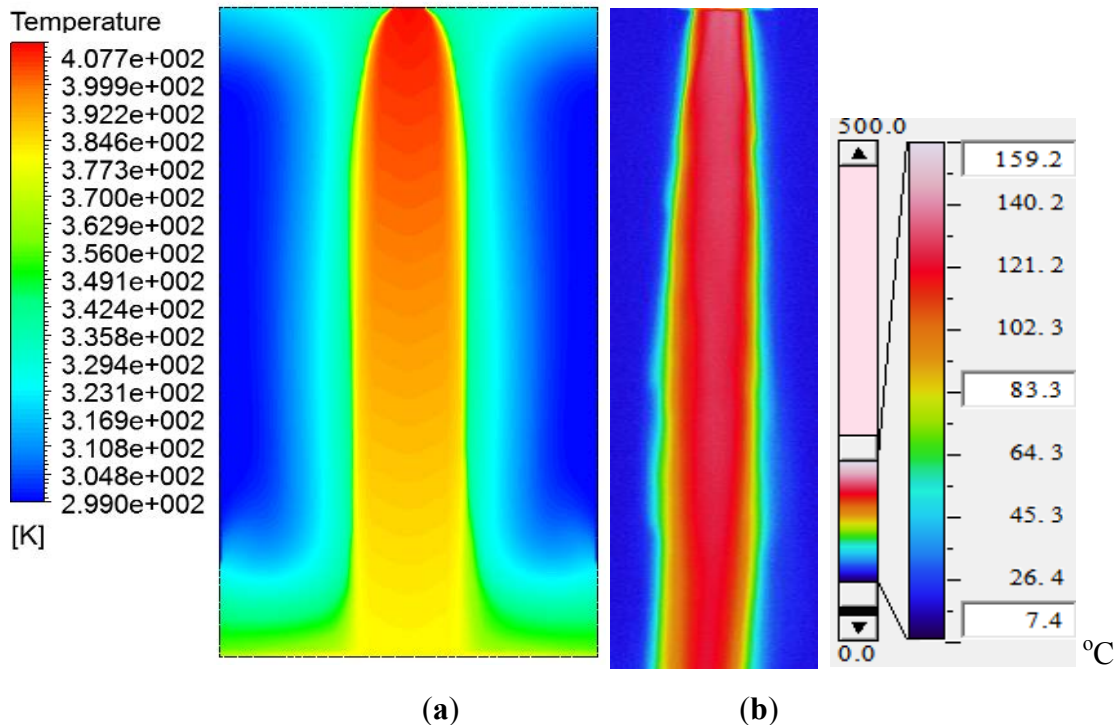


Figure 6.24: 2D temperature profiles, $d_s=290\mu\text{m}$, $m^o=0.15\text{kg/s}$ and slot width=20mm (a) CFD (b) thermal image

6.2.2. Centreline temperature profiles

CFD centreline temperature profile predictions are first evaluated by comparison to measurements made using direct thermocouples (Figures 6.25-28). Thermocouple measurements were taken for a reduced set of conditions. It is worth noting that the thermocouple measurements are not without uncertainties. There is excellent agreement between CFD and experiments at high mass flow rates for both 290 μm and 400 μm particles (Figure 6.25 and 6.27). There is also good agreement at low mass flow rate and 290 μm particles in the early stages of the profile. However, Figure 6.28 demonstrates that CFD predictions are less able to match the particle curtain temperature for the larger particle size (610 μm). The CFD prediction shows a more substantial rate of cooling than the thermocouple measurements indicate. There also appears to be errors in the chosen initial temperature at the spreader box exit, which may arise from background interference in the thermographic data used to estimate the spreader box exit temperature. These figures also demonstrate that the CFD predictions show a more uniform gradient or constant rate of change in temperature with respect to height, than the thermocouple data indicates. The thermocouple data shows a flattening in temperature as the particles fall and suggests a noticeable deterioration in the driving force for cooling. This does not occur in the CFD model predictions. This is because of the complex interaction between drag and heat transfer, and more targeted study in this area is required. However, more direct thermocouple measurements for each particle size are required to obtain more confidence in the conclusions regarding the curve trends.

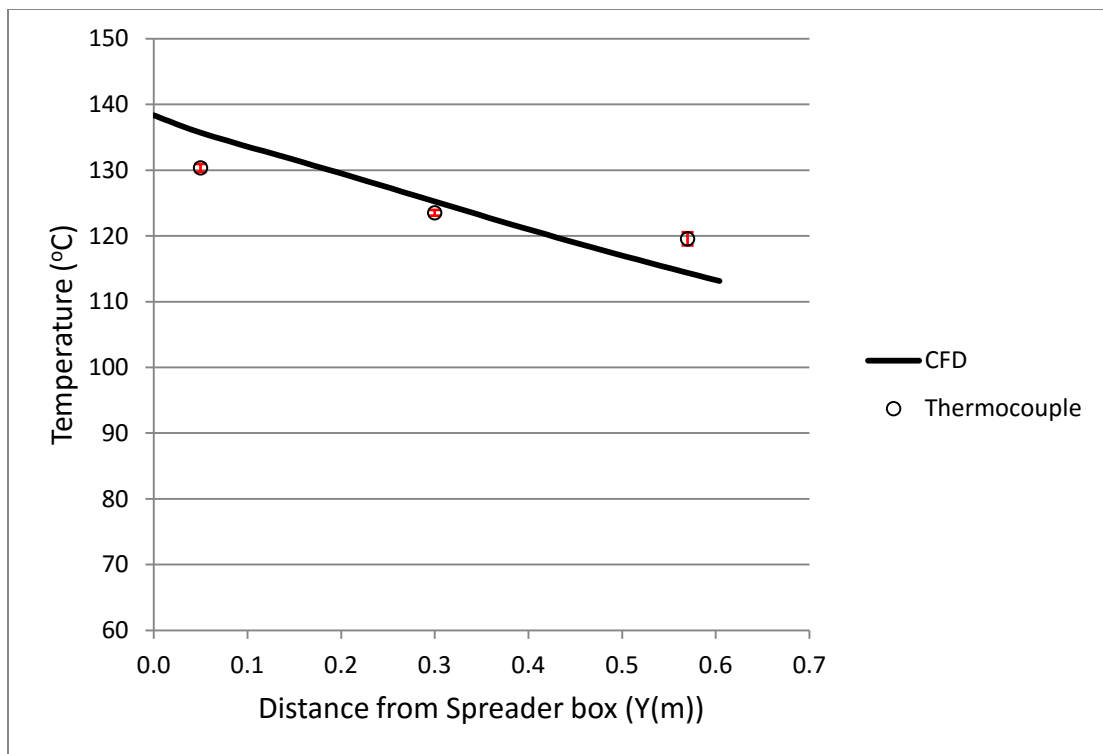


Figure 6.25: Comparison of CFD centreline temperature and discrete thermocouple temperature measurement, $d_s=290\mu\text{m}$, $m^o=0.15\text{kg/s}$ and slot width=20mm

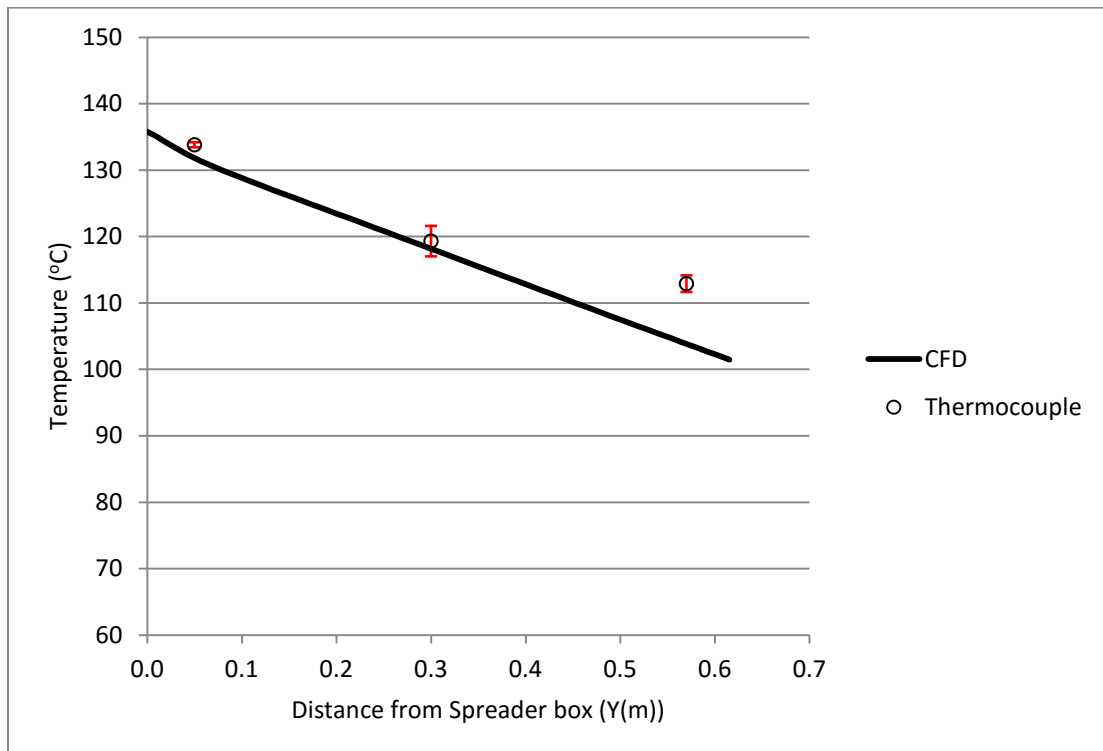


Figure 6.26: Comparison of CFD centreline temperature and discrete thermocouple temperature measurement, $d_s=290\mu\text{m}$, $m^o=0.066\text{kg/s}$ and slot width=20mm

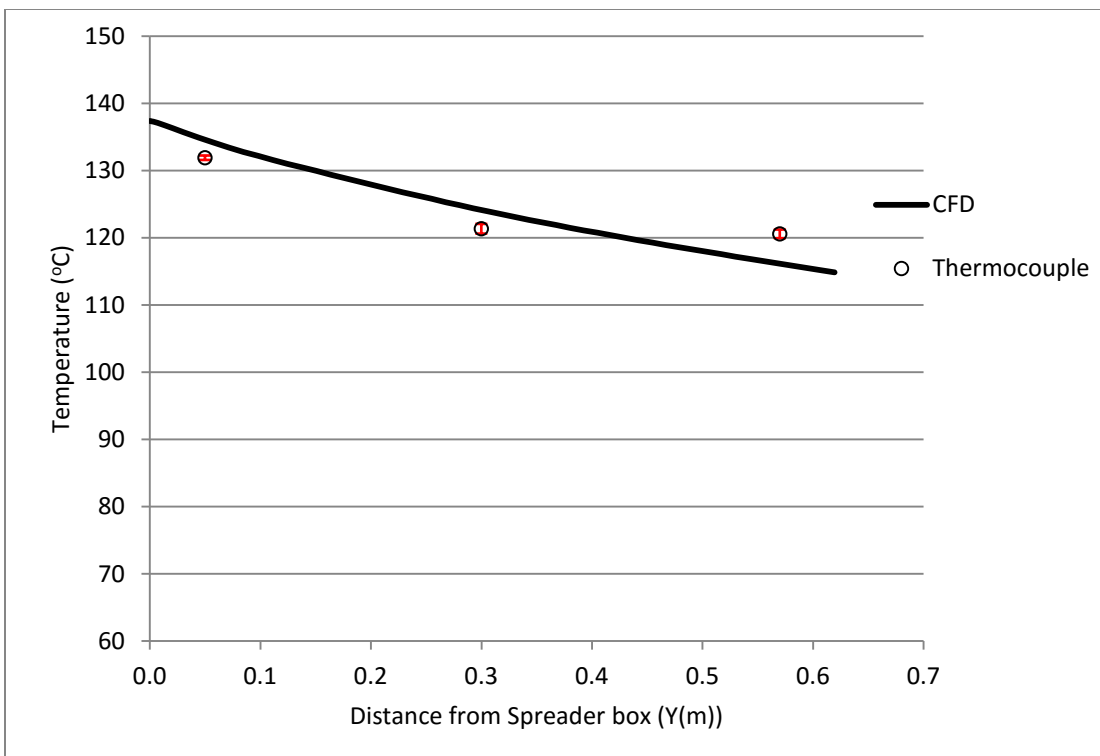


Figure 6.27: Comparison of CFD centreline temperature and discrete thermocouple temperature measurement, $d_s=400\mu\text{m}$, $m^{\circ}=0.132\text{kg/s}$ and slot width=20mm

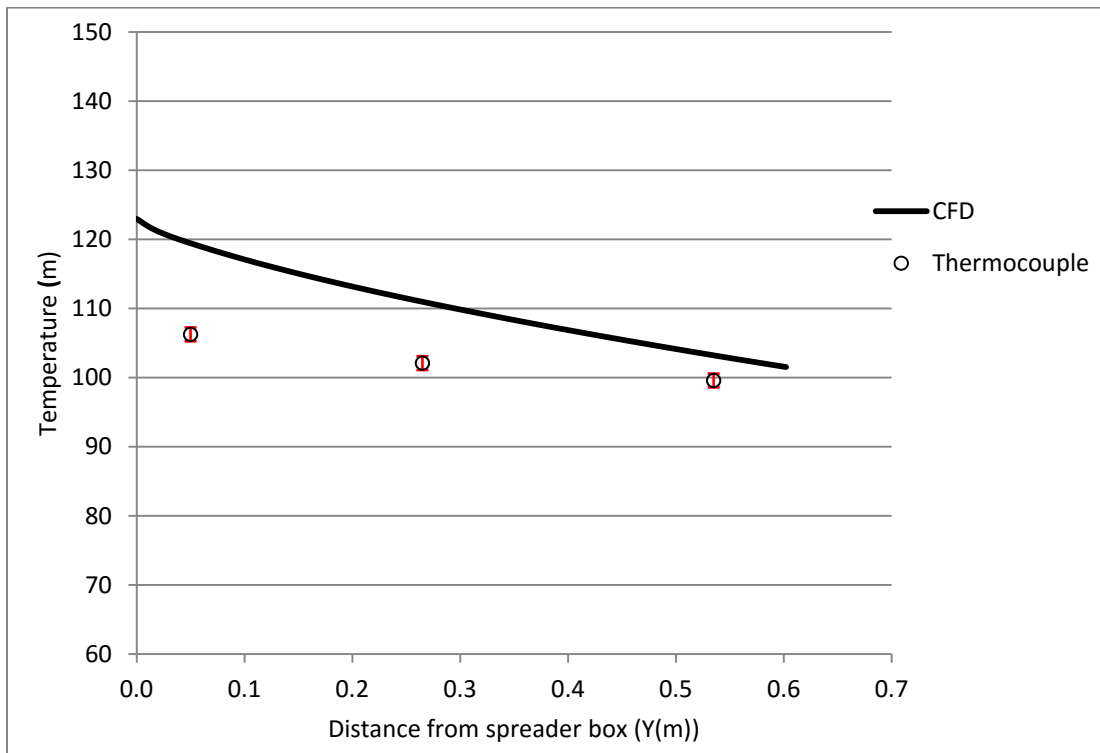


Figure 6.28: Comparison of CFD centreline temperature and discrete thermocouple temperature measurement, $d_s=610\mu\text{m}$, $m^{\circ}=0.047\text{kg/s}$ and slot width=60mm

In the figures that follow, CFD centreline temperature profile predictions are compared to raw thermographic data and modelled thermographic data. Figures 6.29-6.36 show a selection of results obtained for experimental conditions outlined in Table 4.3. For the conditions presented in Figures 6.29-6.32, it can be seen that there is a good agreement between CFD and raw infrared temperature profiles. In Figures 6.29-6.31, the back end of the adjusted infrared temperature profile shows a flattening which matches better the flattening profile shape from the thermocouple data. In Figures 6.33-6.35, the infrared temperature profiles are substantially changed because of low visible image pixel intensity. After adjustment, the profiles become more similar to the CFD model temperature predictions, and show the flattening behaviour expected.

Figure 6.36 shows a condition with very low pixel intensity. In this situation, the adjusted infrared temperature is unrealistic. More thermocouple and visible image data is necessary in these examples. This is because the critical pixel intensity for this particle size (derived at high mass flow rate) may not be suitable in this low mass flow rate condition. Thus, a wider set of conditions should be used to determine critical pixel intensities, including both high and low mass flow rate conditions.

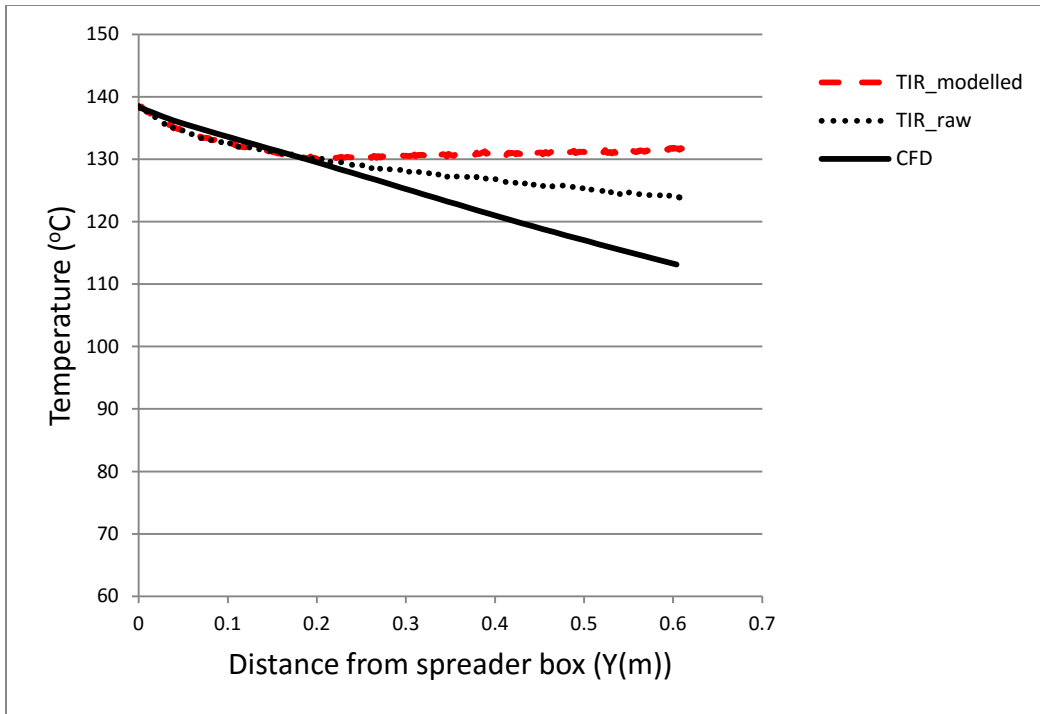


Figure 6.29: Comparison of CFD to raw and modelled infrared centreline temperatures, $d_s=290\mu\text{m}$, $m^o=0.15\text{kg/s}$ and slot width=20mm

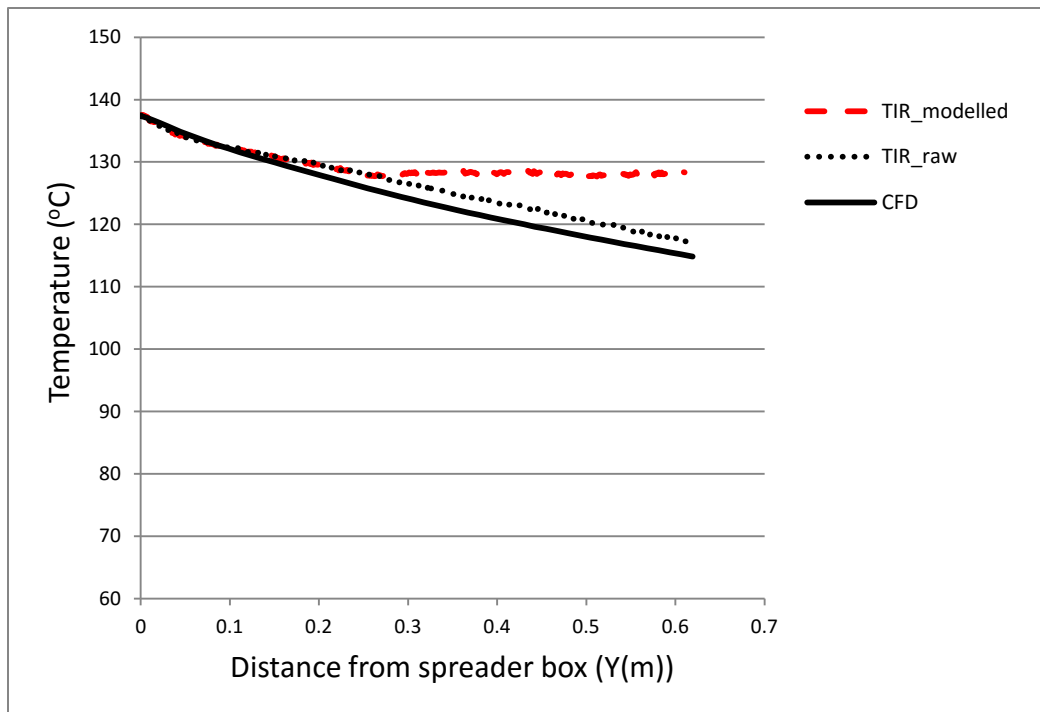


Figure 6.30: Comparison of CFD to raw and modelled infrared centreline temperatures, $d_s=400\mu\text{m}$, $m^o=0.132\text{kg/s}$ and slot width=20mm

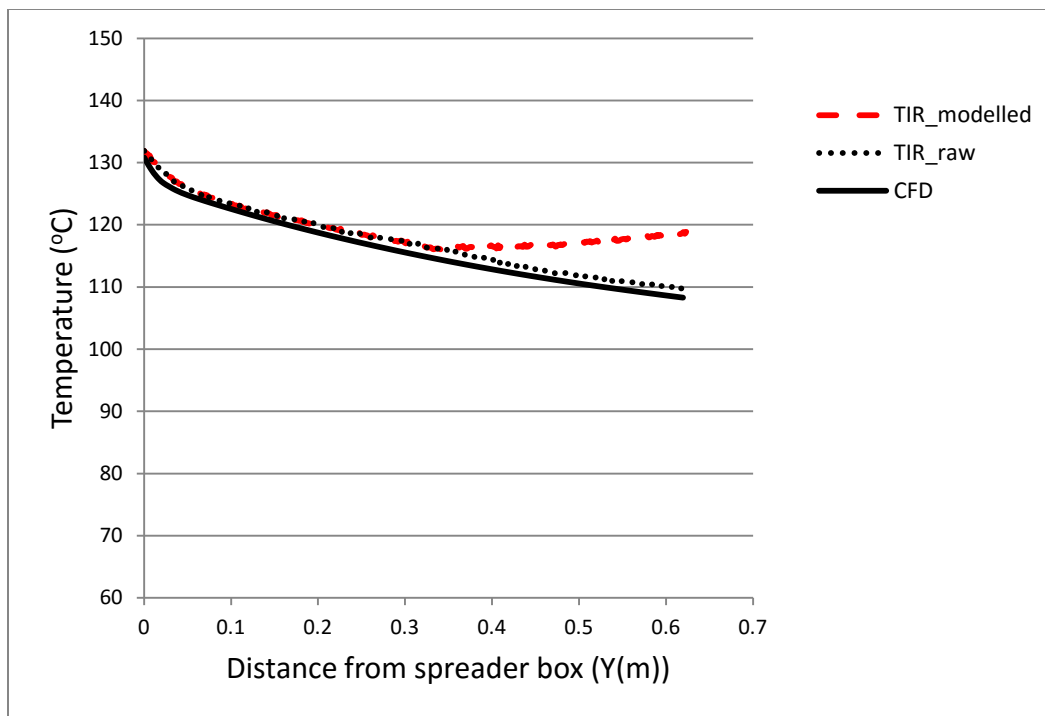


Figure 6.31: Comparison of CFD to raw and modelled infrared centreline temperatures, $d_s=400\mu\text{m}$, $m^o=0.141\text{kg/s}$ and slot width=60mm

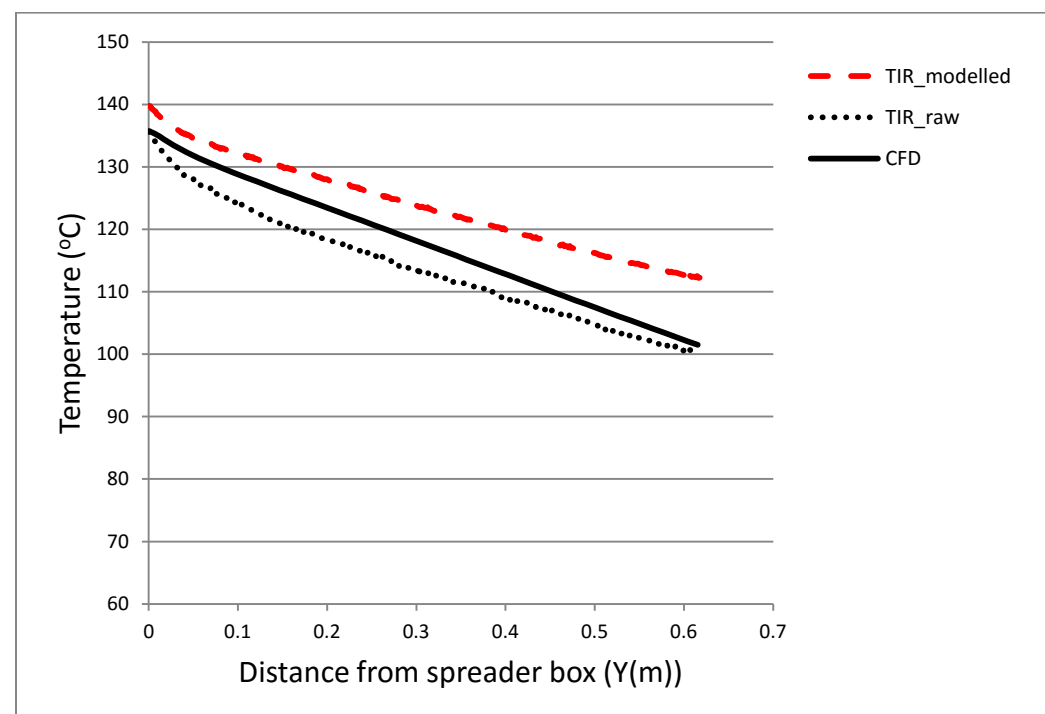


Figure 6.32: Comparison of CFD to raw and modelled infrared centreline temperatures, $d_s=290\mu\text{m}$, $m^o=0.066\text{kg/s}$ and slot width=20mm

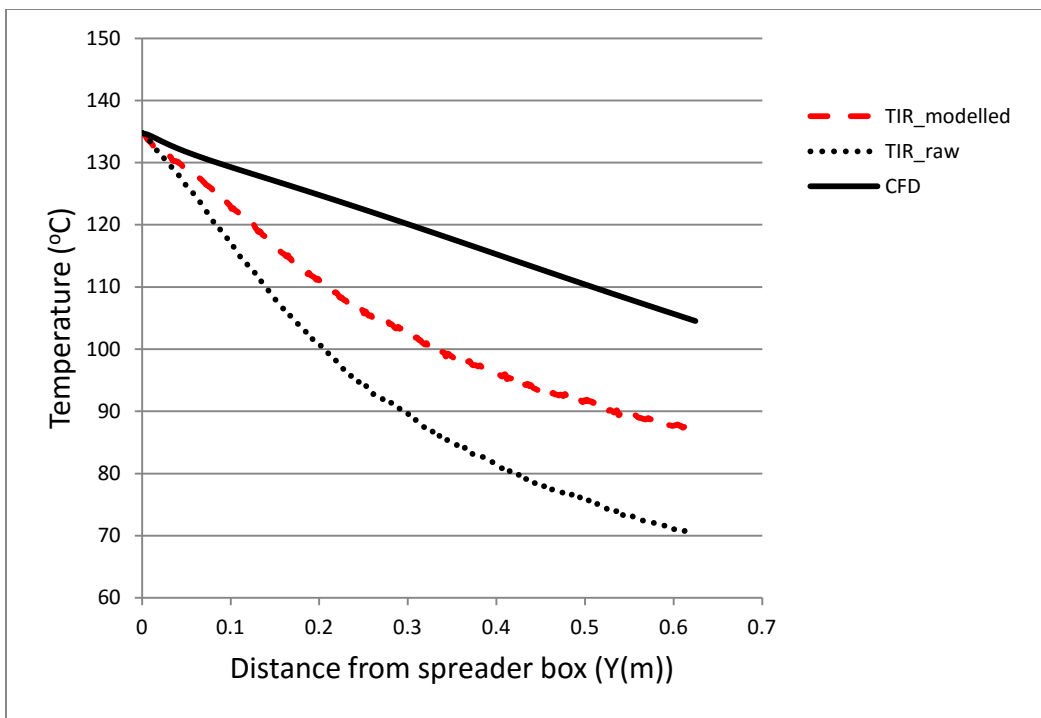


Figure 6.33: Comparison of CFD to raw and modelled infrared centreline temperatures, $d_s=400\mu\text{m}$, $m'=0.141\text{kg/s}$ and slot width=60mm

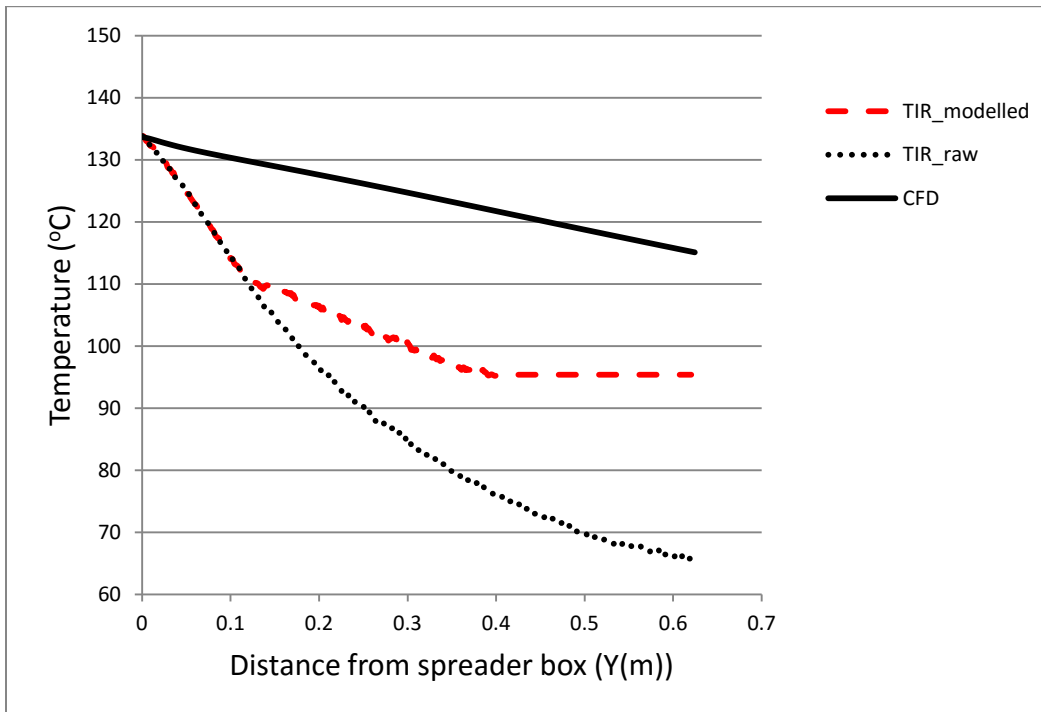


Figure 6.34: Comparison of CFD to raw and modelled infrared centreline temperatures, $d_s=610\mu\text{m}$, $m'=0.088\text{kg/s}$ and slot width=20mm

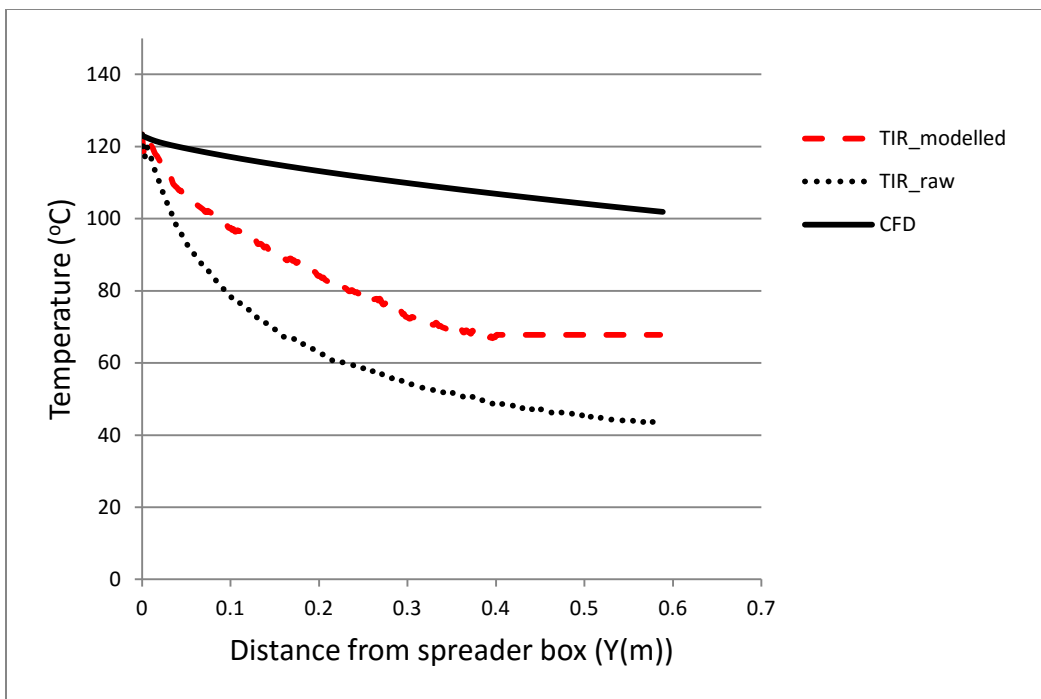


Figure 6.35: Comparison of CFD to raw and modelled infrared centreline temperatures, $d_s=610\mu\text{m}$, $m^o=0.047\text{kg/s}$ and slot width=60mm

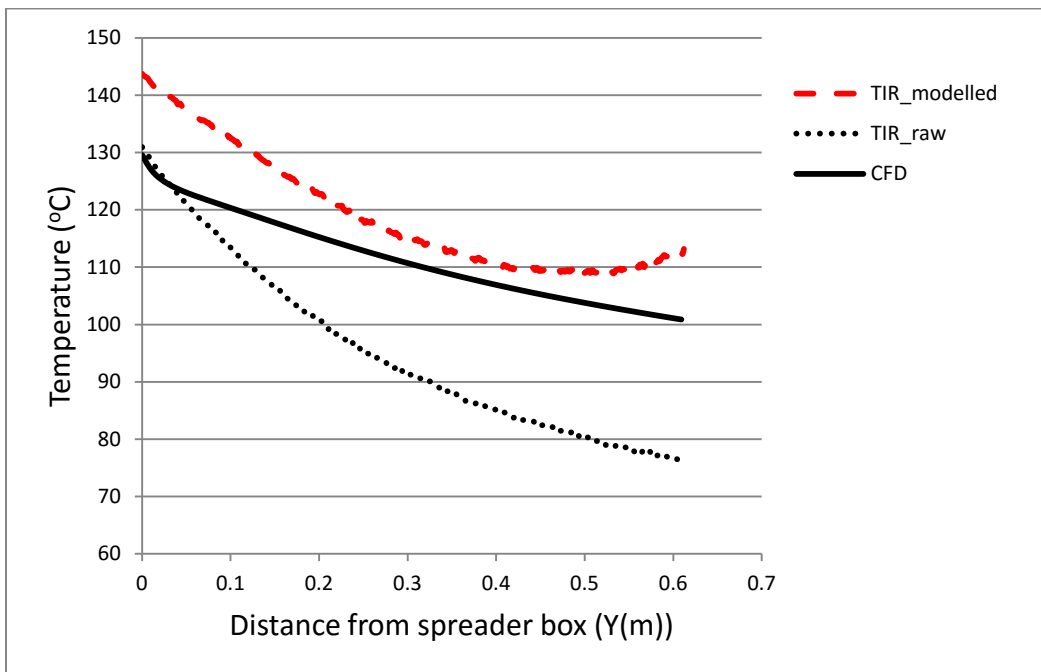


Figure 6.36: Comparison of CFD to raw and modelled infrared centreline temperatures, $d_s=400\mu\text{m}$, $m^o=0.071\text{kg/s}$ and slot width=60mm

6.2.3. CFD model investigations

ANSYS CFX software limitations, limit the ability to include important mechanisms such as internal heat conduction and radiation heat transfer. Therefore, the radiation heat transfer from the particle curtains which is in equilibrium with internal heat conduction of particles is not included in the CFD model. Furthermore, in the Eulerian-Eulerian CFD model, the average or ensemble temperature of particles within a control volume used in calculations. This is very different to the thermographic data where the surface temperature of particles is measured. In this section, a CFD-Hybrid model is introduced which includes internal heat conduction, and radiation heat transfer from the particles. The CFD-Hybrid model includes extracting CFD streamline data and embedding these data within a PDE system description for an isolated sphere undergoing convective and radiative heat transfer as well as internal heat conduction. The isolated sphere model is developed and solved using Matlab with extracted data from CFD modelling (see Appendix B.5). In this approach, a point in the middle of the frontal edge of the slot was defined at ($X=0.2525$, $Y=0.9m$ and $Z=0.075m$) and a streamline was generated using this as a starting point. Properties including heat transfer coefficient, time on streamline, y coordinate (falling distance) and air temperatures were exported to Matlab. To facilitate continuous integration, the heat transfer coefficient, air temperature and falling distance were fitted with polynomials as functions of time. Balance of energy conservation over a sphere is presented in Equation 6.1:

$$\rho_s C_p \frac{\partial T}{\partial t} = \frac{1}{r^2} \frac{\partial}{\partial r} (r^2 k_s \frac{\partial T}{\partial r}) \quad 6.1$$

The initial condition presented in Equation 6.2 describes the sphere initially at a uniform temperature (T_o):

$$T(0, r) = T_o \quad \text{at } t = 0 \quad 6.2$$

The boundary conditions are presented in Equations 6.3 and 6.4:

Heat transfer from the outer surface (R) is by convection and radiation, and in balance with internal heat conduction:

$$-k_s \frac{\partial T}{\partial r} = h(T_s - T_g) + e\sigma(T_s^4 - T_g^4) \quad \text{at } r = R \quad 6.3$$

Where $k_s = 0.18 \left(\frac{W}{m.K}\right)$, C_p is specific heat capacity of particle and is equal to $830 \left(\frac{J}{K.kg}\right)$, $\rho_s =$

$2500 \frac{kg}{m^3}$, σ is the Stefan Boltzmann constant ($\sigma = 5.67 \times 10^{-8} \frac{W}{m^2.K^4}$) and $0 \leq e \leq 1$ is the

emissivity of the object (in this research $e = 1$).

Equation 6.4 corresponds to no heat flow at the centre of the sphere. The temperature gradient at the centre of the sphere is zero:

$$\frac{\partial T}{\partial r}(t, 0) = 0 \quad \text{at } r = 0 \quad 6.4$$

Figure 6.37 shows the internal temperature distribution generated for the condition where internal heat conduction would be most significant (i.e. $610\mu m$). This also corresponding to the conditions where there are the most deviations between modelled and experimental temperature data. It can be seen that the centre of the particle displays higher temperatures compared to the surface of the

particle. However, including internal heat transfer in the model only makes 3°C difference between the surface and the centre of the particle. It is concluded that this can be neglected for the conditions examined in this thesis. Furthermore, the contributions of convective and radiative heat transfer were examined in two scenarios. For example, when $d_s=290\mu\text{m}$, $m^o=0.066\text{kg/s}$ and slot width=20mm, the contributions of convective and radiative heat transfer in the Hybrid model are 95% and 5% of the total heat transfer respectively. The contributions of convective and radiative heat transfer in the Hybrid model when $d_s=610\mu\text{m}$, $m^o=0.088\text{kg/s}$ and slot width=20mm are 89% and 11% of the total heat transfer respectively.

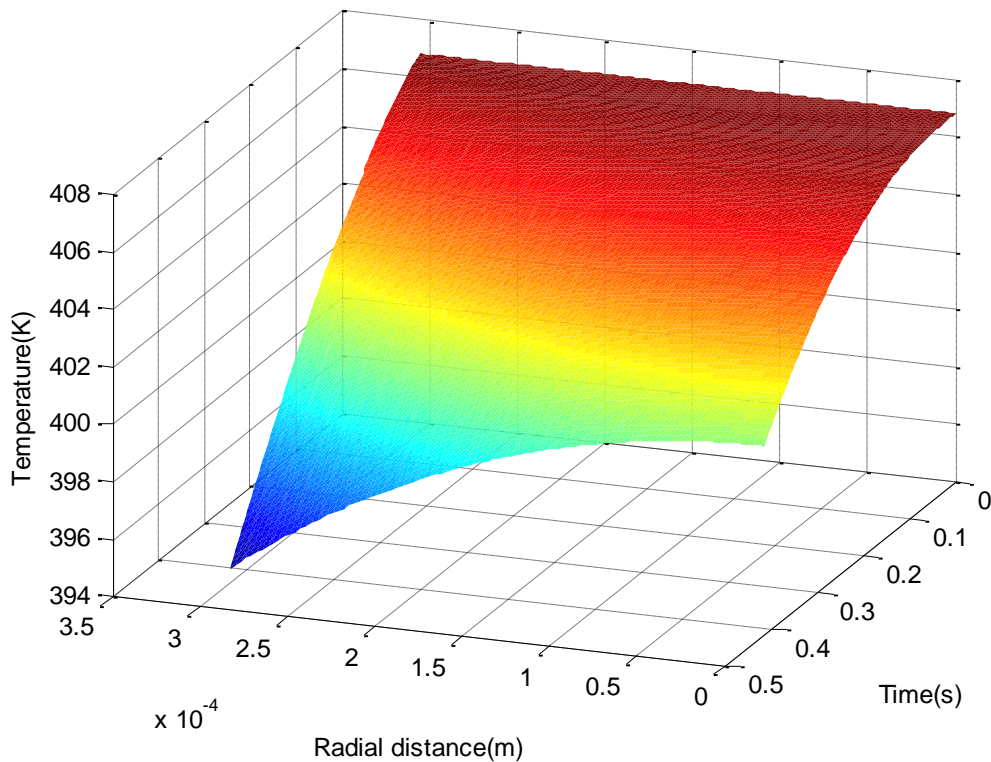


Figure 6.37: Radial distribution of temperature, $d_s=610\mu\text{m}$, $m^o=0.088\text{kg/s}$ and slot width=20mm

6.3. Conclusion

CFD model and thermographic results were presented for comparison. The effects of mass flow rate, particle size and slot width on raw centreline temperature profiles and 2D thermal images were investigated. The curtain centreline temperature showed the greatest drop at large particle sizes and low mass rates. The trends for the effect of particle size were more significant at low mass flow rates. CFD simulations were generally in agreement with the profiles. The gradient technique, based on temperature, was successfully applied to the thermal images. CFD and thermographic edges were well aligned and curtain shapes matched those expected from the literature. The shapes of the curtain were substantially influenced by the slot width. The particle curtains contracted as they fall for the large slot width (60mm) conditions and expanded for the small slot width conditions (20mm). The contracting curtains draw cool air into the bulk and increase heat transfer, despite similar centreline temperature profiles. Good agreement was found between CFD and direct thermocouple measurements, particularly for small and medium particle sizes. To examine the impacts of internal heat conduction and radiation heat transfer, a CFD-Hybrid model was developed. Adding these addition mechanisms, did not make substantial difference to the temperature profiles.

Chapter 7 Conclusions and Recommendations

7.1. Conclusion

Infrared thermography was carried out to investigate the thermal characteristics of hot particle curtains falling through ambient air. Image processing techniques were applied to the thermographic data to obtain edge locations and centreline temperatures, and to enable comparison to numerical predictions. 3D Eulerian-Eulerian modelling was undertaken for comparison to the image data. The CFD model predictions were used to generate reduced order models for reproducing bulk curtain behaviour.

An experimental apparatus was designed to generate a hot particle curtain with consistent mass flow rate and uniform discharge characteristics (temperature and flow). The design of the spreader box was successful, and led to highly consistent mass flow rates and evenly distributed temperature and solid concentrations. Thermal insulation of hopper /spreader box would improve this further. However, the manual valve made repeating precise mass flow rates difficult which makes subtle effects difficult to observe. It is important to undertake these types of experiments in a fully enclosed, climate controlled room, so that curtains are more symmetrical and there is minimal variation in the ambient parameters (air temperature and relative humidity) that influence heat transfer.

An infrared thermal camera and visible manual camera were used in an attempt to capture particle temperature and pixel intensity respectively. Infrared thermography is a fast, non-contact technique that provides a comprehensive 2D temperature map across the entire particle curtains. Image

processing techniques can be successfully applied to the raw image data. Matlab was extensively used to undertake image manipulations and was well-suited to the tasks required. Image manipulation is essential to handle the variations in the thermographic data. For example, Matlab was successfully applied to locate curtain edges using temperature gradient techniques adapted from visible image analysis. Image filtering and analysis makes it easier to compare thermal image data to CFD contour plots and profiles. Image analysis techniques used in this research can be applied in any particulate systems such as fluidised beds and solid particle receivers to calculate the average properties such as solid volume fraction and residence time. Generally, the most significant result in this research is a better understanding of the potentials and limitations of the use of infrared thermography in two-phase systems. Although thermography was demonstrated to be useful to obtain 2D temperature images of falling particle curtains, it was not able to measure the actual temperatures when the field of view is less occupied with the particles. This issue was addressed in this research by simultaneous incorporation of visible image photography to calculate solid volume fractions.

Comparison of infrared thermography to direct thermocouple measurements showed that infrared thermography is unable to accurately measure particle temperatures at some of the conditions investigated. For conditions of high mass flow rate ($m^o \geq 0.132 \text{ kg/s}$) and small and medium particles size ($d_s \leq 400\mu\text{m}$) infrared thermographic results were reliable. Temperature profiles for small particles ($290\mu\text{m}$), even at low mass flow rate conditions, were also reliable. Infrared thermography was found to be unreliable at large particle size and low mass flow rate, where solid volume fractions were low. In these situations, visible image pixel intensities were used to adjust infrared thermal data to account for the influence of background temperature. Combining infrared

and visible images can improve the reliability of infrared temperature data. However, a wider range of direct thermocouple data would help to improve model reliability.

Qualitative and quantitative observations of both centreline and 2D temperature profiles indicated that wide slot width (60mm), and low mass flow rates lead to maximum particle cooling. Centreline temperature profiles and 2D thermal contours are both necessary to understand particle cooling, reinforcing the value and usefulness of infrared thermography in two-phase systems.

CFD was found to be fast and computationally efficient technique for undertaking particle curtain simulations. This was important, because generating Reduced Order Models requires investigations a wide range of key factors (mass flow rate, particle size and slot width). In this work, ANOVA was used to evaluate the significance of these parameters. The results of thermal imagery mostly supported the conclusion drawn from the ANOVA, leading to confidence in the derived Reduced Order Models. The single particle model was modified to produce the Reduced Order Model, in which the magnitude of drag coefficient was altered. The drag coefficient was

$$\text{modified as follows: } C_D|_{ROM} = \frac{-20.19 + 65.254m^0 + 90175.1d_s}{1 + 22.045m^0 - 2257.49d_s} \times \frac{24}{Re} [1 + 0.15(Re)^{0.687}].$$

In this research, a model for hot particle curtains was obtained. This model can be used in flighted rotary dryers modelling to calculate the heat transfer between the air and particles. Furthermore, the CFD modelling in this work can be utilised to detect the particle curtain edges, but care must be taken within the bonds of reliability.

7.2. Recommendations

Based on the findings discussed in this thesis, the following recommendations are made.

- In characterising the thermal properties of low volume fraction and large particle size curtain, it is essential to obtain simultaneous visible and infrared thermal images. In this way, the visible image pixel intensity can be correlated to the precise infrared thermographic intensity, on a pixel by pixel basis (i.e. registration of images). To ensure high quality images, careful alignment of both the infrared and visible cameras in front of and perpendicular to spreader box and particle curtain is required. Ideally, a camera capable of simultaneous visible and infrared imagery capture is required. Unfortunately, the camera used in this work was unable to capture simultaneous images and the quality resolution of visible images was poor. A high quality manual visible image camera should be coupled to a high resolution infrared thermal camera.
- The use of infrared camera with higher spectral range sensitivity will be useful to obtain thermal images in which the particles are detectable from the background. This will enable us to filter the effect of background and calculate the particle true temperatures.
- In this work, the thermocouple measurements were taken on a limited range of mass flow rates. To generate a more comprehensive correlation for adjustment of recorded infrared temperatures, and accounting for the background influence, more measurements for each particle size are needed.

- In the experimental study, the hopper was fabricated with a valve to manually regulate the mass flow rates of particles and it was not possible to precisely fix the desired mass flow rate. In order to be able to generate and repeat the desired mass flow rates, and reduce experimental variability, there is a need to improve the experimental set-up with an alternative valve.
- Average or bulk properties are required for design. Furthermore, the Reduced Order Models produced using CFD simulations, are also based on average properties. It is important to be able to generate experimental average properties for comparison. To generate these properties, solids volume fraction and particle residence time need to be measured for the curtains, so that it can be correlated to the temperature.
- In this research, CFD model was developed using commercial software (ANSYS CFX V14.5). CFX limits the ability to include internal heat conduction and radiation heat transfer. This is considered as a deficiency of this commercial software. Therefore, to provide greater flexibility, it is recommended that open source software be utilised.
- In this research, Reduced Order Model was developed over a limited range of conditions to suit the experimental validation data set. To be more useful in modelling and design of full-scale flighted rotary dryer, there is a need to expand the range of conditions used to generate the ROM.

References

1. Kerkhof, P.J.A.M. and W.J. Coumans, *Drying : A Fascinating Unit Operation*. Chemical Engineering Journal, 2002. **86**(1-2): p. 1-2.
2. Glikin, P.G., *Transport of Solids Through Flighted Rotating Drums*. Transactions of the Institution of Chemical Engineers, 1978. **56** p. 120-126.
3. Revol, D., C.L. Briens, and J.M. Chabagno, *The Design of Flights in Rotary Dryers*. Powder Technology, 2001. **121**(2-3): p. 230-238.
4. Jamaleddine, T.J. and M.B. Ray, *Application of Computational Fluid Dynamics for Simulation of Drying Processes: A Review*. Drying Technology, 2010. **28**(2): p. 120-154.
5. Dufour, P., *Control Engineering in Drying Technology: Review and Trends*. Drying Technology, 2006. **24**(7): p. 889-904.
6. Lee, A., M.E. Sheehan, and P. Schneider. *Multi-Scale Process Models to Enable the Embedding of CFD Derived Functions: Curtian Drag in Flighted Rotary Dryers*. 10th International Conference on CFD in Oil and Gas, Metallurgical and Process Industries. 17-19 June 2014. Trondheim, Norway.
7. Britton, P.F., M.E. Sheehan, and P.A. Schneider, *A Physical Description of Solids Transport in Flighted Rotary Dryers*. Powder Technology, 2006. **165**(3): p. 153-160.
8. Sheehan, M.E., P.F. Britton, and P.A. Schneider, *A Model for Solids Transport in Flighted Rotary Dryers Based on Physical Considerations*. Chemical Engineering Science, 2005. **60**(15): p. 4171-4182.
9. Harker, J.H., et al., *Coulson and Richardson's Chemical Engineering, Volume 2, Particle Technology and Separation Processes*. Fourth ed., 1990, Woburn, Butterworth-Heinemann.
10. Kemp, I.C. and D.E. Oakley, *Modelling of Particulate Drying in Theory and Practice*. Drying Technology, 2002. **20**(9): p. 1699-1750.
11. Papadakis, S.E., et al., *Scale-up of Cascading Rotary Dryers*. Drying Technology, 1994. **21**(1-2): p. 259-277.
12. Reay, D., *A Scientific Approach to the Design of Continuous Flow Dryers for Particulate Solids*. Multiphase Science and Technology, 1989. **4**: p. 1-102.

13. Allen, T., *Particle Size Measurement- Volume 1- Powder Sampling and Particle Size Measurement*. Fifth ed., 1997, London, Weinheim, New York, Tokyo, Melbourne, Madras, Chapman and Hall.
14. Sherritt, R.G., et al., *The Movement of Solids Through Flighted Rotating Drums. Part I: Model Formulation*. The Canadian Journal of Chemical Engineering, 1993. **71**(3): p. 337-346.
15. Sherritt, R.G., et al., *The Movement of Solids Through Flighted Rotating Drums. Part II Solids-Gas Interaction and Model Validation*. . The Canadian Journal of Chemical Engineering, 1994. **72**(2): p. 240-248.
16. Lee, A., *Modelling the Solids Transport Phenomena within Flighted Rotary Dryer*. 2008, School of Science and Engineering, James Cook University, Townsville, Australia, PhD Thesis.
17. Kemp, I.C. and D.E. Oakley, *Simulation and Scale-Up of Pneumatic Conveying and Cascading Rotary Dryers* Drying Technology, 1997. **15**(6): p. 1699-1710.
18. Friedman, S.J. and J.R. Marshall, *Studies in Rotary Drying, Part I - Holdup and Dusting*. Chemical Engineering Progress, 1949. **45**(8): p. 482-493.
19. Shahhosseini, S., I.T. Cameron, and F.Y. Wang, *A Simple Dynamic Model for Solid Transport in Rotary Dryers*. Drying Technology, 2000. **18**(4-5): p. 867 - 886.
20. Song, Y., J. Thibault, and T. Kudra, *Dynamic Characteristics of Solids Transportation in Rotary Dryers*. Drying Technology, 2003. **21**(5): p. 755 - 773.
21. Cao, W.F. and T.A.G. Langrish, *Comparison of Residence Time Models for Cascading Rotary Dryers*. Drying Technology, 1999. **17**(4-5): p. 825-836.
22. Renaud, M., J. Thibault, and A. Trusiak, *Solids Transportation Model of an Industrial Rotary Dryer*. Drying Technology, 2000. **18**(4-5): p. 843-865.
23. Matchett, A.J. and M.S. Sheikh, *An Improved Model of Particle Motion in Cascading Rotary Dryers*. Chemical Engineering Research and Design, 1990. **68**(2): p. 139-148.
24. Wang, E.Y., et al., *A Distributed Parameter Approach to the Dynamics of Rotary Drying Process*. Drying Technology, 1993. **11**(7): p. 1641-1656.
25. Schofield, F.R. and P.G. Glikin, *Rotary Dryers and Coolers for Granular Fertilizers*. Transactions of the Institute of Chemical Engineers, 1962. **40**: p. 183-190.
26. Baker, C.G.J., *Air-Solids Drag in Cascading Rotary Dryers*. Drying Technology, 1992. **10**(2): p. 365-393.

27. Matchett, A.J. and C.G.J. Baker, *Particle Residence Times in Cascading Rotary Dryers Part 2- Application of the Two-Stream Model to Experimental and Industrial Data*. Journal of Separatoin Process Technology 1988. **9**: p. 5-13.
28. Duchesne, C., J. Thibault, and C. Bazin, *Modeling of the Solids Transportation within an Industrial Rotary Dryer: A Simple Model*. Industrial and Engineering Chemistry Research, 1996. **35**(7): p. 2334-2341.
29. Ajayi, O.O. and M.E. Sheehan, *Pseudophysical Compartment Modeling of an Industrial Rotary Dryer with Flighted and Unflighted Sections: Solids Transport*. Industrial and Engineering Chemistry Research, 2014. **53**(41): p. 15980–15989.
30. Schofield, F.R. and P.G. Glikin, *Rotary Dryers and Coolers for Granular Fertilizers*. Transactions of Institute of Chemical Engineers, 1962. **40**: p. 183-190.
31. Gidaspow, D., *Multiphase Flow and Fluidization: Continuum and Kinetic Theory Descriptions*. First ed., 1994, Academic Press, San Diego.
32. Lun, C.K.K., et al., *Kinetic Theories for Granular Flow: Inelastic Particles in Couette Flow and Slightly Inelastic Particles in a General Flowfield*. Journal of Fluid Mechanics, 1984. **140**: p. 223-256.
33. Xiaofang, W., et al., *Flow Behaviors of Gas-Solid Injector by 3D Simulation with Kinetic Theory of Granular Flow*. Chinese Journal of Chemical Engineering, 2008. **16**(6): p. 823-831.
34. Huilin, L., et al., *Hydrodynamic Simulation of Gas–Solid Flow in a Riser Using Kinetic Theory of Granular Flow*. Chemical Engineering Journal, 2003. **95**(1–3): p. 1-13.
35. Stokes, G.G., *On the Effect of the Internal Friction of Fluids on the Motion of Pendulums*. Transactions of the Cambridge Philosophical Society, 1851. **9**: p. 8-106.
36. Lundberg, J., *CFD Study of a Bubbling Fluidized Bed*. 2008, Faculty of Technology, Telemark University College, Porsgrunn, Norway, Master Thesis.
37. Wen, C.Y. and Y.H. Yu, *Mechanics of Fluidization*. Chemical Engineering Progress Symposium Series, 1966. **62**: p. 100-111.
38. Kuan, B. and P. Schwarz. *Numerical Prediction of Particulate Flows with Dilute Suspension in a Vertical Upflow Circular Duct: A Parametric Study*. DMR-1930, CSIRO-Minerals. 2002. Melbourne, Australia.
39. Richardson, J.F. and W.N. Zaki, *Sedimentation and Fluidisation:Part I*. Transactions of the Institution of Chemical Engineering, 1954. **32**(1): p. 35-53.

40. Schiller, L. and A.Z. Naumann, *Über Die Grundlegenden Berechnungen Bei Der Schwerkraftaubereitung*. Zeitschrift Verein Deutscher Ingenieure, 1933. **77**(12): p. 318-320.
41. Syamlal, M. and T.J. O'Brien, *Simulation of Granular Layer Inversion in Liquid Fluidized Beds*. International Journal of Multiphase Flow, 1988. **14**(4): p. 473-481.
42. Dalla Valle, J.M., *Micromeritics*. Second ed., 1948, New York, Toronto, London, Pitman Publishing Corp.
43. Di Felice, R., *The Voidage Function for Fluid-Particle Interaction Systems*. International Journal of Multiphase Flow, 1994. **20**(1): p. 153-159.
44. Papadikis, K., S. Gu, and A.V. Bridgwater, *Computational Modelling of the Impact of Particle Size to the Heat Transfer Coefficient Between Biomass Particles and a Fluidised Bed*. Fuel Processing Technology, 2010. **91**(1): p. 68-79.
45. Ma, A.C., et al., *Numerical Study on Pressure Prediction and Its Main Influence Factors in Pneumatic Conveyors*. Chemical Engineering Science, 2010. **65**(23): p. 6247-6258.
46. Zhang, K., J. Zhang, and B. Zhang, *CFD Simulation of Jet Behaviour and Voidage Profile in a Gas-Solid Fluidized Bed*. International Journal of Energy Research, 2004. **28**(12): p. 1065-1074.
47. Wardjiman, C., et al., *Behaviour of a Curtain of Particles Falling Through a Horizontally-Flowing Gas Stream*. Powder Technology, 2008. **188**(2): p. 110-118.
48. Wardjiman, C., et al., *Shape of a Particle Curtain Falling in Stagnant Air*. Powder Technology, 2009. **192**(3): p. 384-388.
49. Hurby, J., et al., *An Experimental and Numerical Study of Flow and Convective Heat Transfer in a Freely Falling Curtain of Particles*. Journal of Fluids Engineering, Transactions of the ASME, 1988. **110**(2): p. 172-181.
50. Kassoy, D.R., T.C. Adamson, and A.F. Messiter, *Compressible Low Reynolds Number Flow Around a Sphere*. The Physics of Fluids, 1966. **9**(4): p. 671-681.
51. Babiy, V.I. and I.P. Ivanova, *Aerodynamic Resistance of a Particle in a Nonisothermal Condition*. Teploenergetika, 1965. **9**: p. 19-23.
52. Basina, I.P. and I.A. Maksimov, *Effect of Nonisothermicity on the Aerodynamic Drag on a Spherical Particle*. Heat Tranfer-Soviet Research, 1970. **2**(6): p. 69-75.
53. Gaitone, U., *Quality Criteria for Large Eddy Simulation* 2008, University of Manchester, Manchester, UK, First Year Transfer of Report.

54. Chen, C.J. and S.Y. Jaw, *Fundamentals of Turbulence Modeling*. 1998, Washington, DC., Taylor and Francis.
55. Kuang, S.B., et al., *Application of Periodic Boundary Conditions to CFD-DEM Simulation of Gas–Solid Flow in Pneumatic Conveying*. Chemical Engineering Science, 2013. **93**: p. 214-228.
56. Ranz, W.E. and W.R. Marshall, *Evaporation from Drops*. Chemical Engineering Progress, 1952. **48**(3): p. 141-146.
57. Issa, S.A., *Experimental Investigation and CFD Validation of Two-Phase Phenomena Related to Nuclear Safety Research During LUCA Accidents*. 2014, Faculty of Mechanical Engineering, Technical University of Munich, Munich, Germany, Ph.D Thesis.
58. Chen, H., et al., *Computational Fluid Dynamics Modeling of Gas-Particle Flow Within a Solid-Particle Solar Receiver*. Journal of Solar Energy Engineering, 2007. **129**(2): p. 160-170.
59. Rickelt, S., et al., *Coupled DEM/CFD Simulation of Heat Transfer in a Generic Grate System Agitated by Bars*. Powder Technology, 2013. **249**: p. 360-372.
60. Kreith, F. and M.S. Bohn, *Principles of Heat Transfer*. Forth ed., 1986, New York, Cambridge, Philadelphia, San Francisco, Washington, London, Mexico City, Sao Paulo, Singapore, Sydney, Harper and Row, Publishers, Inc.
61. Incropera, F.P. and D.P. DeWitt, *Fundamentals of Heat and Mass Transfer*. 5th ed., 2002, John Wiley & Sons, Inc.
62. Langrish, T.A.G., *Multi-Scale Mathematical Modelling of Spray Dryers*. Journal of Food Engineering, 2009. **93**(2): p. 218-228.
63. Dehnavi, M.A., et al., *CFD Simulation of Hydrodynamics and Heat Transfer in Gas Phase Ethylene Polymerization Reactors*. International Communications in Heat and Mass Transfer, 2010. **37**(4): p. 437-442.
64. Wang, Y., et al., *A New Drag Model for TFM Simulation of Gas–Solid Bubbling Fluidized Beds with Geldart-B Particles*. Particuology, 2014. **15**: p. 151-159.
65. Grena, R., *Thermal Simulation of a Single Particle in a Falling-Particle Solar Receiver*. Solar Energy, 2009. **83**(8): p. 1186-1199.
66. Papadikis, K., S. Gu, and A.V. Bridgwater, *CFD Modelling of the Fast Pyrolysis of Biomass in Fluidised Bed Reactors: Modelling the Impact of Biomass Shrinkage*. Chemical Engineering Journal, 2009. **149**(1-3): p. 417-427.

67. Papadikis, K., A.V. Bridgwater, and S. Gu, *CFD Modelling of the Fast Pyrolysis of Biomass in Fluidised Bed Reactors, Part A: Eulerian Computation of Momentum Transport in Bubbling Fluidised Beds*. Chemical Engineering Science, 2008. **63**(16): p. 4218-4227.
68. Papadikis, K., S. Gu, and A.V. Bridgwater, *CFD Modelling of the Fast Pyrolysis of Biomass in Fluidised Bed Reactors. Part B: Heat, Momentum and Mass Transport in Bubbling Fluidised Beds*. Chemical Engineering Science, 2009. **64**(5): p. 1036-1045.
69. Ogata, K., K. Funatsu, and Y. Tomita, *Experimental Investigation of a Free Falling Powder Jet and the Air Entrainment*. Powder Technology, 2001. **115**(1): p. 90-95.
70. Wardjiman, C. and M. Rhodes, *Heat Transfer in a Particle Curtain Falling Through a Horizontally-Flowing Gas Stream*. Powder Technology, 2009. **191**(3): p. 247-253.
71. McGaw, D.R., *Gas-Particle Heat Transfer in a Crossflow Moving Packed Bed Heat Exchanger*. Powder Technology, 1976. **13**(2): p. 231-239.
72. McGaw, D.R., *Heat Transfer in Shallow Crossflow Fluidised bed Heat Exchangers- I. A Generalised Theory* International Journal of Heat and Mass Transfer, 1976. **19**(6): p. 657-663.
73. Frain, M.J., D.P. Schmidt, and W.A. Fiveland, *An Experimental Investigation of the Influence of Gas and Solid Particle Interaction on the Heat Transfer Effectiveness of a Falling-Bed Heat Exchanger*. ASME, Journal of Heat Transfer, 2005. **127**(10): p. 1077-1086.
74. Kim, K., et al., *A Study of Solid Particle Flow Characterization in Solar Particle Receiver*. Solar Energy, 2009. **83**(10): p. 1784-1793.
75. Pei, P., K. Zhang, and D. Wen, *Comparative Analysis of CFD Models for Jetting Fluidized Beds: The Effect of Inter-Phase Drag Force*. Powder Technology, 2012. **221**: p. 114-122.
76. *Engineering Equation Solver (EES)*, Academic Commercial V9.447 © 1992-2013,Klein, S.A. Available at www.jchart.com.
77. Melling, A., et al., *Interpolation Correlations for Fluid Properties of Humid Air in the Temperature Range 100°C to 200°C*. Journal of Physical and Chemical Reference data, 1997. **26**(4): p. 1111-1123.
78. *ANSYS CFX-Pre, Release 14.5, 2013*, ANSYS Inc., Canonsberg.
79. Thanh, T.B., K. Will Cox, and O. Ghattas, *Parametric Reduced-Order Models for Probabilistic Analysis of Unsteady Aerodynamic Applications*. American Institute of Aeronautics and Astronautics, 2008. **46**(10): p. 2520-2529.

80. *CurveExpert Professional, version 2.04, Copyright©2011-2014, Daniel G. Hyams, available at <http://www.curveexpert.net/products/curveexpert-professional/>.*
81. Dodds, D.S. and J. Naser. *The Effect of Particle Concentration on the Coefficient of Drag of a Spherical Particle.* 15th Australian Mechanics Conference. 13-17 December 2004. Sydney, Australia.
82. Hildebrandt, C., C. Raschner, and K. Ammer, *An Overview of Recent Application of Medical Infrared Thermography in Sports Medicine in Austria.* Sensors, 2010. **10**(2): p. 4700-4715.
83. Esteve Agelet, L., et al., *Feasibility of Near Infrared Spectroscopy for Analyzing Corn Kernel Damage and Viability of Soybean and Corn Kernels.* Journal of Cereal Science, 2012. **55**(2): p. 160-165.
84. Adib, A.M., et al., *Two-Dimensional Correlation Infrared Spectroscopy Applied to Analyzing and Identifying the Extracts of Baeckea Frutescens Medicinal Materials.* Journal of Pharmaceutical and Biomedical Analysis, 2014. **96**: p. 104-110.
85. Akafuah, N.K., A.J. Salazar, and K. Saito, *Infrared Thermography-Based Visualization of Droplet Transport in Liquid Sprays.* Infrared Physics & Technology, 2010. **53**(3): p. 218-226.
86. Lahiri, B.B., et al., *Quantification of Defects in Composites and Rubber Materials Using Active Thermography.* Infrared Physics and Technology, 2012. **55**(2-3): p. 191-199.
87. Maldague, X., *Theory and Practice of Infrared Technology for Nondestructive Testing.* first ed., 2001, New York, John Wiley and Sons Inc.
88. Fauci, M.A., et al., *Medical Infrared Imaging—Differentiating Facts from Friction, and the Impact of High Precision Quantum Well Infrared Photodetector Camera Systems, and Other Factors, in its Reemergence.* Infrared Physics and Technology, 2001. **42**(3-5): p. 334–344.
89. Kylili, A., et al., *Infrared Thermography (IRT) Applications for Building Diagnostics: A Review.* Applied Energy, 2014. **134**: p. 531-549.
90. Budzier, H. and G. Gerlach, *Thermal Infrared Sensors, Theory, Optimisation and Practice.* First ed., 2011, Chichester, John Wiley and Sons, Ltd.
91. Astarita, T., et al., *A Survey on Infrared Thermography for Convective Heat Transfer Measurements.* Optics and Laser Technology, 2000. **32**(7–8): p. 593-610.

92. Yamada, J., et al., *Direct-Contact Heat Exchange Between Fluidized Particles and a Heat Transfer Surface in a Fluidized Bed: Temperature Visualization of Fluidizing Particles*. Heat Transfer-Asian Research, 2002. **31**(2): p. 165-181.
93. Dang, T.Y.N., et al., *Development of a Novel Infrared Technique for Instantaneous, Whole-Field, Non Invasive Gas Concentration Measurements in Gas–Solid Fluidized Beds*. Chemical Engineering Journal, 2013. **219**: p. 545-557.
94. Patil, A.V., et al., *Modeling Bubble Heat Transfer in Gas–Solid Fluidized Beds Using DEM*. Chemical Engineering Science, 2014. **105**: p. 121-131.
95. Hergert, W. and T. Wriedt, *The Mie Theory: Basics and Applications*. 2012, Bremen, Springer.
96. Bas, N., *Mathematical Modelling and Optimisation of the Formulation and Manufacture of Aggregate Food Products*. 2010, Department of Process and Chemical Engineering, University College Cork, Cork, Irland, PhD Thesis.
97. Dawson, S.G.B., B.J. Harris, and C.E. Davies. *Charactristics of Venturi Feeders for Powders*. in *Chemeca*.23-25 August 1989,Broadbeach, QLD, Australia.
98. *Thermal imaging guidebook for industrial applications*. 2011, ©Copyright, FLIR Systems AB.
99. Rice, P., *Digital Infrared Photography-Professional Techniques and Images*. 2005, Buffalo, Amherst Media.
100. *ImageJ 1.45s*, Wayne Rasband, National Institutes of Health, USA. Available at <http://imagej.nih.gov/ij/>.
101. Buades, A., B. Coll, and J.M. Morel, *A Review of Image Denoising Algorithms, With a New One*. Multiscale Modeling and Simulation: A SIAM Interdisciplinary Journal, 2005. **4**(2): p. 490-530.
102. Dare, J.W., *Experimental Analysis of Heat Transfer in Particle Curtains*. 2014, School of Science and Engineering, James Cook University, Townsville, Australia B.Sc.
103. *Infrared Thermometers Handbook* available at www.scigiene.com.
104. Buijtenen, M.S., et al., *An Experimental Study of the Effect of Collision Properties on Spout Fluidized Bed Dynamics*. Powder Technology, 2011. **209**(1-2): p. 139-148.
105. Catté, F., et al., *Image Selective Smoothing and Edge Detection by Nonlinear Diffusion*. SIAM Journal on Numerical Analysis, 1992. **29**(1): p. 182-193.

106. NEC Avio Infrared Technologies Co., L., Infrared Thermography H2600 Series Operation Manual.

Appendix A, Engineering Equation Solver[©] Code

Single Particle Model (SPM)

{Constants}

v_0 = 0.0486[m/s]	"Initial velocity of particle"
z_0=0 [m]	"initial position"
Temp_p_i = 400 [K]	"Initial particle temperature"
Temp_air = 300 [K]	"Air temperature"

{Physical Properties}

D_p = 0.0006 [m]	"Particle diameter"
rho_air = 1.1614 [kg/m^3]	"Air density" {ideal gas equation}
rho_p=2634 [kg/m^3]	"Particle density"
L_c = D_p/6	"Characteristic length"
Kinematic_visc_air = 0.00001589 [m^2/s]	"Kinematic viscosity of air"
alpha = 0.0000225 [m^2/s]	"Thermal diffusivity"
Pr = Kinematic_visc_air /alpha	"Prandtl number"
g = 9.81[m/s^2]	"Gravitational acceleration"
A_circle = Pi *(D_p^2)/4	"Cross-sectional area of the particle"
A_sphere= Pi *(D_p^2)	"Particle surface area"
Vol = Pi * (D_p^3) / 6	"Volume of the particle"
Mass_p=Vol*rho_p	"Mass of the particle"

{Cp and K equations }

Cp_RM_p=0.9125*Temp_RM_p+522.5	[J/kg K]	"Heat capacity of the particle"
--------------------------------	----------	---------------------------------

Cond_p=0.0000005*Temp_RM_p^2+0.0017*Temp_RM_p+0.6545	[W/m K]
--	---------

"Thermal conductivity of particle"

Cond_air=0.002741	[W/m K]	"Thermal conductivity of air"
-------------------	---------	-------------------------------

{Drag Using Schiller-Naumann Equation}

$$Cd_{RM_p} = (24 / Re_p) * (1 + 0.15 * (Re_p^{0.687})) \quad "Drag coefficient"$$

$$Re_p = v * D_p / Kinematic_visc_air \quad "Reynolds number"$$

$$dv/dt = g - (\rho_{air} * v^2 * Cd_{RM_p} * A_{circle}) / (2 * Mass_p)$$

$$F_{grav} = Mass_p * 9.81 \quad "Gravitational force"$$

$$F_{drag} = 1/2 * \rho_{air} * Cd_{RM_p} * A_{circle} * v^3 \quad "Drag force"$$

$$v = v_0 + \int (dv/dt, t, 0, t_f) \quad "Particle velocity"$$

$$dz/dt = v$$

$$z = z_0 + \int (dz/dt, t, 0, t_f) \quad "Particle falling distance"$$

$$t_f = 0.6[s] \quad "Final time"$$

\$integraltable

t, v, dv/dt, z, Temp_RM_p, dz/dt, h_RM_p, Re_p, Cd_RM_p, Nus_RM_p, Cp_RM_p, Cond_p, Bi_RM_p,

F_drag, HeatLoss, dTemp_RM_pdt,

{Heat transfer using Ranz-Marshall Correlation}

$$Nus_{RM_p} = 2 + 0.6 * Re_p^{0.5} * Pr^{(0.3)} \quad "Nusselt number"$$

$$h_{RM_p} = cond_air * Nus_{RM_p} / D_p \quad "Heat transfer coefficient"$$

$$dT_{temp_RM_pdt} = ((A_{sphere} * h_{RM_p}) / (Mass_p * Cp_RM_p)) * (Temp_air - Temp_RM_p)$$

$$Temp_RM_p = Temp_p_i + \int (dT_{temp_RM_pdt}, t, 0, t_f) \quad "Particle temperature"$$

$$Bi_{RM_p} = h_{RM_p} * L_c / Cond_p \quad "Biot number"$$

HeatLoss =Cp_RM_p * dTemp_RM_pdt "Particle heat loss"

Appendix B, Matlab® Codes

B.1 Reduced Order Model (ROM)

```
% this section defines the single particle model in the absence of internal heat conduction
function [dim_Temp_SP]= SingleParticle(A_param,CFD_z, CFD_Tf)
% A_param is a single float constant used for optimising the model
% (Cd_RM_p(t)=A*(24 /Re_p(t))*(1+0.15*(Re_p(t)^0.687)). )
% particle and air properties
Temp_p_i = 400; % initial particle temperature [K]
Temp_air = 300; % initial air temperature [K]
D_p=0.0006; % particle diameter [m]
rho_air = 1.1614; % air density
Cond_air=0.002741; % air thermal conductivity
rho_p=2634; % particle density [kg/m3]
L_c = D_p/6; % characteristic length of the particle
Kinematic_visc_air = 0.00001589; % kinematic viscosity of the air
alpha = 0.0000225; % thermal diffusivity
Pr = Kinematic_visc_air /alpha; % Parndtle number
g = 9.81 ; % gravity
A_circle = 3.14 *( D_p^2)/4 ; % frontal area of the particle
A_sphere= 3.14 *( D_p^2); % area of the particle
Vol = 3.14 * (D_p^3) / 6; % volume of the particle
Mass_p=Vol*rho_p; % mass of the particle
time=[0:0.00125:5]; % time discritisation
n=size(time,2);
v=zeros(1,n);
z=zeros(1,n);
Re_p=zeros(1,n);
Cd_RM_p=zeros(1,n);
```

```

dvdt=zeros(1,n);
dzdt=zeros(1,n);
h_RM_p=zeros(1,n);
Nus_RM_p=zeros(1,n);
Cp_RM_p=zeros(1,n);
dTemp_RM_pdt=zeros(1,n);
Temp_RM_p=zeros(1,n);

% initialising

v(1) = 0.0199; %initial velocities at  $m^o$  = 0.041,0.1,0.2kg/s are 0.0199,0.0486,0.0973m/s
%respectively

z(1) = 0; %initial height

Re_p(1)=v(1)*D_p/Kinematic_visc_air; %Reynolds number

Cd_RM_p(1)=A_param*(24 /Re_p(1))*(1+0.15*(Re_p(1)^0.687)); %drag coefficient

dvdt(1)=g-(rho_air*v(1)^2*Cd_RM_p(1)*A_circle/(2*Mass_p));
dzdt(1)= v(1);

Nus_RM_p(1)=2+0.6*Re_p(1)^0.5*Pr^(0.3);
Temp_RM_p(1)=400; %initial particle temperature

h_RM_p(1)=Cond_air*Nus_RM_p(1)/D_p;

Cp_RM_p(1)=0.9125*Temp_RM_p(1)+522.5 ;

dTemp_RM_pdt(1)=((A_sphere*h_RM_p(1))/(Mass_p*Cp_RM_p(1)))*(Temp_air-
Temp_RM_p(1));

for t=2:1:n % starts from t=2

v(t)=v(1)+(sum(dvdt(1:t-1))*(time(t)-time(t-1)));

```

```

Re_p(t)=v(t)*D_p/Kinematic_visc_air;
Cd_RM_p(t)=A_param* ( (24/Re_p(t))*(1+0.15*(Re_p(t)^0.687)) );
dvdt(t)=g-(rho_air*v(t)^2*Cd_RM_p(t)*A_circle/(2*Mass_p));
dzdt(t)=v(t);
z(t)=z(1)+( sum(dzdt(1:t-1))*(time(t)-time(t-1)));
Nus_RM_p(t)=2+0.6*Re_p(t)^0.5*Pr^(0.3);
h_RM_p(t)=Cond_air*Nus_RM_p(t)/D_p;
Temp_RM_p(t)=Temp_RM_p(1)+( sum(dTemp_RM_pdt(1:t-1))*(time(t)-time(t-1)));
Cp_RM_p(t)=0.9125*Temp_RM_p(t)+522.5 ;
dTTemp_RM_pdt(t)=((A_sphere*h_RM_p(t))/(Mass_p*Cp_RM_p(t)))*(Temp_air-
Temp_RM_p(t));
end

%range of temperature and z
Z=z(z<=0.9);
TempSPindex=find(z<=0.9);
TempSP=Temp_RM_p(TempSPindex);

%non-dimensionalised temperature
dim_Temp_SP=(TempSP-CFD_Tf)/(400-CFD_Tf);
z_SP_adjusted1=0.9-Z;
dim_Temp_SP = dim_Temp_SP(end:-1:1); % reorder the results in ascending fashion
z_SP_adjusted1 = z_SP_adjusted1(end:-1:1); % reorder the results in ascending fashion

```

```

dim_Temp_SP=interp1(Z,dim_Temp_SP ,CFD_z,'spline');

end

%=====

%This section is the entry point for the algorithm which controls the pre-defined parameters,
%optimization and evaluation steps.

function [ cost ] = myCostFunction( X, singleParticleConstants )

CFD_Tf = singleParticleConstants(1);

CFD_z = singleParticleConstants(2:101)';

dim_T_CFD = singleParticleConstants(102:end)';

A_param = X(1);

cost=0;

fprintf('A parameter value is %f\n',A_param)

% limit the range where your parameter can vary in

if(A_param >0 || A_param<5)

    cost=10000;

end

[dim_Temp_SP]= SingleParticle(A_param,CFD_z,CFD_Tf);

cost= cost+sum(abs( dim_T_CFD - dim_Temp_SP ));
```

```
end
```

```
%=====
```

```
%This section computes the difference between the expected and simulated temperatures %given  
the hypothetical parameter value
```

```
% CFD is a variable in which the first column is the curtain height values and second column %is  
the particle temperature values
```

```
CFD_z=CFD(:,1); %curtain height
```

```
CFD_Temp=CFD(:,2); %particle curtain temperatures
```

```
CFD_Tf=CFD(1,2); %final temperature
```

```
CFD_Ti=CFD(end,2); %initial temperature
```

```
dim_T_CFD=(CFD_Temp-CFD_Tf)/(400-CFD_Tf); %dimensionless temperature
```

```
options = optimset('MaxFunEvals', 8000, 'MaxIter', 8000,'FunValCheck','on');
```

```
[X, fval, flage] = fminsearch( @(X) myCostFunction(X, [CFD_Tf, CFD_z', dim_T_CFD']),  
[1],options);
```

```
[dim_Temp_SP]= SingleParticle(X(1),CFD_z, CFD_Tf);
```

```
figure;hold on;
```

```
plot(CFD_z,dim_T_CFD);
```

```
plot(CFD_z,dim_Temp_SP,'r');
```

```
title(['Optimum parameter found at ' num2str(X)])
```

```
grid on; legend('Experimental Data','Estimated Data')
```

B.2 Calculation of Particle Curtain Edges in the Thermal Images

%matrix PIXEL includes the temperatures data and corresponding pixel data in X direction.
%Matrix Y includes images pixels corresponding to Y direction

```
x=PIXEL(1,:);           % image pixels corresponding to the X direction.
T=PIXEL(2:end,:);       % temperature data
scale=659;               %scaling factor
X=x/scale;              %conversion of X direction pixels to meter
NewX=X-X(1);            % adjust X values from zero
y=Y/scale;              % conversion of Y direction pixels to meter

[Tmax row_int]=max(T,[],2);          % maximum temperature in each row
[initialTemp row_intMax]=max(Tmax);  % initial maximum temperature
newT=T(row_intMax:end,:);           % new matrix of temperature started from initial
%maximum temperature
newy=y(row_intMax:end,:);          % new matrix of y started from initial maximum temperature
Y1=newy-newy(1);                  % adjust Y values from zero
Y2=flipud(Y1);                   %returns "Y1" with its rows flipped in the up-down direction

figure (1);
plot(NewX,newT);
ylabel('Temperature (^oC)',FontSize',12);
xlabel('Curtain width (X(m))',FontSize',12);

%this section smoothes temperature profiles
SHAPE='valid';
sigma=1;
kernel_size=sigma*6;
if(mod(kernel_size,2)==0)
```

```

kernel_size=kernel_size+1;
end

h= genGaussian(kernel_size, sigma);
smoothedT=[];
for i=1:size(newT,1)
    pixel_values = newT(i,:);
    res = conv(pixel_values,h,SHAPE);
    smoothedT=[smoothedT;res];
end

if (SHAPE=='valid')
    X(end-((kernel_size-1)/2)+1:end)=[];
    X(1:((kernel_size-1)/2))=[];
end

NewX2=X-X(1);

figure(2);
plot(NewX2,smoothedT);
ylabel('Temperature (^oC)', 'FontSize', 12);
xlabel('Curtain width (X(m))', 'FontSize', 12);
TG=abs(gradient(smoothedT)); %gradient temperatures

figure(3);
plot(NewX2,TG);
ylabel('Temperature gradient (\sigmaT / \sigmaX)', 'FontSize', 12);
xlabel('Curtain width (X(m))', 'FontSize', 12);

[R C]=size(smoothedT);
[R1 C1]=size(NewX2);
if mod(C,2)==0;

```

```

halfX=mat2cell(NewX2,1,[C/2 C/2]);
halfTG=mat2cell(TG,R,[C/2 C/2]);
halfSmoothedT=mat2cell(smoothedT,R,[C/2 C/2]);
else
halfX=mat2cell(NewX2,1,floor([C/2+1 C/2]));
halfTG=mat2cell(TG,R,floor([C/2+1 C/2]));
halfSmoothedT=mat2cell(smoothedT,R,floor([C/2+1 C/2]));
end

[TGmax_1_val Col_int1]=max(halfTG{1},[],2); % Maximum temp-gradients that occur on the
%left edge
[TGmax_2_val Col_int2]=max(halfTG[106],[],2); % Maximum temp-gradients that occur on
%the right edge

for i=1:R;
xMax1(i)=halfX{1}(Col_int1(i));
xMax2(i)=halfX[106](Col_int2(i));
end

%this section defined extra points on the right and left sides of the maximum gradient
%temperature

for i=1:R;
ColintLeftL1(i)=Col_int1(i)-1;
ColintRightL1(i)=Col_int2(i)-1;
ColintRightR1(i)=Col_int2(i)+1;
ColintLeftR1(i)=Col_int1(i)+1;
end

```

```

ColintLeftL1D=ColintLeftL1';
ColintLeftR1D=ColintLeftR1';
ColintRightL1D=ColintRightL1';
ColintRightR1D=ColintRightR1';

ColintLeft=[ColintLeftL1D,Col_int1,ColintLeftR1D] ;
ColintRight=[ColintRightL1D,Col_int2,ColintRightR1D];

[colintLeftrowT colintLeftcolT]=size(halfTG{1});
[colintRightrowT colintRightcolT]=size(halfTG[106]);
[colintLeftrowX colintLeftcolX]=size(halfX{1});
[colintRightrowX colintRightcolX]=size(halfX[106]);

for i=1:colintLeftrowT
    LeftTG(i,:)=halfTG{1}(i,ColintLeft(i,:));      %temperature gradient at the left edge
    LeftSmoothedT(i)=halfSmoothedT{1}(i,Col_int1(i)); %temperature at the left edge
end

Xleft=halfX{1}(ColintLeft);
Xright=halfX[106](ColintRight);

for i=1:colintRightrowT
    RightTG(i,:)=halfTG[106](i,ColintRight(i,:));      %temperature gradient at the right edge
    RightSmoothedT(i)=halfSmoothedT[106](i,Col_int2(i)); %temperature at the right edge
end

exactXL=halfX{1}(Col_int1);
exactXR=halfX[106](Col_int2);

% this section fits polynomial on maximum temperature gradients
for e=1:R

```

```

TGfuncLeft(e,:)=polyfit(Xleft(e,:),LeftTG(e,:),2);
derivL(e,:)=polyder(TGfuncLeft(e,:));
realMaxL(e,:)=roots(derivL(e,:));

TGfuncRight(e,:)=polyfit(Xright(e,:),RightTG(e,:),2);
derivR(e,:)=polyder(TGfuncRight(e,:));
realMaxR(e,:)=roots(derivR(e,:));
end

figure(4);
Y2New=flipud(Y2);
plot(realMaxL,Y2New);
hold all
plot(realMaxR,Y2New);
set(gca,'YDir','reverse');
ylabel('Curtain height (Y(m))','FontSize',12);
xlabel('Curtain width (X(m))','FontSize',12);

```

B.3 Optimisation Code for Calculation of γ and δ

% In this section the residuals of equations are calculated

```
function obj_f = fitting_objective_fnc_11equ ( X, flags )  
% X(1)= gamma  
% X(2)= delta  
condition = flags(1);  
debug_flag = flags(2);  
  
% Equations to optimise  
if (condition==1 | condition==4)  
    E1 = 6.5 - 109.92 * X(1)*X(2) + 22.25 *X(1);  
    E2 = 17.17 - 89.66 * X(1)*X(2) + 18.75 *X(1);  
    E3 = 9.76 - 116.4 * X(1)*X(2) + 21.75 *X(1);  
    E4 = 24.64 - 83.5 * X(1)*X(2) + 17.5 *X(1);  
    E5 = 24.6 - 71.12 * X(1)*X(2) + 15.75 *X(1);  
end  
if (condition==2 | condition==4)  
    E6 = 1.95 - 126.62 * X(1)*X(2) + 24 *X(1);  
    E7 = 21.85 - 91 * X(1)*X(2) + 18.75 *X(1);  
    E8 = 22.82 - 78.37 * X(1)*X(2) + 16.25 *X(1);  
  
end  
if (condition==3 | condition==4)  
    E9 = 29.4 - 46.75 * X(1)*X(2) + 11 *X(1);  
    E10 = 5.29 - 33.68 * X(1)*X(2) + 8.25 *X(1);  
    E11 = -2.39 - 16.92 * X(1)*X(2) + 4.25 *X(1);  
end  
weight=0;  
if(X(1)<0 || X(1)>1 || X(2)<0 || X(2)>1)
```

```

weight=999999;
end

if (condition==1 )
    obj_f = weight + (E1 .^ 2) + (E2 .^ 2)+(E3 .^ 2) + (E4 .^ 2) + (E5 .^ 2);
    if debug_flag==1
        fprintf('*- For Gamma=<%f> and Delta=<%f> the errors are:\n E1 = %f\n E2 = %f\n E3
= %f\n E4 = %f\n E5= %f\n', X(1), X(2), E1, E2, E3, E4, E5) ;
    end
elseif (condition==2)
    obj_f = weight + (E6 .^ 2) + (E7 .^ 2) + (E8 .^ 2);
    if debug_flag==1
        fprintf('*- For Gamma=<%f> and Delta=<%f> the errors are:\n E6 = %f\n E7 = %f\n E8
= %f\n', X(1), X(2), E6, E7, E8 ) ;
    end
elseif (condition==3)
    obj_f = weight + (E9 .^ 2) + (E10 .^ 2) + (E11 .^ 2);
    if debug_flag==1
        fprintf('*- For Gamma=<%f> and Delta=<%f> the errors are:\n E9 = %f\n E10 = %f\n E11
= %f\n',X(1), X(2), E9, E10, E11 ) ;
    end
elseif (condition==4)
    obj_f = weight + (E1 .^ 2) + (E2 .^ 2) + (E3 .^ 2) + (E4 .^ 2) + (E5 .^ 2) + (E6 .^ 2) + (E7 .^ 2)
+ (E8 .^ 2)+(E9 .^ 2) + (E10 .^ 2) + (E11 .^ 2);
    if debug_flag==1
        fprintf('*- For Gamma =<%f> and Delta =<%f> the errors are:\n E1 = %f\n E2 = %f\n E3
= %f\n E4 = %f\n E5 = %f\n E6 = %f\n E7 = %f\n E8 = %f\n E9 = %f\n E10 = %f\n E11
= %f\n ',X(1), X(2), E1, E2, E3, E4, E5, E6, E7, E8, E9, E10, E11 ) ;
    end
end

```

```

%=====

% In this section nonlinear equations are solved using an optimization approach
options = optimset('MaxFunEvals', 800000, 'MaxIter', 800000,'FunValCheck','on', 'Display','on');

initial_gamma = 0.1;
initial_delta = 0.1;
condition = 4;           % condition 4 solves all eleven equations together
debug_flag = 0;
% optimization
[X, fval, flage] =fminsearch( @(X) fitting_objective_fnc_11equ (X, [condition, debug_flag]),
[initial_gamma, initial_delta], options);
if flage ~= 1
    fprintf('\n The process did not converge! Something is up ... \n')
end

optimized_gamma = X(1);
optimized_delta= X(2);

% check the optimized values in the equations
debug_flag = 1;
obj_f= fitting_objective_fnc_11equ ( [optimized_gamma,optimized_delta], [condition,
debug_flag] );

```

B.4 Optimisation Code for Calculation of x' Parameter

```
% this section defines the new particle pixel intensity (new_intensity_values) and adjusted  
%infrared temperature (Ttt )
```

```
function [Ttt,Ieq]= I_equation_3(A_param, Y, TIR, intensity_values)
```

```
Ic=57.57; %critical pixel intensity for conditions 1-6 (it varies at different conditions)
```

```
intensity_grdient = diff(intensity_values); % find the gradient of the input  
intensityintensity_grdient_step = A_param* intensity_grdient; % modify the constant gradient  
%based on the A_param  
new_intensity_values=[intensity_values(1)]; % this array will hold the newly computed  
%intensities based on the new gradient
```

```
for i=1:length(intensity_grdient_step)
```

```
    new_intensity_values=[new_intensity_values (new_intensity_values(end) +  
    intensity_grdient_step(i))];
```

```
end
```

```
Ieq = new_intensity_values';
```

```
Ttt = TIR.* (Ic./Ieq)-25*( (Ic./Ieq)-1); %calculation of adjusted infrared temperature (Ttt)
```

```
end
```

```
%=====
```

```
%This section is the entry point for the algorithm which controls the pre-defined parameters,  
%optimization and evaluation steps.
```

```
function [ cost ] = myCostFunction_3( X, CurveConstants )
```

```

TtY_costf= cell2mat( CurveConstants(1) );
Tt_costf = cell2mat( CurveConstants(2) );
TIR_costf = cell2mat( CurveConstants(3) );
intensity_values_costf = cell2mat( CurveConstants(4) );

A_param = X(1); % x parameter

cost=0;

fprintf('A parameter value is %f\n',A_param)

% limit the range where your parameter can vary in

[Ttt]= I_equation_3(A_param, TtY_costf, TIR_costf, intensity_values_costf);

p = polyfit([1:1:length(Tt_costf)],Tt_costf,1);m1=p(1);
p = polyfit([1:1:length(Ttt)],Ttt,1);m2=p(1);
% if(A_param >=2 || A_param <=-2 )
%     cost=999999999;
% end
% cost = cost + sum( ( m1 - m2 ).^2 );

cost= cost + sum( abs( Tt_costf - Ttt ) );
if( sum(Ttt > Tt_costf) > 10 )
    cost=999999999;
end

end

```

```
%=====
```

```
%This section computes the difference between the thermocouple and adjusted infrared  
%temperatures at various A_param (x parameter)
```

```
clc  
clear all  
close all  
load data.mat % Excel data contains  
options = optimset('MaxFunEvals', 88888888, 'MaxIter', 88888888, 'FunValCheck', 'on', 'TolX', 1e-  
6, 'TolX', 1e-6);  
[X, fval, flage] = fminsearch( @(X) myCostFunction_3(X, [ {Y}, {Tt}, {TIR},  
{intensity_values} ]), [0.05], options);  
[Ttt_opt, I_eq_opt]= I_equation_3(X(1),Y, TIR, intensity_values);  
fprintf('The convergence value is %f\n',fval)  
figure;hold on;  
plot(Y,Tt);  
plot(Y,Ttt_opt,'r');  
grid on; legend('T_{thermocouple}', 'T_{IR}_{-adjusted}')  
[Ttt_opt, I_eq_opt]= I_equation_3(X(1),Y, TIR, intensity_values);  
figure;hold on;  
plot(Y,Tt,'b');  
plot(Y,Ttt_opt,'r');  
plot(Y,TIR,'g');  
grid on; legend('T_{thermocouple}', 'T_{IR}_{-adjusted}', 'T_{IR}')  
figure;hold on;  
grid on; legend('T_{thermocouple}', 'T_{IR}_{-adjusted}')  
h1=plot(Y,Tt,'b');  
h2=plot(Y,TIR,'r');  
for A_param=[0.05,0.09,0.5,1] % 0 has been exluded since it would be identical to TIR (in red)  
    [Ttt,Ieq]= I_equation_3(A_param,Y, TIR, intensity_values);
```

```

h3=plot(Y,Ttt,'--g');
xlabel ('Curtain height (Y(m))');
ylabel ('Temperature (^oC)');
end

[Ttt_opt, I_eq_opt]=I_equation_3(X(1),Y, TIR, intensity_values);
h5=plot(Y,Ttt_opt,'black');
legend([h1 h2 h3 h5],{'T_{thermocouple}', 'T_{IR}', 'T_{IR}' at different parameters', 'T_{IR}_adjusted'});

figure ;hold on;h6=plot(Y,intensity_values,'r');

grid on;
for A_param=[0,0.05,0.09,0.5]

[Ttt,Ieq]=I_equation_3(A_param,Y, TIR, intensity_values);
h7=plot(Y,Ieq,'--b');
xlabel ('Curtain height (Y(m))');
ylabel ('Pixel intensity (I)');

end

h8=plot(Y,I_eq_opt,'black');
legend([h6 h7 h8],{'I_{Original}', 'I at different parameters', 'I_{adjusted}'});

```

B.5 CFD-Hybrid Model

```
function PDEsphere
Qconv = []; %convection heat transfer
Radiation=[]; %radiation heat transfer

%different particle sizes
d290=0.00029; %diameter[m]
d400=0.0004; %diameter[m]
d610=0.000610; %diameter[m]
r290=d290/2; %m
r400=d400/2; %m
r610=d610/2; %m

tmax=0.445; %falling time taken from CFD results[s]

% determining the equations for air temperature and particle heat transfer coefficient
polynomial_degree=8;
input_xls_file = 'matlab.xls'; % excel file containing heat transfer coefficient, time on
%streamline, curtain height and air temperature
contain_header_row = false;
time_column=2;
Y_column=3;
temperature_column=4;
HT_coef_column=1;
exclude_range_begin_T = NaN ;
exclude_range_begin_H = NaN ;

% read the xls file to load the input values
input_num = xlsread(input_xls_file);
```

```

% removing the text headers
if contain_header_row
    input_num(1,:)=[];
end

input_middle=ceil(size(input_num,1)/2); % data middle
[ dummy exclude_range_begin_T ]= min(input_num(input_middle:end, temperature_column) ); % index associated with the minimum of T (starts from middle)
[ dummy exclude_range_begin_H ]= min(input_num(input_middle:end, HT_coef_column) ); % index associated with the minimum of H (starts from middle)

common_min=input_middle + min([exclude_range_begin_T, exclude_range_begin_H]); % common minimum index between H and T

input_num([common_min:end],:)=[]; % removing the increasing tail of the data
T = input_num(:,temperature_column); % temperatures
t = input_num(:,time_column); % time
H = input_num(:,HT_coef_column); % HT_coef
Y=input_num(:,Y_column); %Y
equation_coef_T = polyfit(t, T, polynomial_degree);
equation_coef_H = polyfit(t, H, polynomial_degree);
equation_coef_Y = polyfit(t, Y, 3);
Y_value=polyval(equation_coef_Y,t);
figure(1); TT=polyval(equation_coef_T,t);[r2 rmse]=rsquare(T,TT); hold on;
plot(t,T,'r');plot(t,TT,'b');title([' R^2:' num2str(r2)])
ylabel('Air temperature (K)',FontSize',12);
xlabel('Time(s)',FontSize',12);
leg1 = legend('Original data','Fitted curve');

figure(2); HH=polyval(equation_coef_H,t);[r2 rmse]=rsquare(H,HH); hold on;
plot(t,H,'r');plot(t,HH,'b');title([' R^2:' num2str(r2)])
ylabel('Heat transfer coefficient (W.m^-^2.K^-^1)',FontSize',12);
xlabel('Time(s)',FontSize',12);
leg2 = legend('Original data','Fitted curve');

```

```

figure(3); plot(t,Y,'r');hold on;plot(t,Y_value,'b'); [r2 rmse]=rsquare(Y,Y_value);ylabel('Y
(m)', 'FontSize',12);title([' R^2:' num2str(r2) ])
xlabel('Time(s)', 'FontSize',12);
leg3 = legend('Original data','Fitted curve');

m=2;
r = linspace(0,r610,100); % in this example particle diameter is selected
t = linspace(0,t(end),100); %time is discretised between 0 to 100

%=====

T = pdepe(m,@pdefunc,@icfunc,@bcfunc,r,t) ;

```

```

figure(4), surf(r,t,T,...'FaceColor','interp',...
'EdgeColor','none',...
'FaceLighting','phong')

 xlabel('Radial distance(m)'), ylabel('Time(s)'),zlabel ('Temperature(K)')
figure(5), plot(t,T(:,end));
Tsurface=T(:,end);
TsurfaceNew=Tsurface';
xlabel('Time (s)'), ylabel('Tsurafce (K)')
Tcentre=T(:,1); %Centre Temperature [K]
Tradial=T(2,:);
assignin('base','Tcentre', Tcentre);
assignin('base','Tradial', Tradial);
assignin('base','T', T);
assignin('base','t', t);
assignin('base','r', r);

```

```

assignin('base','Tsurface',Tsurface);
assignin('base','Qconv',Qconv);
assignin('base','Radiation',Radiation);
assignin('base','equation_coef_Y',equation_coef_Y);
%=====

```

```
function [c,f,s] = pdefunc(r,t,T,DTDr)
```

```

rho = 2500;      % density [kg/m3]
cp = 830;        % heat capacity [J/kg.K]
k = 0.18;        % thermal conductivity [W/m.K]
c = rho*cp;
f = k.*DTDr;
s = 0;
end

```

```
%=====
```

```
% this section provides initial conditions
```

```
function T0 = icfunc(r)
```

```
T0 = 406.84;      %an example of initial particle temperature [K]
end

```

```
%=====
```

```
%this section describes boundary conditions
```

```
function [pl,ql,pr,qr] = bcfunc(rl,Tl,rr,Tr,t)
```

```

h = polyval(equation_coef_H,t);          %heat transfer coefficient correlation
Tinf = polyval(equation_coef_T,t);        %air temperature correlation

```

```

epsilon=5.67*10^-8; %W/(m^2.K^4) %Stefan Boltzmann constant
emissivity=1; %particle emissivity

pl = 0;
ql = 1/0.18;
pr= h*(Tr-Tinf)+epsilon*emissivity*(Tr^4-Tinf^4);
qr = 1;

qconv=3.14*(0.00061)^2*h*(Tr-Tinf); %[W] convective heat transfer
radiation=3.14*(0.00061)^2*epsilon*emissivity*(Tr^4-Tinf^4); %[W] radiation heat
%transfer
Qconv(end+1)=qconv;
Radiation(end+1)=radiation;

fprintf('t=%f Qconv=%f Radiation=%f TInf=%f H=%f TR=%f\n' ,t,qconv, radiation, Tinf, h,
Tr);
assignin('base','h', h);
end
end

%=====

%in this section the regression constant ( $R^2$ ) of the curves is calculated

function [r2 rmse] = rsquare(y,f,varargin)

if isempty(varargin); c = true;
elseif length(varargin)>1; error 'Too many input arguments';
elseif ~islogical(varargin{1}); error 'C must be logical (TRUE||FALSE)'
else c = varargin{1};
end

if isempty(varargin); c = true;
elseif length(varargin)>1; error 'Too many input arguments';
elseif ~islogical(varargin{1}); error 'C must be logical (TRUE||FALSE)'
else c = varargin{1};
end

```

```

% Compare inputs
if ~all(size(y)==size(f)); error 'Y and F must be the same size'; end

% Check for NaN
tmp = ~or(isnan(y),isnan(f));
y = y(tmp);
f = f(tmp);

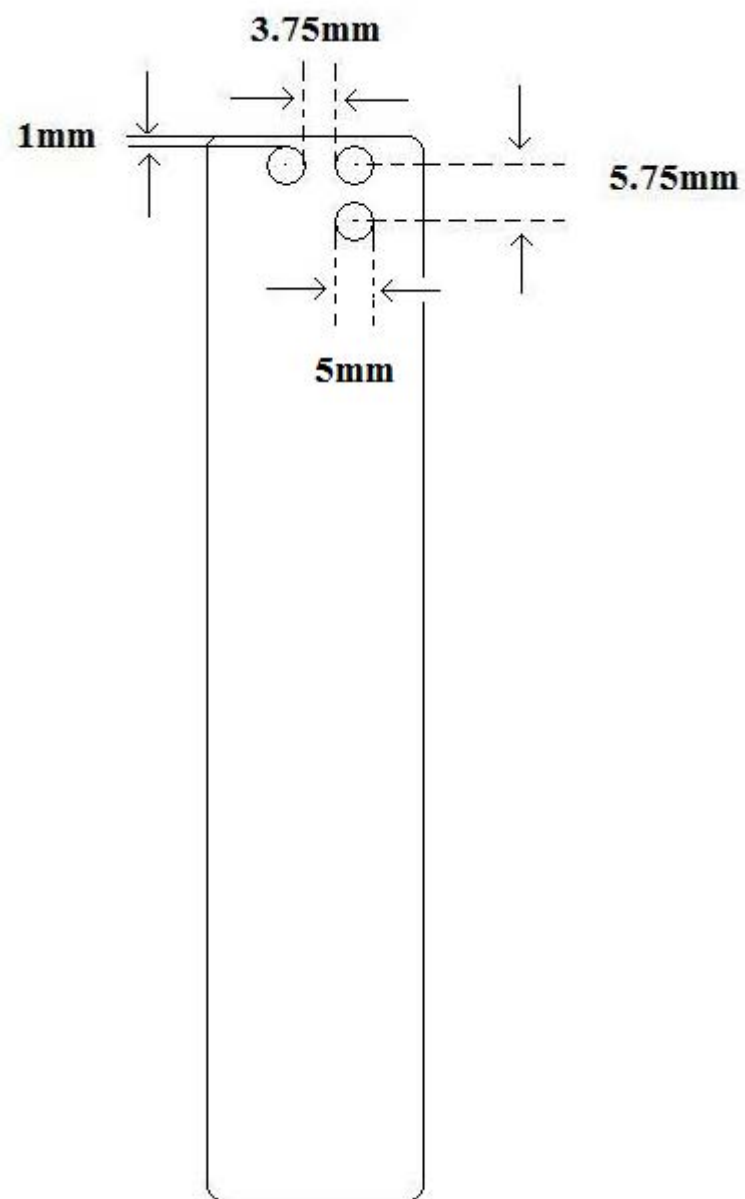
if c; r2 = max(0,1 - sum((y(:)-f(:)).^2)/sum((y(:)-mean(y(:))).^2));
else r2 = 1 - sum((y(:)-f(:)).^2)/sum((y(:)).^2);
    if r2<0

        r2 = 0;
    end
end
rmse = sqrt(mean((y(:) - f(:)).^2));
end

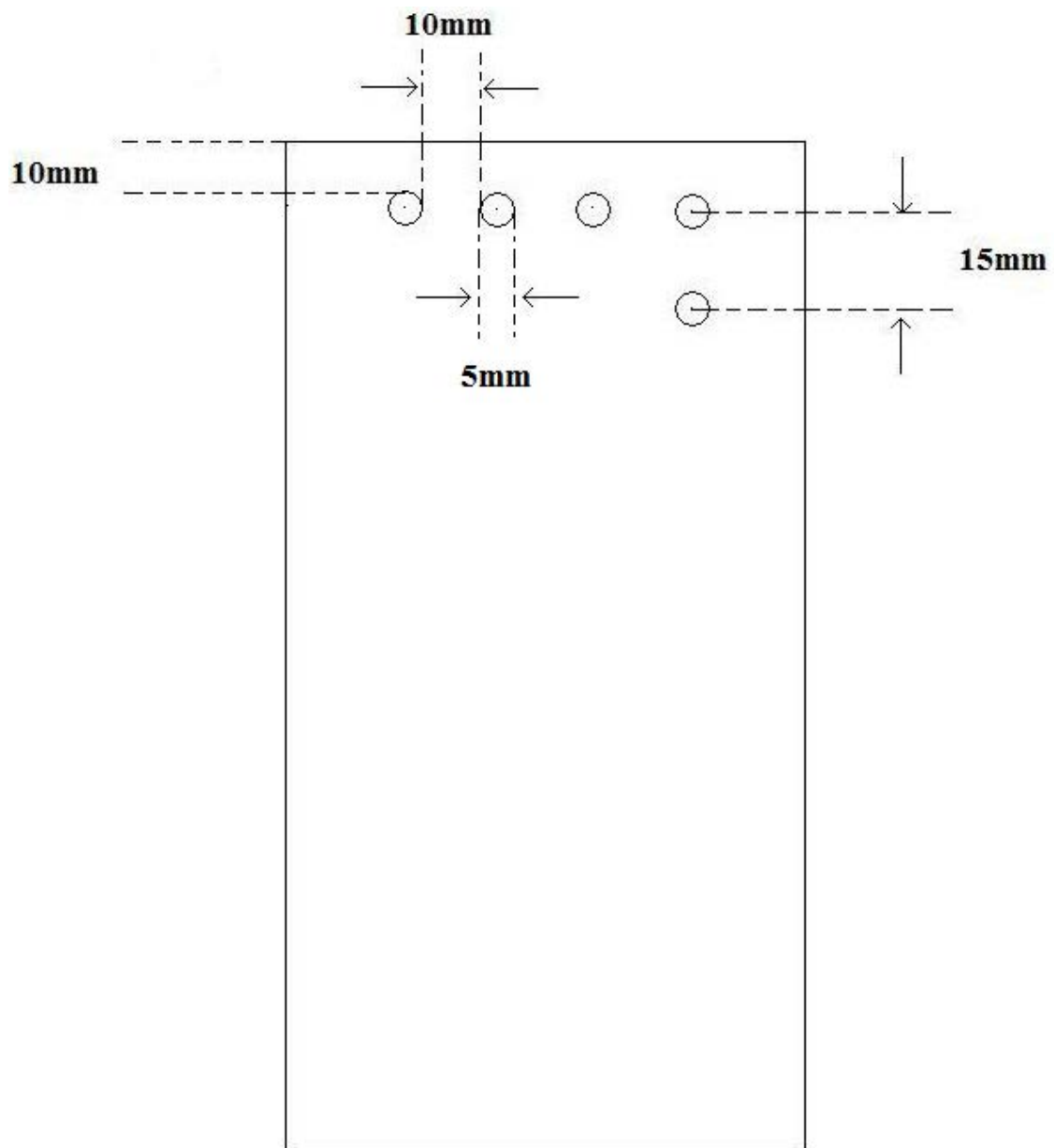
```

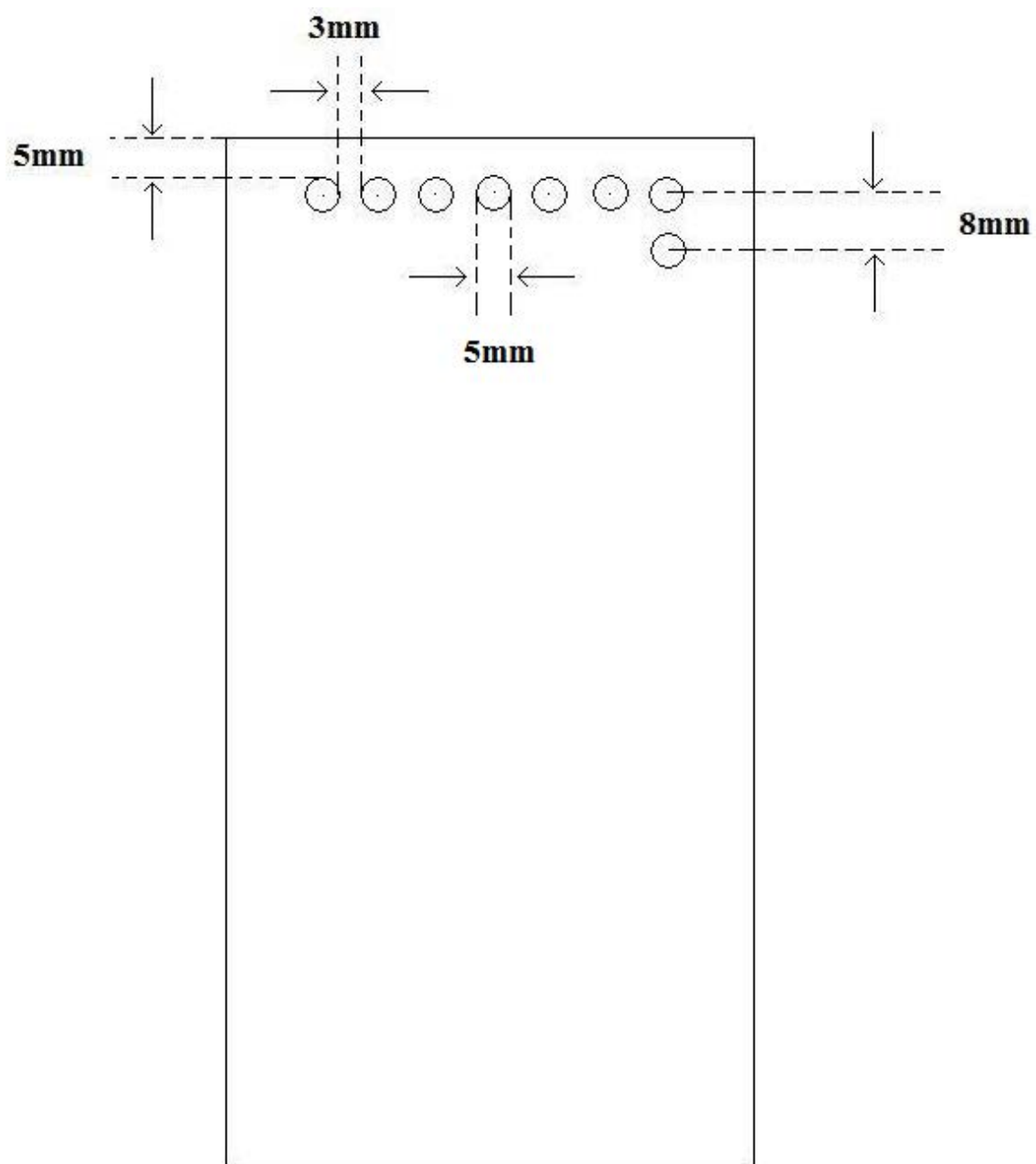
Appendix C, Apparatus Design

C.1 Perforated Plate for Slot width of 20mm

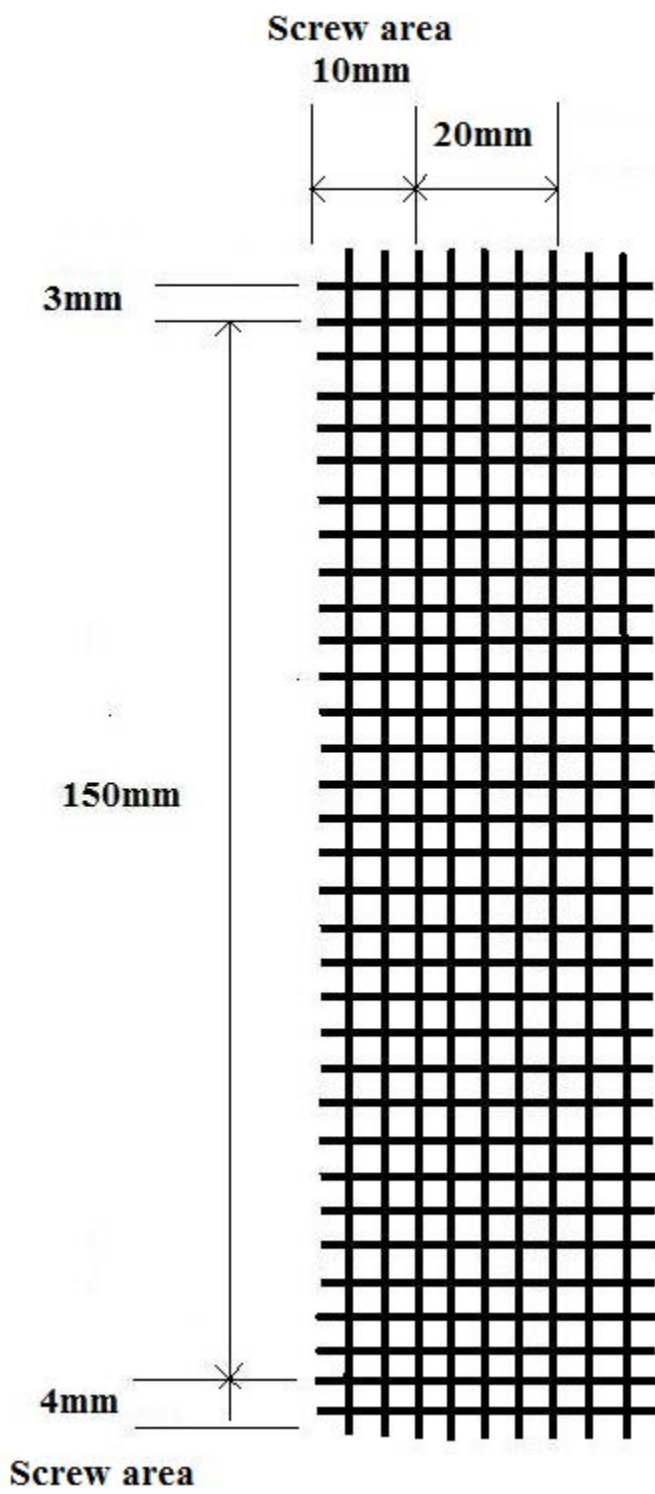


C.2 Perforated Plates for Slot Width of 60mm

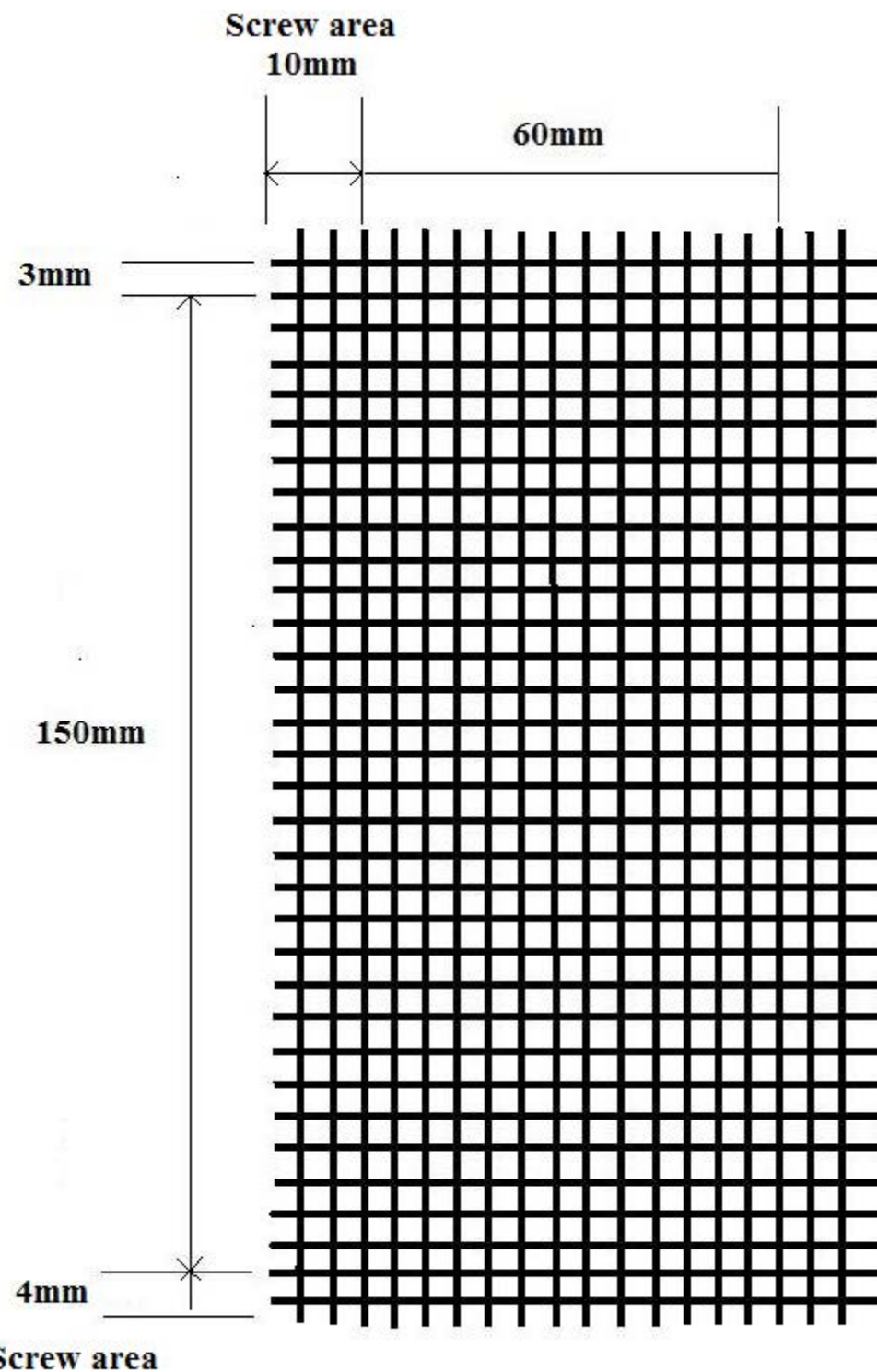




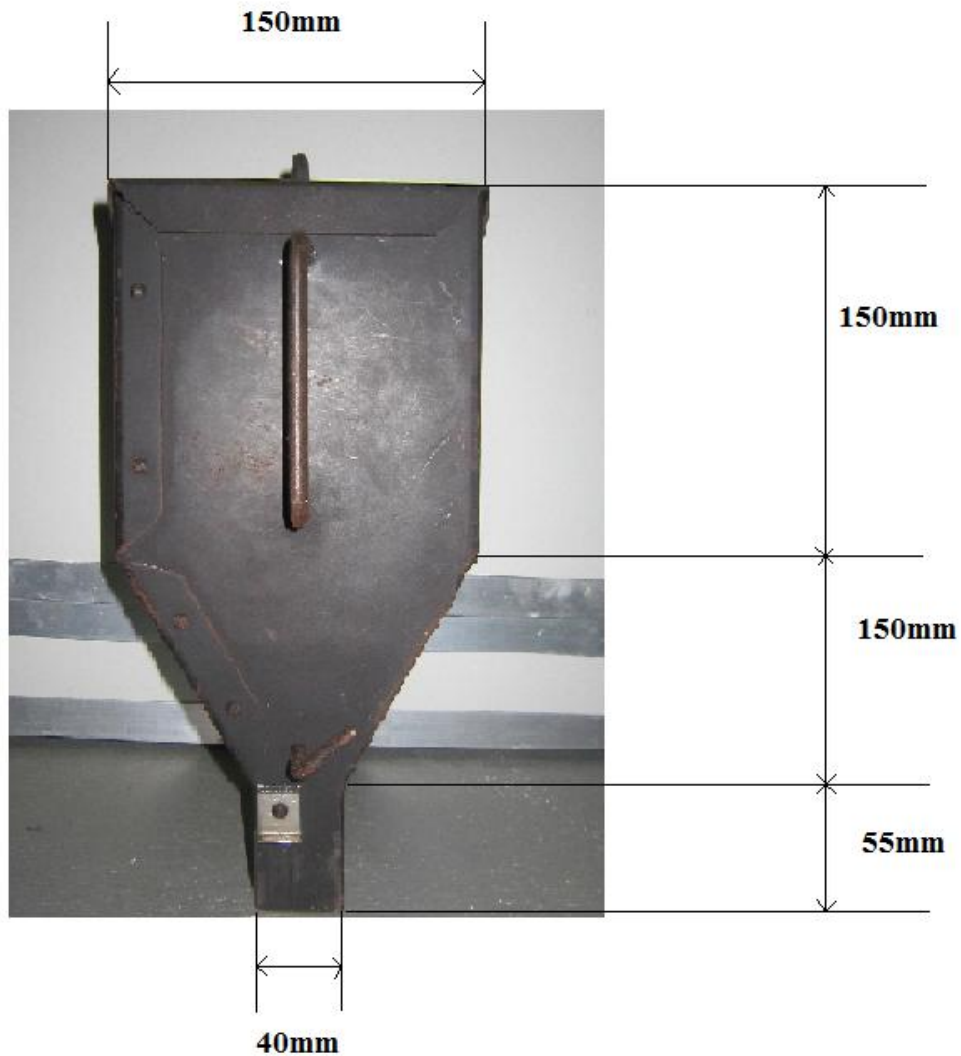
C.3 Wire Mesh Screen for Slot Width of 20mm



C.4 Wire Mesh Screen for Slot Width of 60mm



C.5 Hopper Dimensions



C.6 Hopper Valve

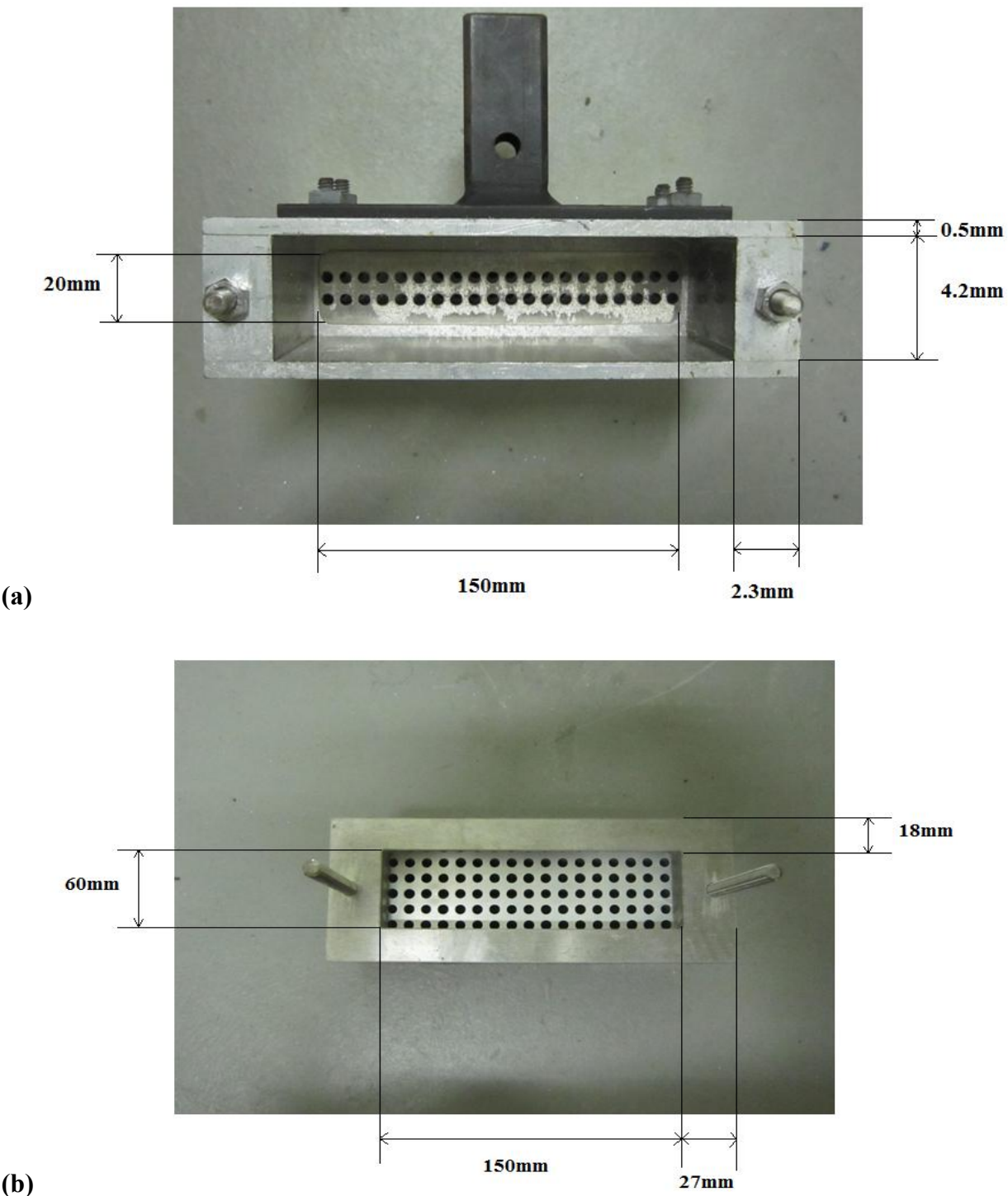


Fully Opened



Closed valve

C.7 Top View of Spreader Boxes: (a) 20mm (b) 60mm



C.8 Frontal View of Spreader Boxes: (a) 20mm (b) 60mm

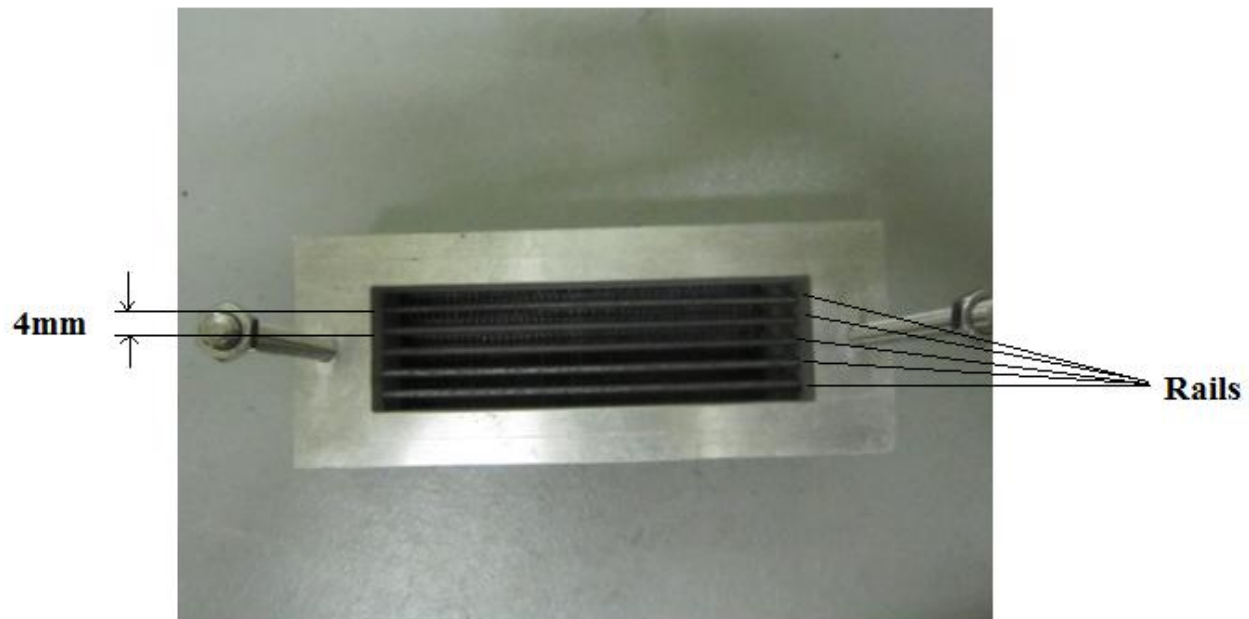


(a)



(b)

C.9 Top View of Rails in 60mm Spreader Box



Appendix D, Temperature Profiles from Thermocouple

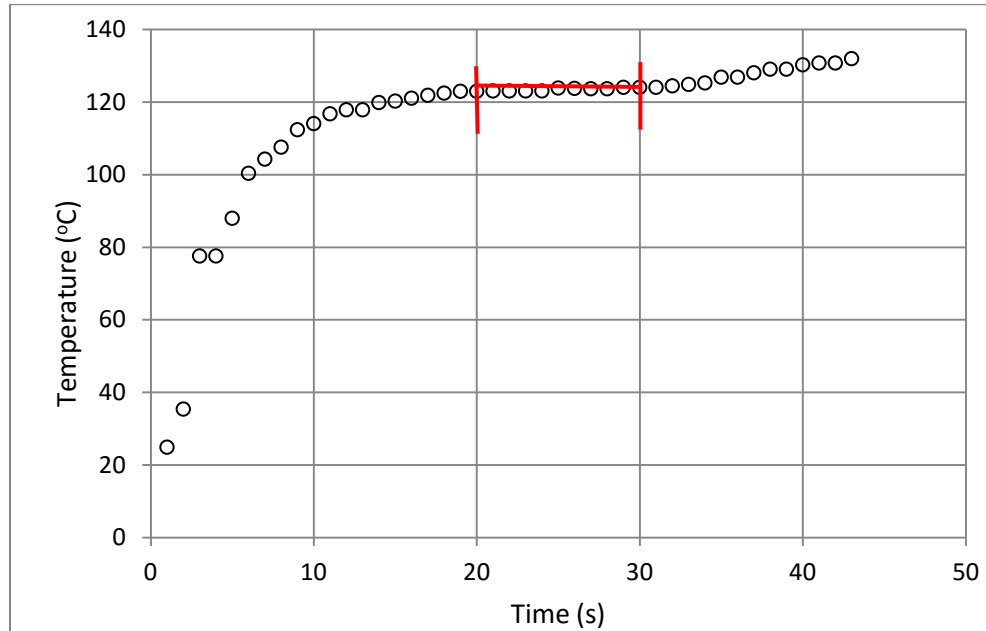


Figure D.1: Direct thermocouple temperature measurements, $Y=0.3\text{m}$, $d_s=290\mu\text{m}$, $m^o=0.15\text{kg/s}$, slot width= 20mm

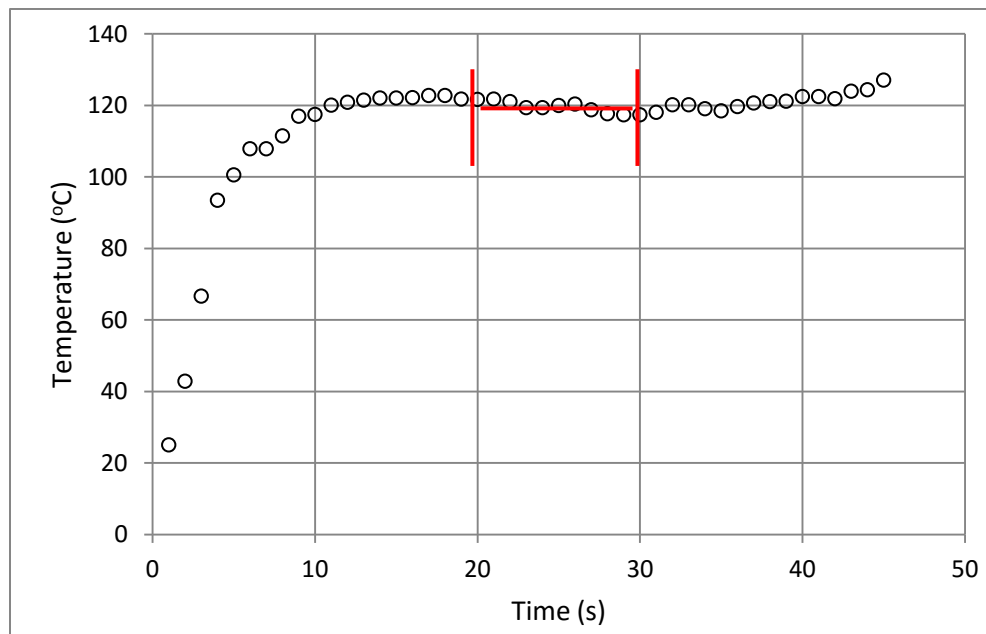


Figure D.2: Direct thermocouple temperature measurements, $Y=0.57\text{m}$, $d_s=290\mu\text{m}$, $m^o=0.151\text{kg/s}$, slot width=20mm

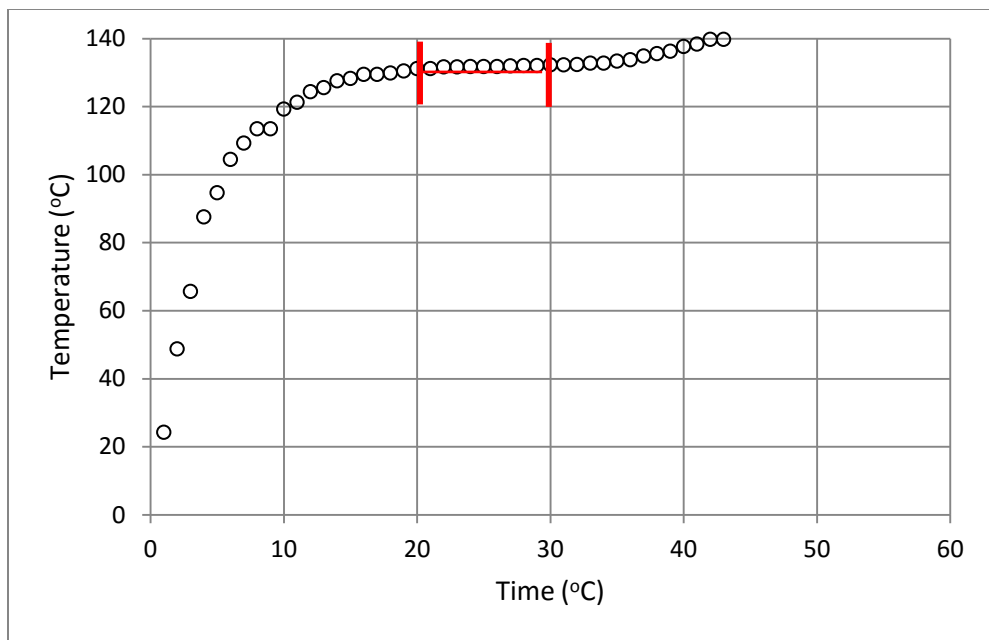


Figure D.3: Direct thermocouple temperature measurements, $Y=0.05\text{m}$, $d_s=400\mu\text{m}$, $m^o=0.137\text{kg/s}$, slot width=20mm

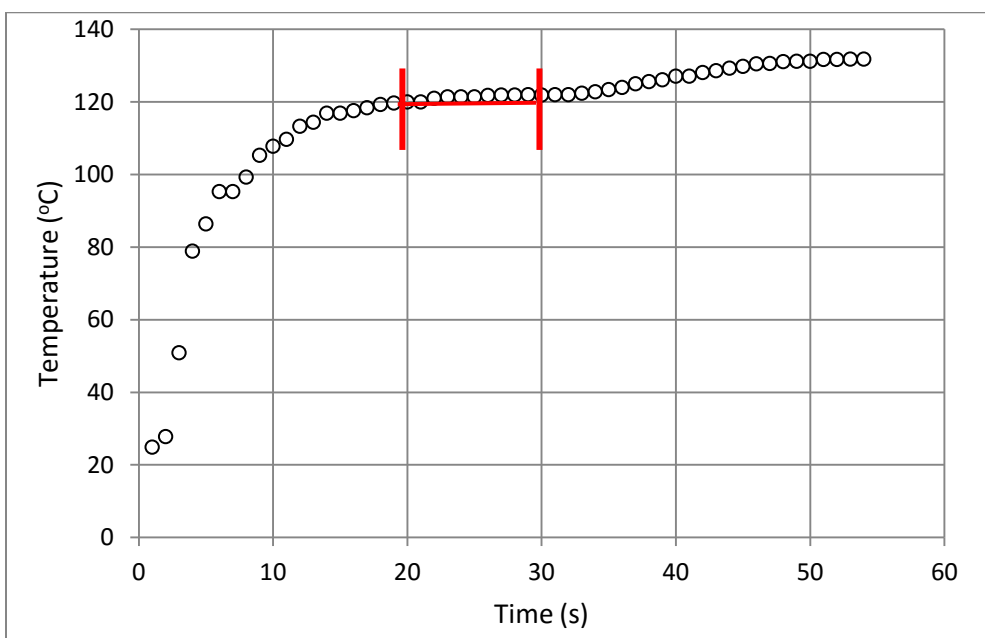


Figure D.4: Direct thermocouple temperature measurements, $Y=0.3\text{m}$, $d_s=400\mu\text{m}$, $m^o=0.131\text{kg/s}$, slot width=20mm

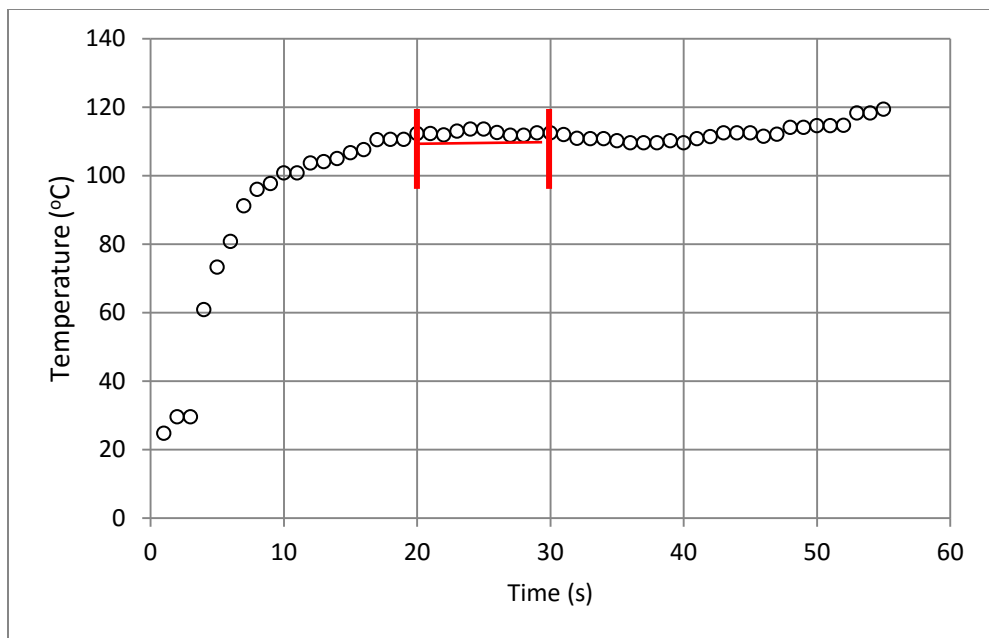


Figure D.5: Direct thermocouple temperature measurements, $\text{Y}=0.57\text{m}$, $d_s=400\mu\text{m}$, $m^o=0.127\text{kg/s}$, slot width=20mm

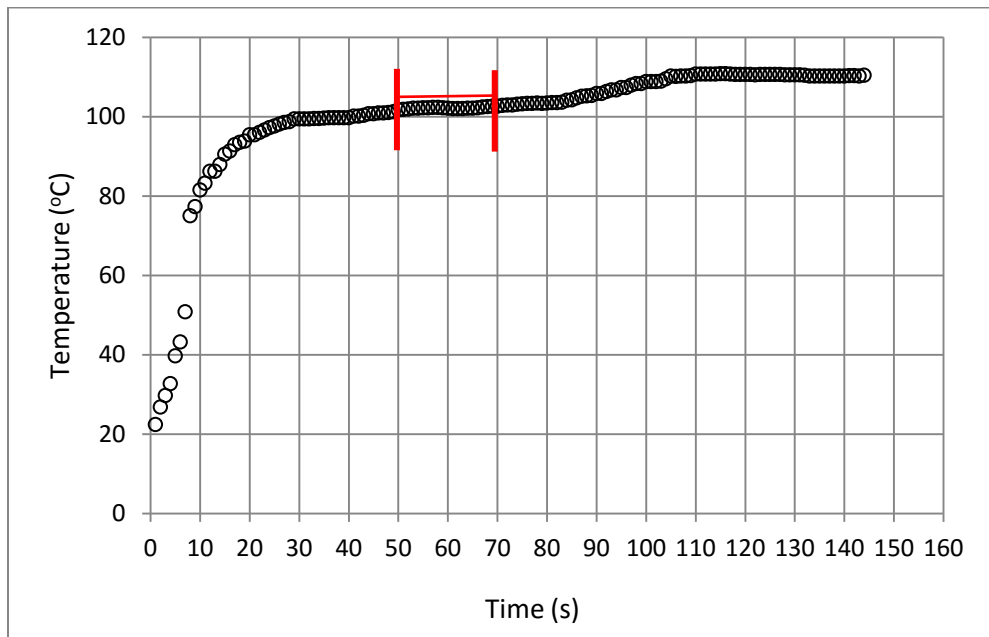


Figure D.6: Direct thermocouple temperature measurements, $\text{Y}=0.265\text{m}$, $d_s=610\mu\text{m}$, $m^o=0.045\text{kg/s}$, slot width=60mm

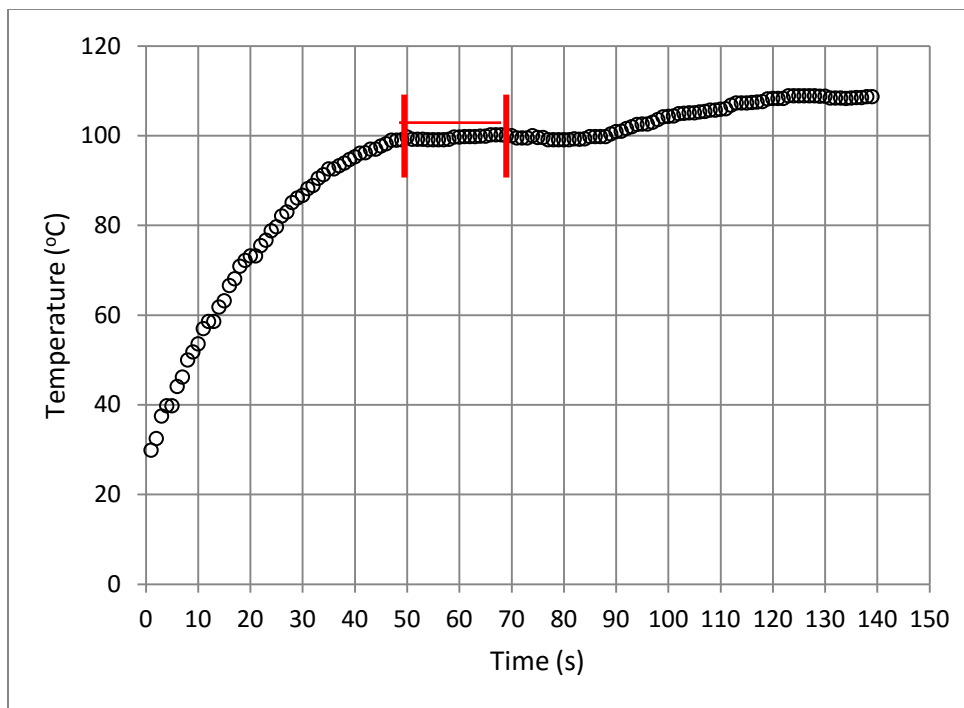


Figure D.7: Direct thermocouple temperature measurements, $Y=0.535\text{m}$, $d_s=610\mu\text{m}$, $m^o=0.045\text{kg/s}$, slot width=60mm

Appendix E, Filtered Visible Images

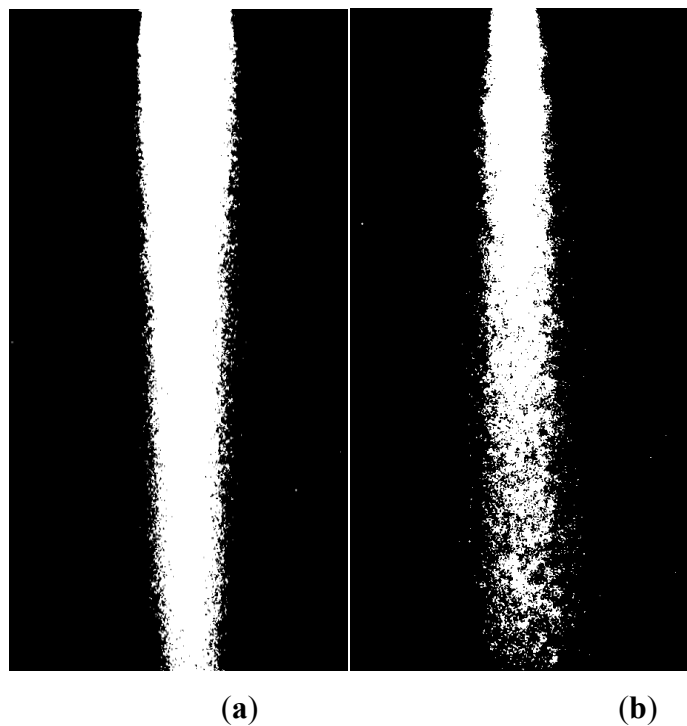


Figure E.1: Filtered visible images of the particle curtain using ImageJ (a) $d_s=290\mu\text{m}$, $m^o=0.145\text{kg/s}$ and slot width=60mm, Threshold value=27 (b) $d_s=610\mu\text{m}$, $m^o=0.089\text{kg/s}$ and slot width=20mm, Threshold value=21